DESIGN OF AN INSTRUMENTATION SYSTEM FOR A BOUNDARY LAYER TRANSITION WING GLOVE EXPERIMENT

A Thesis

by

THOMAS CLIFFORD WILLIAMS

Submitted to the Office of Graduate Studies of
Texas A&M University
in partial fulfillment of the requirements for the degree of

MASTER OF SCIENCE

Approved by:

Chair of Committee,	William S. Saric
Committee Members,	Helen L. Reed
	Andrew Duggleby
Head of Department,	Dimitris Lagoudas

December 2012

Major Subject: Aerospace Engineering

ABSTRACT

Laminar flow control holds major promise for increasing aircraft efficiency and increasing laminar flow over aerodynamic surfaces could decrease drag by up to 30 percent. The Flight Research Lab at Texas A&M University has studied laminar flow over a wing with 30 degrees of leading edge sweep with Discrete Roughness Elements (DREs) installed and has indicated that DREs can be used to increase laminar flow at Reynolds numbers up to 7.5 million at Mach 0.3. A new project, termed SARGE, has been commissioned in conjunction with NASA for studying DREs on a swept wing glove at conditions relevant to jet transports.

The SARGE project must have an instrumentation system capable of accurately measuring flow conditions and transition location on the suction side of the glove. Infrared (IR) thermography has been selected as the primary transition detection tool. A heat transfer analysis has shown that solar radiation will warm the surface of the glove above the adiabatic wall temperature and therefore the laminar region will appear to be warmer. The FLIR SC8000 IR camera has been selected for this application due to its ability to produce high-resolution images in the appropriate IR band.

High quality air data is also required for the experiment. A five-hole probe will be used to measure flow angle and velocity near the glove. This instrument will provide meanflow conditions due to its limited frequency response. High quality pressure transducers coupled with careful probe calibration will allow for differential measurements to be made with an uncertainty of ±0.03º. Static pressure ports and high frequency response Kulite transducers will also be employed.

Hotfilm sensors will be used to verify the state of the boundary layer on the glove through spectral analysis. A unique hotfilm array has been proposed that will enable the measurement of traveling wave vectors through a spectral technique. An experiment on the Flight Research Lab's Cessna O-2 to investigate the veracity of this technique has also been suggested.

Thermocouples will also be installed on the glove's surface to monitor temperatures and verify transition location. The layout of the hotfilms and thermocouples is also detailed.

DEDICATION

This work is dedicated to my parents, John and Yvonne Williams, for their love and support throughout my education. Without their direction none of this would have been possible.

ACKNOWLEDGEMENTS

Flight has captivated me since the earliest days I can remember. I spent countless hours building model airplanes, playing on flight simulators, and reading about aircraft during my childhood and my enthusiasm has only grown to this day. For the past two years I have had the privilege of studying aerospace engineering at Texas A&M University at the Flight Research Laboratory. I will take away many important lessons, both technical and personal, from my time in College Station.

To begin, I would like to thank my advisor, Dr. William Saric, for giving me the opportunity to study and work at the Flight Lab. His strong example of hard work and technical excellence has been instrumental in my development as a student and a professional. I will always benefit from holding to the standards of performance that he sets for his students. Dr. Saric has helped me to enhance my knowledge in technical fields that are too numerous to list here. I would also like to thank the other members of my committee, Dr. Helen Reed and Dr. Andrew Duggleby. I have benefited from their support and guidance throughout the process of my studies. Their insights into technical problems and willingness to assist me whenever possible have truly been an asset to me. A special thank-you also goes to Colleen Leatherman for all that she does to keep our group's logistics running smoothly. The questions she has answered and the travel itineraries she has made for me during my time here have helped me tremendously.

I have had the privilege of working with some of the most talented students and staff I have ever met and with whom I am proud to be associated. I am especially indebted to my fellow graduate students at the Flight Lab: Josh Fanning, Tom Duncan, Brian Crawford, and Simon Hedderman. Their words of advice and encouragement throughout the course of my work have always been warmly received. The individual incidences of homework help, technical suggestions, flight crew duties, and manual labor are too many to list, but their assistance with all of them is deeply appreciated. A special acknowledgement goes to staff members Cecil Rhodes and David West. Cecil's dedicated work maintaining the O-2 has allowed us to perform over 100 safe operations since I began my studies. I am thankful for all of the questions he has answered and the times that he has been on call to help on weekends or holidays.

David's help with making laser scans of my hotfilms and with flight duties around the lab has also been a key to my own success. I wish him the best of luck entering the world of the Flight Lab graduate student this fall, I'm sure he'll do great.

I am also indebted to the graduate students, principle investigators and NASA employees on the SARGE project for their assistance with my work. I would like to acknowledge Dr. Saric and Dr. Reed for their technical guidance and for giving their research assistants so much freedom to learn and solve problems. I would also like to thank Mike Belisle, Matt Roberts, and Matt Tufts, for their assistance with CFD and stability computations. I appreciate their hard work and willingness to assist me whenever I had a computational favor to ask. A special thank-you also goes to Lt. Col. Aaron Tucker, USAF, for his technical insights, example of excellence, and words of advice and encouragement. I also wish to thank Ethan Baumann and Mark Davis of NASA Dryden for their technical interaction and hard work on the SARGE project.

The Flight Lab couldn't live up to its name without test pilots, and I, along with the rest of the Lab's students, am appreciative of the assistance provided by Lt. Col. Tucker and Lee Denham. I am grateful to Lt. Col. Tucker for teaching our crew the lessons he has learned from his experiences as an Air Force test pilot. I have no doubt that our operations were safer, more efficient, and more professional thanks to his inputs. I would also like to thank Lee for all of those early mornings when he showed up eager to help us with our experiments. Additionally, I thank Lee for donating his time to help me learn how to fly a Beech Sundowner and introducing me to instrument procedures. I have learned many lessons about airmanship and what it means to be a professional pilot from both Lee and Aaron and for that I will be forever grateful.

Finally, I would like to acknowledge the special contributions of my family throughout my education. I would like to thank my parents for always demanding that I do my best regardless of what I was doing. Looking back now, I am grateful that they refused to let me take the easy way out and worked so hard to make sure that I had the tools I needed to succeed. I thank them for their selfless sacrifice to ensure that I was able to achieve my goals even at the expense of their own. I will do well to emulate their example going forward. I would also like to thank my grandparents for their support. I have always been able to

count on a weekly note of encouragement and a little extra cash in the mail from my grandmother. I am uniquely blessed to have grandparents who make it a priority to engage in helping me to succeed.

I owe a large portion of my success to those listed above and many more that I haven't the room to list here. My time at Texas A&M has blessed me with new knowledge and new relationships that I will always carry with me. My thanks go to every student who I have worked with on homework problems, projects, or used as a sympathetic party to gripe about classes. I also wish to thank the faculty members who have taught my classes and enabled me to learn material that I would never have dreamed I could have begun to understand. I am truly blessed to call myself a proud Aggie.

My work would not have been possible without the financial support from the following contracts: ViGYAN sub-recipient agreement number C10-00350, ATK Space Systems, Inc. sub-contract number PO-SP00029509, and Analytical Mechanics Associates, Inc. contract number NNL12AA09C. Thank you to these organizations for backing my work in the field of boundary layer stability and transition.

NOMENCLATURE

A/A_0	Disturbance Amplitude Divided by Initial Amplitude
AC	Alternating Current
AoA	Angle of Attack
AoSS	Angle of Sideslip
ASCII	American Standard Code for Information Interchange
ASHRAE	American Society of Heating, Refrigeration and Airconditioning Engineers
BNC	Barrel Nut Connector
c	Chord Length
c_{AIR}	Specific Heat of Air
*	Complex Conjugate
CF	Crossflow
CFD	Computational Fluid Dynamics
c_f	Skin Friction Coefficient
$c_{gr,n}$	Group Velocity Measured by Sensor-n
C_N	ASHRAE Clearness Factor for Solar Radiation
c_p	Pressure Coefficient
c_{pr}	Specific Heat of Air at Constant Pressure
$c_{ph,n}$	Phase Velocity Measured by Sensor-n
dB	Decibel
DC	Direct Current
DREs	Distributed Roughness Elements
°	Degrees
∅	Diameter
d_n	Distance between Datum and Comparison Sensor-n

ERA	Environmentally Responsible Aviation
e^N	Smith-Van Ingen Amplification Factor
ESP	Electronic Pressure Scanner
FRL	Flight Research Lab
F-S	Falkner-Skan
F-S-C	Falkner-Skan-Cooke
ft	Feet
f	Frequency
f_η	Similarity Position Function
$f''_{\eta w}$	Similarity Shear Stress Value at Wall
FTE	Flight Test Engineer
g	Acceleration due to Gravity
G-III	Gulfstream G-III Business Jet
g_{CF}	Crossflow Similarity Variable for the Falkner-Scan-Cooke Boundary Layer
g_{CF_w}	Value of Crossflow Similarity Variable for the Falkner-Scan-Cooke Boundary Layer at the Wall
G_d	Diffuse Solar Radiation
G_D	Direct Radiation Incident on Surface Under Evaluation
GigE	Gigabit Ethernet
GPS	Global Positioning System
G_{ND}	Normal, Direct Solar Radiation
G_{SUN}	Total Solar Radiation Incident on Surface Under Evaluation
G_{xx}	Auto-Spectral Correlation of the Datum Signal
G_{xy}	Cross-Spectral Correlation
G_{yy}	Auto-Spectral Correlation of the Comparison Signal
Hz	Hertz

h	Convection Coefficient
h_e	Stagnation Enthalpy at the Boundary Layer Edge
h_s	Stagnation Enthalpy at an Arbitrary Location in the Boundary Layer
h_w	Stagnation Enthalpy at the Wall
h_0	Freestream Stagnation Enthalpy
Im	Imaginary Part of Complex Number
in	Inches
∞	Infinity
InSb	Indium Antimonide
I/O	Input/Output
IR	Infrared
K	Kelvin
k_{AIR}	Thermal Conductivity of Air
k_f	Thermal Conductivity of Fluid Under Evaluation
kHz	Kilo-Hertz
L	Reference Length for Natural Convection
LAT	Lattitude in Degrees North
L/D	Lift to Drag Ratio
LST	Linear Stability Theory
M	Million
M_e	Edge Mach Number
M_∞	Freestream Mach Number
m_h	Power Law Exponent
mK	Milli-Kelvin
mm	Millimeter
NASA	National Aeronautics and Space Administration

n_d	Number of Window Functions Used
Nu	Nusselt Number
O	Origin
p	Pressure
$\bar{p}$	Average Pressure
p'	Pressure Disturbance Amplitude
$P_{1\text{-}6}$	Differential Pressure between Five-hole Probe Ports 1 and 6
$P_{2\text{-}3}$	Differential Pressure between Five-hole Probe Ports 2 and 3
$P_{4\text{-}5}$	Differential Pressure between Five-hole Probe Ports 4 and 5
P_6	Five-hole Probe Port 6 Pressure
Pa	Pascal
Pa-s	Pascal-Seconds
P_e	Edge Pressure
Pr	Prandtl Number
PSD	Power Spectral Density
PSE	Parabolized Stability Equations
psi	Pounds per Square Inch
psia	Pounds per Square Inch Absolute
psid	Pounds per Square Inch Differential
PPT	Precision Pressure Transducer
q	Normal Mode Amplitude
q'	Disturbance Amplitude
R	Reynolds Number
Re	Real part of Complex Number
Re_c	Chord Reynolds Number
Re_w	Reynolds Number at the Wall

Re_x	Reynolds Number at Position x
rms	Root Mean Squared
RS-232	RS-232 Serial Communication Protocol
RS-485	RS-485 Sserial Communication Protocol
s	Arc Length
S	Similarity Enthalpy Function
S_w	Similarity Enthalpy Function Value at Wall
SARGE	Subsonic Aircraft Roughness Glove Experiment
SWIFT	Swept Wing In-Flight Test
t	Time
T	Temperature
$\bar{T}$	Average Temperature
T'	Temperature Disturbance Amplitude
T_{AL}	Stagnation Temperature of Velocity Component Normal to Leading Edge
T_e	Edge Temperature
T_∞	Freestream Static Temperature
T_w	Wall Temperature
T_s	Surface Temperature
t_w	Time Elapsed per Window Function
T_0	Stagnation Temperature
TAMU	Texas A&M University
T-S	Tollmien-Schlichting
Tu	Turbulence Level
u , v	Orthogonal Velocity Components
$\bar{u}$, $\bar{v}$	Orthogonal Average Velocity Components
u' , v'	Orthogonal Disturbance Velocity Components

U,V,W	Orthogonal Freestream Velocity Components
u_e	Edge Velocity
U_e	Transformed Streamwise Edge Velocity
U_∞	Infinite Freestream Velocity in x-Direction
USB	Universal Serial Bus
V	Volts
$\bar{V}$	Individual Hotfilm Velocity Vector
VGA	Video Graphic Array
$\bar{W}$	Resultant Hotfilm Velocity Vector
w_h	Hann Window
x, y, z	Orthogonal Cartesian Coordinate System
x_s, y_s, z_s	Orthogonal Cartesian Coordinate System with Respect to Leading Edge
x_t, y_t, z_t	Orthogonal Cartesian Coordinate System with Respect to Streamline Tangent
X, Y	Orthogonal Coordinates Transformed with Stewartson's Transformation
X_k	Fourier Transform of the k^{th} Window of the Datum Signal
Y_k	Fourier Transform of the k^{th} Window of the Comparison Signal
y_n	Surface-Normal Direction
α	Streamwise Wavenumber
α_i	Streamwise Wavenumber Imaginary Component
β	Spanwise Wavenumber
β_H	Hartree Parameter
β_r	Spanwise Wavenumber Real Component
β_S	Sun Zenith Angle
γ	Ratio of Specific Heats
γ_{xy}	Cross-spectral Correlation Coherence Function
$\Delta\theta_{xy}$	Phase Shift between Datum and Comparison Sensors

Δx_n	Distance between Datum Sensor and Sensor-n with Same Orientation
θ	Zenith Angle between Sun and Surface Normal Vector
θ_{HT}	Similarity Enthalpy Function for the Falkner-Skan-Cooke Boundary Layer
θ_{xy}	Phase Angle
Λ	Wing Sweep Angle
μ_{AIR}	Dynamic Viscosity of Air at Condition Under Evaluation
μ_0	Dynamic Viscosity Evaluated at Stagnation Temperature
μm	Micrometer
ν_w	Kinematic Viscosity Evaluated at Wall Temperature
ν_0	Kinematic Viscosity Evaluated at Stagnation Temperature
ρ	Density
$\bar{\rho}$	Average Density
ρ'	Density Disturbance Amplitude
ρ_{AIR}	Density of Air at Condition under Evaluation
ρ_∞	Freestream Static ensity
ρ_w	Static Density at the Wall
ρ_0	Stagnation Density
τ_w	Wall Shear Stress
ω	Disturbance Frequency

TABLE OF CONTENTS

Page

LIST OF FIGURES

LIST OF TABLES

1. INTRODUCTION

This thesis describes an instrumentation system designed to support a boundary layer transition wing glove experiment to be conducted on a Gulfstream G-III aircraft. A comprehensive review of previous laminar flow control flight experiments and their respective instrumentation systems can be found in AGARD's report on laminar flow control flight tests (Fisher *et al.* 2003). The experiment detailed herein has been based on NASA's Discrete Roughness Element Laminar Flow Glove Experiment (DRELFGE), colloquially known as the Subsonic Aircraft Roughness Glove Experiment (SARGE). This project is administered by NASA's Environmentally Responsible Aviation (ERA) program, which is responsible for defining requirements and success criteria. The instrumentation package installed for SARGE must be capable of providing data to be used in order to determine if ERA's success criteria have been met. This system is to collect air freestream air-data as well as determine the state of the boundary layer on the model as a function of position. This work puts particular emphasis on analyzing the design stage uncertainty and frequency response of a five-hole probe and Kulite pressure transducer air data system. A heat transfer analysis on the surface of the glove has also been performed in order to identify the dominant physical phenomena that will affect the efficacy of using infrared thermography as the primary means for measuring boundary layer transition location. Additionally, a unique hotfilm array design and analysis technique for measuring traveling wave vectors has been proposed, along with a corresponding experiment to be conducted on a Cessna O-2 aircraft.

The implementation of laminar flow technology is widely regarded as a major opportunity for the aviation community to realize significant cost savings. As part of the effort to realize these savings, the research team at the Texas A&M Flight Research Lab (FRL) has engaged in research exploring boundary layer transition and control on swept wings in the flight environment. Experiments at the FRL have centered around controlling the crossflow instability present on swept wings using Distributed Roughness Elements (DREs) and have shown that DREs, in conjunction with careful sculpting of the pressure distribution along the wing's surface, can successfully control transition to turbulence. This research has been performed on the SWIFT test wing with 30 degrees of leading edge sweep at chord Reynolds

numbers of 7.5 million and 0.3 Mach number using a Cessna O-2 aircraft. Details of these experiments can be found in Carpenter (2009).

The SARGE project is a facet of NASA's ERA program and hopes to extend the DRE work done at 7.5 million chord Reynolds number and Mach 0.3 to Reynolds numbers of 22 to 30 million at Mach numbers between 0.65 and 0.75. The SARGE project intends to install a glove onto the wing of a G-III aircraft in order to modify the outer mold line of the platform aircraft into an airfoil amenable to laminar flow control using DREs. The glove is to be installed near the mid-span of the G-III's port wing and will have a test section that spans six feet. The ERA program has stipulated that the glove must have a leading edge sweep of at least 30 degrees, and that the airfoil must operate at a section lift coefficient of at least 0.5, which is relevant to transonic transport class aircraft. Also, the glove must maintain natural laminar flow to at least 60 % chord at Reynolds numbers between 15 and 22 million. Finally, DREs must be shown to increase the glove's extent of laminar flow in the streamwise direction by 50 % compared to a clean wing configuration. A detailed description of the SARGE project's requirements and the glove's design philosophy can be found in Belisle *et al.* (2011). A rendering of the G-III with the SARGE glove installed is shown in Figure 1.

Figure 1 Rendering of the G-III with wing glove installed.

A. Motivation

Laminar flow control holds major promise for increasing fuel efficiency and thereby reducing aircraft operating costs and increasing range and endurance through the reduction of skin friction drag. It has been estimated that laminar flow technology could reduce the fuel burn of transport aircraft by as much as 30 percent (Braslow 1999). Increasing the extent of laminar flow on aircraft surfaces may hold the most promise for achieving significant efficiency improvements on current airframe designs.

The Breguet Range Equation clearly defines fuel burn in terms of aircraft weight, energy density of fuel, aerodynamic efficiency and propulsive efficiency. The structural weight of aircraft will continue to decrease as stronger materials and better construction practices are introduced. Modern jet fuel has the highest energy density of any alternative fuel source with the exception of liquid hydrogen, which is currently impractical due to safety concerns (Green 2008). The second law of thermodynamics places an upper bound on propulsive efficiency, and many modern engines are approaching this limit (Green 2008). With these considerations in mind, increasing aerodynamic efficiency is the only remaining category that could potentially yield significant improvement in fuel burn rate.

The best measure of an aircraft's aerodynamic efficiency is its lift-to-drag ratio (L/D). This ratio states the obvious: it is desirable to increase lift and decrease drag. High aspect ratio wings and wingtip devices can be used to reduce downwash, which increases lift while reducing lift-induced drag. However, high aspect ratio wings and wing tip devices increase aircraft structural requirements, which may negate any aerodynamic benefit. Additionally, high aspect ratio wings can suffer from high wave drag on high-speed aircraft. Wing tip devices such as blended winglet have been implemented on current airliners with success. However, drag reduction, specifically profile drag reduction through the use of laminar flow, holds the greatest promise for achieving significant gains in fuel efficiency (Green 2008). It has been estimated that nearly 50 percent of drag on modern transport aircraft is the result of skin friction (Marec 2000). A breakdown of aircraft drag components suggested by Marec (2000) is shown in Figure 2.

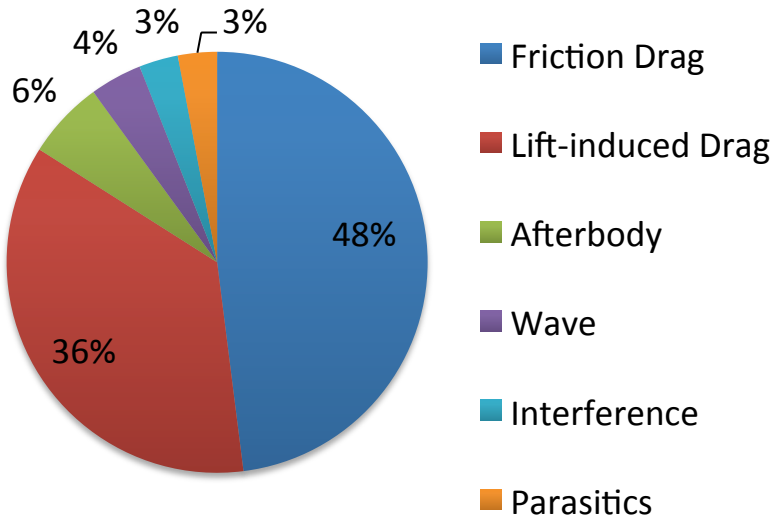

Figure 2 Drag breakdown.

Additionally, the suction side of transonic airfoils accounts for nearly 75 percent of profile drag on a wing; much of which is due to the growth of the boundary layer and its corresponding momentum thickness over the first 50 percent of the wing's chord length (Green 2008). This means that increasing laminar flow on the suction side alone would realize significant savings.

B. Transition Mechanisms on Swept Wings

Most jet transports currently in service have swept wings in order to improve transonic aerodynamic performance. These swept wings are subject to four principle boundary layer instabilities: Tollmien-Schlichting (T-S) waves, attachment line contamination, Görtler vortices, and crossflow vortices (CF). Each of these instabilities is initiated by small perturbations, such as sound and vorticity, which are entrained from the freestream into the boundary layer. These small disturbances grow and eventually lead to transition to turbulent flow within the boundary layer. The transition process is highly dependent on initial conditions. Receptivity is the process through which disturbances enter the boundary layer as fluctuations of the basic state (Morkovin 1969).

The receptivity process is complex and efforts are currently under way to learn more about this phenomenon. However, previous research has shown that the mechanisms through which the boundary layer transitions to turbulence are sensitive to the external forcing of environmental disturbances (Hunt 2011). An operational roadmap to transition was developed by Morkovin *et al.* (1994) and is shown in Figure 3.

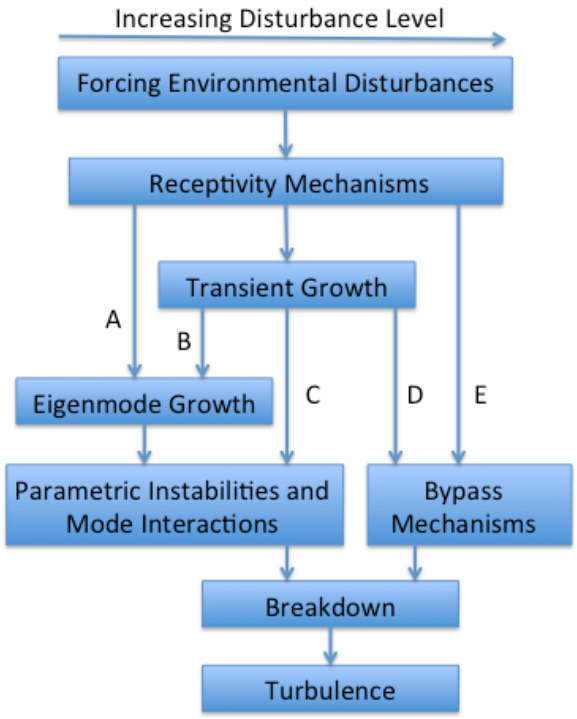

Figure 3 Roadmap to transition.

Transition to turbulence in low freestream disturbance environments follows path A shown in Figure 3 where transient growth is insignificant. The T-S, CF, and Görtler transition mechanisms are found on path A.

Tollmien-Schlichting Waves

Tollmien-Schlichting (T-S) waves are a two-dimensional, streamwise-traveling, viscous instability that propagates with a phase velocity between 0.3 and 0.4 times freestream velocity. A good review of T-S

waves can be found in Reed & Saric (2008). T-S waves are sensitive to two-dimensional roughness and sound (Saric & White 1998), and are not sensitive to isolated three-dimensional roughness.

Stabilizing the T-S instability is a major concern for any laminar flow project. Linear stability theory has shown that the boundary layer velocity profile curvature term, d^2U/dy^2, is a significant factor in determining stability behavior. The more negative the curvature term near the wall, the more stable the boundary layer. Qualitatively, this means that a boundary layer with a "fuller" profile is more stable. Modifying the mean flow in order to maintain a favorable pressure gradient is one of the means for achieving this effect. According to linear stability theory, a Falkner-Skan boundary layer with a Hartree parameter of β_H = 0.1 has a minimum critical Reynolds number for stability nine times higher than a Blasius boundary layer (Saric *et al*. 2011). Applying weak suction at the wall on the order to 10^{-3} to 10^{-4} times the freestream velocity also has the ability to make the boundary layer velocity profile fuller. This technique was used to delay transition successfully by the X-21 program (Pfenninger 1977). Analysis of the boundary layer momentum equation with viscosity written as a function of temperature reveals that wall cooling in air and wall heating in water can also make the velocity curvature term more negative. This technique is reviewed by Reshotko (1978, 1979,1984, 1985).

A hybrid laminar flow control technique has also been shown to be effective at suppressing T-S, CF, and attachment line instability mechanisms. This technique uses suction along the leading edge in order to subdue CF and attachment line instabilities and careful sculpting of the mid-chord pressure gradient is used to delay transition due to T-S waves. This technique was successfully demonstrated by the 757 laminar flow project (Boeing Commercial Airplane Group 1999).

Active cancellation of T-S waves has also been attempted in addition to modifying velocity profile curvature as means of delaying transition due to T-S waves. Pupator & Saric (1989) demonstrated that an active feedback system could successfully cancel broadband two-dimensional waves. However, Thomas (1983) showed that cancellation of the two-dimensional disturbances simply created a situation in which the remaining three-dimensional disturbances would survive to cause transition elsewhere. Active feedback cancellation of T-S waves is not considered a promising method for laminar flow control.

Attachment Line Contamination

Unlike straight wings, swept wings do not have a stagnation point on the leading edge. Rather, there is an area of outboard flow along the wing's attachment line. Turbulence from the fuselage boundary layer can propagate along the attachment line and trip the boundary layer on the wing. Fortunately, this transition mechanism is easy to control through methods such as limiting the leading edge radius (Pfenninger 1977), applying Gaster bumps, or including leading edge suction patches (Arnal *et al*. 2008).

Görtler Instability

The Görtler instability is a centrifugal instability of the Rayleigh type. The Görtler instability exists in boundary layer flows over concave surfaces. It is manifested as periodic, streamwise, counter-rotating vortices. This instability can be avoided by designing surface contours without concave curvature. An overview of the Görtler instability can be found in Saric (1994).

Crossflow Vortices

The crossflow instability appears as a result of a pressure gradient existing on a swept surface. Flow streamlines on a swept wing are curved due to the influence of the span-wise pressure gradient. Streamlines on the wing's suction side are deflected inboard until the pressure minimum, at which time the sign of the span-wise gradient is reversed and the streamlines turn outboard. This scenario is illustrated in Figure 4.

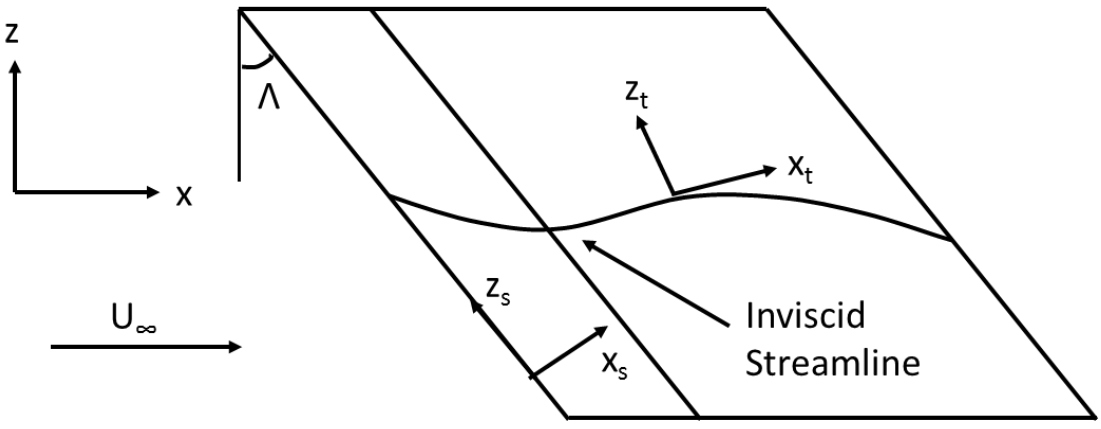

Figure 4 Swept wing streamlines.

Outside of the boundary layer the centrifugal acceleration of the fluid is balanced by the pressure gradient on the surface of the wing. However, inside of the boundary layer the fluid's velocity is reduced but the pressure gradient remains unchanged. This results in an imbalance within the boundary layer that creates a secondary flow, called crossflow, which is perpendicular to the local inviscid streamline. The crossflow boundary layer velocity profile is shown in Figure 5.

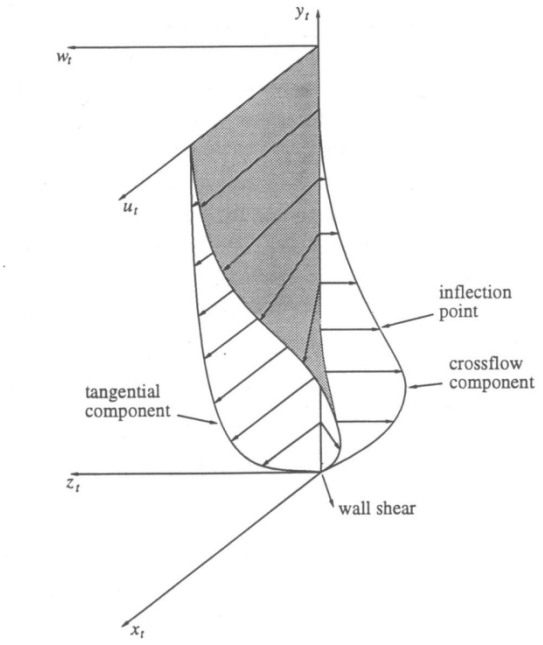

Figure 5 Crossflow boundary layer.

The velocity profile of the crossflow component contains an inflection point, which is subject to an inviscid instability. This instability is manifested as streamwise co-rotating vortices that convect low momentum fluid towards the freestream and high momentum fluid towards the wall (Saric *et al*. 2003). This creates a doubly inflected boundary layer profile that is inviscidly unstable and subject to a high frequency secondary instability (White & Saric 2005).

The crossflow instability can appear as either stationary or traveling waves. Deyhle & Bippes (1996) found that at freestream fluctuations levels greater than Tu = 0.15% traveling crossflow modes dominated

whereas environments with freestream fluctuation levels below this threshold were dominated by stationary crossflow. The wave number vectors of stationary modes are aligned nearly perpendicular to the flow's streamlines. As the frequency of the traveling disturbance increases, the streamwise component of the wavenumber vector increases (Deyhle & Bippes 1996).

Freestream disturbance levels in flight are thought to be low, and indeed disturbance levels have been measured to be between on the order of 0.04 % (Reidel & Sitzmann 1998). Pervious measurements of freestream turbulence on the FRL's O-2 showed levels between Tu = 0.05 % and Tu = 0.07 % (Carpenter 2009). It is important to note that the fluctuation measurements of Carpenter (2009) were not filtered for electronic noise or acoustic disturbances. It is likely that the actual levels of turbulence in the flight environment are lower than those quoted above.

The presence of traveling or stationary modes is a function of the receptivity process. White *et al.* (2001) showed that stationary modes dominated on a swept wing model with a highly polished leading edge at Tu = 0.30 % but traveling modes dominated at this same condition when surface roughness was increased. This work suggests that a single freestream disturbance criterion is not in itself enough to determine the nature of the crossflow instability, but that surface finish must also be included.

Because freestream disturbance levels are low in flight, stationary crossflow waves are thought to dominate (Saric *et al*. 2011). Stationary crossflow develops as co-rotating vortices aligned approximately in the streamwise direction. Natural surface roughness creates a non-spanwise-uniform pattern of vortices with a dominant wavelength equal to the most amplified spacial mode (Reibert & Saric 1997). Artificial surface roughness in the form of DREs can be used to force a specified spacial wavelength by introducing vorticity into the boundary layer (Radeztsky *et al.* 1993). Boundary layer scan data from the experiments of Reibert *et al.* (1996) with DREs spaced at 12mm is shown Figure 6.

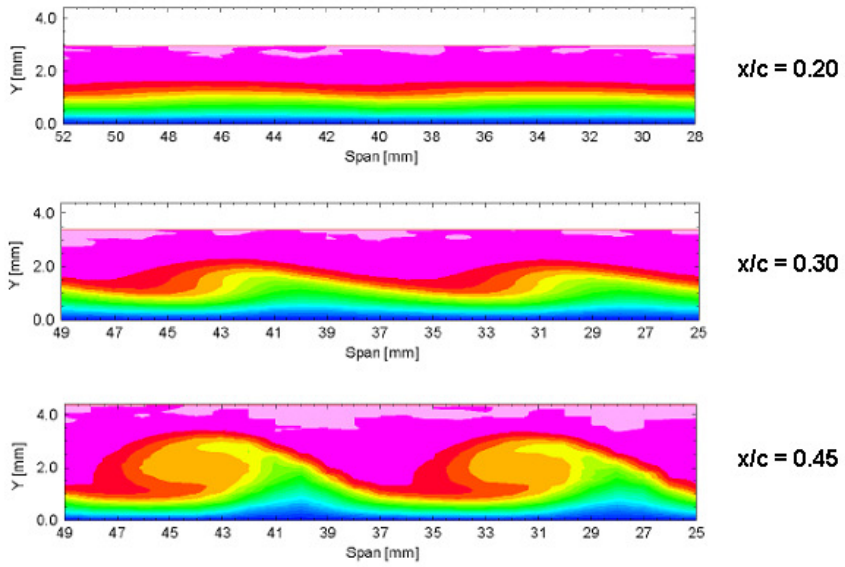

Figure 6 Boundary layer scans of crossflow vortices (Reibert *et al.* 1996).

DREs located near first neutral-point of the critical wavelength can be used to force a subcritical wavelength that will initially grow faster than the critical wavelength, saturate, and then die out (Saric *et al.* 1998). This procedure has been demonstrated to delay transition both in wind tunnel and flight environments (Carpenter 2009). Guidelines for DRE sizing and placement can be found in Radeztsky *et al.* (1993).

Although crossflow has been shown to be sensitive to three-dimensional roughness, it is not sensitive to two-dimensional roughness. It has also proven to be insensitive to sound (Radeztsky *et al.* 1999), (Deyhle & Bippes 1996).

Linear stability theory has proven to be an effective tool for estimating traveling and stationary crossflow initial growth rates prior to amplitude saturation. In incompressible linear theory, velocity and pressure disturbance terms are added to basic state terms in the unsteady Navier-Stokes equations. The basic state terms drop out of the equations identically, leaving only disturbance quantities. Solutions to the disturbance equations are assumed to be in the form of normal modes shown in Eqn (1).

$$q'(t) = q(t)e^{i(\alpha x+\beta z-\omega t)} + C.C. \quad (1)$$

Here α is the complex streamwise wave number, β is the complex spanwise wavenumber, ω is the real frequency, and C.C. stands for complex conjugate. In spacial stability the real part of the complex wavenumber describes the disturbance's wavelength while its imaginary part represents its growth rate. For stationary crossflow $\omega = 0$, β_r is set to the wavelength of interest, and α_i is the disturbance's streamwise growth rate. The disturbance Navier-Stokes equations in conjunction with the normal mode shown in Eqn (1) combine to form the famous Orr-Sommerfeld Equation.

The growth of a particular disturbance can be quantified using the Smith-Van Ingen e^N method (Mack 1984). This method is illustrated in Eqn (2).

$$N = \ln\left(\frac{A}{A_0}\right) = \int_{R_0}^{R} 2\alpha_i dR \tag{2}$$

The ratio of the final amplitude, A, to the initial amplitude, A_0, is equal to twice the integral of the disturbance's growth rate between the Reynolds numbers of interest.

Linear stability provides reasonable estimates of initial disturbance growth of stationary and traveling crossflow. Traveling crossflow has higher growth rates than stationary crossflow according to linear theory. However, stationary crossflow is not a linear process. The experiments of Deyhle & Bippes (1996), Reibert *et al.* (1996), and Saric *et al.* (1998) all showed stationary crossflow disturbance amplitude saturation. Linear theory has not been able to successfully duplicate the results of these experiments. However, nonlinear parabolized stability equations have shown good agreement with experiments by including nonlinearity and non-parallel effects (Haynes & Reed 1996).

2. SARGE INSTRUMENTATION

A. Overview

The SARGE project is designed to collect a wide array of boundary layer transition data. Like the experiments done on the SWIFT model at Texas A&M, the primary boundary layer transition identification tool for the wing glove will be infrared (IR) thermography. Additionally, hotfilms will be used as verification tools for transition location and for traveling wave structure identification. Thermocouples will also serve as transition detection tools through the measurement of wall temperature at selected points on the glove. Two rows of static pressure measurement ports will allow for the measurement of pressure coefficient on the surface of the glove. A five-hole probe mounted to an air-data boom will be used to measure local flow conditions just upstream of the outboard edge of the glove. High frequency response Kulite transducers will also be mounted to the air-data boom as well as the suction-side of the glove and will measure total- and static-pressure perturbations. Strain gauges and accelerometers will be fitted to key structural elements of the glove and wing in order to monitor static and dynamic structural loading. A standard camera will be used in conjunction with markings on the wing's surface in order to measure wing deformation in flight that could introduce spanwise twist and deflection across the glove. This measurement is described in another report.

The suction side of the glove is the primary research interest, so it will utilize IR thermography, hotfilms, and thermocouples to measure transition location. The IR camera will be mounted inside of the G-III's cabin and will view the glove through an IR-transparent window installed in the exit row window port. Two rows of four hotfilm arrays will be installed from 20 % chord to 50 % chord in increments of 10 %. Two rows of two thermocouples will be installed at inboard and outboard stations at 20 % and 60 % chord. A diagram of the proposed surface-mounted suction-side instruments is shown in Figure 7.

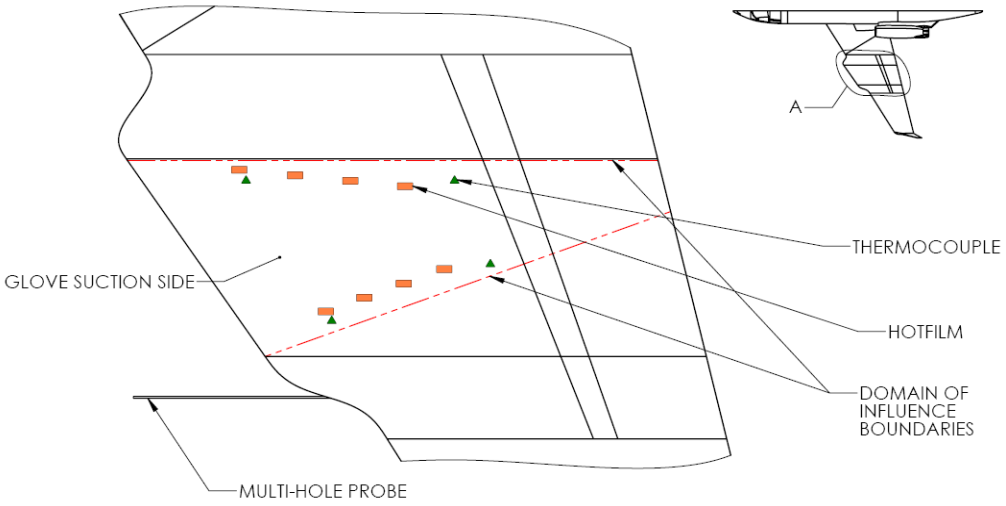

Figure 7 Schematic of suction-side instrumentation layout.

An interesting feature in Figure 7 is the demarcation of domain of influence boundaries. Boundary layer disturbances, such as turbulent wedges, propagate outwards at roughly 10º with respect to the meanflow streamline. These disturbances can be created by surface roughness or discontinuities and change the initial conditions in the growing boundary layer, which is governed by parabolic differential equations. This change in initial conditions means that the flow inside of the domain of influence of the edge of the glove cannot be used for measurements, even if the glove's edge does not trip the boundary layer. The domain of influence boundaries on the swept glove are assumed to be turned inboard approximately 10º due to the streamline deflections on the swept wing.

The laminarization of the pressure side is a secondary objective and therefore hotfilms and thermocouples will be the only transition detection tools on this side of the glove. Two rows of five thermocouples spaced evenly from 20 % to 60 % chord are proposed at inboard and outboard stations. A single row of five hotfilms from 20 % to 60 % chord is also planned for the pressure side. An illustration of the intended layout is shown in Figure 8. As in Figure 7, the domain of influence boundaries from the edge of the glove are noted.

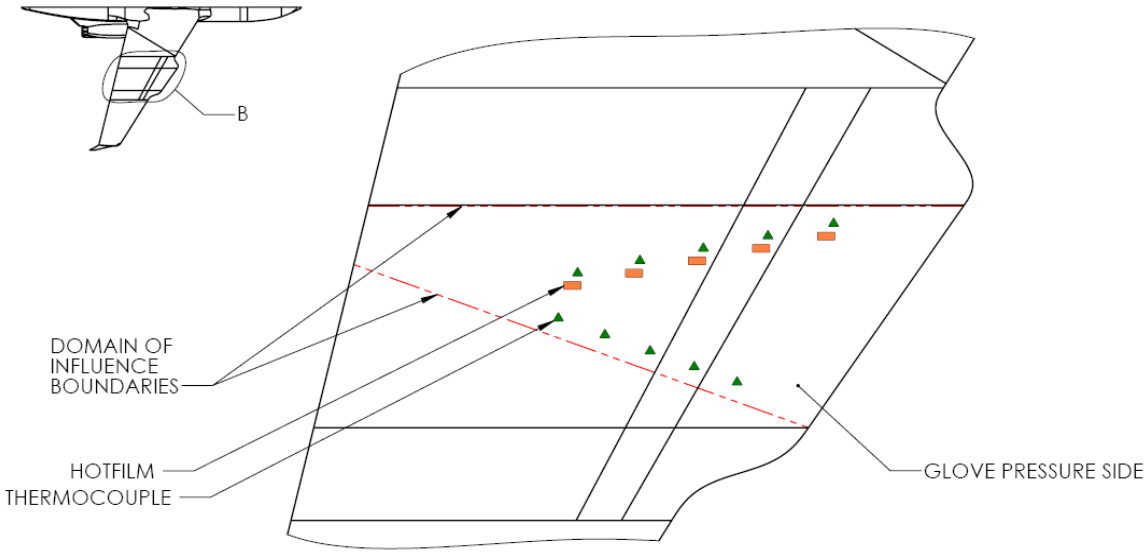

Figure 8 Schematic of pressure-side instrumentation layout.

An air-data boom will be installed near the test section in order to make local flow measurements near the glove. The principal instrument on this boom will be a five-hole probe manufactured by Aeroprobe Corporation. This probe is capable of measuring angle of attack, angle of sideslip, and Mach number. The boom will also have a high-frequency-response Kulite pressure transducer installed in order to measure high-frequency disturbance total pressures. Two additional Kulite transducers will be embedded into the glove's surface at 30 % chord and 55 % chord in order to measure static pressure disturbances. The final piece of the air data system is a total temperature probe. This probe can be mounted to the air-data boom in conjunction with the other pressure measuring systems, or on the aircraft's fuselage. The total temperature must be known in order to facilitate the calculation of glove's in-flight Reynolds number when coupled with velocity data from the five-hole probe.

Table 1 contains a summary of the SARGE instrumentation package as well as the proposed sampling rates for each instrument. Instruments that are seeking to collect frequency data, such as hotfilms, are sampled at rates twice that of the phenomena which they are to measure. Instruments used to collect amplitude data are sampled at rates five times higher than the maximum frequency for which amplitudes

are to be measured. These conventions have been shown to prevent aliasing and yield accurate representations of amplitude (Figliola & Beasley 2006).

Table 1 List of proposed research instrumentation

Sensor	Purpose	Number of Sensors	Sample Rate (Hz)	Maximum Frequency of Interest (Hz)
Static pressure ports	Measure Cp distribution.	2 rows of 29	100	20
IR camera	Visualize laminar-turbulent transition.	1 in cabin	15	15
Standard camera	Measuring wing deflection	1 in cabin	0.1	0.02
Hotfilms	Boundary layer frequency spectra	20 Channels	20,000	10,000
5-hole probe	Measure flow conditions near glove	4	100	20
Kulite	Measure P'_T, P'_S	3	150,000	30,000
Type-T Thermocouple	Wall Temperature	14	50	10

B. IR Camera

IR thermography will be the primary tool used to detect boundary layer transition location on the wing glove. IR thermography is superior to hotfilms or thermocouples in this regard because of its ability to resolve the entire test surface rather than discrete points. The philosophy behind IR thermography on the glove is the measurement of wall temperature difference between laminar and turbulent regions. Ambient solar radiation and the glove's radiation of energy to the cold sky will ensure that the glove will not reach adiabatic conditions except in the unique case of the solar radiation absorbed by the model being perfectly balanced by radiation back to the sky. Therefore the model's surface temperature will be a function of solar radiation and local convective heat transfer coefficient. The laminar region will be warmer than the turbulent region, assuming that the solar irradiation is identical in both zones, due to the difference in convection. A heat transfer analysis has been undertaken to characterize this effect for different combinations of surface colors and solar irradiation and is detailed in Section 3. An analogous technique is currently employed in the Texas A&M SWIFT experiments (Carpenter 2009), except in that case the

model is cooler than the ambient air causing the laminar region to be cooler than the turbulent region. The IR camera selected for this task was the FLIR Systems SC8000.

The SC8000 is a mid-wave infrared camera that uses an Indium Antimonide (InSb) detector and is sensitive to wavelengths from 3 μm to 5 μm. It has 1024x1024 resolution with 18 μm pixel pitch and is capable of recording at frame rates up to 132 frames per second. The camera's detector is sensitive to temperature changes as small as 25 mK. Data for individual pixels is digitally recorded at 14 bit resolution. The SC8000 is controlled using FLIR Systems' proprietary ExaminIR Pro software through either Gigabit Ethernet (GigE) or USB digital connections. Sensor data can be transmitted to either a computer or a portable digital recorder using GigE or a proprietary Camera Link Full interface, respectively. Due to the large file sizes created by the high definition resolution, the GigE port saturates at frame rates lower than the camera's maximum capabilities, so the Camera Link Full interface was developed in order to enable higher data transfer rates to the digital recorder. The camera is designed for operations at temperatures between -10 °C to 50 °C and pressure altitudes from 0 to 40,000 ft. A picture of the SC8000 is shown in Figure 9.

Figure 9 FLIR SC8000 camera (photo from FLIR Systems).

The SC8000 has an array of lenses available to modify the camera's field of view and permit higher fidelity measurements in regions of particular interest. Lenses with focal lengths of 17 mm and 50 mm

were selected for use on the SARGE project. The 17 mm lens has a field of view of 56.9°x56.9° with an f-number of f/4.0 and the 50 mm lens has a field of view of 20.9°x20.9° with an f-number of f/4.0. The center of the SARGE wing glove will be located at a viewing distance of approximately 5 m at an elevation angle of -15°. It can be assumed that the sight line of the camera is perpendicular to the glove's lines of constant span and that the glove surface is perfectly horizontal as a first approximation. Spanwise and chordwise image resolution as well as image depth of focus were calculated using these assumptions and the camera specifications mentioned previously. The circle of confusion assumed for the depth of focus calculations was chosen to be twice the pixel pitch. This means that the depth of focus specified represents the zone in which objects will be rendered in the highest resolution possible given the camera's pixel size. Areas outside of this region will be imaged at lower than maximum resolution, but may still provide usable data. These calculations assume that the camera is focused at the mid-span of the glove. The results of these computations are shown in Table 2.

Table 2 IR camera focus and resolution data

Parameter	17 mm Lens	50 mm Lens
Field of View (º)	56.9x56.9	20.9x20.9
Depth of Focus (m)	∞	3.1
Glove Span in Focus (m)	All	All
Inboard Chord-wise Resolution (mm/pixel)	4	1.5
Inboard Span-wise Resolution (mm/pixel)	13	5
Outboard Chord-wise Resolution (mm/pixel)	6	2
Outboard Span-wise Resolution (mm/pixel)	26	10

The data in Table 2 show that the spanwise resolution is much coarser than the chordwise resolution due to the highly oblique viewing angle. The spanwise resolutions of these lenses are too coarse to enable the imaging of crossflow vortices. IR images taken from the aft-most port window of a G-IIB, which has the same wing as the G-III, are shown in Figure 10 and Figure 11 for the 17 mm and 50 mm lenses respectively.

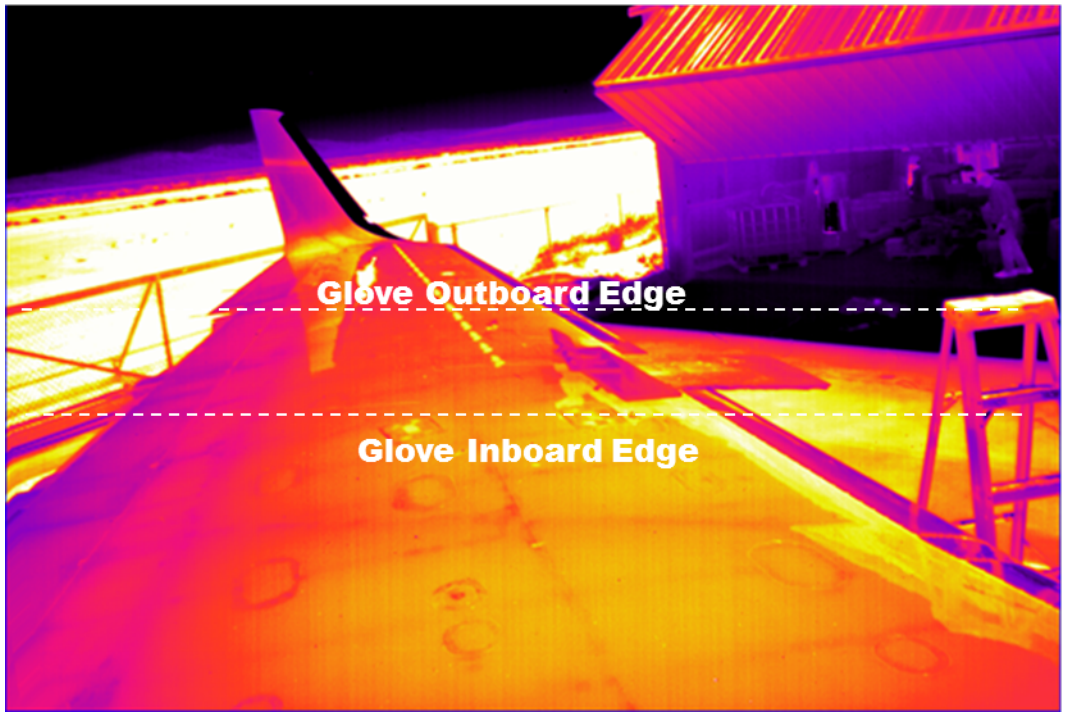

Figure 10 G-III wing IR photo with 17 mm lens.

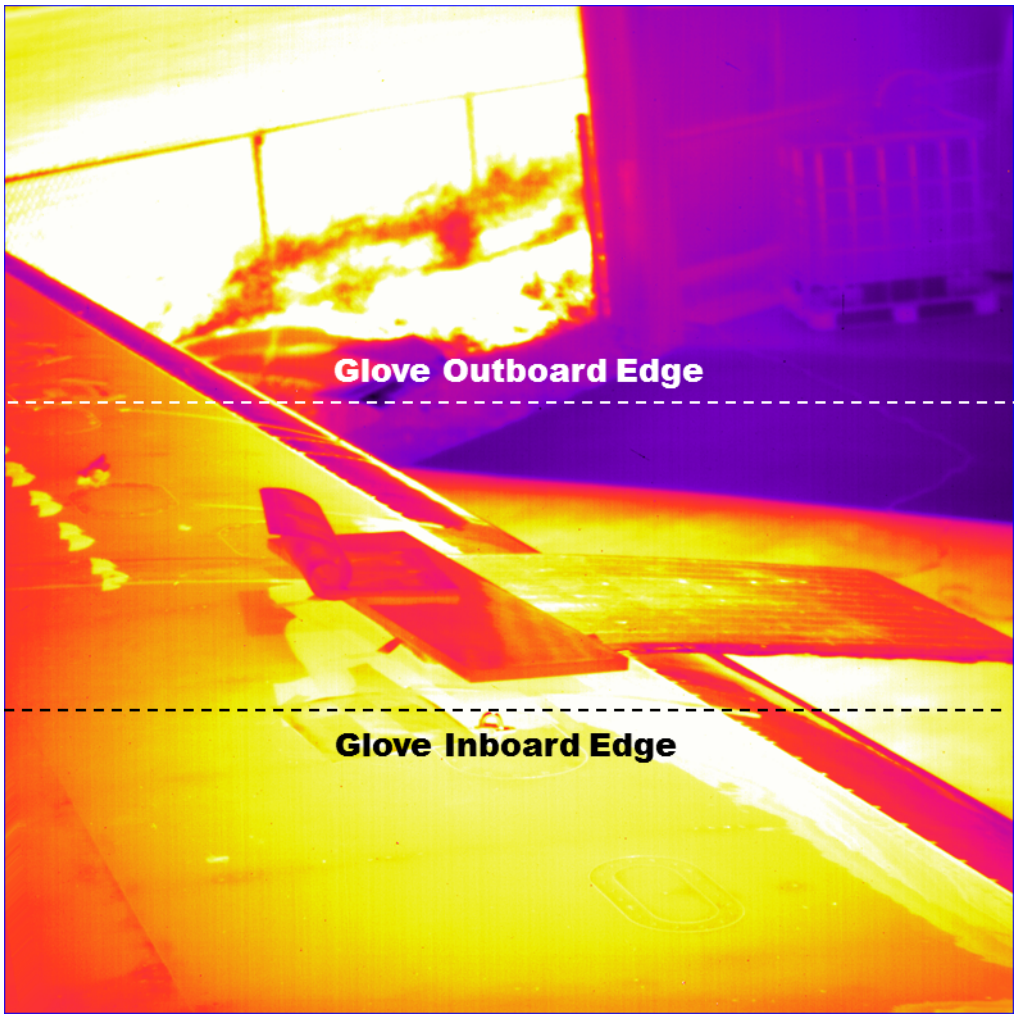

Figure 11 G-III IR photo with 50 mm lens.

C. Static Pressure

Static pressure measurements will be taken on the glove in order to facilitate the calculation and monitoring of pressure and lift coefficients. The purpose of these measurements is threefold. First, the experimental measurement of the glove's pressure profile will allow for the verification of computational fluid dynamics results used during the design stage. Second, static pressure measurements will allow for the calculation of sectional lift coefficient, which is required to be greater than 0.5 per ERA's experiment requirements. Finally, static pressure measurements will permit the experimental determination of the aircraft angle of attack that produces a suction peak on the glove's suction side. This angle of attack will

be the limiting value above which the glove will become T-S unstable and the laminar flow strategy employed on the glove will no longer work.

The glove will have two rows of 29 pressure ports located an inboard and outboard stations for a total of 58 ports. They will be located from 0 % chord to 60 % chord on the suction side of the glove and 0 % to 15 % chord on the pressure side. The pressure ports will have a diameter of 0.020 inches, which is on the order of the boundary layer's displacement thickness over much of the glove. It is important that the diameter of the holes be on the same order as the displacement thickness in order to maximize accuracy (McKeon 2007). A diagram of the proposed port locations is shown in Figure 12.

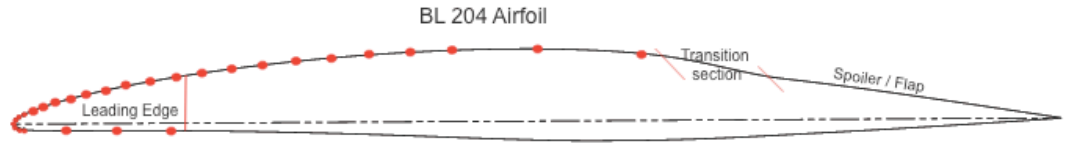

NUMBER	GLOVE CHORD (%)
1	-15.0
2	-10.0
3	-5.0
4	-1.0
5	-0.5
6	-0.2
7	0.0
8	0.2
9	0.5
10	1.0
11	1.8
12	2.8
13	4.0
14	5.4
15	7.0
16	8.8
17	10.8
18	13.0
19	15.4
20	18.0
21	20.8
22	23.8
23	27.0
24	30.4
25	34.0
26	37.8
27	41.8
28	50.0
29	60.0

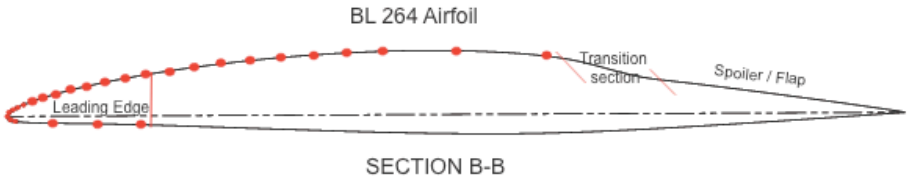

Figure 12 Static pressure port locations.

The instrument selected for measuring static pressure was the Miniature Electronic Pressure Scanner ESP-64HD manufactured by Pressure Systems, Inc. The ESP is a differential pressure scanner with 64 available channels. The ESP has a single, multiplexed analog output whose source pressure is controlled

by six digital I/O ports. The relevant pressure ranges available from the manufacturer are ±1, ±2.5, ±5, ±10, and ±15 psid. The reference pressure can be any other pressure source on the aircraft, but the most convenient source would be the static pressure port on the 5-hole probe. The ESP-64HD can be equipped with an internal heating element for extreme cold environments. This option enables the transducer to operate at temperatures as low as -55°C while maintaining the internal temperature within ±3°C through the use of an RTD for internal temperature measurements.

The ESP measures the pressure of a single port at a given time. It is capable of scanning the channels at a rate of 20,000 channels per second. The ESP also has to ability to purge contamination, such as moisture, from its lines by connecting to a high pressure source during calibration. This capability is especially well suited for the flight test environment where the ports are exposed to humidity, dust, and other debris. ESPs can also be purchased with Quick Disconnect tubing plates, which enable pressure tubing to be installed or removed without exposing the internal calibration manifold.

Computations showed that the maximum expected pressure differential between the glove static and the freestream ambient pressures was on the order of -1.6 psi. If the ESP is referenced to the freestream static pressure, this expected pressure differential calls for the use of the ±2.5 psid sensor. This ESP has an uncertainty of ±0.06 % full scale value, or ±0.0015 psid. A photograph of an ESP is shown in Figure 13.

Figure 13 Photo of ESP multiplexing transducer.

D. 5-Hole Probe

The principle freestream flow measurement instrument in the SARGE experimental setup will be the five-hole probe. This probe will be attached to the tip of a larger air-data boom that also supports a high-frequency-response Kulite transducer. The five-hole probe currently under consideration is manufactured by Aeroprobe Corporation. This probe will have a conical tip and is designed for accurate angle and velocity measurements at transonic Mach numbers. The flow's total pressure is measured by the hole at the cone's tip. Local angle of attack is measured by two holes on the upper and lower faces of the cone, and local angle of side-slip is measured by the holes on the sides of the conical tip. A static pressure measurement ring located several probe diameters aft of the tip provides local static pressure values. A schematic of the probe's holes is shown in Figure 14.

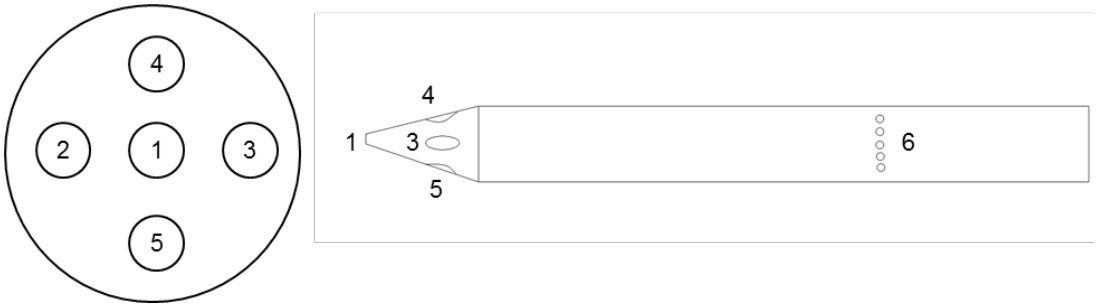

Figure 14 Five-hole probe pressure port numbering convention.

As shown in Figure 14, hole 1 is the total pressure port. Holes 2 and 3 measure angle of sideslip and holes 4 and 5 measure angle of attack. The static pressure ring is denoted as port 6. Four pressure transducers are necessary to determine the flow angles and velocity. Flow angles are measured using differential pressures between ports 2 and 3 and ports 4 and 5, termed $P_{2\text{-}3}$ and $P_{4\text{-}5}$ respectively. The dynamic pressure is measured using a differential transducer between ports 1 and 6, called $P_{1\text{-}6}$ and the static pressure, P_6, is measured using an absolute transducer. Total pressure is the sum of $P_{1\text{-}6}$ and P_6. A schematic of pneumatic tubing connections is shown in Figure 15.

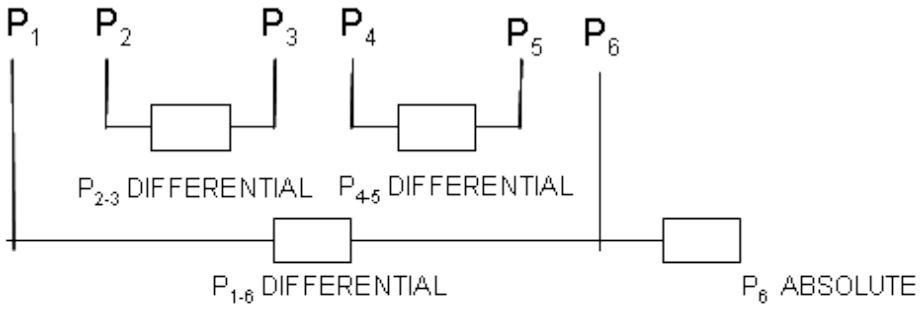

Figure 15 Five-hole probe pressure plumbing schematic.

The readings of the five-hole probe will compose the data used by the test pilots to execute research test points. It is desired that the pilots hold the aircraft to within ±0.1° local angle of attack and local angle of sideslip, ±0.01 Mach, and ±200,000 Reynolds number. These tolerances require measurements of these parameters with uncertainties less than ±0.04°, ±0.004 Mach and ±90,000 Reynolds number. Accurate pressure transducers are integral in making such high quality measurements.

Pressure Transducers

The Paroscientific 6000 Series Intelligent Pressure Transmitter and the Honeywell Precision Pressure Transducer (PPT) were chosen for measuring probe pressures. The Paroscientific 6000 Series is an absolute pressure transducer with a range of 0 to 15 psia and accuracy of 0.01 % full scale, or 0.0015 psia. It outputs a serial ASCII text file using either RS-232 or RS-485 communication protocol. The Series 6000 is rated for operation between -54 °C and 60 °C. The Honeywell PPT selected for SARGE is a ±2 psid differential transducer with a standard accuracy of ±0.05 % full scale, or ±0.002 psid. The PPT can also be custom ordered with ±0.025 % accuracy, which is necessary for the SARGE project. The PPT transmits a digital signal using either RS-232 or RS-485 protocol and is rated for accurate readings between -40 °C and 85 °C. Pictures of the Paroscientific 6000 series and Honeywell PPT transducers are shown in Figure 16.

a) b)

Figure 16 Photos of five-hole probe pressure transducers for a) Paroscientific 6000 series and b) Honeywell PPT.

An uncertainty analysis was performed for data measured by the five-hole probe using the Paroscientific 6000 Series and the special accuracy Honeywell PPTs. The details of these calculations are enumerated in Appendix B. The 15 psia Paroscientific transducer paired with the special accuracy ±2 psid PPTs and a total temperature probe with an uncertainty of ±0.4 K has design stage uncertainty values for flow angles, Mach number, and Reynolds number as listed in Table 3.

Table 3 5-hole probe uncertainty analysis results

Flight Conditions			Uncertainties			
Altitude	Mach	Re_c (M)	0° AoA/AoSS	8° AoA/AoSS	Re_c	Mach
42,000	0.68	17.0	0.023	0.032	47,000	0.0009
43,000	0.72	17.2	0.021	0.029	46,000	0.0009
44,500	0.75	16.6	0.021	0.029	45,000	0.0009
36,000	0.68	22.7	0.017	0.024	56,000	0.0007
38,000	0.72	21.9	0.017	0.023	54,000	0.0007
39,000	0.75	21.7	0.016	0.023	53,000	0.0007
31,000	0.68	27.0	0.014	0.020	61,000	0.0006
32,500	0.72	27.2	0.013	0.019	61,000	0.0006
34,000	0.75	26.9	0.013	0.018	61,000	0.0006

Table 3 shows that the design stage uncertainties of these parameters are within the limits stated previously. The uncertainty in the flow angle measurements increases as angle of attack or sideslip

increases due to the higher differential pressures between the probe's ports. The 8º AoA case was included as a worst-case-scenario upper limit on flow angles. Although the aircraft's angle of attack will likely never exceed four degrees during testing, the induced flow near the five-hole probe could cause larger local flow angles.

Boom Location

The air data boom will be mounted on the wing and is therefore subject to aircraft induced flowfield modifications. The primary flow effects caused by the wing and fuselage are upwash and sidewash. Upwash occurs as a result of the reduced pressure on the suction side of the airfoil and sidewash is induced by both the presence of the aircraft's fuselage and the attachment line flow along a swept wing's leading edge. Upwash is qualitatively illustrated in Figure 17.

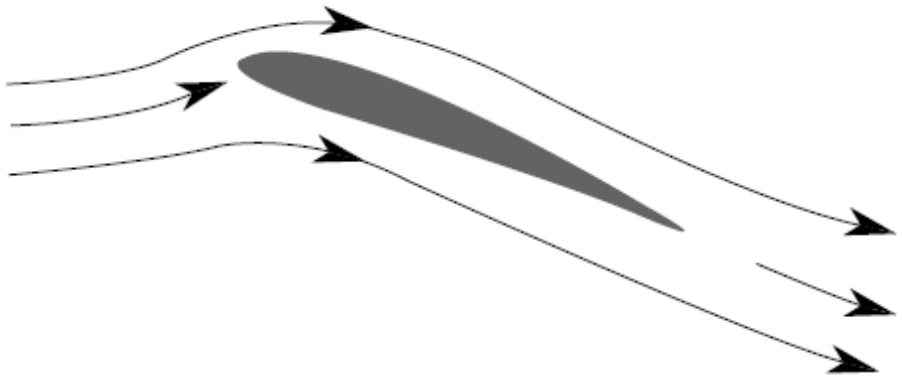

Figure 17 Upwash effect induced by wing (Haering 1995).

These flow effects will be manifested as biases in the angle of attack and angle of sideslip measurements.

Upwash and sidewash effects are magnified near the wing where pressure gradients become steep and flow velocity is changing rapidly. This region of large gradients has several adverse qualities. First, the attachment line on the wing, and the associated high gradient flow around it, moves with changes in angle of attack. Therefore, a probe placed in this region would measure large changes in local flow angles and

velocity that correspond to much smaller changes in aircraft flight conditions. Secondly, the region of large gradients is challenging to resolve computationally and a probe located in this area would make verification of computational results more challenging.

A preliminary boom location study for the SARGE project was undertaken by the computational group at Texas A&M. This study showed that the probe tip should be placed a minimum of three feet in front of the glove's leading edge along the aircraft's longitudinal axis in order to avoid the largest pressure gradients. It was also found that locating the tip on the order of 18 inches above or below the glove's chord line could also reduce the effect of large pressure gradients. It is important to note that there was no feasible boom length that would enable the five-hole probe to directly measure freestream conditions. Its flow velocity and static pressure measurements will both have biases created by the aircraft's presence.

Dynamic Response of Pressure Tubing

The 5-hole probe is a low frequency-response instrument that is designed to provide dynamic flow conditions at rates of 20 Hz and below. This frequency has been determined to be sufficiently high so as to avoid pilot induced oscillations. Preliminary investigations have shown that the tip of the five-hole probe should be placed a minimum of three feet in front of the wing and preferably at a vertical offset of 18 inches below the wing's chord line. Structural considerations for a boom of this type would require tubing on the order of six to seven feet long in order to reach from the tip of the 5-hole probe to the inside of the glove's leading edge fairing. An additional two to three feet of additional tubing from the air data boom's structural termination will be required in order to reach the probe's pressure transducers, which are to be housed within the glove's leading edge. This brings the total projected tubing length to approximately 10 feet.

Inertial and viscous effects within a pressure tubing system cause dynamic responses to pressure fluctuations analogous to a spring-mass-damper system. As in the mechanical system, the acoustic response of the tubing can display over-damped, under-damped, or critically damped behavior. Long tubing lengths with small inner diameters are dominated by viscous effects and have high damping. As the inner diameter increases, inertial effects become significant and the system can become under-damped.

An under-damped system is undesirable because it will cause higher frequency signals to be amplified and will result in large, rapid variations in pressure readings.

A proven scheme for modeling the dynamic response of pressure tubing systems was developed by Bergh & Tijdeman (1965). Their model was developed by adding sinusoidal fluctuation terms to the pressure, density, temperature, and velocity terms in the two-dimensional, cylindrical Navier-Stokes equations in the manner shown in Eqn (3) through Eqn (7). Here, variables with an over-bar represent an average value and a prime symbol denotes a disturbance amplitude, while ω represents the disturbance frequency.

$$p = \overline{p} + p'e^{i\omega t} \tag{3}$$

$$\rho = \overline{\rho} + \rho'e^{i\omega t} \tag{4}$$

$$T = \overline{T} + T'e^{i\omega t} \tag{5}$$

$$u = \overline{u} + u'e^{i\omega t} \tag{6}$$

$$v = \overline{v} + v'e^{i\omega t} \tag{7}$$

The equations can then be linearized through the use of the following assumptions: the disturbance amplitudes are very small, the tube's radius is small in comparison to its length, and the flow in the tubing system is completely laminar. Additionally, the following boundary conditions have been prescribed: *u'*, *v'*, and *T'* vanish at the wall, and *v'* is zero at the centerline of the tube. Also, the disturbance at the exit of tube *n* must equal the disturbance at the entrance of tube *n*+1 for multi-tube systems. This linearization enables superposition of solutions. Therefore, the transfer function for a network of tubes with different radii can be determined by multiplying the transfer functions of each segment together. The model of Bergh & Tijdeman (1965) was used to predict the dynamic response of the 5-hole probe and Kulite measurement systems.

The pressure transfer function calculations required the average fluid density, viscosity, and Prandtl number in the tubing system; the tubing length and inner diameter; and the dead volume within the pressure transducers as inputs. The mean pressure within the total pressure port of the five-hole probe and the total pressure Kulite transducer system were assumed to equal the freestream total pressure as a first

approximation. The mean pressure in the 5-hole probe's static pressure ring was approximated as the freestream static pressure. The dynamic responses of the four differential pressure ports on the five-hole probe lie between those of the static and total pressure lines. The temperature within the lines was approximated as the freestream static temperature. Although the flow stagnates within the lines, the long tubing lengths running through the cold-soaked airframe will likely result in lower temperatures inside the tubing. Increasing temperature at a given pressure increases the viscous damping in the system while also decreasing density. Thus, assuming a lower temperature provides a conservative estimate when the goal is to avoid under-damped systems.

The internal pressures within the lines of the pitch and yaw ports (ports 2,3,4, and 5) vary significantly from the pressure within the total pressure port (port 1). Pitch and yaw angles of 8° or below are expected during SARGE data collection. Thus, the average pressures in the lines of ports 4 and 5 at an angle of attack of 8° were used to establish the bounding cases for minimum and maximum pressures within the off-center ports. Calibration data from a similar five-hole probe suggests that the internal pressure within the higher pressure line will be on the order of the total pressure minus 0.5 times the dynamic pressure. Similarly, the low pressure line's internal pressure will be roughly equal to the total pressure minus 0.8 times the dynamic pressure.

The dynamic behavior of the 5-hole probe's tubing system was investigated for three common tube inner diameters: 1/6 inch, 3/32 inch, and 1/8 inch. The physical dimensions used to analyze the five-hole probe system are shown in Table 4.

Table 4 5-hole probe unsteady pressure analysis parameters

System	Tubing Length (in)	Tubing Inner Diameter (in)	Transducer Cavity Volume (mm^3)
5-Hole Probe Tip Ports	120	1/16, 3/32, 1/8	120
5-Hole Probe Static Pressure Ring	107 13	1/16, 3/32, 1/8 0.03	90

The effect of tubing diameter on frequency response was investigated using the tubing inner diameters listed in Table 3 for the tip port and pressure ring systems at a Reynolds number of 22 million and Mach 0.75. The physical properties of the air within the tubing at this flight condition are listed in Table 5.

Table 5 Properties of air assumed to exist inside of pressure tubing

Tubing	Pressure (Pa)	Temperature (K)	Ratio of Specific Heats	Prandtl Number	Viscosity (Pa-s)
Static Ring	19,735	216.65	1.4	0.71	0.0000142
Total Pressure	28,661	216.65	1.4	0.71	0.0000142
High Differential	24,198	216.65	1.4	0.71	0.0000142
Low Differential	21,521	216.65	1.4	0.71	0.0000142

The results of the calculations at Reynolds equal to 22 million at Mach 0.75 are shown in Figure 18a, b and c.

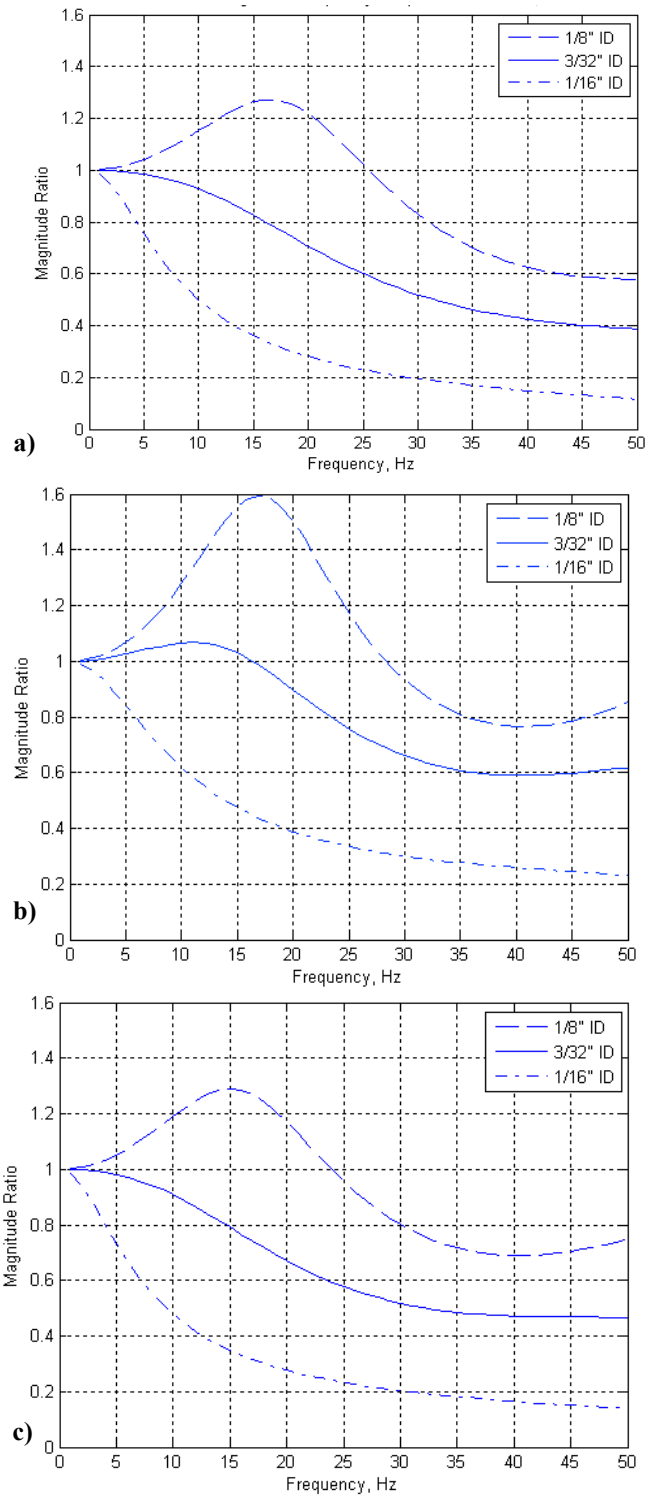

Figure 18 Unsteady pressure magnitude ratio as a function of frequency and tubing inner diameter at 0.75 Mach and 22 million Reynolds number. a) static pressure tube, b) total pressure tube, and c) pitch and yaw angle measurement low pressure line.

As shown in Figure 18, the 1/16 inch inner diameter tubing behaves like an over-damped system and there is a rapid decrease in magnitude ratio above 2 to 3 Hz for both the tip ports and the static ring. The 20 Hz signal is attenuated to less than 40 % of its original amplitude for the tip ports and there is 70 % attenuation in the static ring signal. The 3/32 inch tubing is lightly under-damped for the total pressure port and lightly over-damped for the static pressure ring and the pitch and yaw ports. The total pressure port displays an initial rise in magnitude ratio up to a maximum value of about 1.1 at 11 Hz followed by a more gradual roll-off. Here, the magnitude ratio at 20 Hz is approximately 0.9 for the total port, or ten percent attenuation. The static pressure and pitch and yaw lines are attenuated to about 0.7 times the original amplitude. The 1/8 inch tubing is under-damped for the tip ports and the static pressure ring. There is a rapid rise in the total port's magnitude ratio to a maximum of about 1.6 at 17 Hz. The static pressure and pitch and yaw signals are more lightly under-damped and reach a maximum amplitude ratio of 1.3 at 17 Hz and 15 Hz respectively. The total pressure port's 20 Hz signal is amplified to about 1.5 times its original magnitude while the pitch and yaw ports' and static ring's 20 Hz response is about 120 % of the original amplitude. This figure shows that 3/32 inch inner diameter tubing is optimal for the 5-hole probe system. This diameter limits attenuation up to the 20 Hz limit while avoiding amplification of lower frequencies.

The pressure responses in both the static and probe-tip lines are affected by changes in altitude when Mach number is held constant. In order to illustrate this point, the response of 3/32 inch inner diameter tubing is plotted for Reynolds numbers of 17 million, 22 million, and 27.5 million at Mach 0.75 in Figure 19. The Reynolds numbers of 17 million, 22 million, and 27.5 million at Mach 0.75 correspond to altitudes of 44,500 feet, 39,000 feet, and 34,000 feet respectively according to the standard atmosphere. The relevant properties of the air within the tubes at these conditions are shown in Table 6.

Table 6 Properties of air inside tubes used for Reynolds number dependency calculations

Altitude (ft)	Pressure (Pa)				Temperature (K)	Ratio of Specific Heats	Prandtl Number	Viscosity (Pa-s)
	Static Ring	Total Pressure	High Differential	Low Differential				
44500	15,149	22,001	18,575	16,520	216.65	1.4	0.71	0.0000142
39000	19,735	28,661	24,198	21,521	216.65	1.4	0.71	0.0000142
34000	24,986	36,286	30,636	27,246	220.79	1.4	0.71	0.0000144

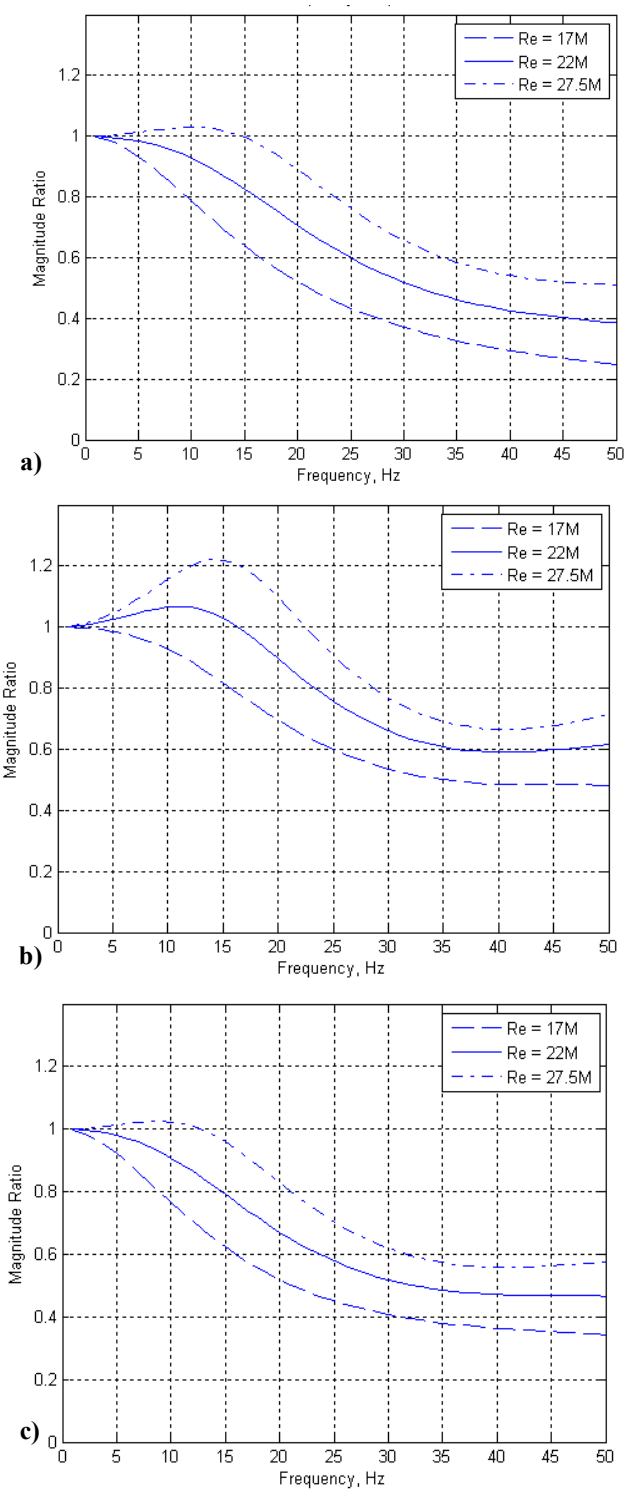

Figure 19 Unsteady pressure magnitude ratio as a function of frequency and Reynolds number for 3/32 inch inner diameter tubing. a) static pressure tube, b) total pressure tube, and c) pitch and yaw angle measurement low pressure line.

The plot shows that an increase in Reynolds number, which corresponds to a decrease in altitude, results in a less damped system. Decreases in altitude correspond to an increase in ambient air density and an increase in the role of mass effects within the tubing. The 5-hole probe's total pressure port's magnitude ratio at 20 Hz drops from about 1.1 at 34,000 ft to approximately 0.7 at 44,500 feet. The peak in the maximum magnitude ratio increases from 1.0 at 44,500 feet to 1.22 at 34,000 feet. A plot showing the variation of frequency response with Mach number at a particular Reynolds number would be qualitatively similar to Figure 19a, b and c. An increase in the density of the air within the tubing corresponds to a reduction in the dominance of viscous damping. For the tip ports the 27.5 million Reynolds number, 0.75 Mach case is the most under-damped of any SARGE flight condition.

The dynamic behavior of the pitch and yaw ports at any angle between 0° and 8° will have its response bounded by those of the low differential pressure tube and the high differential pressure tube. A comparison of the magnitude ratios for the low and high pressure lines with 3/32 inch diameter at 0.75 Mach and 22 million Reynolds number is shown in Figure 20.

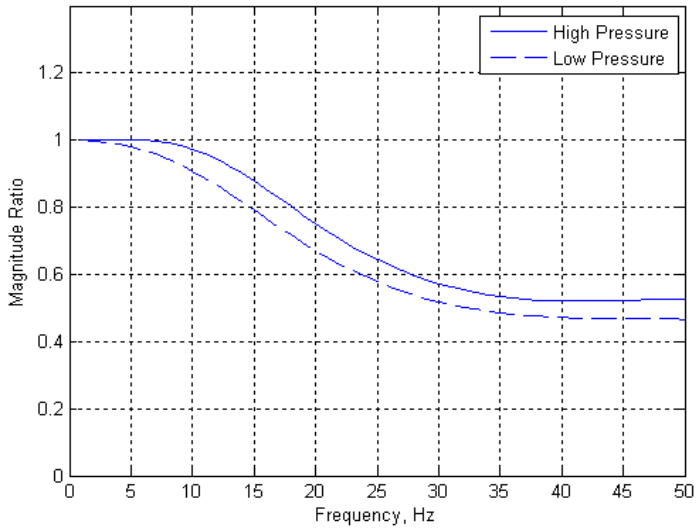

Figure 20 Comparison of magnitude ratio between low and high pressure lines of pitch and yaw angle measurement ports for 3/32 inch inner diameter tubing.

The magnitude ratio plots presented previously show that there is little hope for detecting freestream perturbations beyond frequencies of several tens of Hertz using the five-hole probe.

The phase of signals within the tubing is also modified by inertial and viscous effects. The phase is modulated such that the lag in the signal increases with increasing frequency. This phase shift becomes especially important when combining the outputs from two pressure lines to compute unsteady flow angles or velocities. Phase shifts in control parameters can also incite pilot-induced oscillations during unsteady flight.

The effect of tubing diameter on phase shift was investigated for the 0.75 Mach, 22 million Reynolds number test case using the properties listed in Table 5. The results of these calculations are shown in Figure 21. Here, the negative sign of the phase angle indicates a delay.

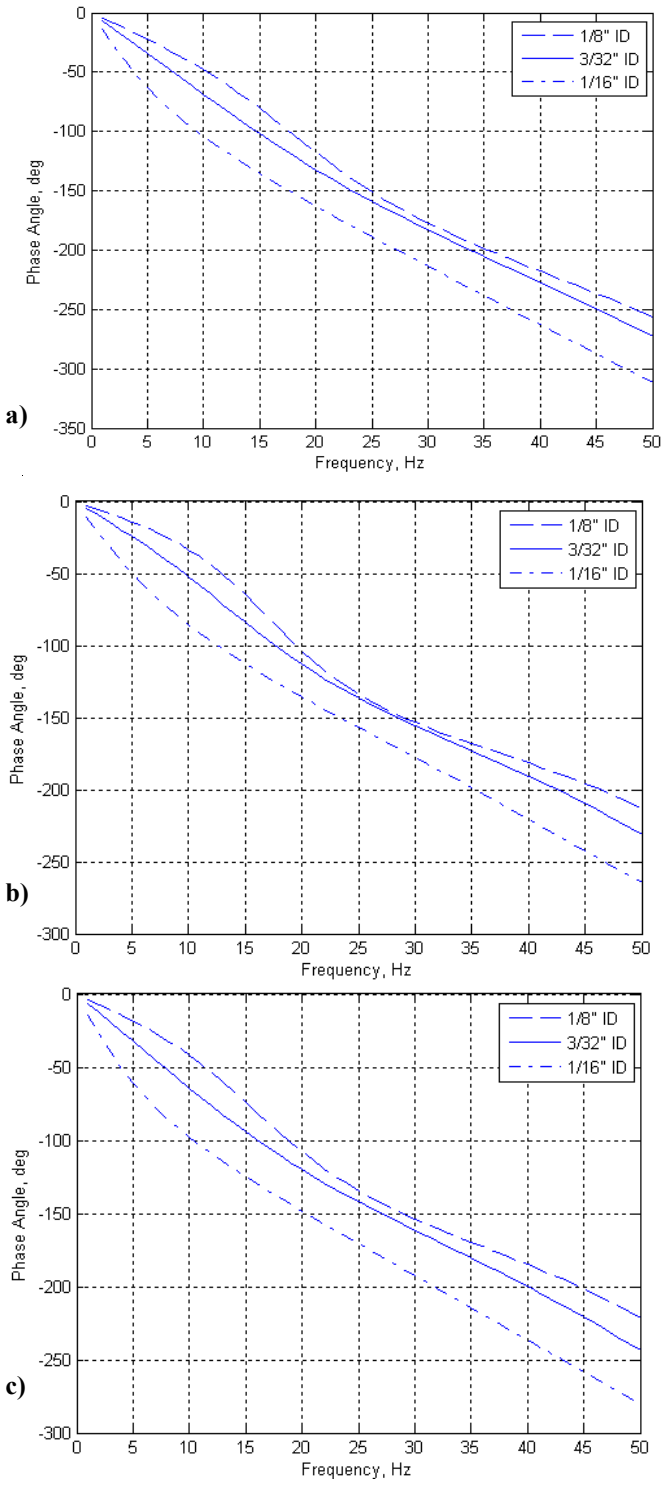

Figure 21 Unsteady pressure phase shift as a function of frequency and tubing inner diameter at 0.75 Mach and 22 million Reynolds number. a) static pressure tube, b) total pressure tube, and c) pitch and yaw angle measurement low pressure line.

Figure 21 shows that the magnitude of the phase shift decreases with increasing pressure for all diameters, as the total pressure port line has the lowest phase angle. The 1/8 inch inner diameter tubing has the lowest phase shift, but has undesirable magnitude response, as shown previously. The 1/16 inch tubing has the highest phase lag for all cases. The 3/32 inch tubing lies between these extremes and its behavior is nearly identical to that of the 1/8 inch tubing near 25 Hz. The phase lag in the 3/32 inch tubing at 20 Hz is 132°, 112°, and 119° for the static pressure, total pressure, and probe differential pressures respectively.

As with magnitude ratio, phase shift is also dependent on altitude for a particular tube inner diameter. The phase effect of altitude on the phase shifts in a 3/32 inch tube at the flight conditions listed in Table 6 are plotted in Figure 22. Again, increasing altitude corresponds to decreasing Reynolds number.

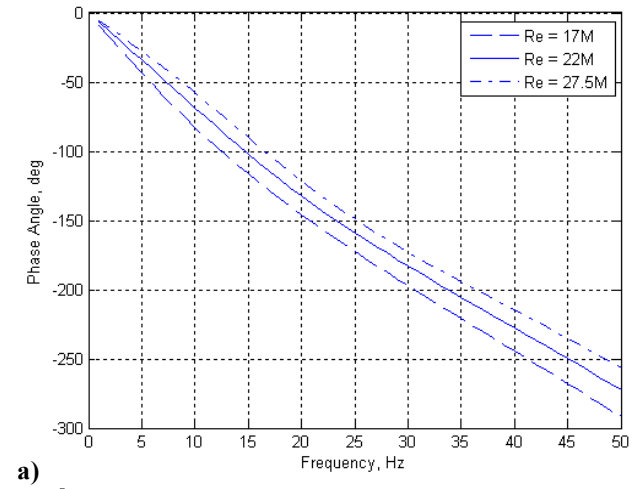

a)

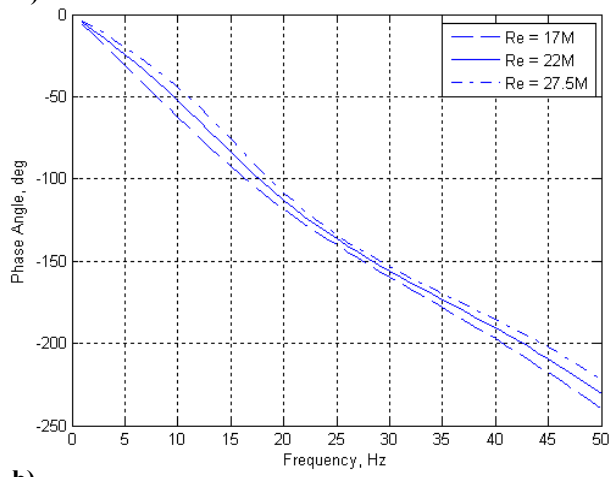

b)

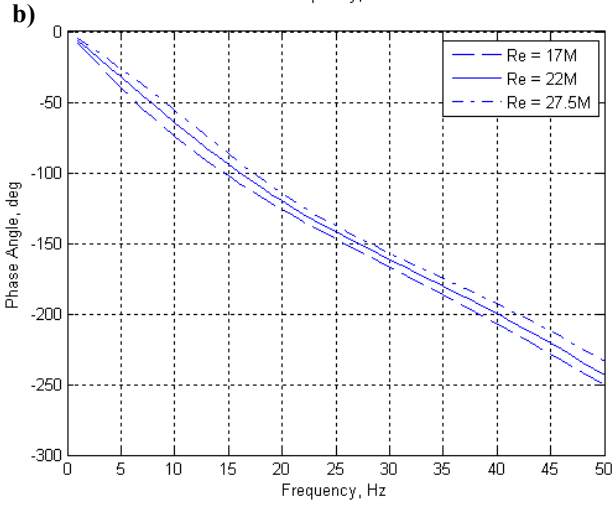

c)

Figure 22 Unsteady pressure phase shift in 3/32 inch tubing as a function of frequency and Reynolds number at 0.75 Mach and 22 million Reynolds number. a) static pressure tube, b) total pressure tube, and c) pitch and yaw angle measurement low pressure line.

In the three cases listed in Figure 22a, b, and c the phase lag increases with increasing altitude (decreasing Reynolds number). The static pressure's phase lag, plotted in Figure 22a, is most affected by changes in altitude.

Phase shift can also be expressed as a time lag by dividing the phase angle by 360° and multiplying by the period of the signal. The total time lag in the 5-hole probe system is a critical factor for avoiding pilot-induced oscillations. The total air-data system lag should be less than 0.12 seconds (Task Group SCI-026 2000). Special attention should be paid to frequencies below 5 Hz, which are within the control capabilities of the pilot. Figure 23 shows that the pressure measurements made with 3/32 inch tubing all have phase angles well below 180° at frequencies below 5 Hz and therefore are capable of being controlled without the possibility of pilot induced oscillations. The time lags for each pressure line are plotted for the case of 22 million Reynolds number at 0.75 Mach in Figure 23.

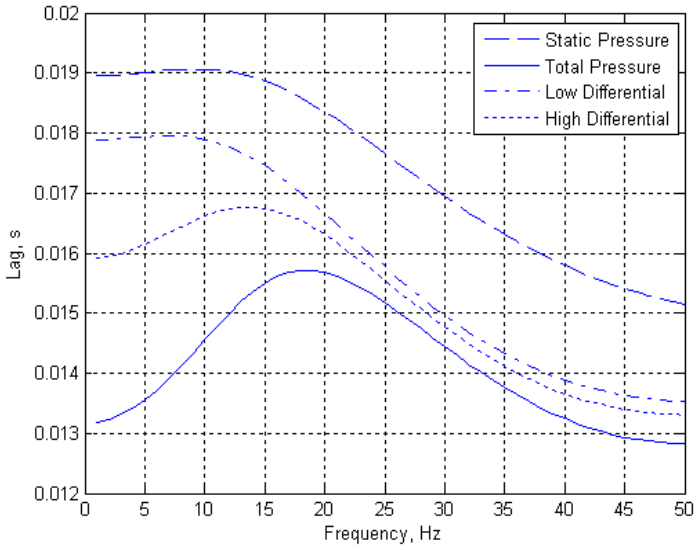

Figure 23 Lag at 22M Re, M = 0.75, ID = 3/32 inches

Figure 23 shows that the lag in each of the tubes is well below 0.12 seconds for frequencies less than or equal to 5 Hz. The total pressure line has the lowest lag while the static pressure lag is the highest. The pitch/yaw port pressures lie between these two extremes.

The measurement of flow angles and velocities is negatively impacted by the presence of phase shifts in the pressure lines. It is important to characterize the differences in phase between the high and low pressure differential ports on the five-hole probe as well as the total and static pressures, as they are used to calculate flow angles and velocity, respectively. A comparison of the phase differences in the velocity and angle measurement input pressures is shown in Figure 24 for the 22 million Reynolds number, 0.75 Mach case.

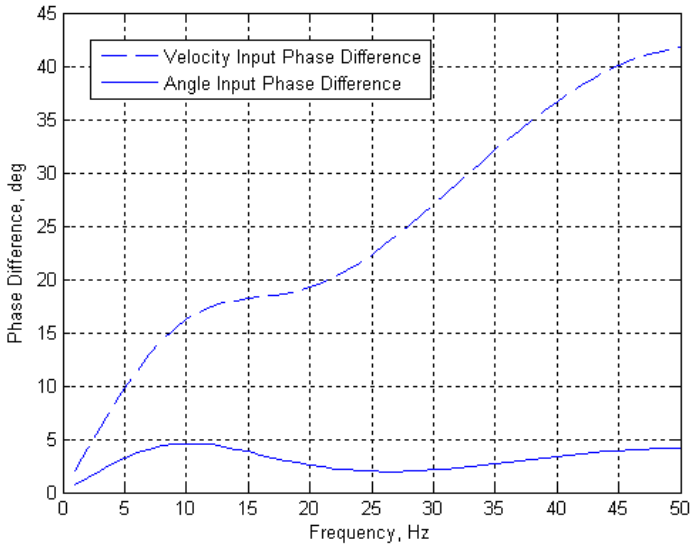

Figure 24 Phase difference between differential pressures used to compute velocity and angle.

Figure 24 shows that the velocity measurement inputs have significant phase differences that grow with frequency. The accuracy of these unsteady velocity measurements declines quickly and cannot be trusted at frequencies greater than a few Hertz without post-processing. Conversely, the phase difference between the pressures used for computing flow angles remains less than 5° for all frequencies surveyed.

This is because the absolute pressures within the pitch and yaw ports are closer in magnitude than those of the total and static pressure ports. The angle measurements will read the correct angles with some time lag whereas the unsteady velocity measurements will not reflect actual conditions in the freestream.

Fortunately, the SARGE flight test plan is designed to maintain quasi-steady state conditions. The pilots will establish the aircraft at a stabilized flight condition in order to take data and will hold this condition for at least 15 seconds. Thus, pilot induced changes in aircraft state will occur at frequencies on the order of 0.1 Hz or less. The previous analysis has been conducted in large part to show the deficiencies of the five-hole probe as a tool for measuring high frequency atmospheric perturbations. Rather, the measurements of the five-hole probe will be regarded as mean-flow conditions.

It is important to point out that a 3/32 inch inner diameter tube has been identified as the optimum diameter for maximizing frequency response and minimizing amplification due to an under-damped system. This inner diameter must extend from the opening of the five-hole probe's holes to the transducer, meaning that the holes in the probe must be 3/32 inch inner diameter for the previous results to be valid. Holes in the tip of the probe smaller than 3/32 inch will severely curtail the response of the system. For example, the holes in the tip of the five-hole probe used at the Texas A&M Flight Research Lab are 1/32 inch inner diameter. A scenario in which an 8 inch segment of 1/32 inch tubing comprises the opening of the probe's tubing has been analyzed for the total pressure port and compared to the response of the purely 3/32 inch tubing. The flight conditions at the 22 million Reynolds number, 0.75 Mach case mentioned previously have been used for the analysis. The results are shown in Figure 25.

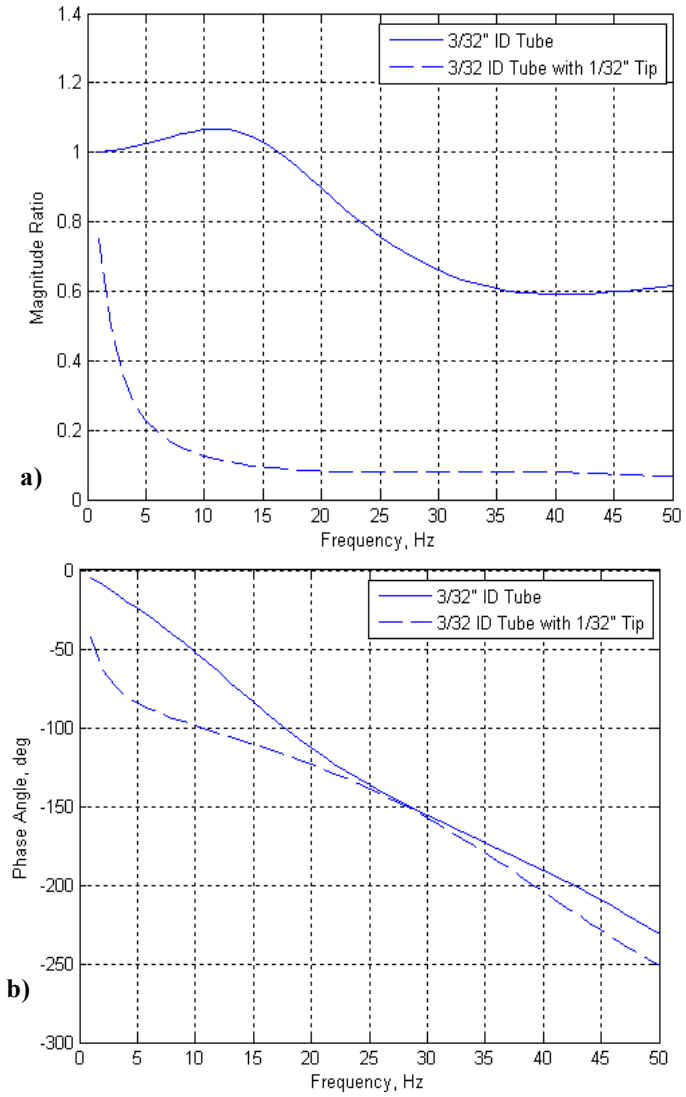

Figure 25 Effect of small diameter tube at entrance to pressure tubing on a) magnitude ratio and b) phase angle.

Figure 25 clearly shows that having a hole smaller than the rest of the tubing in the tip of the probe will have a disastrous effect on both the magnitude ratio and phase shift of the signals of interest. The contraction drops the magnitude ratio at 20 Hz from about 0.9 to approximately 0.1 and increases phase shifts on the order to 50° for low frequencies. Clearly, the size of the hole at the tip of the five-hole probe

will dominate the response properties of the tubing system. It is important to factor this effect into the design process when sizing the five-hole probe.

E. High Frequency Kulite Transducers

Freestream perturbations have a direct impact on boundary layer transition. As mentioned previously, the path to transition is heavily dependent on initial conditions. Freestream disturbances are entrained into the boundary layer through the receptivity process and set the initial conditions for the growth of instabilities. Linear stability theory assumes that departures from the meanflow conditions are small and higher order terms are ignored when developing the disturbance Navier-Stokes equations. Therefore, it is imperative that boundary layer stability experiments attempt to quantify freestream disturbances. The pressures measured by the five-hole probe would not be appropriate for measuring these higher frequency perturbations as shown previously. The pressures measured by the five-hole probe will be effectively low-pass filtered and will represent meanflow quantities. An independent measurement technique designed for maximizing frequency response is required.

The SARGE project will use a minimum of three high-frequency-response transducers manufactured by Kulite Semiconductor Products, Inc. to monitor disturbances at frequencies ranging from 1 Hz to 30 kHz. These probes will be used to measure total and static pressure disturbances. The total pressure measurement can be combined with the known freestream Mach number in order to calculate the streamwise disturbance velocity. Static pressure perturbations are a result of acoustic waves and are correlated with sound intensity. The T-S instability is sensitive to sound in particular.

It was originally thought that disturbance pressures would be most effectively measured by making differential pressure measurements between the pressure sensed at the five-hole probe's transducers and the fast response Kulites. However, this technique is prone to location errors created by measuring perturbations at locations not immediately adjacent to the tip of the five-hole probe. As an alternative, absolute pressure measurements in conjunction with electronic filtering can also yield disturbance pressures.

The transducers selected for the absolute and total pressure measurements are Kulite model XCS-062 series absolute pressure transducers. These sensors are designed for absolute pressures of 0-15 psia and have a full-scale output of 200 mV. The transducers are rated for overpressures as high as two times the design pressure with no change in calibration. The Kulites are temperature compensated and the envelope can be customized for any range spanning 100 °F. The internal diaphragm used in the XCS-062 series has a natural frequency of 200 kHz, well above the frequencies of interest.

The outputs from the absolute transducers will be low-pass filtered from 0 Hz to 30 kHz using an Endevco Model 136 filter/amplifier unit. This unit will also apply a gain of 50 to the transistor's output, bringing the full-scale output to 10 V. This voltage is a standard upper limit for many data acquisition boards. This signal will then be recorded in order to establish the DC component of the signal. The DC component will be noted as the mean pressure and will be used to compare with disturbance pressures. The low-pass-filtered and amplified signal will then be AC coupled using a band-pass filter. The filter will have a pass band between 1 Hz and 30 kHz in order to isolate the frequency band of interest. The remaining signal will then be the disturbance pressure.

Custom probes have been designed to mount the transducers and collect the desired pressure data. The total pressure transducer will be mounted inside of a custom Pitot tube that will be attached to the air-data boom. Two static pressure transducers will be embedded into the surface of the wing glove. Both will be located along the inboard pressure port row with one at 30 % chord and the other at 55 % chord. The transducer at 55 % chord is the most critical, as it is near the suction surface's pressure minimum. The adverse pressure gradient aft of this location is highly susceptible to the T-S instability, which is influenced by sound. The transducer at 30 % chord provides redundancy and is a contingency in case the boundary layer transitions earlier than anticipated. Static pressure disturbance measurements across a turbulent boundary layer are meaningless due to the small, but non-negligible, influence of turbulent flow on wall static pressure. The anticipated pressure coefficients at the inboard and outboard pressure port rows are shown in Figure 26.

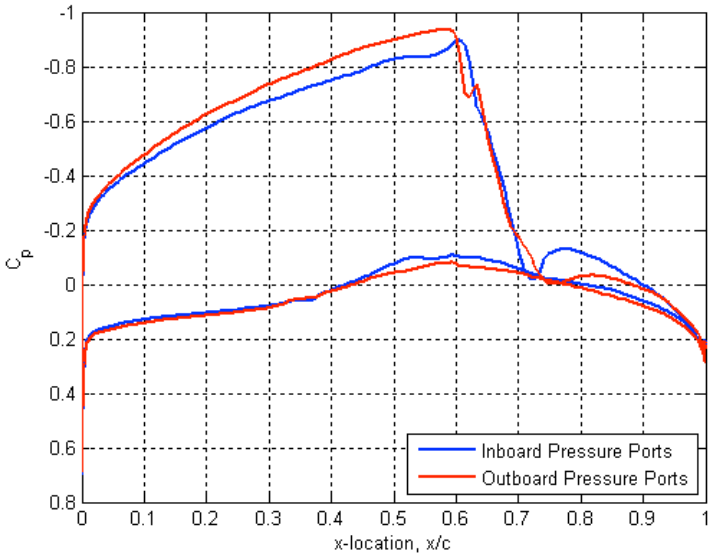

Figure 26 SARGE glove pressure coefficient profiles.

The custom Pitot tube has been designed to facilitate accurate measurements as well as easy swapping of transducers, as their diaphragms are quite delicate. A conical tip design has been selected for the Kulite total pressure probe. Conical-tipped Pitot tubes provide high quality measurements in compressible flows and are typically accurate to within one percent of dynamic pressure for flow angle offsets as high as ±18° (Wuest 1980). Therefore, flow misalignment with the air-data boom due to upwash and sidewash is of little concern.

The dimensions of the Pitot probe were defined using the standards listed in the AGARD pressure and flow measurement report (Wuest 1980). The diameter of the body of the probe should be about 1.8 times larger than the diameter of the hole at the tip. The contraction portion of the conical tip should be approximately 4.2 times the body diameter in length. Finally, the stem of the probe should be placed approximately 12 body diameters away from the tip. An illustration of these recommendations applied to a Pitot-static tube is shown in Figure 27.

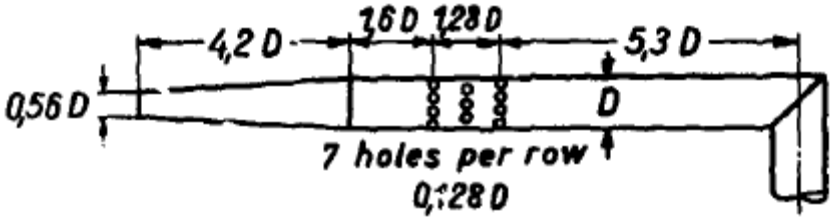

Figure 27 Conical Probe Design Parameters (Wuest 1980)

The aforementioned design criteria were applied to the dimensions of the Kulite transducer system. The proposed design calls for a Kulite transducer with an outer diameter of 0.066 inches to be mounted inside of a hypodermic tube with an inner diameter of 0.67 inches and a wall thickness of 0.008 inches. Mounting the Kulite inside of the hypodermic tubing creates a ruggedized Kulite transducer insert that can be more easily mounted inside of the Pitot tube without risking damage to the Kulite. The body of the Pitot probe is to be divided into two sections: the tip and the base. The tip section will mount to the base section through the use of set screws and/or a threaded insert. This tip must be easily removable in order to facilitate the changing of transducers in the case of a diaphragm failure. A diagram of the proposed setup is shown in Figure 28.

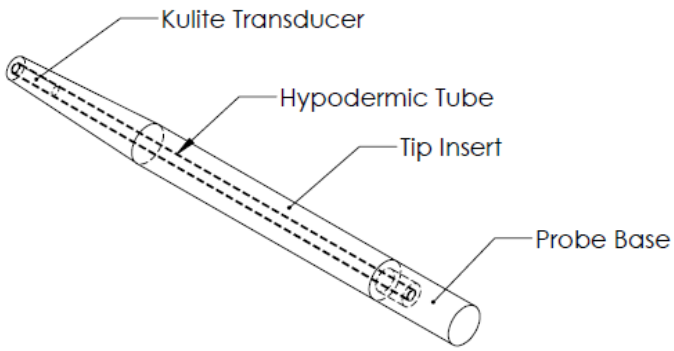

Figure 28 Illustration of proposed Kulite total pressure probe.

The proposed dimensions of this system are shown in Figure 29. The tip of the probe has been thickened beyond the outer diameter of the hypodermic tubing in order to ease manufacturing difficulties associated with extremely thin walls and tight tolerances.

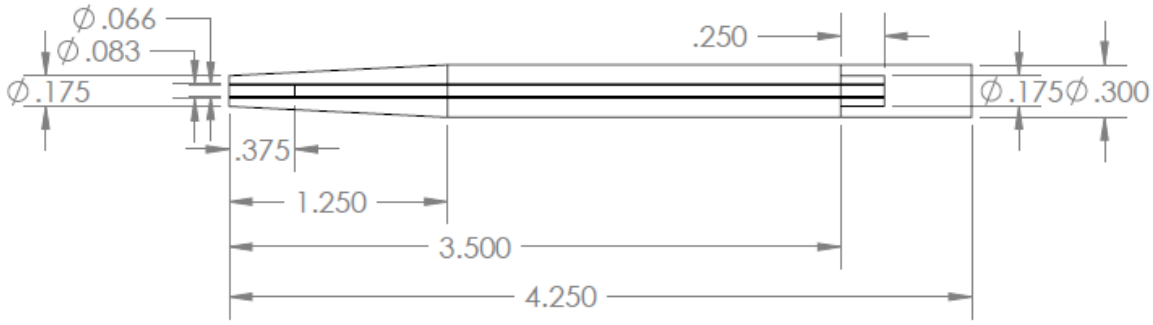

Figure 29 Dimensions of proposed Kulite total pressure probe.

Dynamic Response of Kulite Transducers

The frequency responses of the static and total pressure Kulite transducer systems are critical to understand when making measurements at 30 kHz. The total pressure port's construction makes analysis fairly straightforward. The transducer is to be flush-mounted to the front of the probe, as shown previously. The case where the transducer is offset a distance of 1 mm from the front of the probe is also analyzed in order to investigate the criticality of placing the transducer perfectly flush with the opening of the hole. The results of this analysis are presented in Figure 30. Here, the conditions at the 22 million Reynolds number and 0.75 Mach test point are used for calculations.

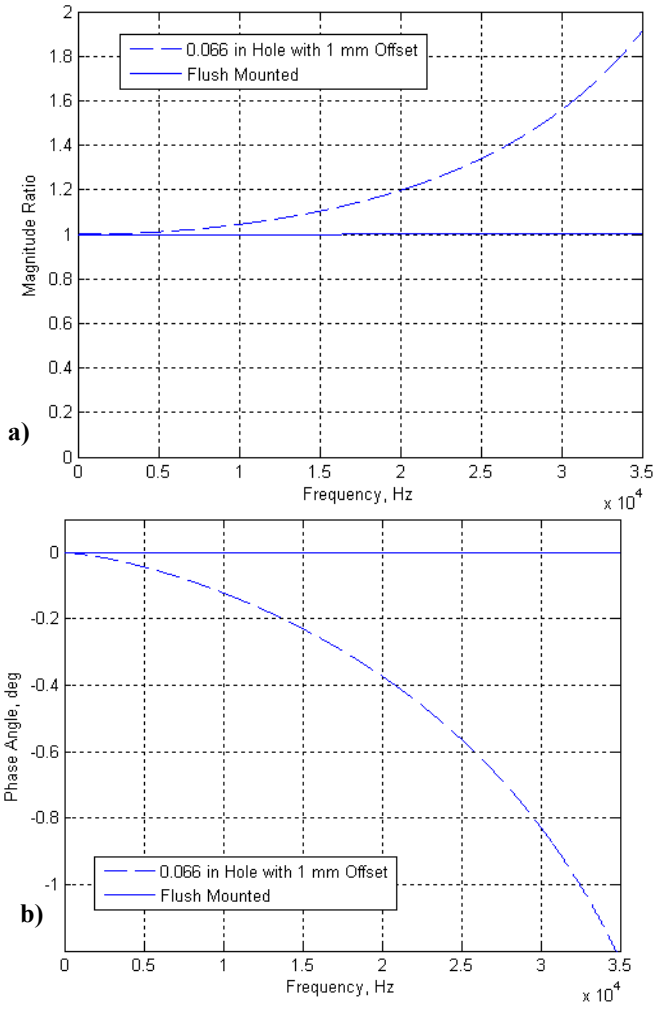

Figure 30 Effect of 1 mm offset on Kulite total pressure measurement for a) magnitude ratio and b) phase shift

Figure 30a shows that the magnitude ratio of the response is highly dependent on offset distances, particularly for frequencies above about 5 kHz. The 1 mm transducer offset amplifies the 30 kHz signal to nearly 1.6 times the original. The phase shift plotted in Figure 30b shows a slight dependence on frequency in the case of the 1 mm offset. However, the phase shift is only about 0.8° for the 30 kHz signal. In the cases of both amplitude ratio and phase shift, the flush mounted transducer has almost zero distortion of the original signal. The magnitude and phase plots for the other test points are qualitatively similar, with small shifts in the locations of each curve being the only difference.

The design of the static pressure Kulites' housings is more complex due to the difficulties associated with making accurate static pressure measurements. Static pressure taps should minimize diameter and depth in order to improve accuracy (McKeon 2007). Additionally, the hole's diameter should be less than the length scale of the perturbation of interest and on the order of no more than several times the displacement thickness of the wall boundary layer, which is the dominant viscous length scale in the system (McKeon 2007). The wavelength of a 30 kHz acoustic wave at the 22 million Reynolds number, 0.75 Mach test point's ambient conditions is approximately 9.8 mm, or 0.38 inches. The displacement thickness at 30% chord has been calculated to be on the order of 0.8 mm, or 0.04 inches. Thus a hole with a diameter equal to the Kulites' out diameter of 0.066 inches would smaller than the smallest acoustic wavelength of interest and about twice the displacement thickness, satisfying the criteria mentioned previously.

The acoustic transfer functions of three static pressure port designs were investigated. The first design was a flush-mounted Kulite transducer. The second design was a 0.066 inch inner diameter hole with the transducer offset 1 mm from the surface. The third design called for a 0.02 inch inner diameter hole of 0.125 inch depth which led to a cavity of 0.066 inch diameter and 1 mm depth. This final design minimized the diameter of the pressure port at the surface by sharing a common diameter with ports used for static pressure measurements. The depth of the 0.02 inch hole was dictated by the projected thickness of the wing glove's skin. A schematic of each design is shown in Figure 31.

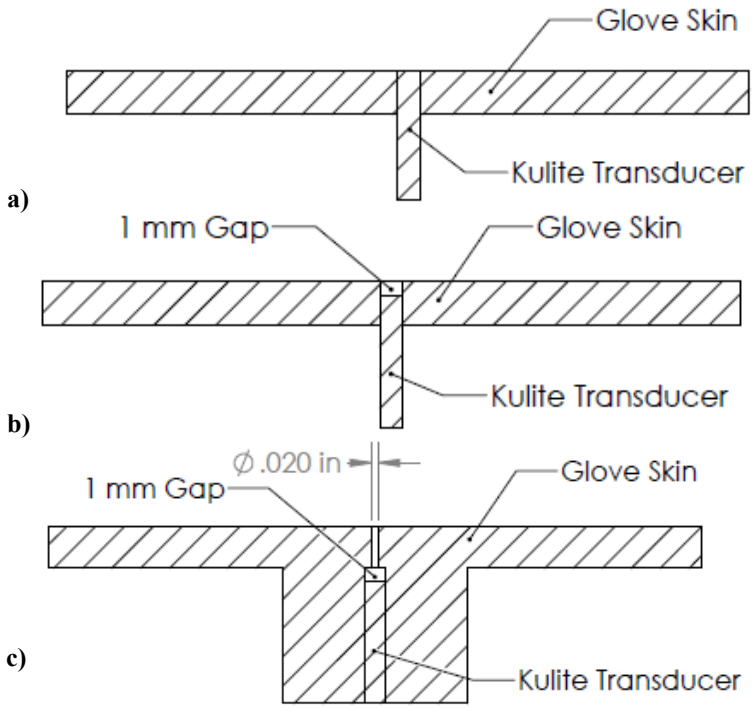

Figure 31 Kulite static pressure port designs

The frequency responses of the transducers' signals within each hole type were investigated at each SARGE test point. The results of the computations done at the 22 million Reynolds number, 0.75 Mach test point at 30% chord are shown in Figure 32.

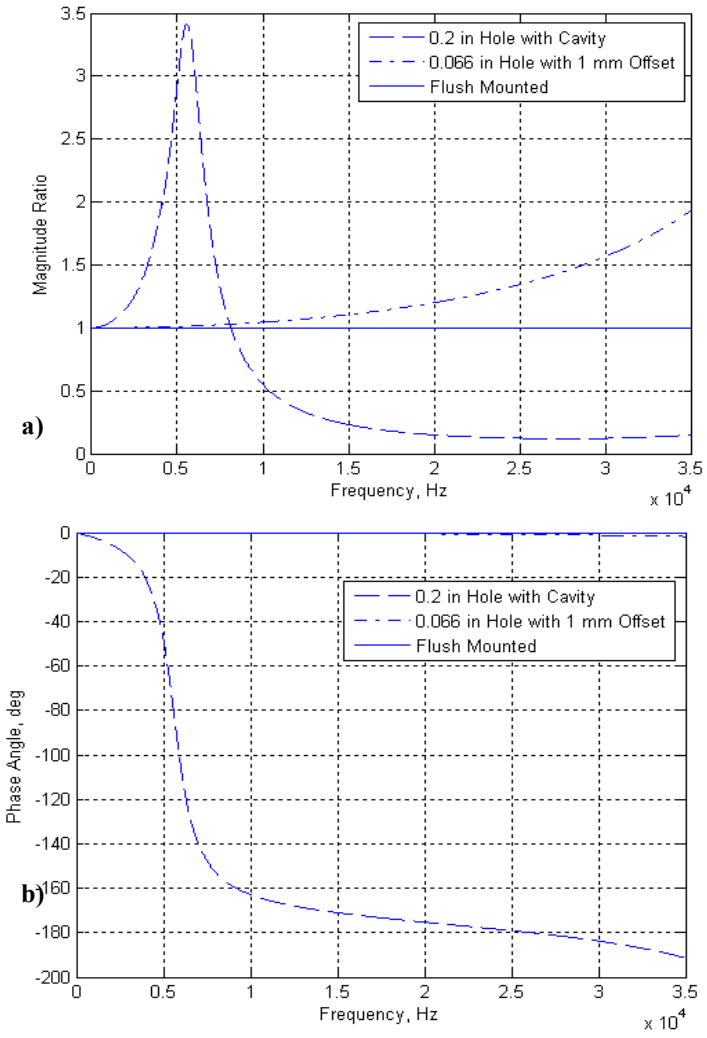

Figure 32 Effect of hole geometry on static pressure Kulite transducer for a) magnitude ratio and b) phase angle.

Figure 32a shows that the 0.02 inch hole is under-damped and has a maximum magnification of nearly 3.5 around 6 kHz. This is then followed by a significant attenuation, resulting in an amplitude ratio of approximately 0.1 for frequencies higher than 20 kHz. The 0.066 inch diameter hole with 1 mm offset is also under-damped, but has a more gradual rise in amplitude ratio. The magnitude ratio of this signal reaches about 1.6 at 30 kHz. The flush mounted transducer's magnitude ratio is essentially one at all frequencies of interest. The phase shifts for these designs are shown in Figure 32b and show that the 0.02

inch hole has a large phase shift at frequencies greater than 5 kHz. The offset transducer does not have a notable phase shift, as was the case for the total pressure measurements. The responses of signals within each design at each test condition and suction-side location are qualitatively similar to those in Figure 32 and uniformly suggest that a flush mounted Kulite transducer is the only configuration capable of providing accurate perturbation measurements at frequencies up to 30 kHz.

F. Thermocouples

Thermocouples will be installed on the suction and pressure surfaces of the SARGE wing glove in order to provide surface temperature measurements at strategic locations. The suction-side thermocouples have two main purposes. First, the thermocouples will provide a time history of the glove's surface temperature at each stabilized test condition. These time histories will allow the research team to determine whether or not the wall has reached adiabatic conditions. Non-adiabatic conditions will change the nature of the IR thermography from measuring recovery temperature to detecting the variation in heat transfer rates. The polarity of the IR images can also change depending on whether the glove has been hot-soaked or cold-soaked. Additionally, a wall temperature above the ambient air conditions is destabilizing for the T-S instability. The second function of the suction-side thermocouples is to verify the results of the IR thermography. The spacial temperature trends of the IR image should qualitatively match the results of the thermocouples.

The pressure-side thermocouples will serve as boundary layer transition detection tools in addition to monitoring the surface temperature's time history. Pressure-side thermocouples will be placed in intervals of 10 % chord from 20 % to 60 % chord. The chordwise temperature profile measured by these sensors will allow transition location to be determined to within ±5 % chord.

The thermocouples chosen for this role are Omega Engineering, Inc. type-T thermocouples with 36 gauge wire leads. Type-T thermocouples were chosen because they are best suited for measurements in the temperature range of interest and have the highest accuracy. Also, type-T thermocouples typically find application in reducing or vacuum environments (Figliola & Beasley 2006). 36 gauge wire leads were chosen in order to minimize the bulk associated with the sensor wiring.

G. Hotfilms

Hotfilm sensors will also be installed on both the suction and pressure sides of the wing glove. Like the thermocouples, the hotfilm sensors will serve to verify boundary layer transition on both sides of the glove. They will serve as the primary transition detection tool on the pressure side of the glove. The hotfilms will be uncalibrated and the transition will be detected through analysis of the sensors' frequency spectra. The spectral content of laminar and turbulent boundary layers is qualitatively different and easily distinguished.

A special hotfilm sensor array has also been designed to measure the wave speed and direction of traveling disturbances. This array utilizes multiple sensors arranged in a known spacial relationship along with spectral correlation techniques to measure these parameters. A further explanation of this technique is found in Section 4.

Hotfilm measurements will be done using an A.A. Labs AN-1003 constant temperature anemometer. This anemometer has been used extensively at the Texas A&M Flight Research Lab and is easily capable of measuring disturbances at or below the desired frequency band of 0 to 10 kHz. The typical overheat ratio for hotfilms ranges from 1.2 to 1.3.

H. Total Temperature

A freestream temperature measurement is required in order to facilitate the calculation of Reynolds number. Total temperature is easy to measure and is not subject to position errors due to the sensor's location on the aircraft. Therefore, a total temperature measurement will be combined with freestream Mach number in order to calculate freestream static temperature and then freestream viscosity. The total temperature probe can be mounted either to the aircraft's fuselage or the side of the air data boom. A common total temperature sensor suitable for the SARGE experiment is the Goodrich Corporation Model 102 non-deiced total temperature probe. The temperature uncertainty for this probe is on the order of ±0.3 °C.

I. Wing Deformation Measurement

The structure of the aircraft's wing will deform in flight due to changes in aircraft weight, fuel loading in the wings, and acceleration forces created by test maneuvers. This deformation will be manifested as both wing deflection and twist. The twist of the wing is especially important to the glove experiment because it will change the glove's incidence angle with respect to the freestream angle of attack. The wing-mounted air data boom will likewise have its incidence angle changed. Therefore, it is important to have a system in place that is capable of measuring this deformation. One approach to measuring deformation is to mark the wing at known locations and take pictures of the markings with a standard camera. The change in relative position of these markings from image to image will correlate with deformations of the wing's structure. Strain gauges and fiber optic wing shape sensing technologies can also be employed but are much more computationally expensive.

J. Recommendations for Air Data System

The research air data system should have the capability to measure freestream Mach number and static pressure. The wing-mounted five-hole probe will measure glove-local static pressure and Mach number, but these measurements will differ from the freestream conditions due to the influence of the aircraft. An accurate measurement of freestream static pressure is necessary in order to measure pressure and lift coefficients on the glove. The ESP proposed for monitoring static port pressures is a differential instrument and requires a reference pressure. This reference pressure must in turn be related to the freestream static pressure in order for the differential pressures to be converted into the local static pressure on the surface of the glove. This local static pressure will then be combined with the freestream Mach number in order to calculate the pressure coefficient. The lowest measurement uncertainty would be achieved by referencing the ESP to the five-hole probe's static ring, which is then calibrated to the freestream static pressure. The measurements of freestream Mach number and flow angles are also desirable since they will assist with the verification of computations.

The calibration of the five-hole probe to freestream conditions can be accomplished through several different strategies. Ideally, the freestream would be directly measured using a nose-mounted, high

fidelity air-data boom. Unfortunately, structural limitations often forbid this technique from being implemented due to the large boom lengths required to acquire data in unmodified flow (Haering 1995). Another option is to use radar or GPS position data in conjunction with an inertial unit inside the aircraft and weather balloon data to calibrate the wing mounted probe. Such techniques and their merits are discussed in Haering (1990). The third option available is the use of a calibrated pacer aircraft to correlate local conditions to the freestream. As a last resort, the aircraft's flight air-data system can be used to provide lower quality freestream measurements. A good review of freestream air data calibration techniques can be found in Haering (1995).

The calibration of the five-hole probe's measured static pressure and Mach number to freestream conditions will be affected by the deformation of the aircraft's wing due to loading varying conditions. These effects can be minimized through the use of thorough calibration and post processing of wing deformation data. The principle parameters affected by these structure-induced variations are the Mach number and the glove's static pressure coefficient. The Mach number will likely have some bias introduced due to the changes in the local static pressure field due to wing twist and deflection. The pressure coefficient measurements will be shifted due to the bias introduced by the static pressure measurements and the coefficient profiles will be either stretched or squashed due to the biases introduced into the Mach number.

Although the wing deformation makes freestream measurements more difficult, the wing mounted boom allows for this effect to be eliminated from differential measurements. The local flow angle measured by the probe will be correlated with static pressure profiles during the science envelope definition phase of the SARGE flights. Primarily, the team will seek to define the maximum local angle of attack that does not result in a pressure peak forming in the chordwise pressure coefficient profile. Because the variation in twist angle across the gloved section of the wing is essentially negligible, this local angle of attack should produce an identical pressure distribution on the test section of the glove regardless of the wing's deformation. This is, of course, assuming that the changes in deformation of the rest of the wing is relatively small and does not modify the flow over the gloved section of the wing at identical local angles of attack with different fuel loads. Careful flight planning that ensures that wing fuel

loads during calibration and experimental flights are approximately equal will also mitigate the effects of wing deformation on glove pressure distributions as a function of local angle of attack.

The ideal approach to air-data collection on the SARGE project would be to employ two five-hole probes. The first probe would be mounted to the nose of the aircraft so as to avoid the effects of wing deformation. This probe would then be calibrated to freestream conditions. A second, wing-mounted probe would then be installed as described previously. The wing-mounted probe's local data could then be used to identify the desired local angle of attack necessary to execute each test point. This approach would provide research quality freestream conditions as well as eliminate the influence of wing deformation assuming that there are negligible changes to the glove's pressure distribution at the relevant deformations. Although this approach provides the highest quality data, it is expensive to implement. It would require modification of the aircraft's nose structure and radome. Additionally, it would double the number of Paroscientific and PPT transducers required and increase onboard data processing requirements.

K. Recommendations for DREs

Carpenter (2009) noticed that the uniformity of DREs placed on a rough surface made a significant impact on their effectiveness. Soft appliqué DREs tended to mold to the shape of underlying roughness and did not delay transition as well as those placed on more uniform sections of the leading edge that maintained their uniform, cylindrical shape. Therefore, it is critical that efforts be made to measure the shape of the DREs after application on SARGE using either profilometry or laser scans. If appliqué DREs are not effective at delaying transition it may be because their shape has been altered by the roughness of the underlying substrate and a stiffer DRE material should be used for further testing. Bench testing of different DRE types should be completed before the flight phase of the project in order to identify the most promising brands of DREs.

3. GLOVE HEAT TRANSFER CALCULATIONS

A. Motivation

Since IR thermography is the principle tool used for imaging boundary layer transition, it is important to understand heat transfer at the surface of the glove. The glove will be mounted on top of the wing's surface, meaning that it will be continually exposed to direct sunlight during the course of the experiment. Additionally, the glove will radiate some of its energy to the cold sky above. Further complicating the situation is the differential convection between the laminar and turbulent regions, and, to a lesser extent, within the laminar and turbulent regions themselves. A true adiabatic wall temperature will only be achieved if solar irradiation is completely balanced by radiation from the glove to the sky and the glove is cold soaked long enough for the surface to reach a steady state value equal to the laminar or turbulent adiabatic wall recovery temperature. Therefore, it is unlikely that the adiabatic wall temperature difference between the laminar and turbulent regions will ever be measured in flight.

This problem has been addressed by previous glove experiments, notably the LFU 205 and VFW 614 projects. The LFU 205 glove was painted red in order to enhance its absorption of solar radiation. This caused the laminar region near the leading edge to warm more than the turbulent region, resulting in IR images similar to that show in Figure 33. Here the light color in the IR image represents a higher surface temperature.

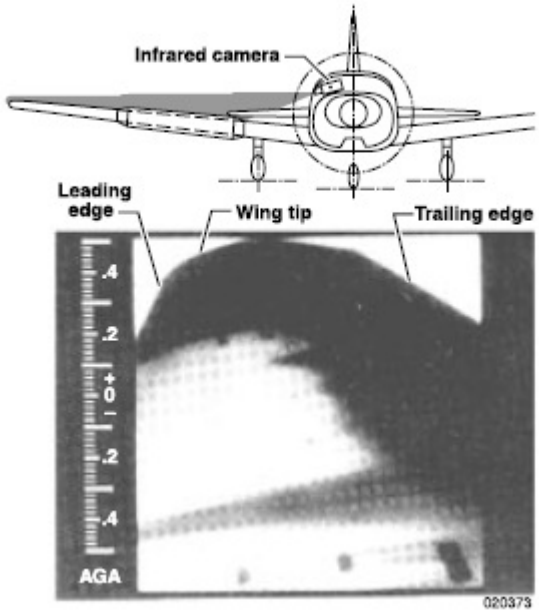

Figure 33 LFU 205 glove IR image (Fisher *et al.* 2003).

The VFW 614 project studied laminar flow over both a wing glove and an engine nacelle. Two different techniques were used for obtaining IR images on the wing glove. A heating sheet was installed beneath the glove's surface to allow for sufficient temperature differences to be achieved during level flight with no solar radiation (Horstmann *et al.* 1990). Heat fluxes around 400 W/m^2 have been suggested for heating sheets and have proven to yield good images with short observation times (Fisher *et al.* 2003). IR images were also taken with the aircraft in a slight dive in order to take advantage of differential heating between the laminar and turbulent zones. It is worth noting that most of the test points planned for the SARGE experiment are to take place in the tropopause, where temperature is essentially constant with altitude and a dive may be of little use. A photo of the VFR 614 in flight with the wing glove attached to the starboard wing is shown in Figure 34. Figure 35 shows an IR image taken through an IR transparent window from within the cabin.

Figure 34 VFW 614 and wing glove in flight (Fisher *et al.* 2003).

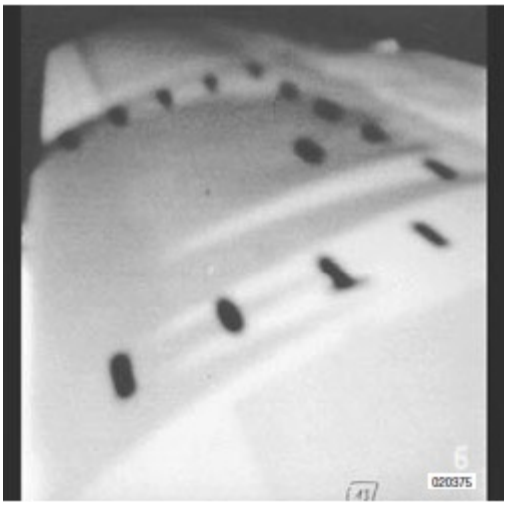

Figure 35 IR image of VFW 614 wing glove (Fisher *et al.* 2003).

Selection of the glove's surface finish is another important parameter that is motivated by heat transfer. Metallic surface finishes, particularly those that are highly polished, have low emissivity and high reflectivity. This means that the IR camera will perceive them as cold surfaces unless they are reflecting solar radiation or other sources of concentrated IR emissions directly into the camera. Additionally,

radiation from metallic surfaces is highly dependent on direction. Metallic surfaces also have the disadvantage of high heat conduction, meaning that the temperature difference between the laminar and turbulent regions will be lower and more diffuse. For these reasons, polished metallic glove surfaces are discouraged if IR thermography is to be employed. Conversely, emission from non-metallic surfaces is nearly independent of the IR camera's viewing angle. A comparison of the directional properties of emission from metallic and non-metallic surfaces can be seen in Figure 36.

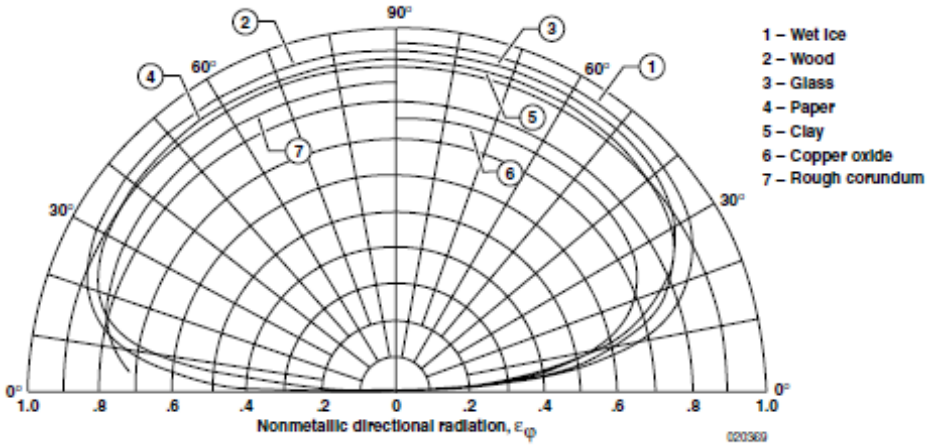

(a) Nonmetallic.

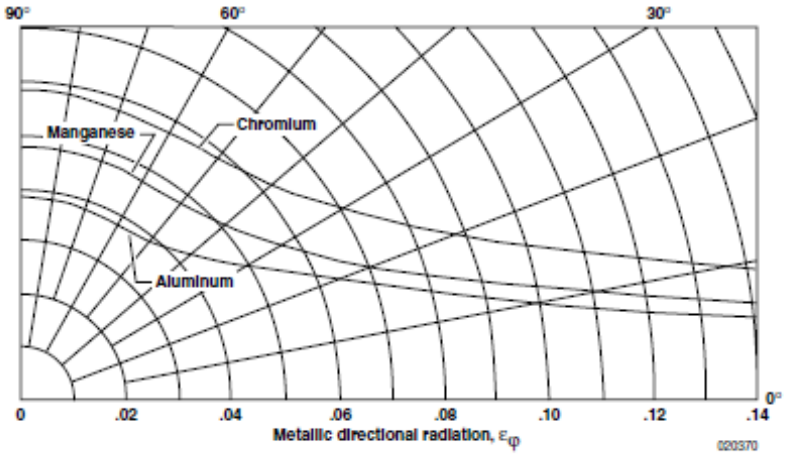

(b) Metallic.

Figure 36 Directional properties of radiation for non-metallic and metallic surfaces (Fisher *et al.* 2003).

Painted, non-metallic gloves have been shown to yield useable IR images as has been shown previously. The paint color has no influence on the IR image except with regard to absorbing solar radiation (Quast 1987). Therefore, paint color can be used to control the response of the glove's surface to solar radiation. The goal of the current analysis is to characterize this response and identify the most effective glove color. Previous work has shown that good to excellent IR images can be obtained when the laminar and turbulent zones have a temperature difference between 1 °C to 2 °C (Fisher *et al.* 2003).

Heat Transfer Models

Two heat transfer models were utilized for evaluating the thermal properties of a wing glove with similar physical properties to the one currently proposed for the SARGE project. A one-dimensional model was used to estimate heat transfer normal to the model's surface. This model assumed that there was no heat transfer in the transverse directions. The primary goal of this analysis was to quantify the responses of black and white painted surfaces to solar radiation and to characterize the influence of aircraft climb profiles on surface temperatures. A second, two-dimensional model was used to increase fidelity of the estimated temperature difference between laminar and turbulent regions. This model analyzed a material cross-section along a line of constant span between 15% and 55% chord. Heat transfer was assumed to occur only in the chord-wise direction.

Both models operated under several general assumptions. First, contact resistance between layers of different material was ignored. Also, the boundary layer on the pressure side of the wing was assumed to be completely turbulent across the region of interest. Also, the wing glove's suction side was assumed to be completely turbulent across the region of interest when being evaluated off of its design condition. Finally, a heating blanket was assumed to lie beneath the glove's skin and was of infinitesimal thickness and infinite thermal conductivity. The heating sheet was assumed to supply a heat flux of 300 W/m^2.

B. Falkner-Skan-Cooke Boundary Layer with Heat Transfer

The convective heat transfer coefficient on the surface of the glove is a function of the local pressure gradient and fluid properties as well as the wall temperature. Simple flat plate equations commonly quoted in introductory heat transfer texts could be used to provide a rough estimate of the convection at

the wall surface, but they neglect the effects of pressure gradients, compressibility, and wall temperature. In order to get a higher fidelity estimate of the convection on the surface of the glove the similarity equations of for the compressible Falkner-Skan and Falkner-Skan-Cooke boundary layers with heat transfer developed by Cohen & Reshotko (1956), and Beckwith (1958), respectively, were solved.

The equations developed by Cohen & Reshotko (1956) and Beckwith (1958) utilized the Stewartson Transformation to convert the compressible equations into the incompressible problem. This, coupled with the assumptions that Prandtl number is equal to unity and specific heat is constant, allows for the development of similarity solutions that are valid for arbitrary Mach number profiles with pressure gradient. The only caveat is that wall temperature must be constant. This situation will not generally be true for the suction surface of the wing glove. However, the temperature gradient in the laminar region forward of the transition location is likely to be low, making this assumption reasonable for the laminar region of greatest interest for IR thermography.

Use of the Falkner-Skan boundary layer equations accounts for the effects of streamwise pressure gradient, but ignores the crossflow pressure gradient present on a swept wing. The similarity solutions for the compressible Falkner-Skan-Cooke boundary layer with heat transfer (Beckwith 1958) included a slight modification from those of Cohen & Reshotko (1956) to account for crossflow. As would be expected, the wall shear stress increased with the inclusion of crossflow in a favorable pressure gradient. The difference in the shear stress affected by the sweep angles less than 35° and pressure gradients considered for the present problem was found to be less than 25 %. Thus, the simpler model of Cohen & Reshotko (1956) was used to make an initial estimate of the convection coefficients. The higher fidelity method of Beckwith (1958) was also utilized and compared to solutions for the Falkner-Skan boundary layer as well as the viscous Navier-Stokes code Fluent.

Laminar Boundary Layer Convection Analysis

Analysis of the laminar boundary layer begins by importing the pressure profile at the location of interest on the glove. Here, the pressure profile used for analysis corresponded to the SARGE test point at 22 million chord Reynolds number, 0.75 Mach, and an altitude of 39,000 ft. A plot of pressure coefficient

versus chord location is shown in Figure 37. Note that only the suction side profile was used for the current computations.

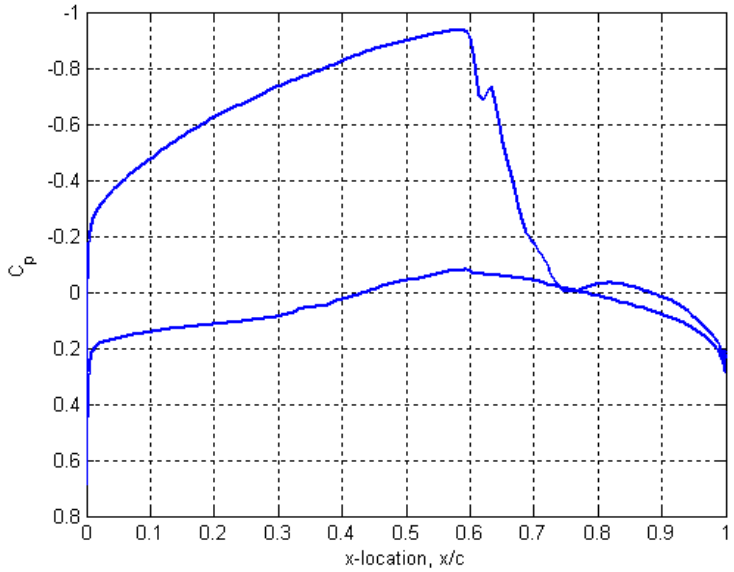

Figure 37 Pressure coefficient profile analyzed for convection model.

The pressure coefficients plotted in Figure 37 were computed using Fluent, a viscous CFD code. The values of edge pressure along the glove's suction side were calculated using Eqn (8).

$$P_e = P_\infty \left(\frac{1}{2}\gamma M_\infty^2 c_p + 1\right) \tag{8}$$

The values of edge Mach number, temperature, and velocity were then found using Eq. (9) through Eqn (11) respectively.

$$M_e = \sqrt{\frac{2}{\gamma - 1}\left(\left(\frac{P_0}{P_e}\right)^{\frac{\gamma-1}{\gamma}} - 1\right)} \tag{9}$$

$$T_e = T_0\left(1 + \frac{\gamma - 1}{2}M_e^2\right)^{-1} \tag{10}$$

$$u_e = M_e\sqrt{\gamma R T_e} \tag{11}$$

Stewartson's transformation is then applied to the wall-tangent and wall-normal directions as well as the edge velocity in order to convert the compressible boundary layer equations into an incompressible form. However, before this process can be completed the chord location and airfoil thickness at each pressure data point must be converted into an arc length. This effectively turns the airfoil profile into a flat plate as the separation between data points is converted into a Pythagorean distance rather than a chord location. This is accomplished using Eqn (12).

$$s = \sum_{i=1}^{n-1} \sqrt{(x_{i+1} - x_i)^2 + (y_{i+1} - y_i)^2} \tag{12}$$

Stewartson's transformation for the wall-tangent and wall-normal directions is shown in Eqn (13) and Eqn (14) respectively.

$$X = \int_0^s \lambda \sqrt{\frac{T_e}{T_0}} \frac{P_e}{P_0} ds \tag{13}$$

$$Y = \sqrt{\frac{T_e}{T_0}} \int_0^{y_n} \lambda \frac{\rho}{\rho_0} dy_n \tag{14}$$

Here λ is defined as

$$\lambda = \frac{T_0 + 110.56}{T_w + 110.56} \sqrt{\frac{T_w}{T_0}} \tag{15}$$

The transformed edge velocity is computed using Eqn (16).

$$U_e = \sqrt{\frac{T_e}{T_0}} u_e \tag{16}$$

Once the transformed wall-tangent coordinate and streamwise velocity have been computed from the pressure distribution and airfoil coordinates, the velocity profile in the region of interest as a function of X can be fit using the power law relation shown in Eqn (17). Here C is a constant of arbitrary value.

$$U_e = CX^{m_h} \tag{17}$$

A plot of the transformed velocity profile and corresponding power law curve fit for the current case under analysis are shown in Figure 38.

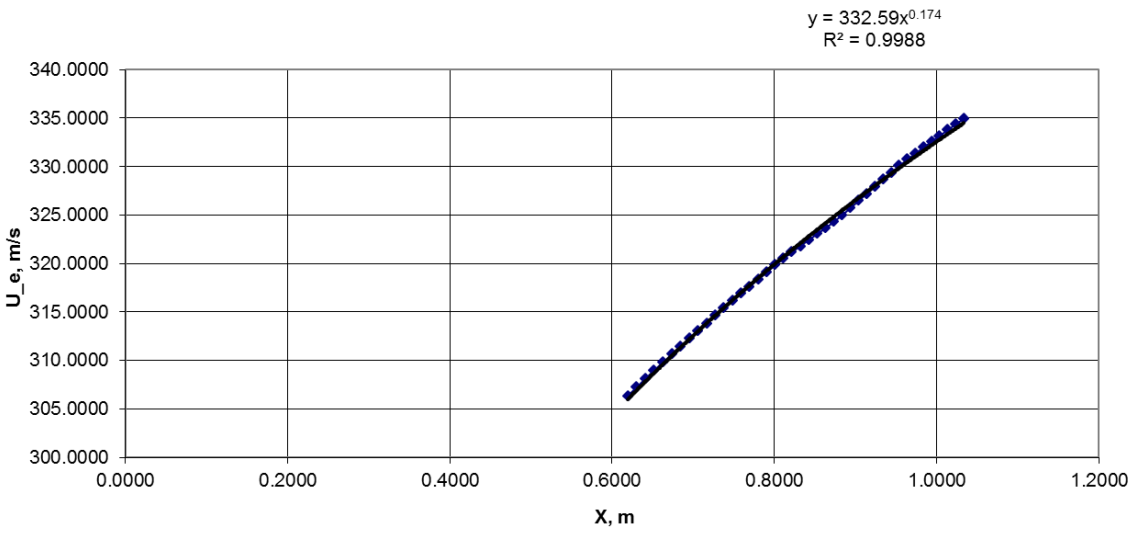

Figure 38 Transformed velocity vs. transformed x-location.

Here the value of m_h was found to be equal to 0.174, which can be converted to the Hartree pressure gradient parameter through Eqn (18). For this case the Hartree parameter was found to equal 0.3.

$$\beta_H = \frac{2m_h}{m_h + 1} \tag{18}$$

Similarity solutions to the Falkner-Skan boundary layer can be found by solving the system of differential equations shown in Eqn (19) and Eqn (20).

$$f_\eta''' = +f_\eta f_\eta'' = \beta_H \left(f_\eta'^2 - S - 1 \right) \tag{19}$$

$$S'' + f_\eta S' = 0 \tag{20}$$

Here f and S are functions of the similarity variable η, which is defined by Eqn (23).

$$f_\eta = f_\eta(\eta) \tag{21}$$

$$S = S(\eta) \tag{22}$$

$$\eta = Y \sqrt{\frac{m_h + 1}{2} \frac{U_e}{\nu_0 X}} \tag{23}$$

The function f_η is related to the streamwise velocity in the boundary layer by Eqn (24).

$$\frac{U}{U_e} = \frac{u}{u_e} = f'_\eta \tag{24}$$

In Eqn (20) S represents the stagnation enthalpy function written in term of stagnation enthalpy in the freestream and at the current location of interest within the boundary layer as shown in Eqn (25).

$$S = \frac{h_s}{h_0} - 1 \tag{25}$$

The value of the stagnation enthalpy function at the wall is determined using Eqn (26).

$$S_w = \frac{h_w}{h_0} - 1 \tag{26}$$

The stagnation enthalpies in the freestream and at the wall are computed using Eqn (27) and Eqn (28) respectively.

$$h_0 = c_{pr}T_\infty + \frac{1}{2}M_\infty^2 \gamma R T_\infty \tag{27}$$

$$h_w = c_{pr}T_w \tag{28}$$

The temperature at the wall can be solved in terms of the wall enthalpy function and freestream stagnation temperature to yield the equation $T_w = T_0(S_w + 1)$ by introducing $\gamma = c_{pr}/c_v$ and $R = c_{pr} - c_v$. The system of differential equations shown in Eqn (19) and Eqn (20) is subject to the boundary conditions listed in Eqn (29) through Eqn (32).

$$f_\eta(0) = f'_\eta(0) = 0 \tag{29}$$

$$S(0) = S_w \tag{30}$$

$$\lim_{\eta\to\infty} f'_\eta = 1 \tag{31}$$

$$\lim_{\eta\to\infty} S = 0 \tag{32}$$

The system of ordinary differential equations for the Falkner-Skan boundary layer with heat transfer shown in Eqn (19) and Eqn (20) was integrated using a 4th order Runge-Kutta numerical technique by decomposing the equations into a system of five simultaneous ordinary differential equations. This integration scheme requires the values of $f''_\eta(0)$ and $S'(0)$, which are not explicitly known from the physical parameters of the system. These boundary conditions were solved by successive approximation using the Newton-Raphson root finding method to converge on the boundary conditions at the opposite

end of the domain listed in Eqn (31) and Eqn (32). The results of this computational method were compared to those found by Cohen & Reshotko (1956) and agreement was excellent. The similarty shear stress parameter is for the Falkner-Skan boundary layer with the wall temperature equal to the total temperature of 240 K is equal to 0.7748, which is identical to the solution of the Falkner-Skan boundary layer for $\beta_H = 0.3$ with no heat transfer.

A slight modification to the equations above was made by Beckwith (1958) to account for crossflow. The similarity variable used for these equations is identical to the one used previously for the Falkner-Skan boundary layer.

$$f_\eta''' + f_\eta f_\eta'' = \beta \left\{ f_\eta'^2 - \frac{T_0}{T_{AL}} \left[\left(1 - \frac{T_w}{T_{AL}} \right) \theta_{HT} - \left(1 - \frac{T_{AL}}{T_0} \right) g_{CF}^2 + \frac{T_W}{T_0} \right] \right\} \tag{33}$$

$$g_{CF}'' + f_\eta g_{CF}' = 0 \tag{34}$$

$$\theta_{HT}'' + f_\eta \theta_{HT}' = 0 \tag{35}$$

Here, the function f_η is as before, g_{CF} is the similarity solution of the crossflow velocity, and θ_{HT} is the enthalpy ratio defined by Eqn (36).

$$\theta_{HT} = \frac{h_s - h_w}{h_e - h_w} \tag{36}$$

The stagnation temperature using the leading-edge normal velocity component is defined as:

$$T_{AL} = T_\infty \left(1 + \frac{\gamma - 1}{2} M_\infty^2 \cos^2 \Lambda \right) \tag{37}$$

The differential equations in Eqn (33) through Eqn (36) are subject to the following boundary conditions:

$$f_\eta(0) = f_\eta'(0) = \theta_{AL}(0) = g_{CF}(0) = 0 \tag{38}$$

$$\lim_{\eta \to \infty} f_\eta' = \lim_{\eta \to \infty} g_{CF} = \lim_{\eta \to \infty} \theta_{HT} = 1 \tag{39}$$

The system of ordinary differential equations shown in Eqn (33) through Eqn (35) can be solved using the same Runge-Kutta and Newton-Raphson methods utilized for the Falkner-Skan boundary layer equations. The system can be reduced from seven simultaneous differential equations to five by invoking the identity $g_{CF} = \theta_{HT}$. This identity is only valid when the Prandtl number is equal to one; in this case the crossflow boundary layer profile will match the thermal boundary layer profile.

The wall skin friction coefficient at the Mach 0.75, 39,000 ft test point can then be computed from the results of the similarity solutions. This process begins by determining the kinematic viscosity based on stagnation values of viscosity and density.

$$\rho_0 = \rho_\infty \left(1 + \frac{\gamma - 1}{2} M_\infty^2\right)^{\frac{1}{(\gamma-1)}} \tag{40}$$

$$\mu_0 = 17.16(10)^{-6} \frac{273.11 + 110.56}{T_o + 110.56} \left(\frac{T_0}{273.11}\right)^{3/2} \tag{41}$$

$$\nu_0 = \frac{\mu_0}{\rho_0} \tag{42}$$

The skin friction coefficient for the Falkner-Skan boundary layer can then be calculated using Eqn (43).

$$c_f = \frac{\tau_w}{\frac{1}{2}\rho_w u_e^2} = f''_{\eta_w}\left(2\lambda(1 + S_w)\right)\sqrt{\frac{m_h + 1}{2}\frac{\upsilon_0}{U_e X}} \tag{43}$$

A slight modification of Eqn (44) leads to the equation for skin friction coefficient for the Falkner-Skan-Cooke boundary layer:

$$c_f = \frac{\tau_w}{\frac{1}{2}\rho_w u_e^2} = \left(f''_{\eta w}\cos\Lambda + g'_{CF_w}\sin\Lambda\right)\left(2\lambda\left(\frac{T_w}{T_0}\right)\right)\sqrt{\frac{m_h + 1}{2}\frac{\upsilon_0}{U_e X}} \tag{44}$$

The derivative of the similarity enthalpy function at the wall, $\theta'_{HT} = -S'_w/S_w$, which is representative of heat transfer, is plotted as a function of wall temperature in Figure 39. The corresponding values of shear stress versus wall temperature are plotted in Figure 40.

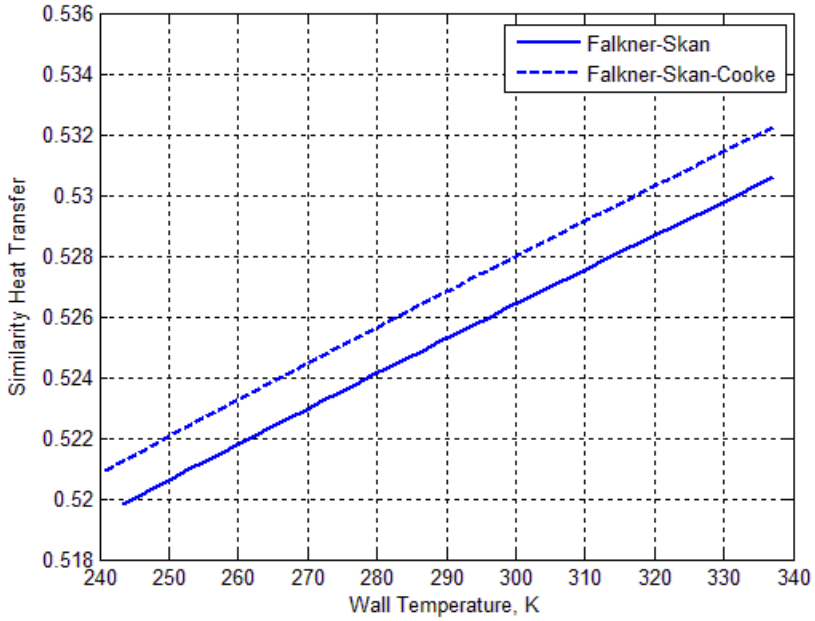

Figure 39 Similarity enthalpy function derivative vs. wall temperature at 30 % chord.

Figure 39 shows that the Falkner-Skan-Cooke boundary layer has a value of the wall enthalpy derivative higher than that of the Falkner-Skan boundary layer. This means that the three-dimensional boundary layer transfers heat away from the warm surface more effectively than the two-dimensional boundary layer. However, at the glove's flight conditions and sweep angle the difference is slight. In fact, the similarity solution for the Falkner-Skan boundary layer is only about 0.3 % lower than the value resulting from the inclusion of crossflow.

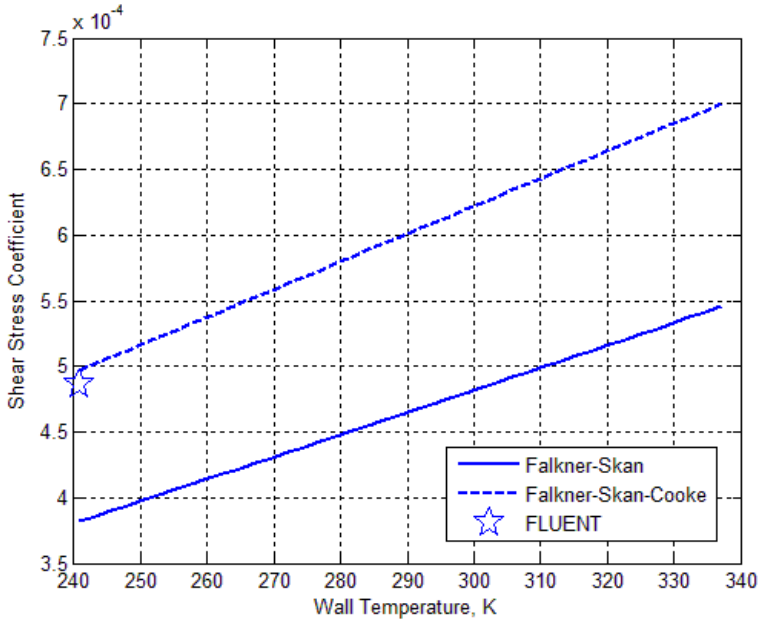

Figure 40 Skin friction coefficient as a function of wall enthalpy at 30% chord.

The value of skin friction coefficient at the 30 % chord location computed with the Falkner-Skan equations for an adiabatic wall, T_w = 240 K, is $4.09(10)^{-4}$, which is 16 % lower than the value of $4.86(10)^{-4}$ predicted at the same location by the viscous Navier-Stokes code Fluent. However, the Falkner-Skan-Cooke solution is $4.97(10)^{-4}$, only 3 % higher than the value predicted by CFD. This discrepancy is likely a result of uncertainty in the value of the Hartree parameter used for computing the similarity solutions.

Once the skin friction coefficient has been established, the Reynolds analogy may be used to convert this value into the convective heat transfer coefficient. The relationship between the wall similarity variables and skin friction for the Falkner-Skan solutions of Cohen & Reshotko (1956) is shown in Eqn (45).

$$\frac{c_f Re_w}{Nu} = \frac{2f''_{\eta_w}}{\left(-\frac{S'_w}{S_w}\right)} \tag{45}$$

This equation can be re-written for the Falkner-Skan-Cooke equations of Beckwith (1958) using the relationship shown in Eqn (46).

$$\theta'_{HT} = -\frac{S'_w}{S_w} \tag{46}$$

$$\frac{c_f Re_w}{Nu} = \frac{2\left(f''_{\eta_w} \cos\Lambda + g'_{CF_w} \sin\Lambda\right)}{(\theta'_{HT})} \tag{47}$$

Here the wall Reynolds number is defined as

$$Re_w = \frac{u_e x}{\nu_w} \tag{48}$$

The definition of the Nusselt number is shown in Eqn (49).

$$Nu = \frac{x\left(\frac{\partial T}{\partial y}\right)_{wall}}{T_0 - T_w} \tag{49}$$

The convective heat transfer coefficient is defined as shown in Eqn (50).

$$h = \frac{k_f\left(\frac{\partial T}{\partial y}\right)_w}{T_0 - T_w} \tag{50}$$

Eqn (45) through Eqn (49) are combined to solve for the convection coefficient in terms of the wall similarity variables, skin friction coefficient, local edge velocity, fluid thermal conductivity, and wall kinematic viscosity as shown in Eqn (51) and Eqn (52).

$$h = \frac{1}{2}\left(-\frac{S'_w}{S_w}\right)\frac{c_f u_e k_f}{f''_{\eta_w}\nu_w} \tag{51}$$

$$h = \frac{1}{2}(\theta'_{HT})\frac{c_f u_e k_f}{\left(f''_{\eta_w}\cos\Lambda + g'_{CF_w}\sin\Lambda\right)\nu_w} \tag{52}$$

A plot of the convective heat transfer coefficients predicted by the methods of Cohen & Reshotko (1956) and Beckwith (1958) as a function of wall temperature at 30 % chord, Mach 0.75, 39,000 ft condition is shown in Figure 41.

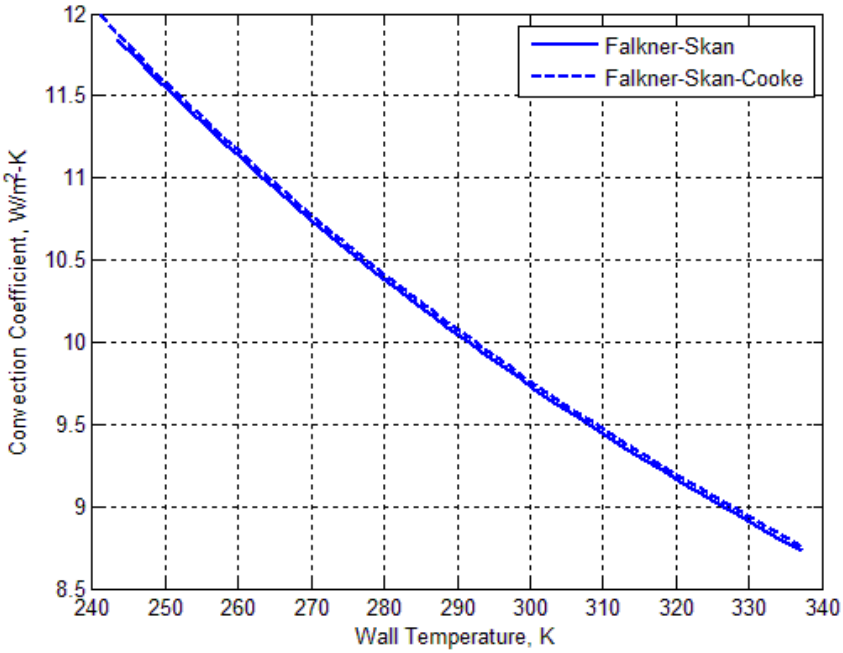

Figure 41 Convection coefficient calculated at 30 % chord.

Figure 41 shows that the convection coefficient decreases as the wall temperature is increased. The coefficient predicted by the Falkner-Skan-Cooke boundary layer is only about 0.3 % higher than that predicted by the Falkner-Skan boundary layer. This plot shows that the simpler two-dimensional boundary layer equations can be substituted in this case without much degradation in accuracy. The wall shear stress is under-predicted by as much as 30 % due to the neglection of crossflow, but the heat transfer coefficient appears to be minimally affected.

A surface plot of the heat transfer coefficient as function of both wall temperature and chord location on the glove was also produced for the Falkner-Skan-Cooke boundary layer at the same flight conditions as the previous figure, as shown in Figure 42. The heat transfer coefficient decreases asymptotically as both wall temperature and chord location are increased.

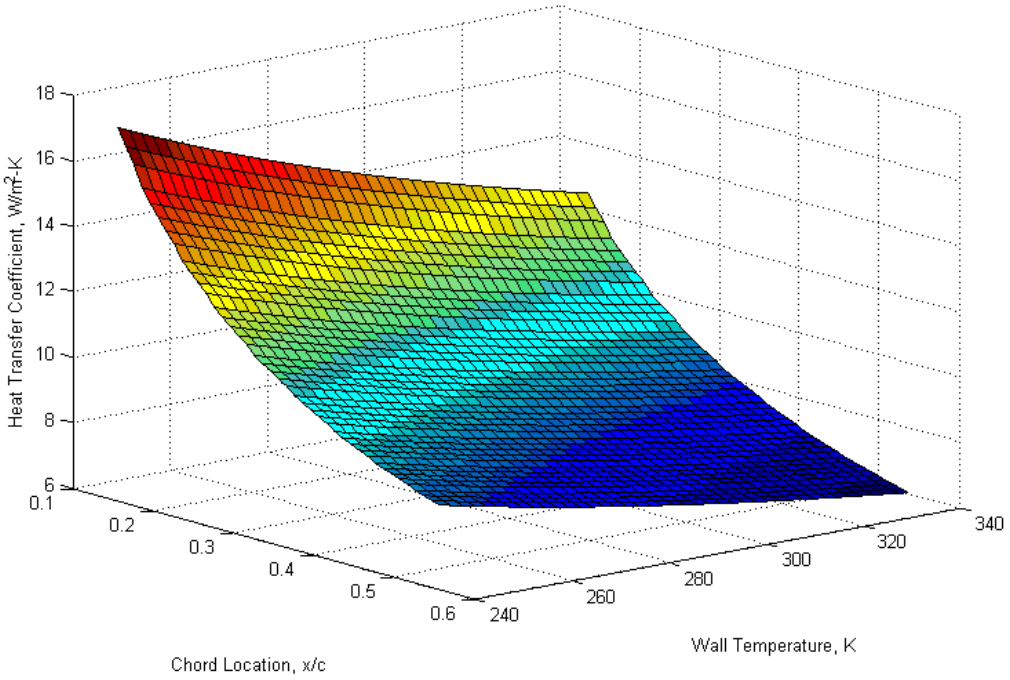

Figure 42 Convection coefficient surface plot.

A third order surface was fit to the surface plot from Figure 42 in order to enable quick calculations of convection coefficient by the heat transfer codes.

It is interesting to note the difference in the trends evident in Figure 39 and Figure 40 versus that in Figure 42. The non-dimensional shear stress parameters of Figure 39 and Figure 40 increase as wall heating is increased. However, the dimensional *h*, which is influenced by the density and viscosity of the fluid at the wall, decreases as wall temperature increases. The qualitative appearance of the convection coefficient in Figure 41 is identical to that of the two-dimensional boundary layer.

C. Heat Transfer Model Radiation Assumptions

Radiation is a topic of great concern to a laminar flow wing glove experiment utilizing IR thermography because it will dictate the nature and quality of the images recorded. Therefore, correctly modeling radiation effects in heat transfer analysis of the glove is critical. The glove designed for the SARGE project is to have a painted Carbon Fiber Reinforced Polymer (CFRP) surface. This surface will

avoid the low emissivity, high reflectivity, and highly directional radiation of metal surfaces that is problematic for IR thermography. Because non-metallic surfaces have emissivities that are nearly independent of direction, the surface emissivity will be assumed to equal the surface-normal emissivity. Also, it is assumed that the glove is opaque to all radiation in the bands of highest energy content: infrared, visible, and ultraviolet wavelengths.

All radiation terms utilized for the glove's heat transfer models were hemispherical averages. The orientation of the radiation source with respect to the glove's surface normal vector was not considered except for the case of direct solar radiation. The three primary sources of radiation accounted for in the one and two-dimensional heat transfer models were the sun, the sky, and the ground. The values of solar radiation used for the model were determined from the solar radiation table published by the American Society of Heating, Refrigeration, and Air-conditioning Engineers (ASHRAE) (Keller & Costa 2009). The ASHRAE solar radiation model accounts for fluctuations in extraterrestrial radiation due to the slightly elliptic orbit of the Earth around the Sun as well as the latitude of the irradiated object. The ASHRAE table of coefficients is shown in Table 7.

Table 7 ASHRAE radiation coefficients

Date	A (W/m^2)	B	C
January 21st	1202	0.141	0.103
February 21st	1187	0.142	0.104
March 21st	1164	0.149	0.109
April 21st	1130	0.164	0.12
May 21st	1106	0.177	0.13
June 21st	1092	0.185	0.137
July 21st	1093	0.186	0.138
August 21st	1107	0.182	0.134
September 21st	1136	0.165	0.121
October 21st	1166	0.152	0.111
November 21st	1190	0.142	0.106
December 21st	1204	0.141	0.103

These coefficients are then input into the Eqn (53) and Eqn (54) in order to determine the normal direct solar radiation and the diffuse solar radiation. Here C_N is a clearness factor that is approximately equal to 1.1 for Southern California, where the glove experiment is assumed to take place.

$$G_{ND} = \frac{A}{e^{B/\sin(\beta_S)}} C_N \tag{53}$$

$$G_d = C \cdot G_{ND} \tag{54}$$

The zenith angle, β_S, that measures the angle between the Earth's surface-normal vector and the vector pointing from the surface towards the sun is computed in degrees using Eqn (55) where LAT is the latitude of the object being irradiated in degrees and n is the number of month of interest.

$$\beta_S = 90 - LAT + 23.5 \cos\left(\frac{(n-6)\pi}{6}\right) \tag{55}$$

The intensity of the direct radiation on the surface of the object can then be calculated from Eqn (56). Here the zenith angle θ between the surface normal and sun vectors is equal to β_S if the surface being analyzed is parallel to the surface of the Earth. The glove's surface was assumed to be parallel to the surface of the Earth for all radiation computations.

$$G_D = G_{ND} \cos(\theta) \tag{56}$$

The total solar irradiation of the surface can then be determined from Eqn (57).

$$G_{SUN} = G_D + G_d \tag{57}$$

The solar radiation values used in the one and two-dimensional glove heat transfer models are shown in Table 8. These values are valid at the sun's highest elevation angle. A similar set of values for the other times of the day can also be found by modifying the values of β_S to be less than the maximum.

Table 8 Solar radiation types and sun angles as a function of month of the year

Month	Normal Direct Radiation (W/m^2)	Diffuse Radiation (W/m^2)	Maximum Sun Elevation Angle (°)
January	1032	106	35
February	1061	110	43
March	1067	116	55
April	1040	125	67
May	1013	132	75
June	995	136	79
July	992	137	75
August	999	134	67
September	1022	124	55
October	1027	114	43
November	1020	108	35
December	1011	104	32

The radiation exchanges between the wing glove and the ground and sky are also important effects to be considered. The ground was assumed to be 288 K for interactions with the lower surface of the wing and the sky was assumed to have a temperature of 215 K. A typical value of sky temperature on the ground on a cold night is 230 K (Incropera *et al.* 2007). This value was lowered to 215 K in order to conservatively account for the effects of a cold sky at higher altitudes. The ground and sky were both assumed to emit as perfect black bodies because their surface areas are much larger than that of the glove. Because the ground, sky, and glove temperatures were all within the same order of magnitude, it was assumed that the glove surface acts as a diffuse, gray emitter in this waveband. This meant that the surface's absorptivity to celestial and terrestrial radiation could be assumed to equal its emissivity at its surface temperature. The absorptivity of the surface to solar radiation was assumed to be gray over the wavelengths of highest energy content and diffuse, but not necessarily equal to the emissivity at the surface's temperature. Table 9 contains the radiation heat transfer properties for black and white painted surfaces.

Table 9 Paint radiation properties (Incropera *et al.* 2007)

Material	Emissivity at 300 K	Solar Absorptivity
Black Paint	0.98	0.98
White Paint	0.9	0.2

D. One-Dimensional Heat Transfer Model

A one dimensional heat transfer model was constructed in order study the effects of radiation on the surface temperature of the glove. The one-dimensional model was designed to lend insight into the behavior of the surface temperature when the changes in surface temperature were small and transverse temperature gradients were negligible. Such a case would exist in the first moments after the boundary layer is laminarized by being brought onto its design condition from a turbulent state. This model also has applicability for determining the heating of the glove's surface while the aircraft is parked on the ground in quiescent air.

The physical parameters of the model represent a highly simplified cross-section of a G-III wing. The glove's CFRP surface is assumed to rest on top of a one inch Rohacell foam layer. The wing's cross section is approximated as two 1/8 inch thick aluminum plates with a six inch fuel layer in between. Since the region of interest on the glove is in an area of low curvature, a rectangular cross-section was analyzed for simplicity. A diagram of this setup is shown in Figure 43.

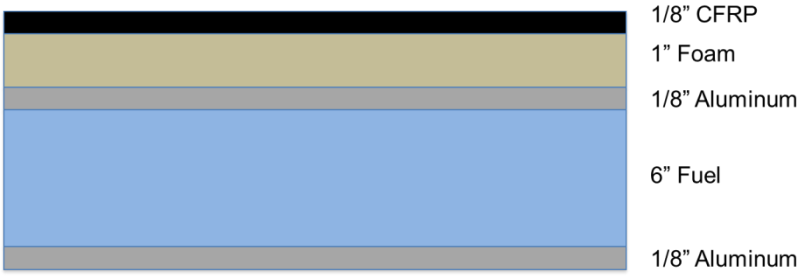

Figure 43 Wing cross-section model.

The material properties of each of the layers are listed in Table 10 as taken from Rohacell's manufacturer, Bruno *et al.* (2000), and Incropera *et al.* (2007).

Table 10 Thermal properties of glove materials

	Air	CFRP	Rohacell 110 WF Foam	Aluminum (6061-T6)	JP-8 Fuel
Density (kg/m^3)	Varies	1400	110	2700	800
Thermal Conductivity (W/m-K)	0.0223	0.78 or 9.9	0.038	167	0.115
Specific Heat (J/kg-K)	1006	790	1000	896	1800

CFRP has two values of thermal conductivity, one parallel to the fibers and one perpendicular to the fibers. The carbon fibers conduct heat better than the polymer substrate, thus the highest value is in the parallel direction. The glove's fibers are assumed to be oriented parallel to the surface of the wing, meaning that the one-dimensional model used the lower value of thermal conductivity. The paint on the surface of the glove was varied between black and white to study the effect of different colors. The bottom surface of the wing was assumed to be white for all cases.

Heat transfer calculations were performed using an explicit finite difference scheme. A time step of 0.001 seconds was used in order to avoid numerical instabilities. The computational grid had 21 nodes in the CFRP, foam, and fuel layers and six nodes in the aluminum layers. The node count began at the edge of each layer and nodes that rested on boundaries between layers were counted once towards each material's total. A grid convergence study was conducted and the aforementioned node density yielded invariant results.

One of the principle goals of the one-dimensional study was to predict the behavior of the combined wing glove/wing system as the aircraft flew a nominal climb profile. The time necessary for the glove to reach a steady state temperature after the aircraft had completed a climb to altitude was the most critical parameter. The freestream properties during the climb to the desired test point altitude were computed

using standard atmosphere equations. These are detailed further in Appendix D. The aircraft was assumed to climb at a moderate climb rate of 2000 ft/min at an airspeed of 180 knots. For the purposes of the computations the aircraft was assumed to instantly accelerate to test point flight conditions after the intended altitude was reached. In order to simulate operations from California's High Desert the climb was initiated from a ground elevation of 2,200 ft.

The one-dimensional analysis was carried out at 30% chord since this location would capture the behavior of the region just upstream of the likely transition location. The boundary layer at this point was assumed to be turbulent during the climb. The turbulent heat transfer coefficient was estimated using Eqn (58) for the incompressible flat plate.

$$h = \frac{k_{AIR}}{x}(0.0296)Re_x^{4/5}Pr^{1/3} \tag{58}$$

Analysis of the turbulent boundary layer cases showed that the surface temperature reached steady state quickly. Additionally, the temperature of the aluminum skin beneath the Rohacell foam did not have an effect on the final skin temperature. The model was refined by assuming that the aluminum beneath the glove had a constant surface temperature equal to the turbulent adiabatic wall temperature. This case is more realistic than assuming that the wing is warmed by the fuel below because of the large surface area of aluminum outside of the glove being convectively cooled and conducting heat away from the aluminum beneath the glove. A plot of the black-painted glove surface temperature at 30% chord for the assumptions of both insulated and cold wing skins is shown in Figure 44.

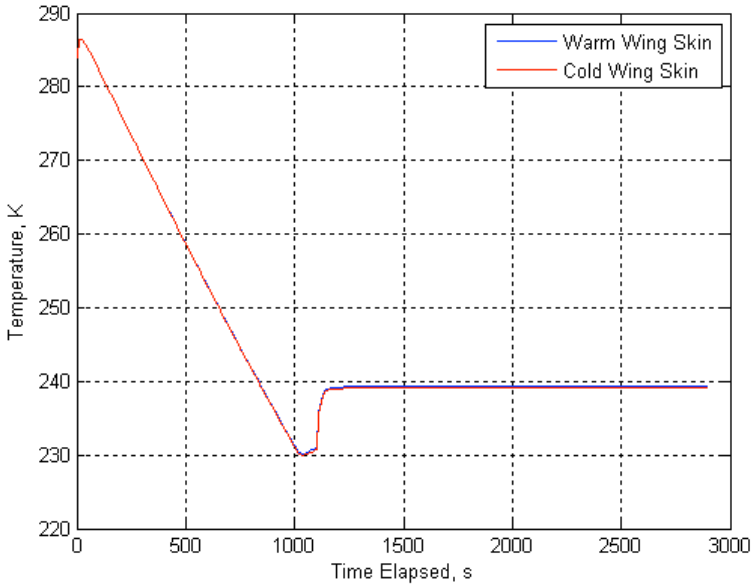

Figure 44 Black glove surface temperature vs. time.

Figure 44 clearly shows that the temperature of the glove during climb out is not affected by the temperature of the aluminum wing skin layer. Also, the responses of the surface temperature to changes in the flight profile are nearly instantaneous. The rapid rise in glove temperature around 1,110 seconds is attributed to the instantaneous acceleration to Mach 0.75 and the corresponding increase in stagnation temperature. After this increase the turbulent boundary layer causes the glove surface to converge on a steady state temperature in less than 100 seconds.

Another important case to consider from an operational standpoint is the effect of having the glove hot soak on the ground prior to flight. A one hour hot-soak on the ground was analyzed for the black glove in summer solar conditions. The only convection on the glove surface was natural convection caused by the warm surface as determined by Eqn (59).

$$h = \frac{k_{AIR}}{x}(0.15)\left(\frac{\rho_{AIR}^2 c_{AIR} g (T_s - T_\infty) L^3}{\mu_{AIR} k_{AIR} T_\infty}\right)^{1/3} \tag{59}$$

The results of this case are plotted in Figure 45. The plot shows that the glove can become very hot, reaching surface temperatures near 80°C after only 20 minutes in the sun for the afternoon case.

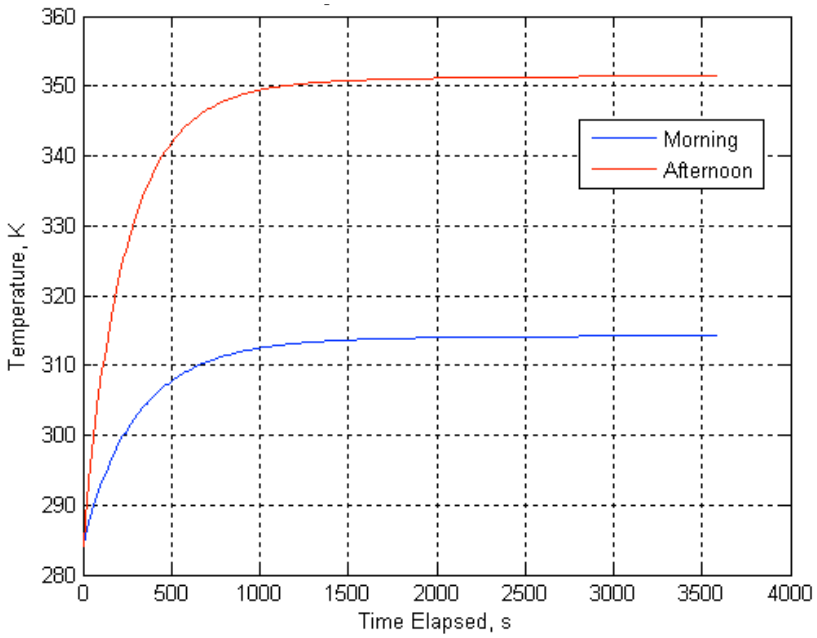

Figure 45 Ground heating of black glove in summer radiation.

The results of the hot soak shown in Figure 45 were input as initial conditions into the climb analysis. In order to analyze the effects of a ground heat soak in the most conservative way possible the boundary layer was assumed to be laminar for this case. The results are shown in Figure 46.

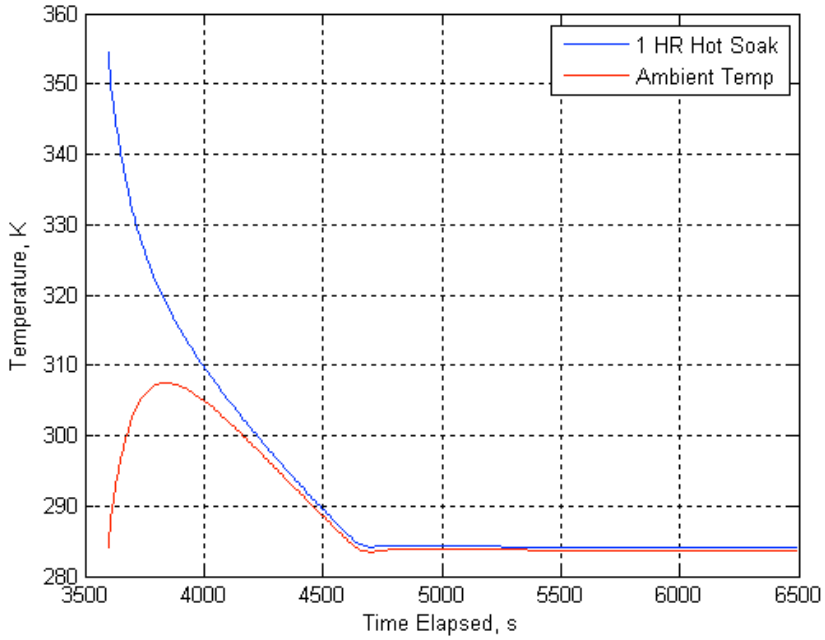

Figure 46 Black glove with hot soak comparison.

This plot shows that the hot soak has no effect on the glove's final temperature, even in this conservative case.

The preceding analysis showed that the initial temperature of the glove before the aircraft takes off and the temperature of the aluminum wing surface are immaterial to the glove's surface temperature at the end of the aircraft's climb. Also, the glove's surface temperature converges on the freestream's stagnation temperature when a turbulent boundary layer is assumed for the climb. The next step in the analysis of the glove was to establish the response of the surface temperature when the boundary layer was suddenly laminarized due to the aircraft flying at the glove's design angle of attack. Both black and white paint jobs were studied at various solar radiation intensities. The final temperatures reached at the end of the climb sequence with the turbulent boundary layer were used as initial conditions for investigating the effects of having a suddenly laminar boundary layer. The temperature of the upper surface of the wing beneath the glove was assumed to be equal to the turbulent adiabatic recovery temperature for each of the following cases.

The case with the greatest effect of solar radiation was that of the glove operating at mid-day in June. The solar radiation intensity on the glove's surface in this case was about 1,110 W/m^2-K. Both black and white surfaces were analyzed at this condition and the effects of heating these surfaces with 300 W/m^2 heating sheets were also investigated. The results from the black surface cases are shown in Figure 47.

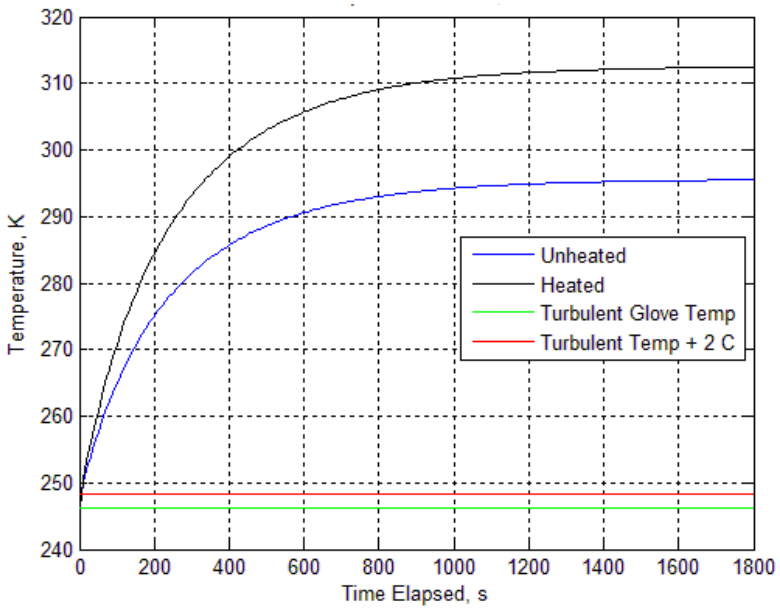

Figure 47 Black glove in 1,110 W/m^2-K solar radiation.

This plot shows that the black glove is highly affected by solar radiation when the boundary layer is laminar. A zoomed in view of the surface temperature response detailing the time for the surface temperature to rise 2°C above the previous turbulent temperature is shown in Figure 48.

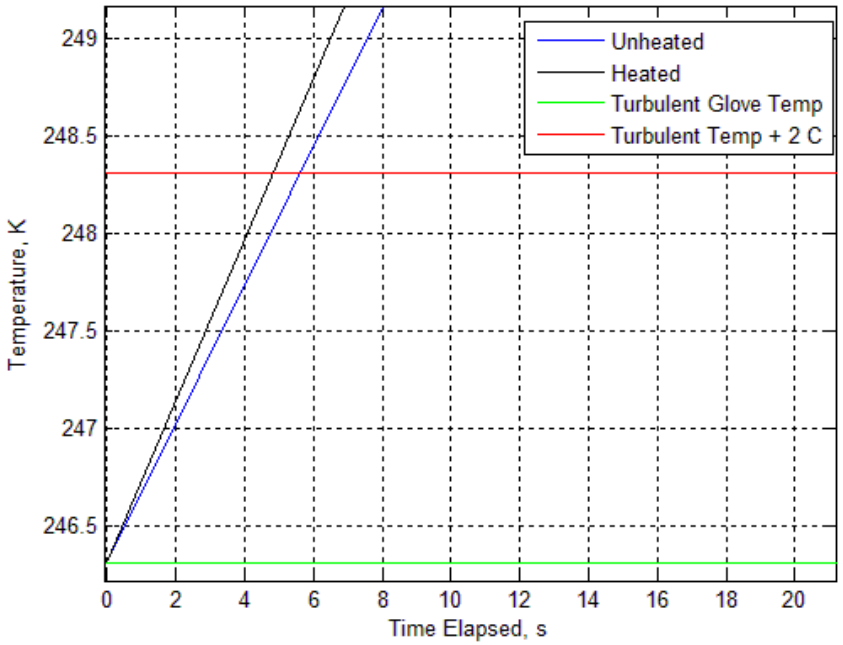

Figure 48 Black glove in 1,110 W/m^2-K solar radiation, initial changes.

Figure 48 shows that the surface temperature rises quickly after the surface is laminarized. It is also apparent that the heating sheet has little value added in terms of decreasing the time to heat.

A similar set of plots can also be generated for a white glove surface in the June, mid-day solar radiation condition. Like the black surface, the white surface is also warmed by the sun, although not as much. Plots of the response of the white glove are shown in Figure 49 and Figure 50.

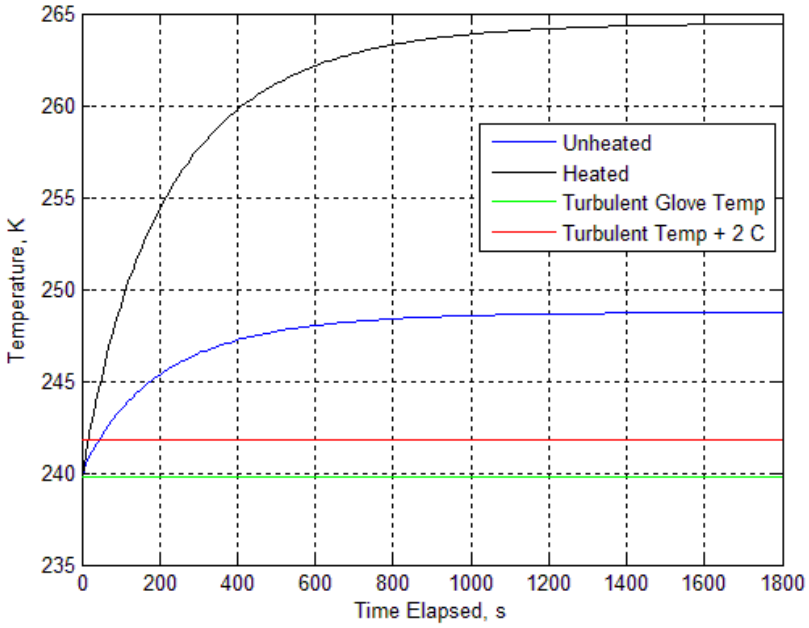

Figure 49 White glove in 1,110 W/m^2-K solar radiation.

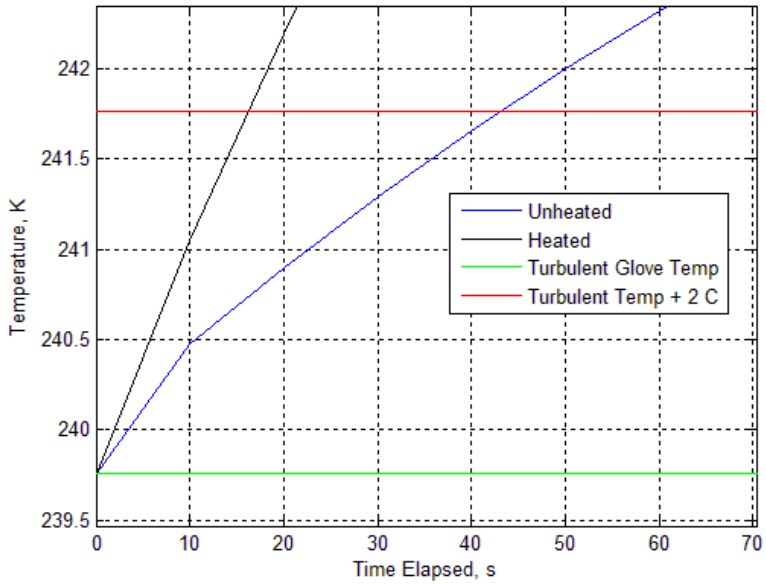

Figure 50 White glove in 1,110 W/m^2-K solar radiation, initial changes.

Figure 50 shows that the white glove heats slower than the black glove, as expected, but still warms relatively quickly. The effect of the heating sheet is more pronounced, but not necessary to make the glove operationally effective.

The opposite end of the solar radiation spectrum corresponds to morning or evening conditions in December. Here the solar radiation is approximately 300 W/m^2-K. The response of the black glove to these conditions is plotted in Figure 51 and Figure 52.

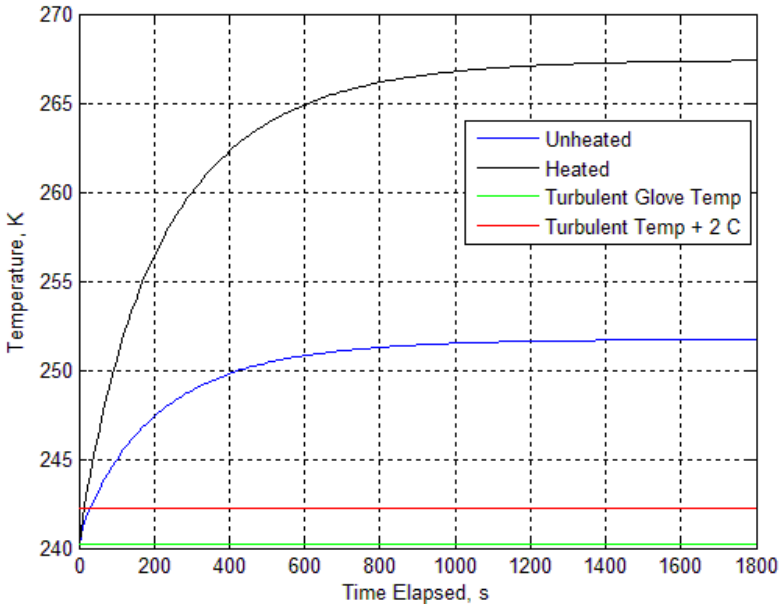

Figure 51 Black glove in 300 W/m^2-K solar radiation.

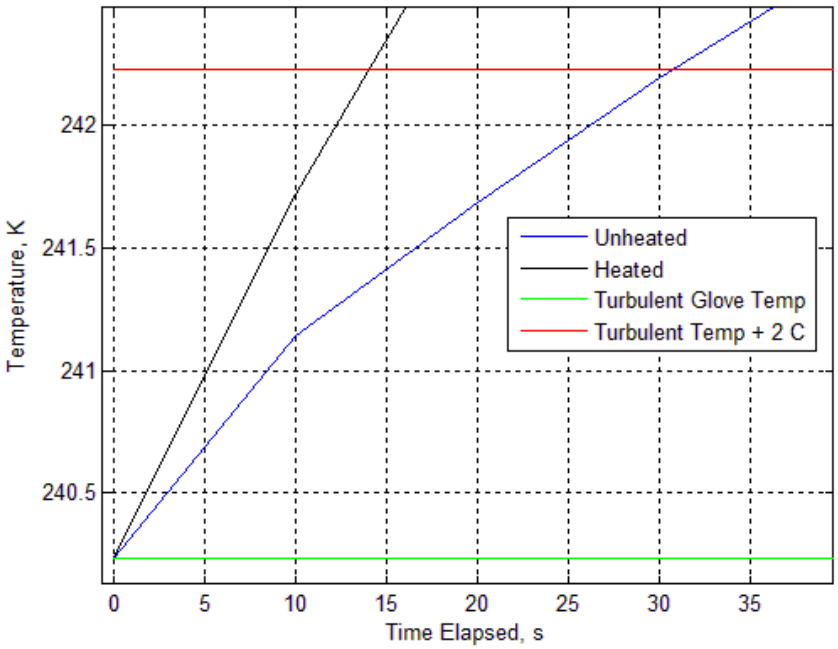

Figure 52 Black glove in 300 W/m^2-K solar radiation, initial changes.

Figure 52 shows that the black glove is still strongly affected by the solar radiation. The heating sheet has a more pronounced effect at this condition, but would not be necessary for flight tests.

The response of the white surface to the 300 W/m^2-K solar radiation condition is documented in Figure 53 and Figure 54. The effect of this solar radiation on the white surface is minimal, but still not negligible. The adiabatic wall condition is not achieved even in the reduced radiation environment.

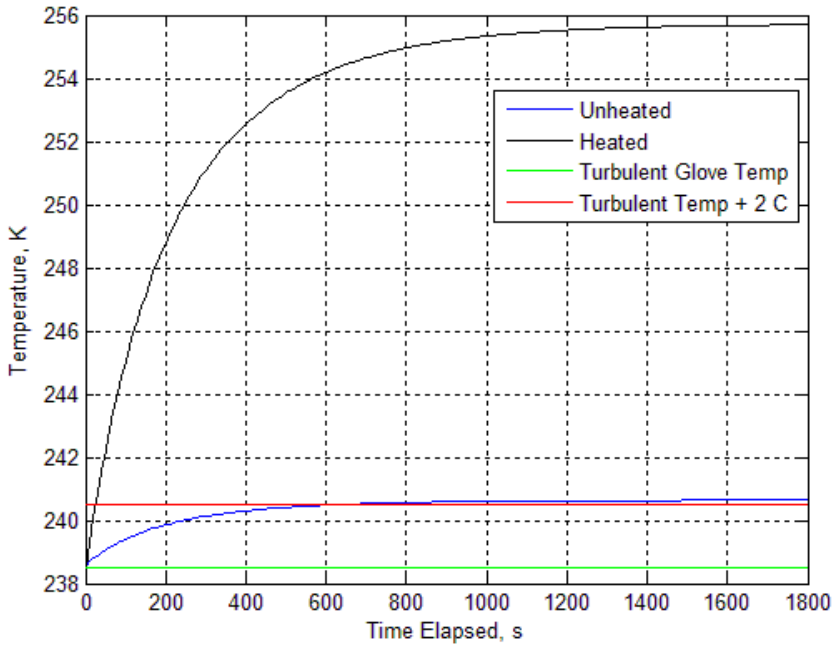

Figure 53 White glove in 300 W/m^2-K solar radiation.

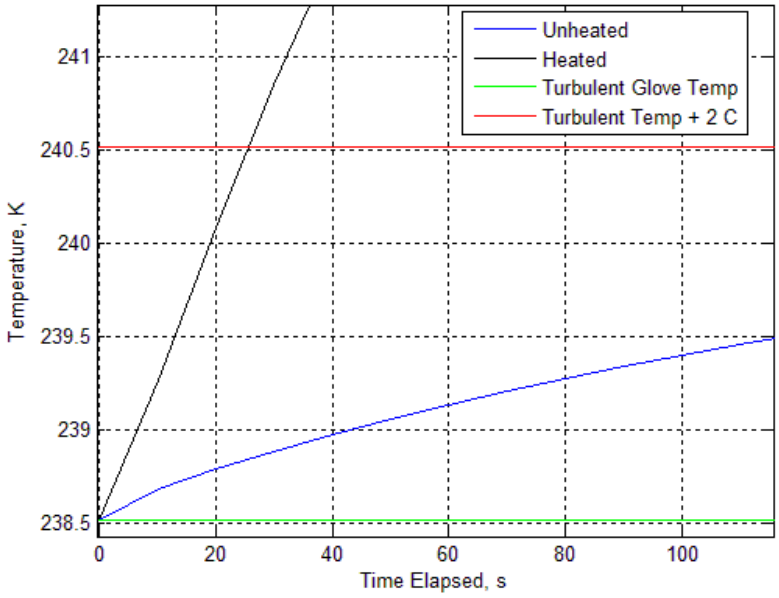

Figure 54 White glove in 300 W/m^2-K solar radiation, initial changes.

The one-dimensional analysis revealed several striking conclusions. First, solar radiation is a significant physical phenomenon that will cause the surface temperature in the laminar region of the glove to rise above the laminar adiabatic wall recovery temperature. Also, the rate of heating, particularly for the black painted surface is significant. This rapid and significant temperature change means that the problem will quickly become two-dimensional and the one-dimensional model should not be used to characterize the temperature difference between the laminar and turbulent regions.

E. Two-Dimensional Heat Transfer Model

A two-dimensional model of the glove's surface between 15 % chord and 55 % chord was constructed in order to gain a higher fidelity characterization of the temperature differential between the laminar and turbulent regions as a function of time. The computations were performed with the glove at a constant flight condition of Mach 0.75 at 39,000 ft. It was assumed that the entirety of the glove was initially at the freestream total temperature per the results of the one-dimensional model. Because it was found that the temperature of the aluminum beneath the construction foam had little influence on the final surface temperature, the bottom surface of the foam was assumed to be an isothermal surface with a temperature equal to the freestream stagnation temperature. The sides of the computational domain at 15 % and 55 % chord were assumed to be adiabatic.

The glove model was simplified such that only the CFRP and construction foam layers were considered. Again the glove was approximated as a rectangle due to the low curvature of the glove in the domain of interest. An illustration of the simplified model is shown in Figure 55.

Figure 55 Simplified 2-dimensional model geometry.

The computational grid had 21 nodes per layer in the direction normal to the surface of the glove and 41 nodes parallel to the surface. The nodes were spaced in intervals of 1 % chord in the direction parallel to the surface. The nodes at the interface between the foam and CFRP layers were counted once towards each material's node count meaning that there were a total of 1681 nodes in the domain. An explicit finite difference scheme with a time step of 0.05 seconds was used to perform the computations. The mathematical details of this model are enumerated in Appendix E.

Convection coefficients on the surface of the model were computed as a function of chord location and surface temperature using the method of Beckwith (1958) as mentioned previously. A third order surface fit of the relationship between chord location, surface temperature, and convection coefficient at the 0.75 Mach, 39,000 ft test point was produced in order to expedite the computational process. Transition was assumed to occur at 40 % chord in this analysis. The convection coefficients in the turbulent region were approximated by multiplying the laminar convection coefficients corresponding to the surface's temperature by a factor of 10.

The 1,110 W/m^2-K radiation case corresponding to a summer afternoon was again analyzed for a black painted glove. The temperature histories of the surface temperature as a function of chord location are plotted in Figure 56. Each line on the plot represents a time step of five seconds from the previous line. The final temperature profile shows the surface temperature 120 seconds after laminarization of the boundary layer on the glove.

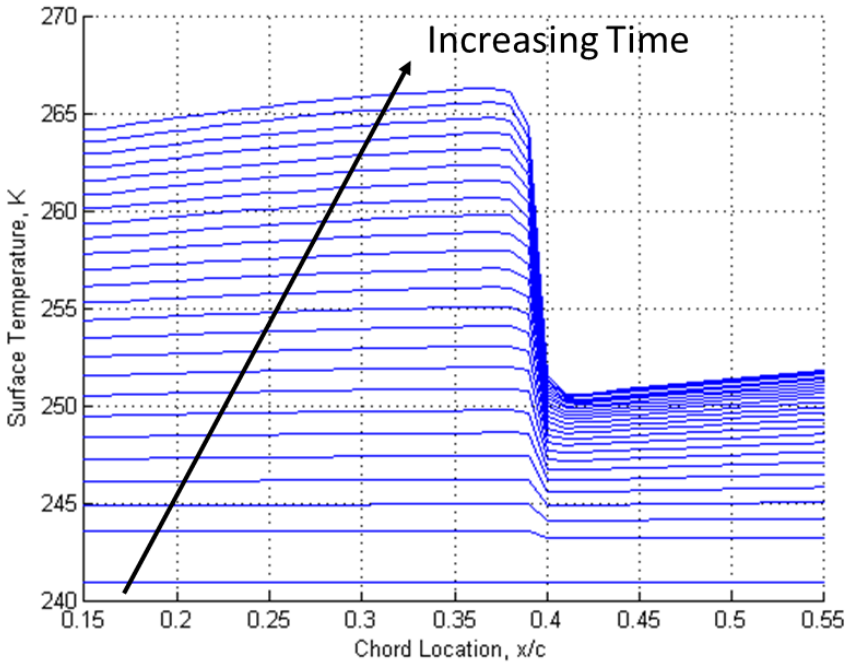

Figure 56 Temperature history of black glove in 1,110 W/m^2-K radiation.

Figure 56 shows that both the laminar and turbulent zones are warmed when by solar radiation. The lines in the turbulent region aft of 40 % chord begin coalescing at around 250 K, suggesting that a steady state condition is being neared. The lines in the laminar region appear to still be far from steady state values. It is also interesting to note that the dip in surface temperature associated with boundary layer transition begins to move forward as the temperature difference between the two zones increases. This effect is why it is best to build the glove's surface using a material with low thermal conductivity.

A plot of the model's internal temperature profile after 120 seconds is displayed in Figure 57. There is an obvious impact of heat conduction parallel to the surface of the glove. The construction foam is a good insulator, meaning that the thermal effects at the surface are preserved for observation rather than conducted away. A more conductive substrate would degrade the quality of the IR images.

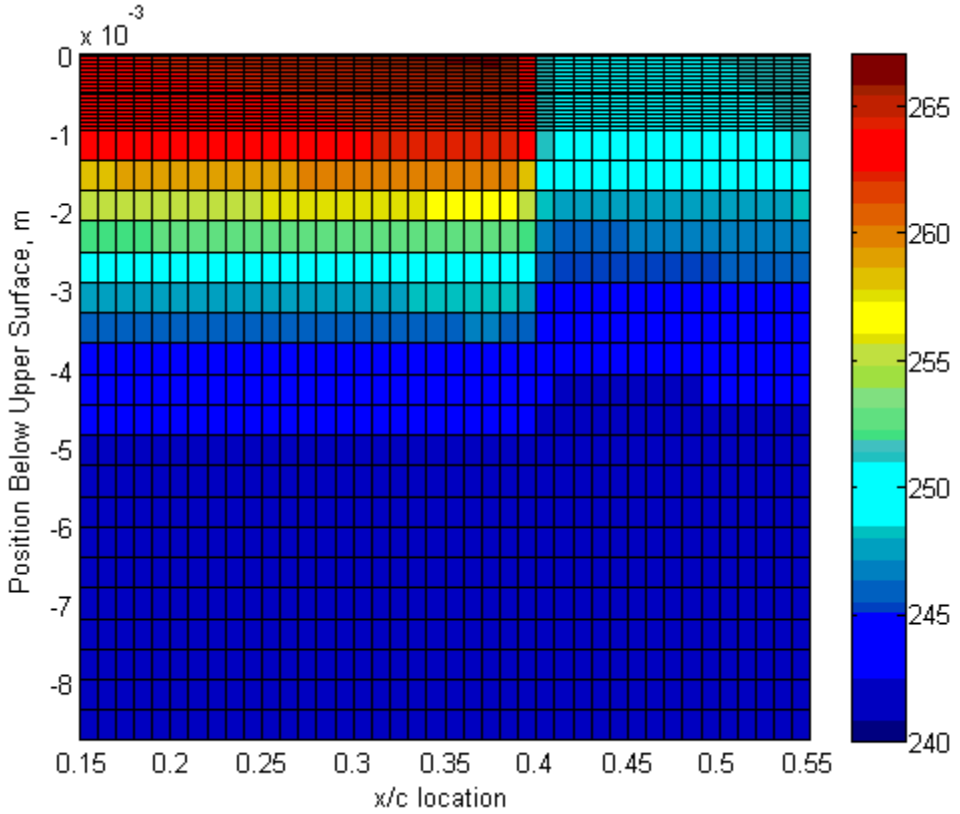

Figure 57 Black glove internal temperature profile after 120 seconds at 1,110 W/m^2-K radiation.

A white glove surface was also analyzed at the 1,110 W/m^2-K solar radiation condition. The temperature history for this surface is shown in Figure 58. Like the black glove the temperature increases, although not as much. However, the white glove also operates with a warmed laminar region when flying at a constant altitude. Again, the time steps between lines are five seconds.

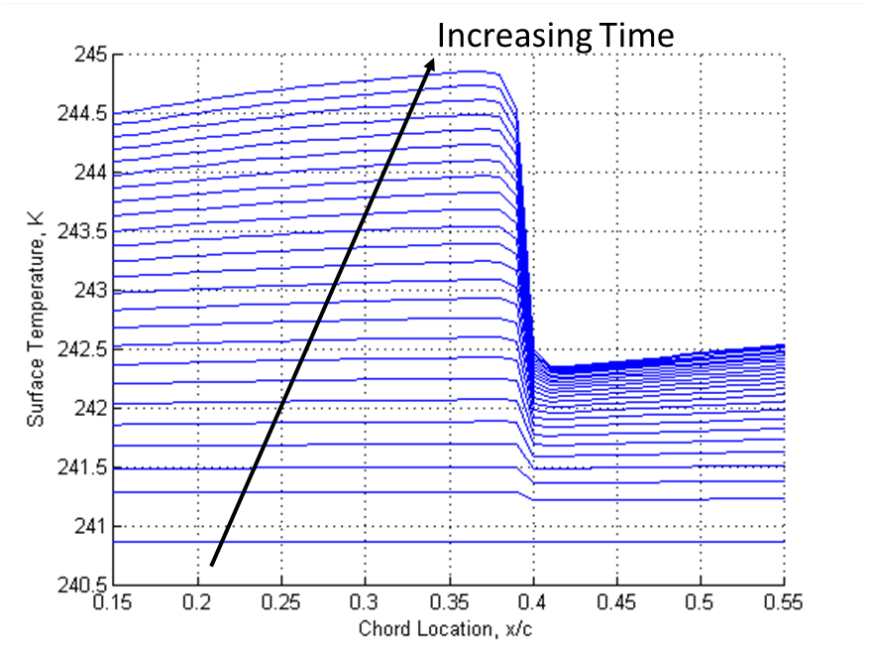

Figure 58 Temperature history of white glove in 1,110 W/m^2-K radiation.

Similar analyses were also carried out for heated and unheated black and white surfaces at solar radiation conditions of 1,110 W/m^2-K, 690 W/m^2-K, and 300 W/m^2-K. These cases represent highest and lowest radiation levels corresponding to a summer day and a winter morning as well as an intermediate case representative of a winter afternoon or a summer morning. The temperature differences between the laminar and turbulent cases as a function of time were plotted for each of the solar radiation and glove surface combinations.

The temperature differences between the laminar and turbulent regions for the 1,110 W/m^2-K cases are shown in Figure 59.

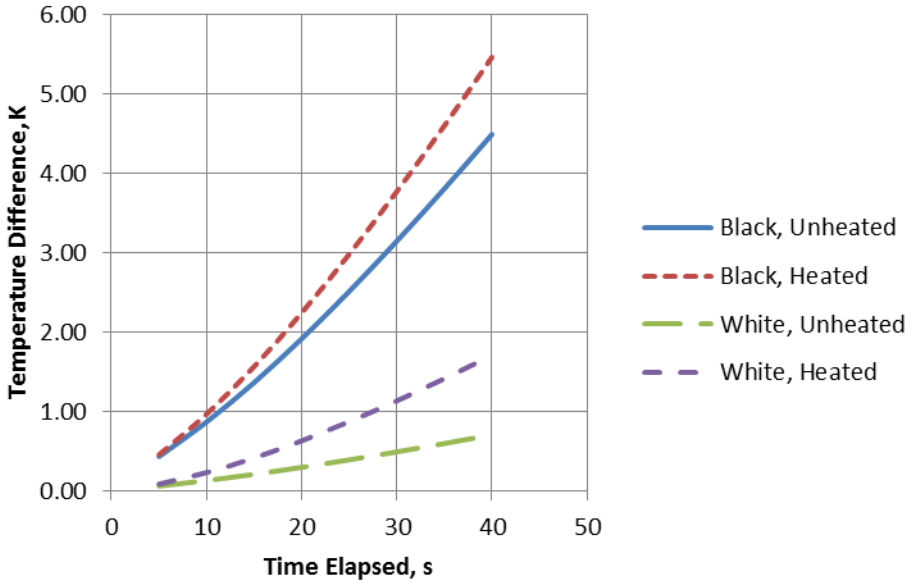

Figure 59 Temperature difference for 1,110 W/m^2-K solar radiation as a function of time.

Figure 59 shows that the black surfaces increase in temperature much quicker than the white ones. The heated and unheated black surfaces reach a 1°C differential within about 10 seconds while the heated white glove takes nearly 25 seconds and the unheated white glove does not achieve the desired differential within 40 seconds. The important trend to note is that each of the surfaces has a positive temperature differential between the laminar and turbulent regions, meaning the laminar region is warmer.

The results of the analysis at 690 W/m^2-K are plotted in Figure 60 and show the same trends as those found for the 1,110 W/m^2-K case.

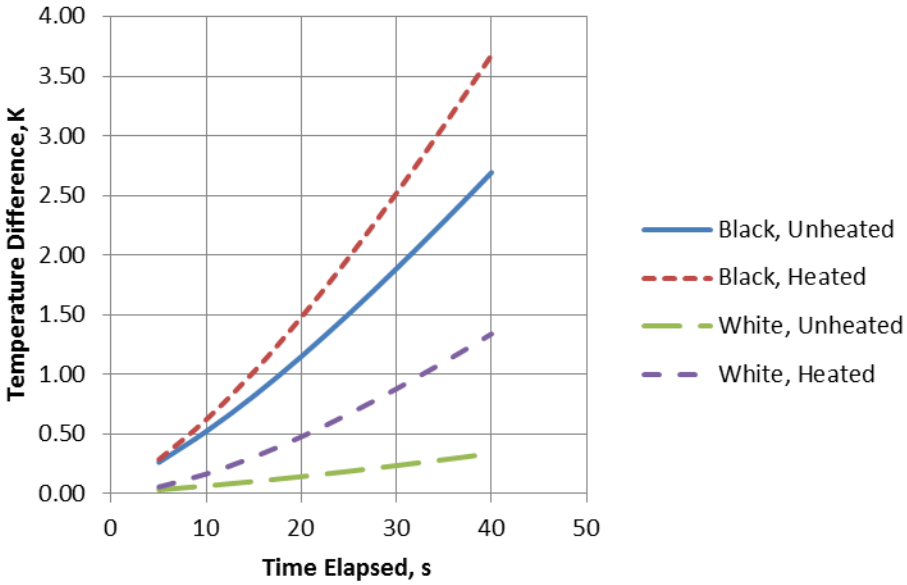

Figure 60 Temperature difference for 690 W/m^2-K solar radiation as a function of time.

The temperature difference profiles in Figure 60 display a slower rate of increase than those for the higher radiation case presented previously. The difference between the heated and unheated surfaces of the same color is also more pronounced. However, the trend for all cases is for the temperature of the surface to rise in the laminar region as a result of solar radiation.

The final solar radiation case analyzed, 300 W/m^2-K, showed a marked increase in the time required to establish a 1°C temperature differential. The results of this case are presented in Figure 61.

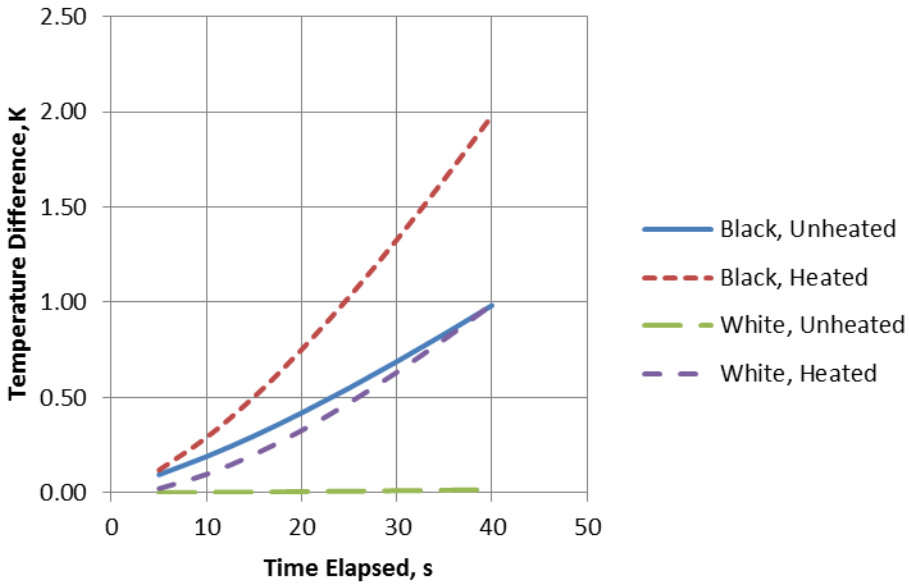

Figure 61 Temperature difference for 300 W/m^2-K solar radiation as a function of time.

The results plotted in Figure 61 indicate that the unheated black surface will still increase in temperature with and without heating. The white surface has nearly zero temperature change without heating. With 300 W/m^2 heating the white surface has nearly the same performance as the unheated black surface.

The results of displayed in Figure 59 through Figure 61 seem to suggest that all glove colors will operate with warmer laminar regions during the times of the day when flight tests are most likely to occur. Therefore, a color should be chosen based on how well it takes advantage of solar heating. A white glove will only be effective if it is heated, which adds expense and complexity to the experiment. A black glove, on the other hand, seems to have acceptable levels of performance during all conceivable times of day. Therefore, it is suggested that a black painted glove surface should be utilized for the SARGE experiment. A compilation of the black painted surface's heating curves for the three solar radiation environments considered is shown in Figure 62. The plot shows that the unheated glove is capable of supplying good quality IR pictures after 40 seconds or less on condition.

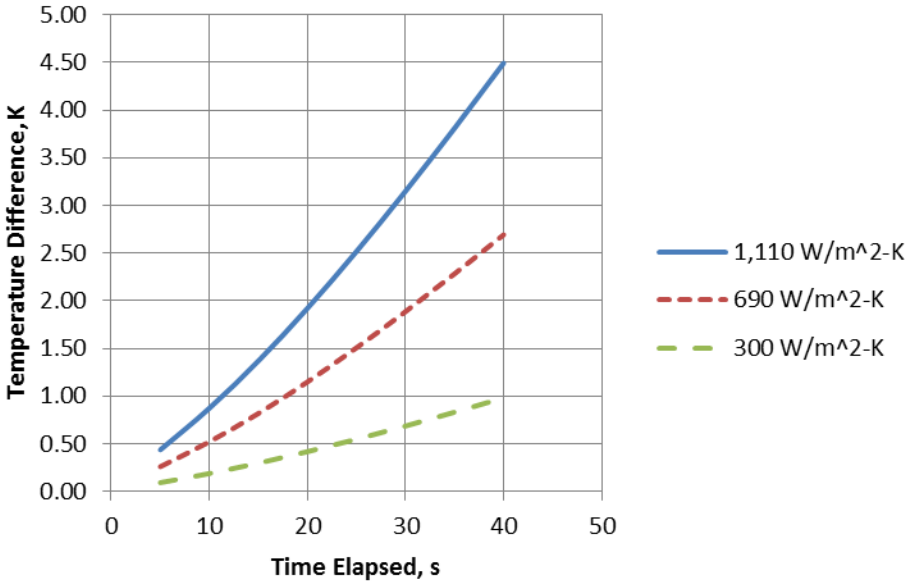

Figure 62 Plot of black glove temperature differences as a function of time.

The skin friction coefficient predicted by the method of Beckwith (1958) was within 5 % of the value predicted using CFD and the corresponding convection coefficient values are presumed to be of similar quality. However, it was desired that an upper bounding case of the convection coefficient be analyzed in order to evaluate the sensitivity of the glove's predicted temperature difference to inaccuracies in this parameter. The upper bound was formed by increasing the convective heat transfer coefficients in the laminar and turbulent regions by a factor of two over the values predicted using the Falkner-Skan-Cooke similarity equations. The 690 W/m^2-K radiation case was used for this analysis because it represented a good median case for investigating the effect of varied convection.

The time history of the black glove's surface temperature as computed with the Falkner-Skan-Cooke equations of Beckwith (1958) is plotted in Figure 63 as a reference for the following analysis.

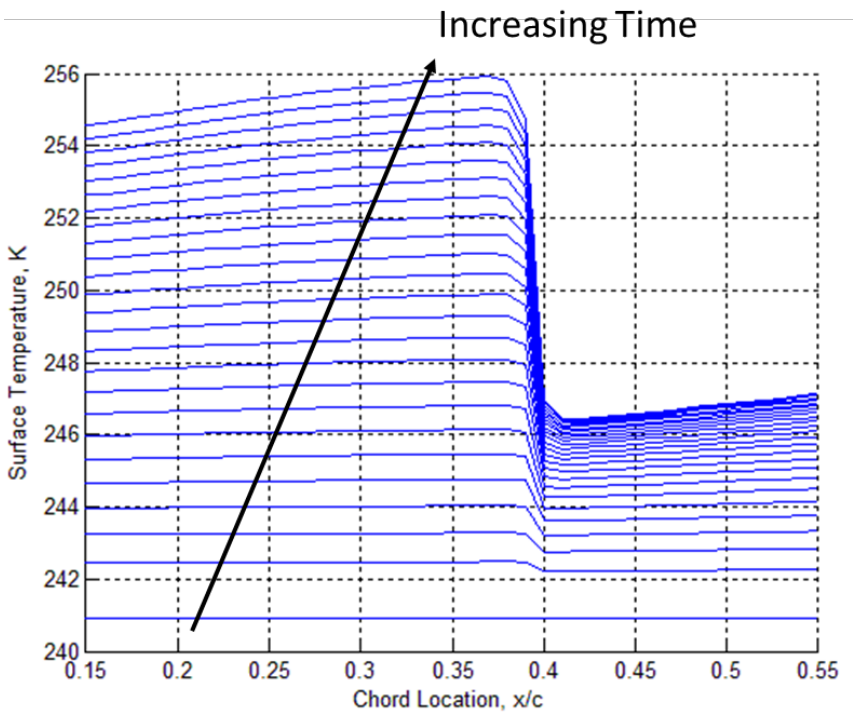

Figure 63 Unheated black glove in 690 W/m^2-K solar radiation, F-S-C equations.

The convection coefficients solved for by the method of Beckwith (1958) were then doubled to yield the results displayed in Figure 64.

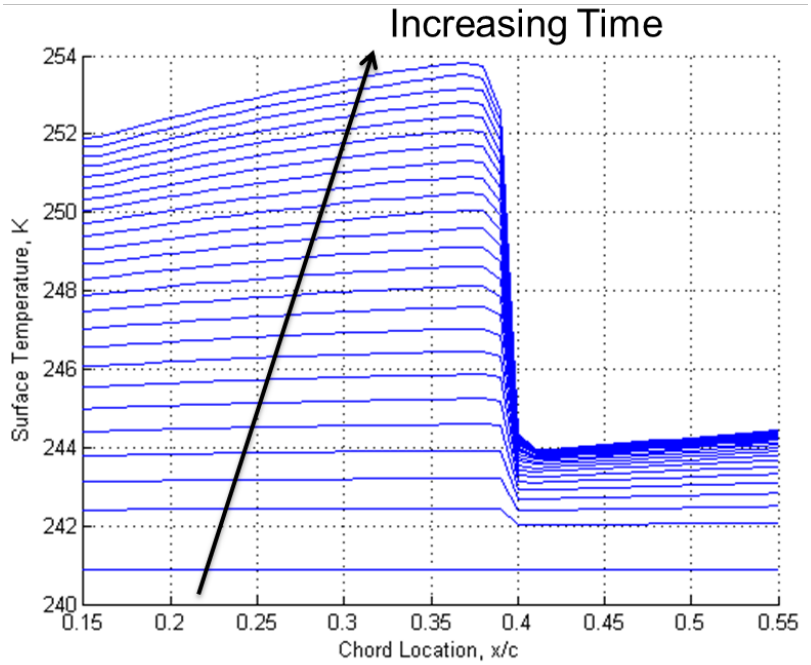

Figure 64 Unheated black glove in 690 W/m^2-K solar radiation, doubled F-S-C convection.

The data presented in Figure 64 suggests that the shape of the curve have been maintained nearly exactly, but they have been shifted to lower temperatures for the case of increased. The temperature profile appears to have been uniformly shifted downwards approximately 2 ºC after 120 seconds.

Contrasting the results of Figure 63 and Figure 64 suggests that it is instructive to compare the plots of temperature difference across the laminar and turbulent regions as a function of time for the bounding convection cases. The temperature differences between the laminar and turbulent zones as a function of time for the 690 W/m^2-K solar radiation case with doubled Falkner-Skan-Cooke convection for the heated and unheated surfaces are shown in Figure 65.

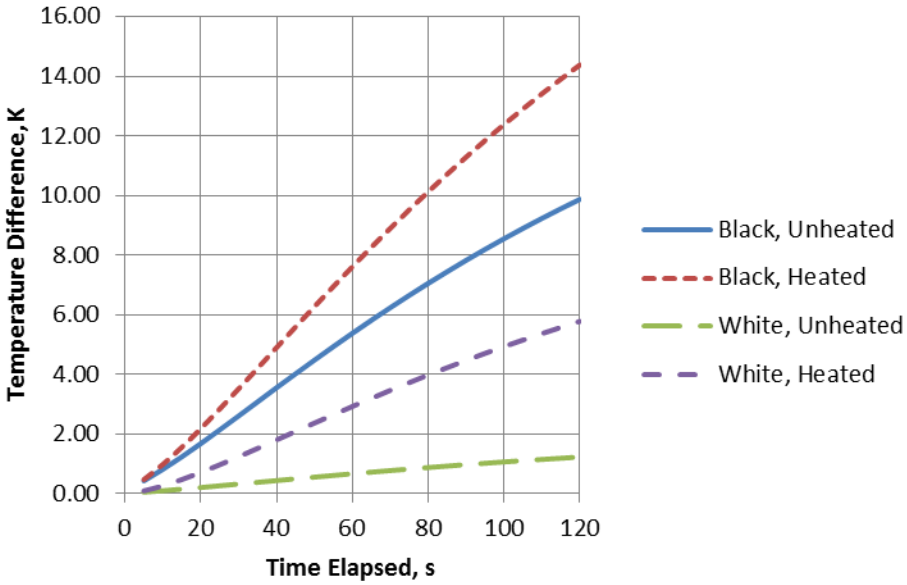

Figure 65 Temperature difference for 690 W/m^2-K solar radiation, doubled F-S-C convection.

The data presented in Figure 65 is nearly identical to the identical to the data from the solutions of the convection coefficients from Falkner-Skan-Cooke boundary layer shown in Figure 66.

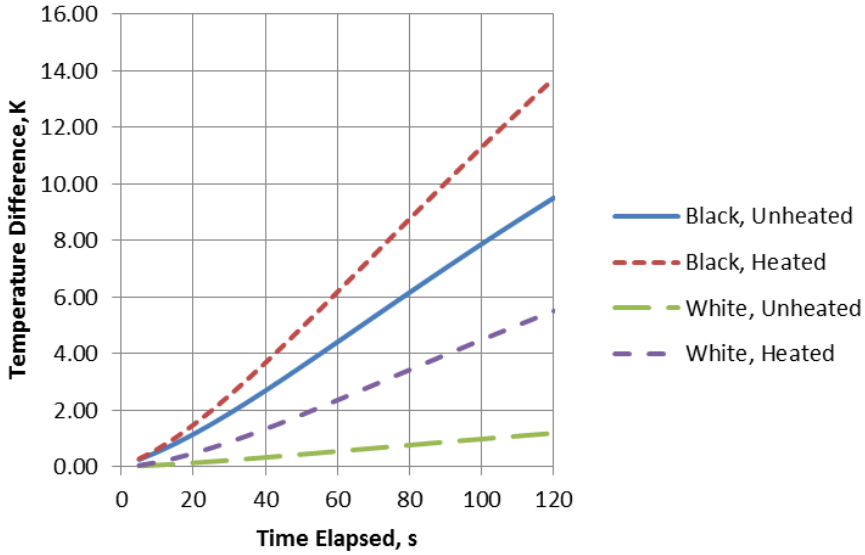

Figure 66 Temperature difference for 690 W/m^2-K solar radiation, F-S-C convection.

The temperature difference across the transition front of a black glove's surface was also analyzed for the three solar radiation cases used previously with the Falkner-Skan-Cooke convection coefficient doubled. The results of this analysis are shown in Figure 67.

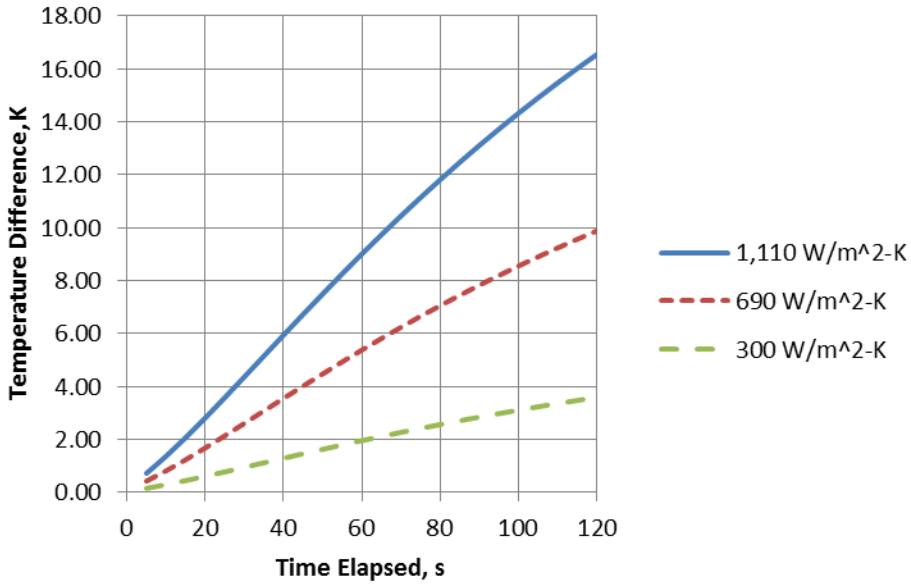

Figure 67 Plot of black glove temperature differences, doubled F-S-C convection.

Doubling the convection coefficient on the black glove appears to have almost no effect on the temperature difference across the laminar and turbulent regions, meaning that the conclusions drawn previously can be used confidently moving forward. Higher fidelity estimations of the heat transfer coefficient can be made by using the methods of Beckwith (1958) coupled with more careful analysis of the glove's streamlines or the solutions of a viscous Navier-Stokes code if additional accuracy is desired.

The heat transfer analysis of the glove has revealed that the sun's radiation will dominate the glove's surface temperatures unless flights are conducted at times of minimal solar radiation. Previous glove experiments have shown that harnessing solar radiation to heat the glove is an effective strategy for performing IR thermography. Painting the glove surface black will allow missions to be flown during most daylight hours without requiring additional heating.

The glove's surface should be insulated from the wing surface below as best as possible through the use of substrates such as Rohacell 110 construction foam. A substrate with low thermal conductivity will result in crisper IR images of transition than one with high thermal conductivity. Metal linkages that lead directly from the wing to the glove will likely create local cold patches which could ruin the IR images of transition. A glove that is directly bonded to the surface works best for providing a uniform, insulated substrate.

Finally, attention should be paid to the effect of wall heating on the T-S instability. The T-S instability is destabilized by a warm wall in air. This means that a glove whose laminar region is purposely warmed should be very T-S stable and stability computations that include heat transfer should be done to confirm this if there is any doubt.

4. HOTFILMS FOR WAVE VECTOR IDENTIFICATION

A. Motivation

An intermediate design of a laminar flow wing glove for a G-III test platform was described in Belisle *et al.* (2011). Malik *et al.* (2011) analyzed this design using both Linear Stability Theory (LST) and Parabolized Stability Equations (PSE). The PSE analysis included terms for both wall curvature and non-parallel effects while LST did not. Their analysis revealed that the intermediate glove design's stationary crossflow n-factors predicted by PSE were drastically reduced when compared to LST as a result of the inclusion of curvature and non-parallel effects. However, the inclusion of curvature and non-parallel effects had almost no effect on traveling crossflow n-factors. They concluded that wall curvature had a strongly stabilizing effect on stationary crossflow, but minimal influence on traveling crossflow.

This result served as a caution to the design team because of the lack of precise understanding about the nature of crossflow waves at high Reynolds numbers. Stationary crossflow has been shown to dominate in low freestream disturbance environments with turbulence levels less than 0.15 percent (Deyhle & Bippes 1996) and flight has been shown to meet this criterion (Carpenter 2009), (Riedel & Sitzmann 1998). The selection of traveling or stationary waves is a result of the receptivity process and thus is influenced by the interaction of freestream disturbances with surface roughness. White *et al.* (2001) demonstrated that a polished leading edge with 5μm rms roughness could sustain stationary crossflow dominated transition at turbulence levels equal to 0.30 %; but traveling waves would dominate when 50 μm DREs were applied at 8 mm spacing for this same freestream condition. These experiments were carried out at 2.4 million chord Reynolds number. The bulk of detailed stationary crossflow work thus far has been done at Reynolds numbers below eight million. The SARGE project will be operating at Reynolds numbers between 15 and 30 million.

The results of Malik *et al.* (2011) and White *et al.* (2001) combined with uncertainty about the receptivity process prompted the development of a hotfilm sensor design capable of detecting traveling disturbances. It was desired that the sensor be capable of resolving a wave's frequency and wave vector. This would permit the detection of traveling disturbances of either the CF or T-S type that could lead to

unexpected, premature transition on the wing glove. As a secondary objective, it was also useful for the array to have the capability of detecting stationary crossflow wavelengths. It was decided that a hotfilm should be designed that would be capable of identifying the presence of traveling instabilities. The sensor design detailed in this section was driven by the desire to test the concept on the SWIFT model at the TAMU FRL by exciting the CF and T-S instabilities prior to applying the sensors to the wing glove project.

B. Design Theory

A sensor with capability to measure both streamwise and crossflow disturbances was designed based on past experiments. The work of Glauser *et al.* (2011) demonstrated that an array of hotfilms consisting of streamwise-spaced sensors oriented normal to lines of constant span combined with chordwise-spaced sensors perpendicular to lines of constant chord could resolve boundary layer disturbances in both directions. With this in mind, it was decided that an array of orthogonal elements would be necessary so that the sensor would be capable of resolving planar waves propagating in any direction on the wing's surface. The spanwise spacing of the sensors was driven by the desire to resolve crossflow vortices. The critical wavelength for stationary crossflow on the SWIFT model is 4.5 mm (Rhodes *et al.* 2008). Therefore, streamwise and crossflow elements required spanwise spacing of no greater than 2.25 mm from adjacent elements of the same orientation in order to resolve the critical stationary mode.

The wave vector of traveling disturbances was successfully resolved by Deyhle *et al.* (1993). Their technique involved mounting a sensor array, with elements spaced one behind another with the vector connecting the centerline of each sensor being perpendicular to the long side of the sensor element itself, to a rotatable disk. This rotating disk was then embedded into a swept flat plate model with an imposed pressure gradient. The sensor array could be rotated, and allowed for the measurement of the phase angle between each sensor at a specified orientation and disturbance frequency. This phase angle, combined with the known spacing of the hotfilm's elements and the frequency of the wave under analysis, could then be used to calculate the phase speed in the direction of the array's orientation.

The rotatable disk was swept through a 180° arc and phase velocity measurements were made at regular intervals. The phase velocities were plotted in polar coordinates. The magnitude of each vector was the phase speed calculated from the phase angles and the direction was the orientation of the vector connecting the center of the hotfilm elements. A line drawn through the tips of the plotted vectors represents the wave front of each disturbance and the wave vector is perpendicular to this line. The magnitude of the wave's phase speed is equal to the magnitude of the vector normal to the wave front that intersects with the plot's origin. An illustration of this measurement technique is shown in Figure 68. Here c_{ph} is an individual velocity vector and $\overrightarrow{W}$ is the resultant wave vector plotted on the x-y plane.

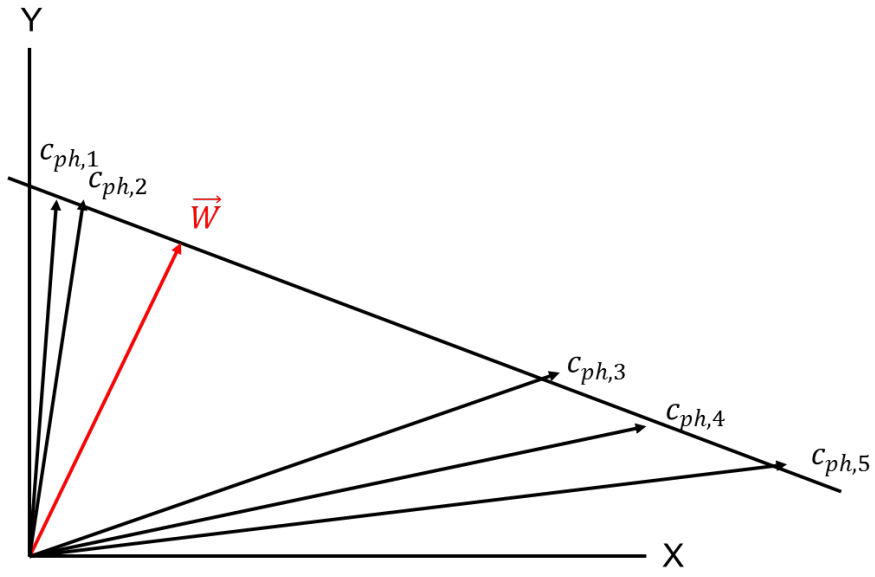

Figure 68 Illustration of wave vector determination technique.

The identification of phase shifts can be accomplished through the use of cross-correlations in either the time or frequency domains. Cross-spectral analysis was used in the work of Deyhle *et al.* (1993) due to the dispersive nature of boundary layer flows. In cross-spectral analysis the phase and coherence relationships of the signals from each sensor element exist as functions of frequency.

The process of performing a cross-spectral analysis begins by subdividing the data into n_d temporal records of elapsed time t_w such that the total length of the signal is equal to $n_d t_w$. The period of the subdivisions should be such that it is larger than the period of interest. A window function is then applied to the subdivisions in order to satisfy the periodicity requirement of the Fourier transform. A Hann window was used for this analysis and its definition is shown in Eqn (60).

$$w_h(t) = \frac{1}{2}\left(1 - \cos\frac{2\pi t}{t_w}\right), \quad 0 \le t \le t_w \tag{60}$$

One of the sensor elements is then dubbed the datum element, against which all of the other sensor's signals will be compared. The discrete Fourier transform, $X_k(f, t_w)$, of each windowed subdivision of the datum signal is then computed using a fast Fourier transform algorithm. This process is done for the datum sensor and each of the sensors whose signal is being compared against the datum in order to determine the phase shift of the traveling wave. The Fourier transforms of these comparison sensors are termed $Y_k(f, t_w)$. The auto-spectral correlations of the datum and comparison sensors are approximated using the formulas shown in Eqn (61) and Eqn (62).

$$G_{xx}(f) = \frac{2}{n_d t_w}\sum_{k=1}^{n_d} |X_k(f, t_w)|^2 \tag{61}$$

$$G_{yy}(f) = \frac{2}{n_d t_w}\sum_{k=1}^{n_d} |Y_k(f, t_w)|^2 \tag{62}$$

These equations are an ensemble average of the auto-spectral correlation of each of the signal's windows. An average cross-spectral correlation between the datum and comparison sensors can be computed using Eqn (63).

$$G_{xy}(f) = \frac{2}{n_d t_w}\sum_{k=1}^{n_d} X_k^*(f, t_w) Y_k(f, t_w) \tag{63}$$

Here * means complex conjugate. The coherence function relating the two signals can then be computed as

$$\gamma_{xy}^2(f) = \frac{\left|G_{xy}(f)\right|^2}{G_{xx}(f)G_{yy}(f)} \qquad 0 \le \gamma_{xy}^2 \le 1 \tag{64}$$

The coherence function describes how well the spectral content of the two signals are correlated. A value of one represents perfect correlation at the frequency in question; and zero means that the signals are not correlated, as would be the case with random noise. The coherence function is equal to the trivial solution of one by definition if $n_d = 1$ (Bendat and Piersol 1993).

The phase angle between the two sensors at each frequency can be calculated using the complex values of G_{xy}. This allows for a precise determination of the phase shift of a traveling wave with a specified frequency. The phase angle is calculated using the formula shown in Eqn (65).

$$\theta_{xy}(f) = \tan^{-1}\left(\frac{\mathrm{Im}\left(G_{xy}(f)\right)}{\mathrm{Re}\left(G_{xy}(f)\right)}\right) \tag{65}$$

Analysis of multiple hotfilm signals would begin with calculating the Power Spectral Densities (PSDs) of each signal. The PSDs would then be analyzed in order to determine whether traveling crossflow or T-S waves are present and what frequency bands they inhabit. Once the frequency bands of interest had been determined, the spectral correlation procedure above would be employed in order to determine the coherence and phase shift of the hotfilm signals at the frequencies of interest.

A sample output of this procedure is shown in Figure 69. Here two hotfilm signals are correlated using the method described previously. The signals come from sensing elements on the same hotfilm used for taking measurements on an unrelated experiment. The plot clearly shows this method's power in that the correlation function's maxima correspond nicely to peaks which look qualitatively similar. Also, the phase angle is relatively uniform until higher frequencies with low correlation are reached.

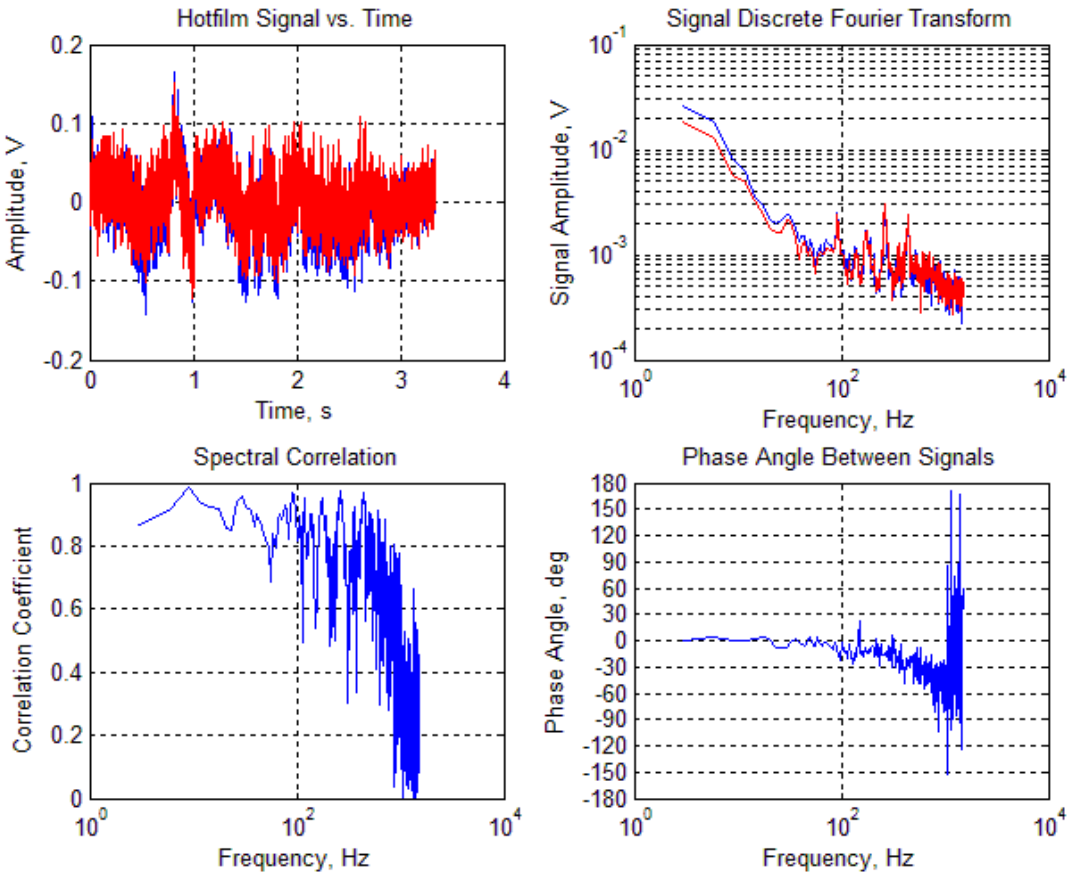

Figure 69 Spectral correlation outputs.

The calculation of phase shift as a function of frequency permits the calculation of phase and group velocities. These velocities are calculated by selecting a frequency of interest, *f*, and identifying the phase shift, $\Delta\theta_{xy}(f)$, between the datum and comparison sensors that are a distance d_n apart. The relationships between these parameters for the phase and group velocities are shown in Eqn (66) and Eqn (67).

$$c_{ph,n}(f) = 2\pi d_n \frac{f}{\Delta\theta_{xy}(f)} \tag{66}$$

$$c_{gr,n}(f) = 2\pi d_n \frac{df}{d(\Delta\theta_{xy})} \tag{67}$$

In the equation for group velocity, the term $df/d(\Delta\theta_{xy})$ represents the inverse of the slope of the plot of phase angle with respect to frequency.

The measurement of phase shifts between sensors spaced at intermediate locations between crossflow vortices can also be used to identify spacial crossflow structures. This method was first used by Mangalam *et al.* (1990), who demonstrated that the signals from hotfilm elements spaced half of a stationary crossflow wavelength apart had a 180 degree phase shift.

C. Design Methodology

The hotfilm design detailed herein was motivated by the desire to test an orthogonal hotfilm array on the FRL's SWIFT model prior to application on the glove project. The spanwise spacing of the orthogonal hotfilm array was driven by the spacing of the critical crossflow wavelength on the SWIFT model; however, the streamwise spacing of the elements was a free design parameter. A minimum of three sensors arranged in a triangular fashion was required in order to resolve every possible wave vector direction. A linear array would only be capable of measuring one component of the wave's phase velocity. The streamwise spacing was determined by the desire to minimize the uncertainty in phase speed and direction.

The principle cause of uncertainty in the wave speed and direction was the length of the hotfilm sensor element. The position of the wave on the sensor at the moment the sensor registers its presence was not known. Hence, the wave front could theoretically be located anywhere along the element's length at the moment that the signal notes its presence. Therefore, the length of the individual sensor elements was minimized to the shortest length achievable by the manufacturer, which was 0.01 inches. The width of each sensor element was 0.002 inches.

An uncertainty analysis was conducted using a jitter approach. The configuration assumed was a cluster of three elements in a triangular shape. The base of the triangle was formed by two crossflow-sensing elements with a streamwise sensing element at the apex. The wave vector calculation algorithm assumed that the sensors always registered the presence of the wave in the middle of each element. A random number generator with uniform distribution would vary the position of the wave's actual measurement location on a particular sensor element between the extreme ends of the wire. Velocity calculations would then be performed using the assumed measurement location coupled with the actual

time required for propagation between each random location. The equations used to perform this analysis are detailed in Appendix F. 1,000 iterations were found to converge to the mean velocity and angle sought, meaning that the statistical completeness of the error extremum was acceptable for design purposes. The standard deviations of the velocities and angles calculated with this approach were not recorded because the goal of the exercise was to establish the maximum error possible for a particular geometry. Uncertainty in the measurements decreased as the length of the elements became a smaller fraction of the total distance between the sensors.

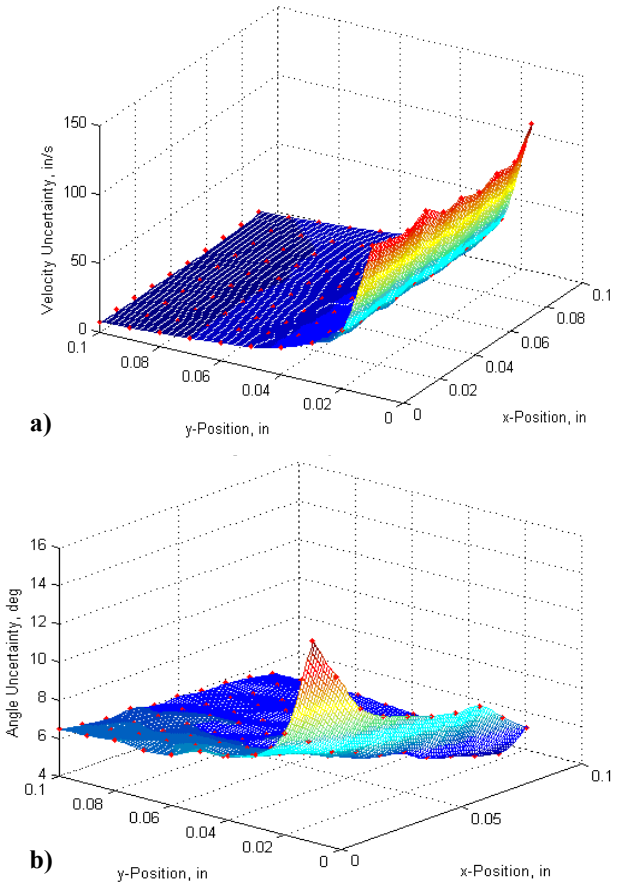

Figure 70 Uncertainty in measurements as a function of element spacing for (a) phase and (b) velocity.

Figure 70 shows the uncertainty in velocity and angle measurements as a function of the position of the crossflow wire at the apex of the sensor triangle for T-S waves on the SWIFT model hotfilm configuration. Figure 70a shows that the velocity error rapidly decreases with streamwise separation (y-position) up to approximately 0.06 inches, after which there is a diminishing but still positive rate of return with increasing distance. The velocity error is not affected by the spanwise (x-position) position of the element. Figure 70b shows that the angle error is dependent on both streamwise and spanwise spacing. However, the calculations show spanwise spacing becomes of less importance as streamwise distance increases. The plots of Figure 70 suggest that a streamwise element positioned approximately between the two crossflow sensors in the spanwise direction at 0.1 inches streamwise spacing would minimize error while also accounting for manufacturing limitations. Uncertainty plots in similar to Figure 70 were also generated for wave vectors more likely to be encountered in the SARGE project and showed qualitatively similar behavior, meaning that the current design is universally applicable.

The final design called for seven crossflow sensors and six streamwise sensors to be arranged into a 13 element array. Crossflow sensors were spaced 2.25 mm apart, which is one half of the critical crossflow wavelength. Streamwise sensors were placed between the crossflow sensors with a 0.1 inch offset in the streamwise direction. An illustration of this design is shown in Figure 71.

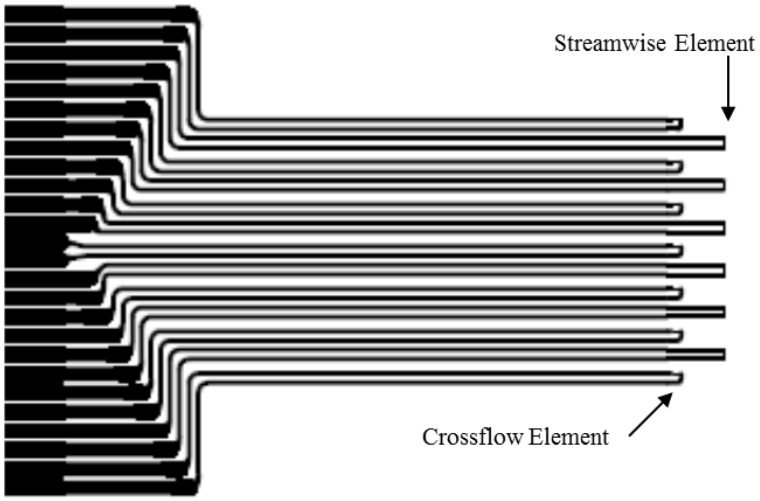

Figure 71 Hotfilm sensor illustration.

An uncertainty analysis was performed for this arrangement as was done previously for the three-element array. The most inboard crossflow element was chosen as the datum sensor. The results are shown in Table 11.

Table 11 Uncertainty as a function of sensors used to compute wave vector

	Sensors 1-3	Sensors 1-4	Sensors 1-5	Sensors 1-6	Sensors 1-7	Sensors 1-8	Sensors 1-9	Sensors 1-10	Sensors 1-11	Sensors 1-12	Sensors 1-13
Angle Uncertainty (º)	6.18	5.85	5.33	4.92	4.63	4.02	3.78	3.10	2.81	1.79	1.75
Speed Uncertainty (%)	5.79	7.68	7.09	8.06	5.60	9.78	6.89	13.60	10.33	16.32	13.87

Table 11 shows that the uncertainty in the angle measurement decreases as more sensors are used in the vector direction calculations. Uncertainty in the angle ranges from approximately 2° to 6°. Unlike the angle measurement, the speed uncertainty increases as more sensors are added. These uncertainties ranged from about 6 to 10 percent. This is an artifact of the geometry of the sensors and the T-S wave direction on the SWIFT. Other wave directions show decreasing uncertainties for both angle and speed as the number of sensors used to make the measurements was increased.

D. Hotfilm Sensors

The hotfilms previously described were manufactured by Tao of Systems, Inc. for use on the SWIFT model. These hotfilms are composed of copper leads deposited on a 0.002 inch thick substrate. The sensor elements are made of nickel and are beam deposited to a thickness of approximately 0.20 μm. The resistance of each sensor element in the 13 sensor custom array at 25ºC is shown in Table 12.

Table 12 Hotfilm sensor resistance

Sensor	Sensor Resistance (Ohms)	Lead Resistance (Ohms)	Total Resistance (Ohms)
1	2.0	1.5	3.5
2	1.9	1.5	3.4
3	2.0	1.5	3.5
4	1.9	1.4	3.3
5	2.0	1.4	3.4
6	1.8	1.5	3.3
7	2.0	1.5	3.5
8	1.8	1.5	3.3
9	2.0	1.4	3.4
10	1.8	1.5	3.3
11	2.0	1.4	3.4
12	1.8	1.5	3.3
13	2.0	1.4	3.4

The sensors are numbered from left to right. A photo of the hotfilm sensor array was taken using a confocal laser microscope and is shown in Figure 72. The datum sensor is assumed to be the element in the bottom left corner of the image. The coordinate system for the analysis is also illustrated in the figure.

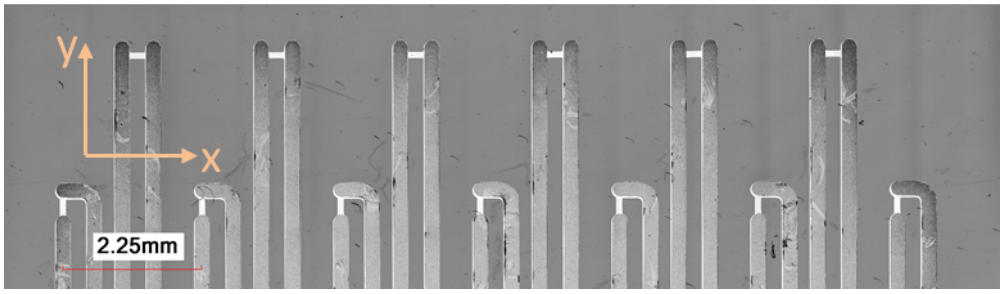

Figure 72 Confocal laser microscope image of proposed hotfilm for SWIFT.

The coordinates of the center points of each of the sensor elements with respect to the datum element are listed in Table 13.

Table 13 Coordinates of hotfilm elements

Sensor	x (mm)	y (mm)	Sensor Length (mm)
1	0.00	0.00	0.24
2	1.24	2.45	0.24
3	2.24	0.00	0.24
4	3.48	2.45	0.24
5	4.51	0.00	0.25
6	5.75	2.45	0.24
7	6.77	0.00	0.25
8	7.97	2.45	0.24
9	8.99	0.00	0.24
10	10.21	2.45	0.24
11	11.23	0.00	0.24
12	12.43	2.45	0.24
13	13.48	0.00	0.24

It is important to note that the hotfilms should be installed such that the *x* axis is parallel to the leading edge. If the hotfilm is aligned such that the *y* axis is parallel to lines of constant span the spacing of the sensors will not correspond to an even multiple of the critical crossflow wavelength.

An uncertainty analysis was performed for sensor geometry listed in Table 13. A T-S wave was approximated by a wave traveling at 40 m/s at a wave angle of 280º referenced to the hotfilm's *x* axis. The results of this analysis are presented in Figure 73. The concentric rings on the polar plot are in units of inches per second.

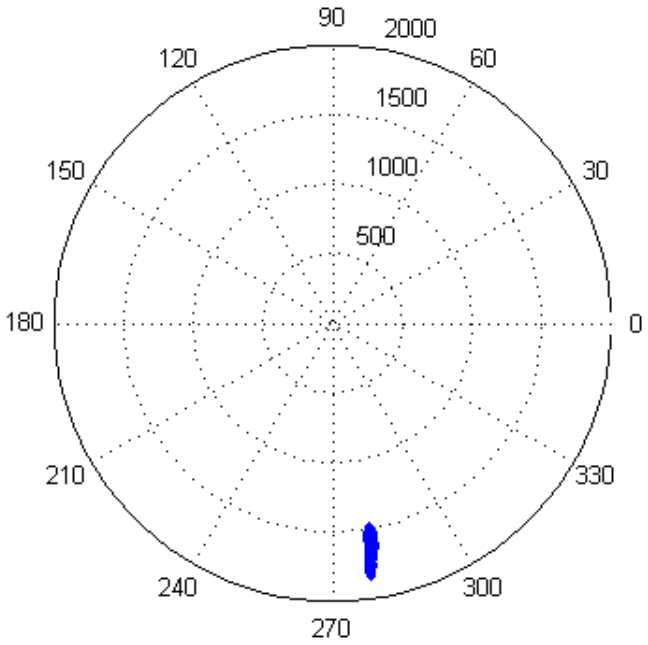

Figure 73 Polar plot of possible velocity vectors.

The range of velocity errors was found to be from -7% to 15% and the angle uncertainty was found to be ±2º. The shape of the uncertainty can change with wave angle such that the angle uncertainty can become somewhat larger while velocity uncertainty decreases.

The traveling wave identification hotfilm's design is to be verified in a T-S dominated boundary layer on the SWIFT model. As the experimental test plan for the hotfilms was being developed, it was feared that the hotfilm substrate along the leading edge of the sensor would act as a two-dimensional step and trip the T-S dominated boundary layer. This would cause the sensor elements to measure a useless turbulent spectrum. In order to avoid this difficulty, single, streamwise hotfilm sensors were purchased. These sensors have a 2 mm long streamwise element mounted on a substrate that was 8 mm wide. The dimensions of these hotfilms are smaller than the centimeter scale T-S wavelengths and will be perceived as three-dimensional roughness. These sensors may be arranged in any orientation deemed acceptable for resolving the disturbance wavelengths of interest. The only requirement is that the individual elements cannot be arranged such that a straight line can be drawn through all elements simultaneously. Also,

attention should be paid to the wavelength of the disturbances of interest because too large a spacing will results in phase angle differences greater than the ±180º limit of the spectral technique. The difficulties associated with the two dimensional step created by the 13 sensor array's substrate would not be present in a CF dominated boundary layer.

5. SWIFT EXPERIMENTAL SETUP

A. Aircraft

The aircraft employed in the hotfilm array flight test experiments is a tandem twin-engine Cessna O-2A Skymaster. This aircraft was built in 1968 and completed a tour in Vietnam as a reconnaissance and light attack platform. It is a militarized version of the Cessna 337 light transport plane and features wing hardpoints convenient for hanging flight experiments. The outboard munitions pylons are ideal for flight experiments because they are outboard of the limits of the propeller wash's influence. The tandem engine arrangement limits propeller wash over the wings and provides added safety because the configuration does not have a critical engine. The two engines also add safety because the aircraft is able to maintain altitude when operating with a single engine. The O-2's nominal experimental configuration has three place seating for a pilot, copilot, and flight test engineer (FTE). The pilot and copilot sit side by side in the first seating row and the FTE sits behind the copilot. A fourth seating place is available next to the FTE but the seat is typically removed in order to reduce weight and increase space for instrumentation. The aircraft's original radio stack behind the FTE's seat has been repurposed as an instrumentation rack. The instrumentation rack contains a power inverter, signal conditioners, data acquisition boards, and hotfilm anemometers necessary to complete a research flight. The aircraft's useful load typically allows for a crew of three plus requisite instrumentation and test articles to fly one hour missions with a half hour fuel reserve. A picture of Texas A&M's O-2 is shown in Figure 74.

Figure 74 Photo of the FRL's Cessna O-2A.

B. Swept Wing In-Flight Test (SWIFT)

The Swept Wing In-Flight Test (SWIFT) is a test article used to perform boundary layer stability and transition research on the O-2. The model measures 42 inches in span with a 54 inch chord and a 30° leading edge sweep. The first 15 % of the SWIFT's chord is comprised of a removable leading edge. The removable leading edge allows researchers to investigate the effects of various surface finishes, such as painted and polished aluminum, on transition. One of the leading edges also allows for the introduction of two-dimensional step through the use of an insert. The surface aft of the leading edge is painted with black powder-coat to a nominal surface finish of 1 μm rms roughness in order to facilitate IR thermography. The test side of the model, analogous to the upper surface of an aircraft wing, faces the cabin. A Photo of the SWIFT installed on the O-2 is shown in Figure 75.

Figure 75 SWIFT model with 5-hole probe installed.

The SWIFT is mounted to the aircraft vertically using the port-side outboard hard point and munitions pylon. A photo of the SWIFT attached to the aircraft in flight is shown in Figure 76.

Figure 76 O-2A with SWIFT installed in flight.

The test wing's airfoil is a custom natural laminar flow design that places the pressure minimum at 70 percent chord and is free of concave curvature forward of the pressure minimum. This design seeks to simultaneously suppress the T-S and Görtler instabilities while exciting the crossflow instability. The attachment line contamination instability is not present on the SWIFT because the inboard and outboard edges of the model are free surfaces. Two rows of static pressure ports have been installed at spanwise stations 13 and 29 inches below the top of the model. Each row contains 25 pressure ports. Carpenter (2009) performed static pressure measurements on the SWIFT in order to compare with the pressure coefficients calculated by Rhodes *et al.* (2008). The results of this comparison for the root and tip pressure port rows at SWIFT angles of attack of -2.6° and -4.7° are shown in Figure 77 and Figure 78, and Figure 79 and Figure 80 respectively. Each of the cases plotted below has a favorable pressure gradient from the attachment line to 70 % chord. It is worthwhile to note that the pressure gradient is not as steep at the tip row as it is at the root.

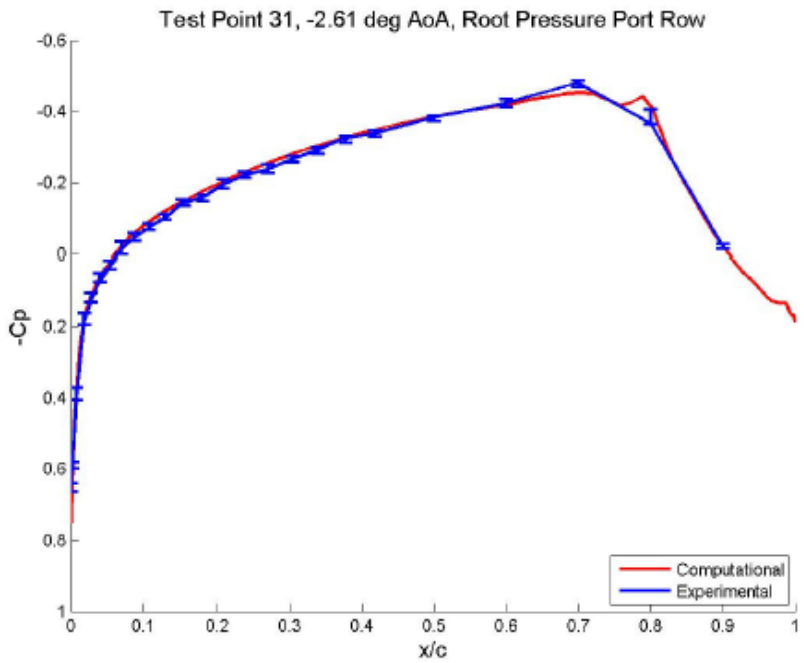

Figure 77 SWIFT root pressure coefficient at -2.6º SWIFT AoA (Carpenter 2009).

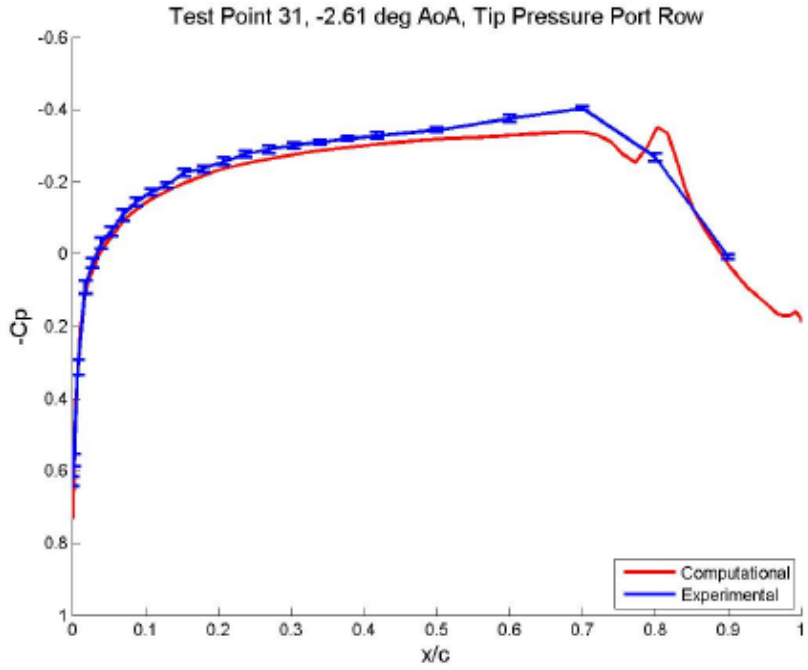

Figure 78 SWIFT tip pressure coefficient at -2.6º SWIFT AoA (Carpenter 2009).

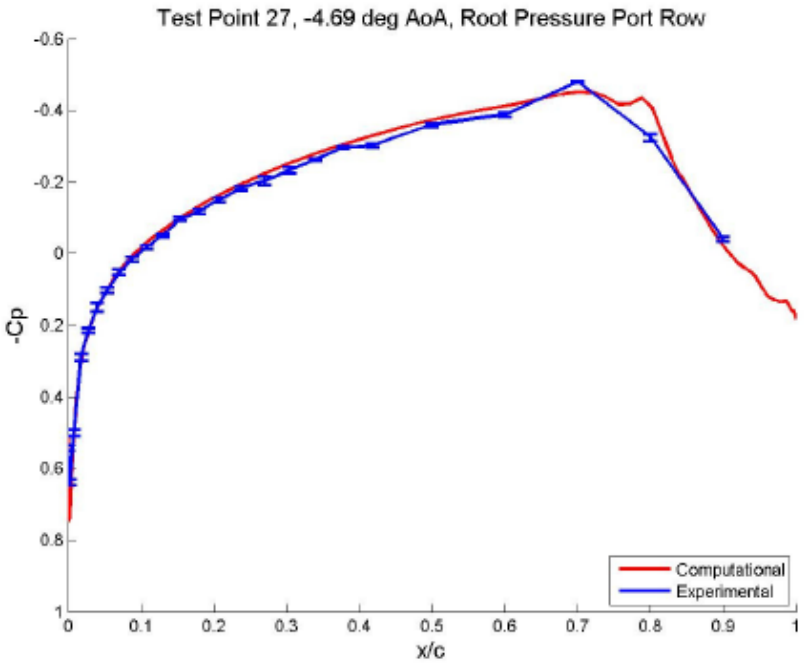

Figure 79 SWIFT root pressure coefficient at -4.7º SWIFT AoA (Carpenter 2009).

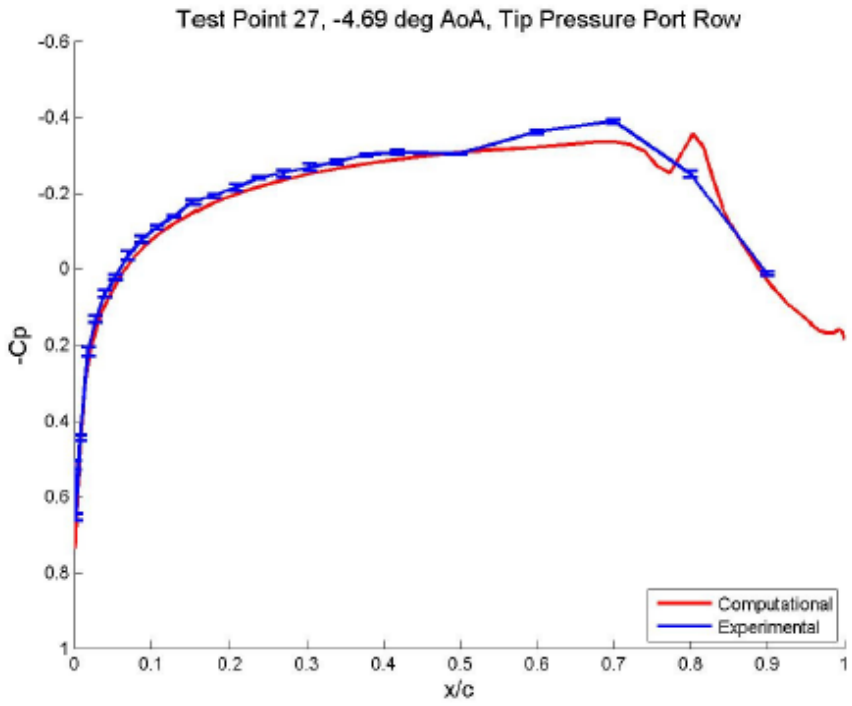

Figure 80 SWIFT tip pressure coefficient at -4.7º SWIFT AoA (Carpenter 2009).

Figures Figure 77 and Figure 79 show that computational results agree with the pressures measured experimentally at the root row. The tip row has a steeper pressure gradient than that predicted by CFD; however, the general shapes of the pressure profiles are qualitatively similar. These plots show that CFD results can be confidently used in order to predict pressure coefficient profiles on the SWIFT.

Linear stability analysis of the SWIFT's crossflow instability was performed by Rhodes *et al.* (2008) using the inboard and outboard pressure profiles calculated using CFD and plotted previously in Figure 77 through Figure 80. The results of these computations for the -2.6º and -4.7º SWIFT angle of attack cases are shown in Figure 81 and Figure 82 respectively.

a)

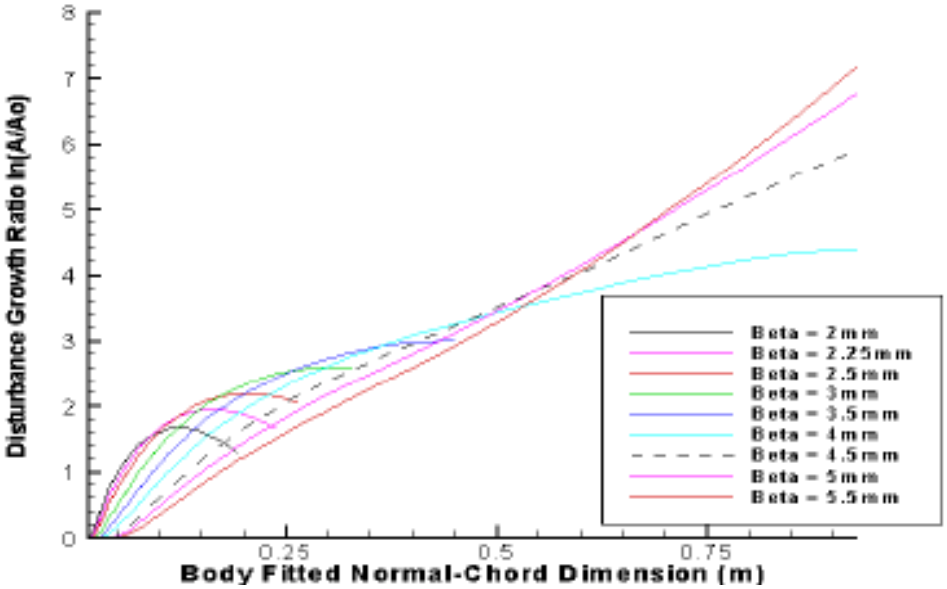

b)

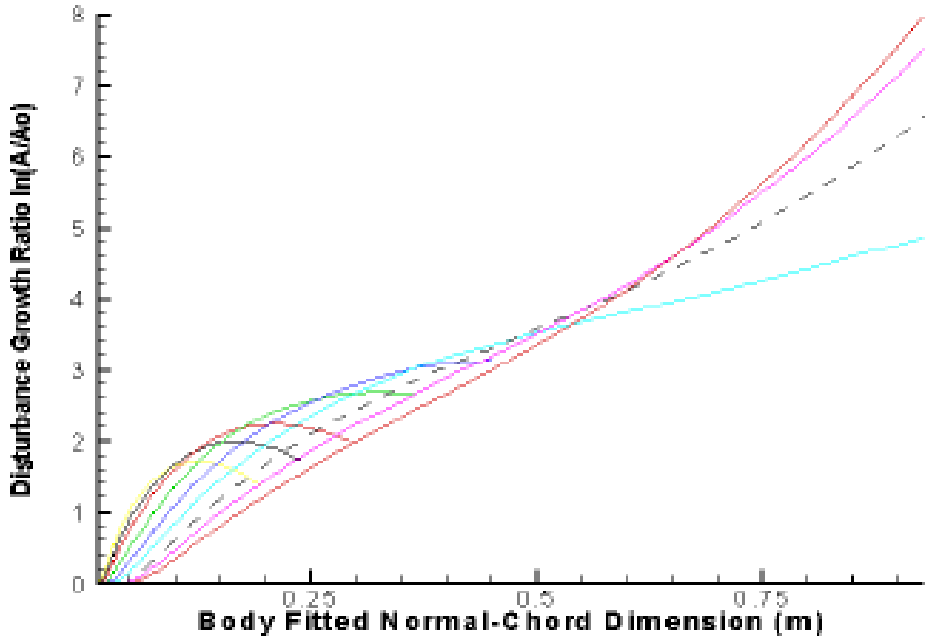

Figure 81 SWIFT n-factors at -2.6º SWIFT AoA for a) root pressure port row and b) tip pressure port row (Rhodes *et al.* 2008).

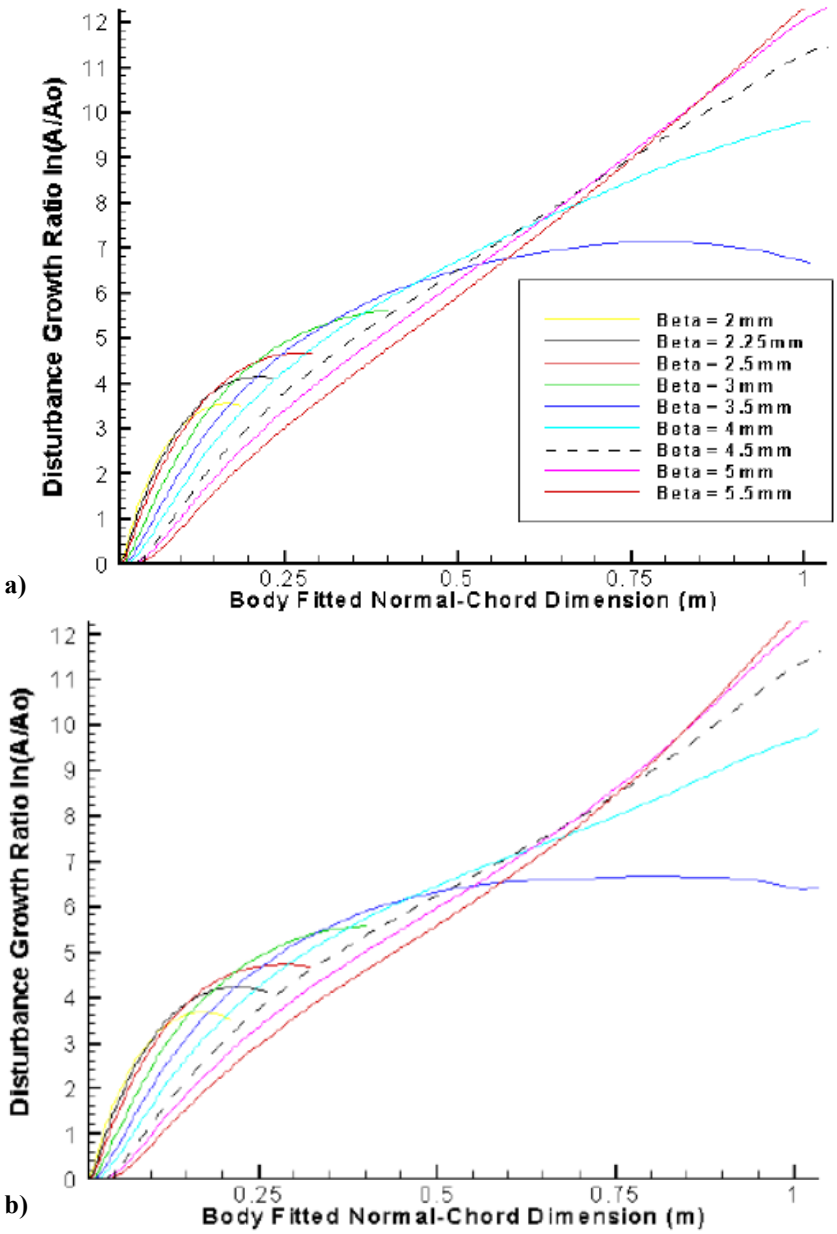

Figure 82 SWIFT n-factors at -4.7º SWIFT AoA for a) root pressure port row and b) tip pressure port row (Rhodes *et al.* 2008).

The linear stability analysis presented previously led Rhodes *et al.* (2008) to identify the 4.5 mm crossflow wavelength as the most unstable mode that was likeliest to cause transition on the model. The

2.25 mm wavelength was identified as the best control wavelength because it quickly grew to a moderate amplitude and then attenuated.

Because the SWIFT is mounted vertically beneath the O-2's port wing, its coordinate system differs from the aircraft's. An increase in aircraft angle of attack results in a decrease in the SWIFT's effective sweep angle. Similarly, an increase in aircraft angle of sideslip results in a decrease in the SWIFT's angle of attack. This concept is illustrated in Figure 83.

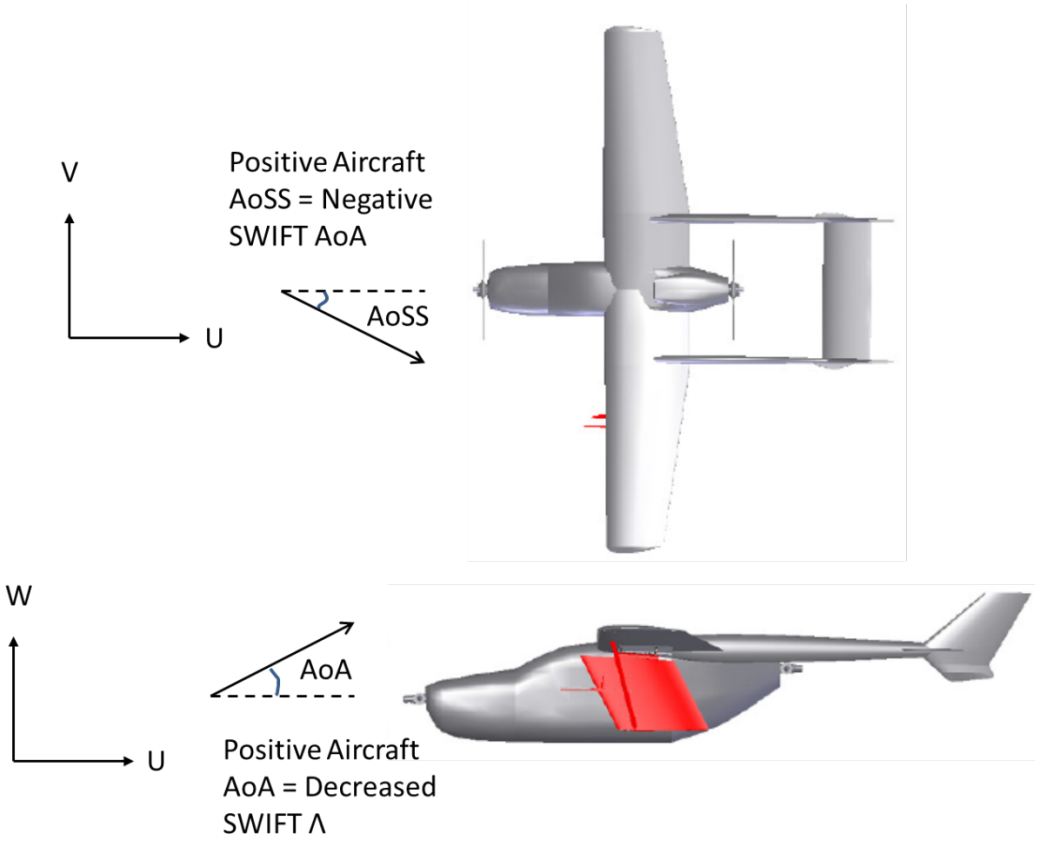

Figure 83 SWIFT coordinate system.

The SWIFT model is also used as an instrumentation platform. The primary instrument installed on the exterior of the SWIFT is the five-hole probe. This probe was manufactured by Aeroprobe Corporation and is capable of resolving the local flow velocity and flow angles in a manner identical to that described

previously for SARGE's proposed probe. The readings of this probe are used to define the flight conditions of the SWIFT, such as the model's angle of attack which was previously shown in Figure 83. A detailed explanation of the placement of the five-hole probe can be found in Rhodes (2008). Four Honeywell FP2000 pressure transducers are mounted inside of the SWIFT's hollow interior and perform the pressure measurements required for the five-hole probe. A National Instruments USB NI-9211 thermocouple device is also installed within the SWIFT and enables thermocouple measurements either within the model or on the test surface when necessary.

A detailed description of the design methodology, boundary layer stability experiments, and operational considerations of the SWIFT model can be found in Carpenter (2009). A detailed structural analysis of the SWIFT is documented in McKnight (2006). Rhodes (2008) documents the aforementioned CFD and stability calculations performed in support of the experimental effort.

C. Experiment Instrumentation

The instrumentation system installed on the O-2 is designed to deliver high quality air-data, IR thermography, and hotfilm anemometry. Instrumentation power is delivered by a 1000 Watt, 120 Volt AC power inverter. The air-data and hotfilm data acquisition system is based on LabVIEW data acquisition software manufactured by National Instruments. The software is installed on a Panasonic Toughbook laptop computer, which is used for all data processing and recording in flight. The instrumentation suite is completely controlled by the flight test engineer during flight. The primary instruments used for the current experiment include: the SWIFT-mounted five-hole probe, an Aero-Instruments total temperature probe, the SC8000 IR camera, and an A.A. Lab AN-1003 constant temperature anemometer.

The most important instrument in the air-data suite is the five-hole probe mounted on the side of the SWIFT model. This probe records the SWIFT-local flow velocity and the SWIFT's angle of attack and effective sweep angle. The five-hole probe is aligned with the chord line of the SWIFT prior to flight and any bias resulting from residual misalignment is measured and subtracted using LabVIEW prior to the data being recorded or displayed to the test pilot. Carpenter (2009) estimated that the errors in velocity and Reynolds number are 0.2 percent and that the errors in SWIFT angle of attack and effective sweep

angle are on the order of ±0.2°. The majority of the error in the angles is a result of uncertainty in the alignment of the probe with respect to the SWIFT. The pressures in each of the five-hole probe's ports are measured using Honeywell FP2000 pressure transducers mounted within SWIFT as described previously. A picture of the five-hole probe attached to the SWIFT is shown in Figure 84.

Figure 84 5-hole probe attached to SWIFT

Total temperature measurements are made using an Aero-Instruments 4222 Temperature Probe. This probe is mounted on the O-2's port wing between the cabin and the SWIFT model. The total temperature reading from this probe can be combined with the total and static pressure measurements from the five-hole probe in order to calculate static temperature. The static temperature can then be combined with Sutherland's Law and the SWIFT's chord length in order to calculate the SWIFT's current chord Reynolds number. All calculations are carried out within the LabVIEW software.

Infrared thermography is used as the principle method for identifying boundary layer transition on the SWIFT model. The IR camera currently used at the Texas A&M Flight Research Lab is a FLIR SC8000, the same camera proposed for the SARGE project and described previously. The camera is sensitive to the 3-5 μm wave band and has 1024x1024 pixel resolution. Currently, the lab owns 17 mm and 50 mm lenses for the SC8000 that are capable of spacial resolutions on the SWIFT of 2.3 mm per pixel and 0.8

mm per pixel, respectively. The 17 mm lens is capable of imaging the entire SWIFT model while the 50 mm lens can resolve approximately 80 percent of the its span and 60 percent of its chord.

Hotfilm anemometry is performed using an A.A. Labs AN-1003 constant temperature anemometer and Tao Systems hotfilm arrays. The AN-1003 anemometer has ten channels that feature built-in gain and zero-offset adjustments to optimize signal output to the user's data acquisition system. The AN-1003 also offers a built-in pulse mode that passes a square wave through a selected channel in order to facilitate the dynamic tuning of hotfilm channels. The AN-1003 is stored on the O-2's instrumentation rack during flight.

A small liquid crystal display mounted to the pilot's yoke is used to display mission critical data to the test pilots. On a typical IR thermography mission this data is confined to the atmospheric static temperature profile, the Reynolds number, and SWIFT angle of attack measured by the five-hole probe during the data collection phase of the flight. Displaying the atmospheric temperature profile has been found to be particularly useful when the pilots are charged with maintaining a specified Reynolds number while changing altitude. A picture of the display mounted to the pilot's yoke is shown in Figure 85.

Figure 85 Yoke-mounted pilot display

D. Data Acquisition and Signal Conditioning

A variety of signal conditioning and data acquisition devices are employed in the O-2 in order to facilitate easy, accurate data collection. All analog air-data and hotfilm signals are connected to the data acquisition system using BNC cables via two BNC connector blocks. The air-data stream uses two National Instruments BNC-2110 connector blocks and the hotfilm signals are attached to a National Instruments BNC-2115 connector block. The two BNC-2110 blocks are then attached to a National Instruments NI USB-6259 and the BNC-2115 is attached to an NI USB-6255 for analog to digital conversion with 16 bit resolution. The 6259 and 6255 boards each have a USB cable that is then attached to the FTE's laptop for processing and recording. The USB 9211 thermocouple device installed within the SWIFT model also connects to the laptop via a USB cable and provides 24 bit digital data. The SC8000 IR camera is connected directly to the laptop via a gigabit Ethernet port on the camera. This cable enables the computer to control the camera and download image data using custom FLIR software.

The laptop computer acts a both a data processor and a recorder. All data from the pressure transducers, thermocouples, total temperature probe, and hotfilms are processed and recorded using LabVIEW software. LabVIEW is used in conjunction with Matlab software in order to compute the values of SWIFT's angle of attack, angle of sideslip, Mach number, chord Reynolds number, indicated airspeed, true airspeed, and altitude. The computer then generates the pilot's display information and outputs it through a VGA cable. LabView is also used to record the hotfilm anemometer's output voltages. The IR camera's control and data acquisition is facilitated by FLIR's proprietary ExaminIR software. All data is written to the computer's hard drive during flight.

The output voltages from the AN-1003 hotfilm anemometers are passed through a Krohn-Hite 3016 filter for filtering and amplification before reaching the BNC-2110 connector block. The signal is AC coupled using a 1 Hz to 15 kHz band-pass filter. The low-pass and high-pass filters used for this operation each have four poles. The 15 kHz low-pass filter can also double as an anti-aliasing filter when the digital sampling rate of the data acquisition system is set to 30 kHz. A 10 dB gain is also applied to enhance the digital system's resolution of the analog signal.

Data is sampled at rates commensurate with the purposes of the measurements. The outputs from the five-hole probe's transducers and the total temperature measurement are sampled at 20 Hz because these parameters vary with time scales longer than 0.1 seconds. Likewise, the SC8000 IR camera is operated at 20 frames per second. The SC 8000's sample rate is limited by the data transfer capabilities of the gigabit Ethernet connection. Hotfilm signals are sampled at no less than 30 kHz in order to capture disturbances in the boundary layer at frequencies below 15 kHz and to use the Krohn-Hite filter for anti-aliasing.

6. EXPERIMENTAL PROCEDURE

The purpose of the experiment proposed herein is to investigate the ability of the hotfilm design presented in Section 4 to resolve traveling and stationary disturbances in the boundary layer. The T-S instability on the SWIFT model can be excited in order to create streamwise-traveling waves. The crossflow instability can also be used for investigating the ability of phase measurement techniques to resolve spanwise, stationary wave structures. IR thermography using the SC-8000 can used to determine the location of the hotfilm's installation and to verify the nature of the dominant instability.

A. Typical Mission Profile

A typical research flight begins with the O-2 climbing to 10,500 ft in one of two designated local test areas. These test areas are located to the west and northwest of College Station's Easterwood Airport and are situated between federal airways in order to de-conflict with transient aircraft. After reaching 10,500 ft, the aircraft loiters for approximately 20 minutes in order to cold soak the SWIFT model to approximately the ambient air temperature. Once the cold soak is completed, the aircraft will dive to 3,000 ft at an airspeed of 175 KIAS. Hotfilm and IR research data are collected during the dive.

The dive serves two purposes. First, diving through the steadily warming atmosphere is necessary to enable IR thermography to detect the laminar and turbulent regions on the SWIFT. The difference between the convective heat transfer rates in laminar and turbulent boundary layers creates different surface temperatures between the two zones as the cold model is warmed. The laminar region is perceived as being cooler than turbulent region as the aircraft descends rapidly into warmer air. Secondly, the dive is necessary in order to reach the SWIFT's target chord Reynolds number of 7.5 million. The O-2 is not capable of achieving this Reynolds number in level flight.

The SWIFT model's local angle of attack is controlled during the dive in order to match desired conditions specified for each experiment. The SWIFT's local angle of attack reading from the five-hole probe is displayed to the pilot via the yoke-mounted display described in Section 5. The pilot can easily modulate this angle using the aircraft's rudder controls. The SWIFT's effective angle of sweep is a function of the aircraft's gross weight and airspeed and cannot be changed during steady maneuvers.

However, this angle is typically on the order of 0.5° when the aircraft is on condition at 7.5 million Reynolds number.

B. Baseline Flights

Baseline flights must be performed in order to establish the nature of the transition on the model at specified flight conditions as well as the location of the transition front. These flights can be completed using either the solid leading edge or the leading edge with a two-dimensional leading edge insert. The leading edge insert acts to further destabilized the T-S waves if necessary through the introduction of a two-dimensional roughness.

The process begins by sweeping the aircraft through positive SWIFT angles of attack from 2° to 4° in increments of 0.5°. The goal is to increase the angle of attack until a suction peak forms near the model's leading edge. This creates a localized region of adverse pressure gradient, which destabilized T-S. Computations performed by Matthew Tufts of Texas A&M showed that a SWIFT local angle of attack of 3.3º would produce a suction peak near 2.5 percent chord. This result is shown in Figure 86.

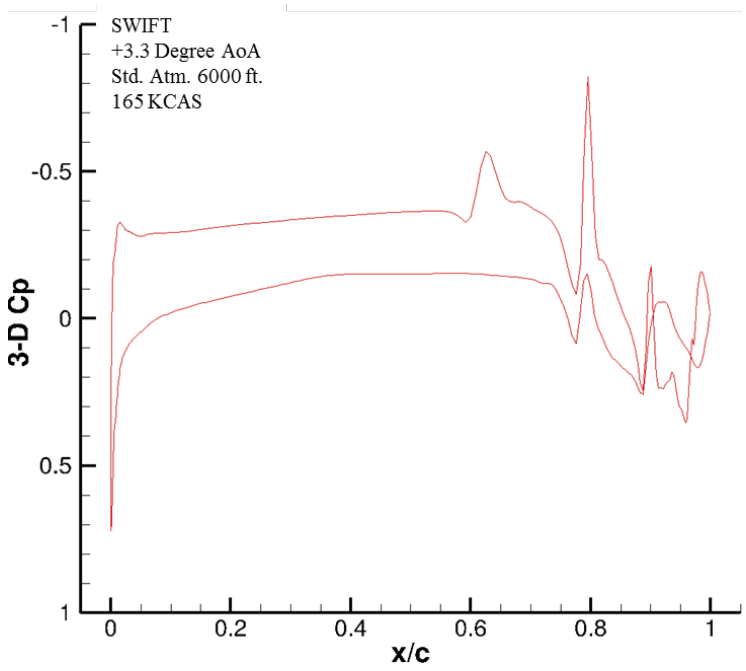

Figure 86 SWIFT pressure coefficient at 3.3º AoA.

An angle of attack is sought such that the T-S instability will be excited enough to create a measureable streamwise, traveling wave, but no so much that transition will occur near the leading edge of the SWIFT. The switch from the crossflow dominated transition typically investigated on the SWIFT model to T-S dominated transition is detectable using IR thermography. The crossflow transition front is jagged, with a distinct saw-tooth pattern. Conversely, T-S dominated transition produces a diffuse, spanwise-uniform transition front. IR thermography should be performed using the 50 mm lens on the SC8000. This lens provides resolution on the order of 0.8 to 1.0 mm/pixel on the surface of the model, which is required for accurately identifying the nature of the transition front. An example of a crossflow transition front on SWIFT imaged with the SC8000's 50 mm lens is shown in Figure 87.

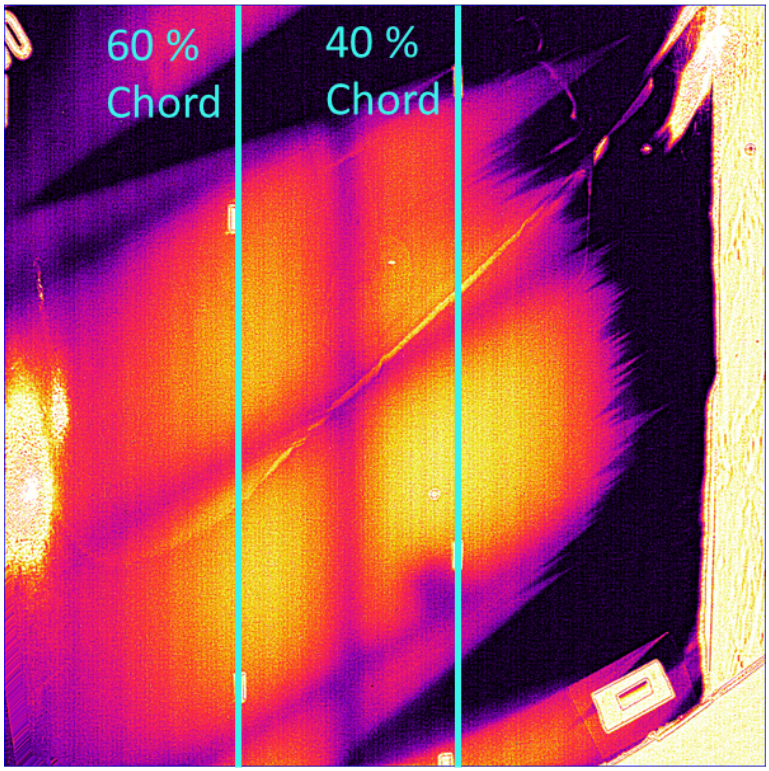

Figure 87 Crossflow transition front on SWIFT imaged with SC8000 50mm lens.

C. Hotfilm Experiment Procedure

Once the location of T-S dominated transition has been identified from the baseline flights the hotfilm should be installed. The hotfilm is to be placed such that the sensing elements are just forward of the baseline transition location. A buffer of 5 % chord between the sensors and the transition front may be added to account for the additional disturbance introduced by the two-dimensional step created by the forward edge of the hotfilm. It is to be noted that the streamwise-measuring sensor elements on the hotfilms described in Section 4 are designed to be installed parallel to the leading edge. Misalignment of the hotfilm will result in crossflow elements being spaced at non-integer multiples of the critical crossflow wavelength. If T-S dominated transition is occurs at the forward edge of the hotfilm after installation, lower angles of attack can be tried in order to stabilize the T-S instability. If this technique does not work the individual elements mentioned in Section 4 can be installed in a known spacial configuration. The narrow substrates of these sensors should act as three-dimensional roughness elements and not influence the T-S transition location.

The crossflow instability can be excited by operating the model at negative angles of attack. Typical values range from -3.0º to -6.0º depending on the leading edge in use and the desired transition location. An angle of attack should be selected such that the transition front is located immediately aft of the hotfilm's sensing elements. This will ensure that the disturbances grow to the highest amplitude possible in order to make measurements of the small velocity perturbations easier. Identification of the crossflow wavelength is accomplished by measuring the phase shift of a signal at a specific frequency between adjacent crossflow sensors. It should be emphasized that only the channels whose sensing elements are oriented normal to the leading edge should be used for this test. The formula used to convert the distance and phase shift between the adjacent sensors into wavelength is shown in Eqn (68).

$$\lambda = \Delta x_n \frac{2\pi}{\Delta\theta_{xy}} \tag{68}$$

The frequency of the disturbance used can be arbitrary so long as its wavelength is low enough such that no more than one period is present between sensors. This technique is described in detail in Mangalam *et al*. (1990).

Data acquisition will play a key role in determining the success of the experiment. The Krohn-Hite 3016 filter installed in the O-2 is capable of band-pass filtering the hotfilm data from 1 Hz to 15 kHz. It also applies a 10 dB gain to the signal output. Sampling should occur at no less than 30 kHz so that the filter can be used for anti-aliasing. The AN-1003 anemometer is also capable of adding a gain to the signal that it outputs to the Krohn-Hite filter. Applying the maximum permissible amount of gain to the hotfilm signals without exceeding the data acquisition board's limit is important due to the small amplitudes of the disturbances being measured.

7. CONCLUSIONS

A. Wing Glove Instrumentation System

The instrumentation system described in the previous sections is designed to provide a comprehensive set of data to researchers studying boundary layer stability and transition on a wing glove. The instrumentation suite proposed for the SARGE project includes an IR camera, static pressure ports, a 5-hole probe, high frequency response Kulite transducers, thermocouples, hotfilms, and a total temperature probe. These instruments will allow researchers to precisely measure boundary layer transition location and correlate it to accurate measurements of flow conditions.

IR Camera

The IR camera selected to support the SARGE glove experiment is a FLIR SC8000. This camera features 1024x1024 resolution and has been shown to produce high quality images of the wing glove area of interest. A 17 mm lens and a 50 mm lens are proposed to enable flexibility in viewing both global and local phenomena on the glove and wing surfaces. The spacial resolution and depth of focus provided by these lenses have been computed and are deemed acceptable.

Static Pressure Measurements

The SARGE glove will feature 58 static pressure ports arranged in two rows of 29 ports each on the inboard and outboard edges of the test surface. These pressures will enable the research team to measure the pressure coefficient on the surface of the wing and compare it to computations. The pressure coefficient profile will also be used to define the glove's desired angle of attack for each test point as measured with the five-hole probe. The static pressures will be measured using an ESP-64HD multiplexing pressure transducer. The ESP is a differential transducer so a calibrated static pressure source or other known pressure must be provided to enable accurate pressure coefficient calculations.

Five-Hole Probe

A glove-mounted five-hole probe will provide measurements of the flow in the immediate vicinity of the glove. The measurements from the probe will be used by SARGE's pilots and onboard researchers to determine when the aircraft is established on a test point since five-hole probe measurements are to be

calibrated to pressure coefficients on the wing. The glove's sensitivity to angle of attack means that accurate measurements of the flow are necessary. High accuracy Honeywell PPT and Paroscientific 6000 series transducers have been selected to perform pressure measurements. The design stage uncertainty for the flow angles with these transducers was calculated to be ±0.03º, which is acceptable for controlling to a tolerance of ±0.10 º.

The location of the boom is another important parameter that will require detailed study. The boom should be placed away from regions near the wing that have high gradients. These areas have large changes in local flow conditions that correspond to small changes in aircraft attitude. This will make it difficult to use the probe's outputs to precisely hold the aircraft on a test point. It was found that placing the probe around 18 inches above or below the wing at least three feet in front of the leading edge should provide reasonable measurements. A second five-hole probe mounted to the nose of the aircraft or an analogous system should also be considered for providing calibrated freestream conditions. Two flow data-points make comparing with computational results easier, especially if one is calibrated to infinite freestream conditions.

The dynamic response of the five-hole probe was also analyzed to determine the inner diameter of the pressure tubing required for measuring unsteady fluctuations up to 20 Hz. It was found that a 3/32 inch inner diameter would allow for minimal attenuation up to 20 Hz without allowing the system to become under-damped. The frequency response is highly sensitive to the diameter of the entrance to the tubing and narrowing at the tube's entrance was found to be detrimental to its response characteristics. This point should be considered carefully when sizing the holes at the tip of the five-hole probe. The phase shift introduced by the tubing also influences the accuracy of the unsteady velocity and flow angle measurements. Phase shifts between the signals used to measure angles were found to remain small for all frequencies. However, large shifts between signals occurred for the pressures used for velocity measurement. The five-hole probe should not be used for measuring unsteady flow properties with frequencies higher than several Hertz.

High Frequency Transducers

High frequency measurements of static and total pressure will be made using Kulite XCS-062 pressure transducers. These small transducers have an outer diameter of 0.060 inches and have a frequency response of 200 kHz. Disturbance pressures will be measured by band-pass filtering and amplifying the signals from the Kulites using Endevco 136 filter/amplifier units. A custom Pitot tube was designed for the total pressure transducer and it is proposed that the static pressure Kulite be embedded into the wing glove's surface. An analysis of the frequency responses of the total and static pressure Kulites revealed that both types of transducers should be flush-mounted to the edges of their enclosures. Offsetting the static pressure transducer from the surface of the glove has an especially deleterious effect on the magnitude and phase shift of the pressure measurement.

Thermocouples

Thermocouples are to be installed on the pressure and suction sides of the SARGE glove. These instruments serve to measure surface temperatures and to verify the boundary layer transition location. Type-T thermocouples were selected because they are appropriate for the flight environment and provide the highest accuracy under such conditions.

Hotfilms

Hotfilms will also be installed on the surface of the glove and serve principally to identify transition location through spectral analysis. These hotfilms are to be operated uncalibrated and the qualitative properties of the frequency spectra will be used to verify transition location predicted by the IR camera on the glove's suction-side and establish the transition location on the pressure-side.

Total Temperature

A total temperature measurement is also required in order for Reynolds number to be computed. A total temperature probe can be mounted to either the boom attached to the five-hole probe or elsewhere on the surface of the aircraft.

Surface Roughness

Surface measurements on the glove's surface will also be an important parameter to monitor during the course of the experiment. Surface roughness can be measured by both physical and optical techniques. A

profilometer that drags a fine needle along the surface can be used to spot check small regions on the glove's surface. Optical techniques provide greater ability to establish a more global picture of the surface roughness. Roughness plays an important role along the first 15% of the airfoil and applique DREs are especially sensitive to underlying surface roughness.

B. Heat Transfer

A heat transfer analysis was performed on the glove's surface in order to determine which physical parameters would dictate the characteristics of the IR images. The glove's surface can be painted with any color paint, but black and white were used to establish the extreme ends of the spectrum. Paint emits diffusely and the low viewing angle from the G-III's window will not be an issue. The convection on the surface of the glove was predicted using a three-dimensional similarity solution for the Falkner-Skan-Cooke boundary layer. This method was found to match the skin friction coefficient on the wing to within 3 % of the value predicted by viscous CFD. It is believed that the convection coefficient is predicted to a similar level of accuracy. A bounding case was analyzed in which the convection coefficient on the gloves surface was doubled from that predicted by the similarity solution. The behavior of the surface temperature was found to be nearly identical for these two cases.

One and two-dimensional heat transfer models were developed using a cross-section of the wing glove's recommended construction materials. The one dimensional model was used to predict surface temperatures that the glove could attain by sitting in quiescent air on the ground and also to establish the importance of radiation in the flight environment. It was found that solar radiation has a significant effect on the final surface temperature the glove reaches in flight. A two-dimensional model was produced to account for the temperature gradient along the surface of the glove. It was found that solar radiation would act to warm the laminar region of the glove to a temperature above that of the turbulent region for both black and white gloves. Therefore, it is recommended that the glove's surface be painted black in order to enhance the absorption of solar radiation.

The glove will operate with a warm region beneath the laminar boundary layer. It is important to note that the T-S instability is destabilized by a warm wall. Therefore, the glove should be designed such that

T-S is not a concern for causing transition. Otherwise the glove' boundary layer could be tripped early as its surface is heated.

C. Hotfilm Array Design and Experiment

An array of hotfilms designed to measure traveling waves has also been presented. The hotfilm array uses a minimum of three sensors spaced in a triangular fashion to determine the direction and magnitude of a traveling disturbance. The proposed hotfilms have thirteen sensors arranged such that every sensor is orthogonal to its neighbor and offset in the horizontal and vertical axes. Spectral correlation along with the geometry of the sensor can then be used to determine the velocity of the wave and the equations to accomplish this have been presented. Stationary wave structures can also be determined by measuring phase shifts present in the unsteady content of the signals between each sensor. An experiment to test this hotfilm has been proposed with the FRL's O-2 aircraft and SWIFT test article as the platform.

REFERENCES

Arnal D, Perraud J, Séraudie A. 2008. Attachment line and surface imperfection problems. In *Advances in Laminar-Turbulent Transition Modeling*. VKI Lecture Series. Brussels, Belgium: Von Karman Institute for Fluid Dynamics.

Beckwith IE. 1958. Similar solutions for the laminar boundary layer on a yawed cylinder with transpiration cooling. *NACA Tech. Note 4345*

Belisle MJ, Roberts MW, Tufts MW, Tucker AA, Williams TC, Saric WS, Reed HL. 2011. Design of the subsonic aircraft roughness glove experiment. *AIAA Pap. No. 2011-3524*

Bendat JS, Piersol AG. 1993. *Engineering Applications of Correlation and Spectral Analysis*, pp. 71-72. New York: John Wiley and Sons, Inc. 2nd ed.

Bergh H, Tijdeman H. 1965. Theoretical and experimental results for the dynamic response of pressure measuring systems. *NLR-TR F.318*

Boeing Commercial Airplane Group. 1999. High Reynolds number hybrid laminar flow control flight experiment II. aerodynamic design. *NASA Contract. Rep. 1999-209324*

Braslow AL. 1999. *A History of Suction-Type Laminar Flow Control with Emphasis on Flight Research,* p. 1. Washington, DC: NASA History Division Office of Policy and Plans.

Bruno TJ, Huber M, Laesecke A, Lemmon E, McLinden M Outcalt SL, Perkins R, Smith BL, Widgren JA. 2010. Thermodynamic, transport, and chemical properties of "reference" JP-8. *NISTIR 6659*

Carpenter AL. 2009. *In-flight receptivity experiments on a 30-degree swept-wing using micron-sized discrete roughness elements.* PhD dissertation. Texas A&M University

Cohen CB, Reshotko E. 1956. Similar solutions for the compressible boundary layer with heat transfer and pressure gradient. *NACA Rep. 1293*

Deyhle H, Bippes H. 1996. Disturbance growth in an unstable three-dimensional boundary layer and its dependence on initial conditions. *J. Fluid Mech.* 316:73–113

Deyhle H, Höhler G, Bippes H. 1993. Experimental investigation of instability wave propagation in a 3D boundary-layer flow. *AIAA J.* 31(4):637-45

Figliola RS, Beasley DE. 2006. *Theory and Design for Mechanical Measurement,* pp. 109-340. Hoboken, NJ: John Wiley and Son, Inc. 4th ed.

Fisher D, Horstmann KH, Riedel H, eds. 2003. *Flight Test Measurements Techniques for Laminar Flow,* RTO-AG-300 Vol. 23

Glauser MN, Saric WS, Chapman KL, Reibert MS. 2011. Insight into swept wing boundary-layer transition and turbulent flow physics from multi-point measurements. *AIAA Pap. No. 2011-3076*

Green JE. 2008. Laminar flow control- back to the future?. *AIAA Pap. No. 2008-3738*

Haering EA Jr. 1990. Airdata calibration of a high-performance aircraft for measuring atmospheric wind profiles. *NASA Tech.Memo. 101714*

Haering EA Jr. 1995. Airdata measurement and calibration. *NASA Tech.Memo. 104316*

Haynes TS, Reed HL. 1996. Computations in nonlinear saturation of stationary crossflow vortices in a swept-wing boundary layer. *AIAA Pap. No. 96-0182*

Horstman KH, Redeker G, Quast A. 1990. Flight tests with a natural laminar flow glove on a transport aircraft. *AIAA Pap. No. 90-3044*

Hunt LE. 2011. *Boundary-layer receptivity to three-dimensional roughness arrays on a swept wing*. PhD dissertation. Texas A&M University

Incropera FD, DeWitt DP, Bergman TL, Lavine AS. 2007. *Fundamentals of Heat and Mass Transfer*, pp. 1-774. Hoboken, NJ: John Wiley and Son, Inc. 6th ed.

Keller B, Costa AMS. 2009. A Matlab GUI for calculating the solar radiation and shading of surfaces on the Earth. *Computer Applications in Engineering Education*. 19(1):161-70

Mack LM. 1984. Boundary-layer linear stability theory. *AGARD Report No. 709*

Malik M, Liao W, Lee-Rausch E, Li F, Choudhari M, Chang C-L. Computational analysis of the G-III laminar flow glove. *AIAA Pap. No. 2011-3525*

Mangalam SM, Maddalon DV, Saric WS, Agarwal NK. 1990. Measurement of crossflow vortices, attachment-line flow, and transition using micro-thin hot films. *AIAA Pap. No. 90-1636*

McKeon BJ. 2007. Measurement of pressure with wall tappings. In *Springer Handbook of Experimental Fluid Mechanics*, ed. C. Tropea, A. Yarin, J.F. Foss, pp. 179-87. Heidelberg: Springer-Verlag

McKnight CW. 2006. *Design and safety analysis of an in-flight test airfoil*. MS thesis. Texas A&M University

Morkovin, MV. 1969. Critical evaluation of transition from laminar to turbulent shear layers with emphasis on hypersonically traveling bodies. *Air Force Flight Dyn. Lab. Rep. AFFDL-TR-68-149*

Morkovin MV, Reshotko E, Herbert T. 1994. Transition in open flow systems- a reassessment. *Bull. Am. Phys. Soc.* 39(9):1-31

Pfenninger W. 1977. Laminar flow control-laminarization. *AGARD Rep. 654: Spec. Course on Drag Reduct.* 1: 3-1 – 75

Quast A. 1987. Detection of transition by infrared image technique. *ICIASF Proc.*, Williamsburg, VA

Pupator PT, Saric WS. 1989. Control of random disturbances in a boundary layer. *AIAA Pap. No.89-1007*

Radeztsky RH Jr, Reibert MS, Saric WS. 1999. Effect of isolated micron-sized roughness on transition in swept-wing flows. *AIAA J.* 37(11):1370-77

Radeztsky RH Jr, Reibert MS, Saric WS, Takagi S. 1993. Effect of micron-sized roughness on transition in swept-wing flows. *AIAA Pap. No. 93-0076*

Reed HL, Saric WS. 2008. Transition mechanisms for transport aircraft. *AIAA Pap. No. 2008-3743*

Reibert MS, Saric WS. 1997. Review of swept-wing transition. *AIAA Pap. No. 1997-1816*

Reibert MS, Saric WS, Carrillo RB Jr., Chapman KL. 1996. Experiments in nonlinear saturation of stationary crossflow vortices in a swept-wing boundary layer. *AIAA Pap. No. 96-0184*

Reshotko E. 1978. Heated boundary layers. *Proc. 12th Symp. on Nav. Hydrodyn.,* Washington, DC

Reshotko E. 1979. Drag reduction by cooling in hydrogen-fueled aircraft. *J. Aircr.* 16(9):584-90

Reshotko E. 1984. Laminar flow control – viscous simulation. *AGARD Rep. No. 709*

Reshotko E. 1985. Control of boundary layer transition. *AIAA Pap. No.85-05602*

Riedel H, Sitzmann M. 1997. In-flight investigations of atmospheric turbulence. *Aero. Sci. Tech.* 5:301-19

Rhodes RG. 2008. *Computations of laminar flow control on swept wings as a companion to flight test research.* MS thesis. Texas A&M University.

Rhodes RG, Carpenter AL, Reed HL, Saric WS. 2008. CFD analysis of flight-test configuration for LFC on swept wings. *AIAA Pap. No. 2008-7336*

Saric WS. 1994. Görtler vortices. *Ann. Rev. Fluid Mech.* 26:379-409

Saric WS, Carpenter AL, Reed HL. 2011. Passive control of transition in three-dimensional boundary layers, with emphasis on discrete roughness elements. *Phil. Trans. R. Soc. A* 369:1352-64

Saric WS, Carrillo RB, Reibert MS. 1998. Leading-edge roughness as a transition control mechanism. *AIAA Pap. No. 98-0781*

Saric WS, Reed HL, White EB. 2003. Stability and transition of three-dimensional boundary layers. *Ann. Rev. Fluid Mech.* 35:413-40

Saric WS, White EB. 1998. Influence of high-amplitude noise on boundary-layer transition to turbulence. *AIAA Pap. No. 98-2645*

Task Group SCI-026. 2000. Flight control design – best practices. *RTO-TR-029*

Thomas AS. 1983. Control of boundary layer transition using a wave-superimposed principle. *J. Fluid Mech.* 137:233-50

White EB, Saric WS. 2005. Secondary instability of crossflow vortices. *J. Fluid Mech.* 525:275-308

White EB, Saric WS, Gladden RD, Gabet PM. 2001. Stages of swept-wing transition. *AIAA Pap. No. 2001-0271*

Wuest W. 1980. Pressure and flow measurement. In *AGARD Flight Test Instrumentation Series*, Vol. 11, pp. 21-39, AGARD AG-160

Zeiger M. 2011. Manufacturing, calibration, and applications process summary. *Hill AFB Rep.*

APPENDIX A

INFRARED CAMERA IMAGE QUALITY CALCULATIONS

A-1: Camera Resolution Calculation Script

This script is used to calculate the SC8000 camera's resolution of the glove's surface in units of mm/pixel in Matlab. The wing is assumed to be a horizontal plane and the wing's lines of constant span are assumed to be perpendicular to the camera's line of sight. Input parameters are the viewing angle and total distance to the focal point at the center of the glove as well as the resolution of the camera.

```
%Resolution calculator to determine the spanwise extent of a single pixel
%based on IR camera resolution and lens selection.

clear all
clc

res = 1024; % camera resolution along axis of interest (pixels)
fovv = 20.9; % lens field of view along axis of interst, deg
fovh = 20.9; %lens horizontal field of view, deg
phi = 75; % angle between surface normal vector and camera vector
d = 196*25.4; %distance from camera to focal point on object, mm

dat = zeros(res,2); %initialization of data collection matrix
n = 1; %placeholder for data entry
L=0; %placeholder for glove span (mm)

%Loop to calculate resolution on outboard half of glove
for theta = fovv/res:fovv/res:fovv/2

    dat(n,2) = d*sind(theta)/sind(90-theta-phi)-d*sind(theta-
fovv/res)/(sind(90-phi-(theta-fovv/res))); %resolution at each angle interval,
mm
    dat(n,1) = dat(n,2)+L; % glove span, mm
    L = dat(n,1);
    n=n+1;

end

if abs(dat(n-1,1))>3600*25.4
    %     [r c]=find(dat(:,1)>=36*25.4,1,'first');
    %     L1 = dat(r,c);
    L1=10000;
else
    L1 = dat(n-1,1);
end

L=0; %placeholder for glove span (mm)

%Loop to calculate resolution on inboard half of glove
for theta = fovv/res:fovv/res:fovv/2

    dat(n,2) = d*sind(theta)/sind(90-theta+phi)-d*sind(theta-
fovv/res)/(sind(90+phi-(theta-fovv/res))); %resolution at each angle interval,
mm
    dat(n,1) = -dat(n,2)+L; % glove span, mm
    L = dat(n,1);
```

```
    n=n+1;

end

% if dat(n-1,1)<-36*25.4
%     [r c]=find(dat(:,1)<=-36*25.4,1,'first');
%     L2 = dat(r,c);
% else
L2 = dat(n-1,1);
% end

%% Plotting Module

hold on
plot(dat(:,1)/25.4,dat(:,2),'b.');
plot(-36,0:.01:30,'r.');
plot(36,0:.01:30,'r.');
% plot(-36,2.5:.01:6,'r.');
% plot(36,2.5:.01:6,'r.');

title('Camera Resolution as a Function of Span, SC8000 17 mm Lens')
xlabel('Distance from Glove Centerline, inches')
ylabel('Span per Pixel, mm')
grid on
legend('Resolution','Glove Spanwise Extent')
axis([-40 40 0 30])

%% Chordwise resolution calculator

if abs(L1)<36
    wf = 2*abs(L1)*sind(90+phi)/sind(fovv/2)*tand(fovh/2)/25.4 %outboard width
of view, inches
else
    psi = atand(d*sind(90-phi)/(d*cosd(90-phi)+36*25.4));
    w2 = 90-phi-psi;
    A2 = sqrt((d*sind(90-phi))^2+(d*cosd(90-phi)+36*25.4)^2);
    wf = 2*A2/25.4*cosd(w2)*tand(fovh/2) %outboard width of view, inches
end

if abs(L2)<36
    wn = 2*abs(L2)*sind(90-phi)/sind(fovv/2)*tand(fovh/2)/25.4 %inboard width
of view, inches
else
    A1 = sqrt((d*cosd(90-phi)-36*25.4)^2+(d*sind(90-phi))^2);
    w1 = asind(36*25.4*sind(90-phi)/A1);
    wn = 2*A1/25.4*cosd(w1)*tand(fovh/2) %inboard width of view, inches
end

hresn = wn*25.4/1024 % mm/pixel resolution in chordwise direction, inboard
hresf = wf*25.4/1024 % mm/pixel resolution in chordwise direction, outboard
```

A-2: Camera Depth of Focus

The following Matlab script is used to calculate the SC8000's depth of focus when focused on the center of the wing glove. Again, the wing is approximated as a horizontal plane with the camera's line of sight perpendicular to lines of constant span. The inputs to the script are the distance to the object being focused, the f-number of the lens being used, and the camera's circle of confusion. The SC8000's circle of confusion is assumed to be twice the camera's pixel pitch of 0.018 mm. This means that any object within the computed depth of focus will be imaged at the highest clarity possible given the camera's resolution and pixel size.

```
clear all
clc

s = 196*25.4; %mm, distance to object
c = .036; %mm, circle of confusion
N = 4; % lens f number

dof = zeros(5,5); % [lens focal length, hyperfocal distance, depth of field,
DN, DF]
dof(1,1) = 17; %mm, focal length
dof(2,1) = 25; %mm, focal length
dof(3,1) = 50; %mm, focal length
dof(4,1) = 100; %mm, focal length
dof(5,1) = 200; %mm, focal length

[row col] = size(dof);

for i =1:row

    dof(i,2) = dof(i,1)^2/(N*c); %mm, hyperfocal distance
    dof(i,4) = dof(i,2)*s/(dof(i,2)+s); %mm, near focus distance

    if s<dof(i,2)
        dof(i,3) = 2*N*c*s^2*dof(i,1)^2/(dof(i,1)^4-N^2*c^2*s^2); %mm, depth of
field
        dof(i,5) = dof(i,2)*s/(dof(i,2)-s); %mm, far focus distance
    else
        dof(i,3) = 0; %mm, depth of field (use 0 to represent infinite depth
past Dn)
        dof(i,5) = 0; %mm, far focus distance (use 0 to represent infinity)
    end
end

dofm = dof(:,3)/1000 %depth of field, m
dnm = dof(:,4)/1000 % near focus distance, m
dfm = dof(:,5)/1000 % far focus distance, m
hfocm = dof(:,2)/1000 %hyperfocal distance, m
dof_eng = dof(:,3)/1000/.3048*12 %in, dof
dn_eng = dnm/.3048*12 % near focus distance, in
```

```
df_eng = dfm/.3048*12 % far focus distance, in

results = zeros(5,8); %[ lens focal length (mm), depth of field (m), depth of
field (in), near focus distance (m), near focus distance (in), far focus
distance (m), far focus distance (in), hyperfocal distance (m)]
results(:,1) = dof(:,1);
results(:,2) = dofm;
results(:,3) = dof_eng;
results(:,4) = dnm;
results(:,5) = dn_eng;
results(:,6) = dfm;
results(:,7) = df_eng;
results(:,8) = hfocm;

results

save 'DOF_calculations.txt' results -ASCII -double -tabs % saves into 16 digit
ascII .txt file
```

APPENDIX B

FIVE-HOLE PROBE UNCERTAINTY ANALYSIS

A. Motivation

The uncertainty in the five-hole probe's measurements is important to understand because it has a significant impact on the pilots' ability to hold tight angle of attack tolerances. The five-hole probe will be used to make differential measurements between a reference angle of attack and the current aircraft angle of attack to determine whether or not the aircraft is operating within the acceptable data band. The reference angle of attack will be set by correlating five-hole probe readings to pressure distributions on the wing measured by static pressure ports. This technique means that the probe's absolute reading is arbitrary so long as the ends of the data band are correlated to the readings of the probe.

The current flight test plan eliminates several significant sources of uncertainty typically present in freestream air-data measurements. First, alignment of the probe is not important so long as its readings are correlated to surface pressure distributions. This means that bias errors due to installation will be absent. Also, the bending of the probe and its support boom is negligible because all measurements will be taken within approximately 1º aircraft AoA. Therefore, the bending of the structure should not change significantly within the AoA data band. The only exception to this would be if the probe were mounted with the entirety of its structure within a region of high gradients near the wing. The change in local angle of attack at the probe should be computed during the design stage to verify that the loads on the boom stay relatively constant within the data band.

The current uncertainty analysis assumes that all bias error due to uncertainty in position and structural bending are eliminated by the experiment's test plan. Thus, only random errors were considered in the following analysis. The uncertainty analysis procedure was adapted from an Aeroprobe uncertainty analysis (Zeiger 2011) prepared for Hill Air Force Base's five-hole probe.

B. Propagation of Error

The uncertainties of parameters determined from a composition of individual measurements are a result of the propagation of error from each input. Consider a result, R, which is a function of the variables x_1, $x_2, x_3, \ldots, x_L$.

$$R = f\left(x_1, x_2, x_3, ..., x_L\right) \tag{B-1}$$

The true value of R lies within a band of uncertainty, $\pm u_R$, at some probability, *P%*, which is also a function of the variables x_1, x_2, x_3,…, x_L. The value of u_R can be estimated using Eqn (B-2).

$$u_R = \pm \left[\sum_{i=1}^{L} \left(\frac{\partial R}{\partial x_i} u_{x_i} \right)^2 \right]^{1/2} (P\%) \tag{B-2}$$

Angle of Attack Coefficient

A pseudo-dynamic pressure, $P_{1\text{-}6}$, can be defined as the pressure difference between the probe's center port and its static ring. The angle of attack coefficient, C_α, is then calculated using the pressure difference between the upper and lower ports, $P_{4\text{-}5}$, as shown in Eqn (B-3).

$$C_\alpha = \frac{P_{4-5}}{P_{1-6}} \tag{B-3}$$

The uncertainty in angle of attack coefficient is a result of the propagation of errors in pressures $P_{1\text{-}6}$ and $P_{4\text{-}5}$. This expression is shown in Eqn (B-4).

$$\Delta C_\alpha = \sqrt{\left[\frac{1}{P_{1-6}}\right]^2 \left(\Delta P_{4-5}\right)^2 + \left[\frac{-P_{4-5}}{P_{1-6}^2}\right]^2 \left(\Delta P_{1-6}\right)^2} \tag{B-4}$$

Sideslip Angle Coefficient

The probe's sideslip angle coefficient, C_β, can be defined in a similar manner as the angle of attack coefficient as shown in Eqn (B-3). Here $P_{2\text{-}3}$ is the pressure difference between the probe's lateral holes. The uncertainty in sideslip coefficient can likewise be calculated, as shown in Eqn (B-14).

$$C_\beta = \frac{P_{2-3}}{P_{1-6}} \tag{B-5}$$

$$\Delta C_\beta = \sqrt{\left[\frac{1}{P_{1-6}}\right]^2 \left(\Delta P_{2-3}\right)^2 + \left[\frac{-P_{2-3}}{P_{1-6}^2}\right]^2 \left(\Delta P_{1-6}\right)^2} \tag{B-6}$$

Dynamic Pressure Coefficient

The dynamic pressure measured by the probe has a weak dependence on angle of attack. This dependence can be quantified during the probe calibration process using the dynamic pressure coefficient defined in Eqn (B-7). Here, $P_{T\text{-}S}$ is the difference between the calibration tunnel's total and static pressures measured by another source. The uncertainty of dynamic pressure coefficient measurement is then given by Eqn (B-8).

$$C_q = \frac{P_{T-S}}{P_{1-6}} \tag{B-7}$$

$$\Delta C_q = \sqrt{\left[\frac{1}{P_{1-6}}\right]^2 \left(\Delta P_{T-S}\right)^2 + \left[\frac{-P_{T-S}}{P_{1-6}^2}\right]^2 \left(\Delta P_{1-6}\right)^2} \tag{B-8}$$

The magnitude of this variation is negligible at low flow angles and has been ignored in the remaining analysis.

Angle of Attack Calibration Curve Slope

The linear calibration curve slope is determined by plotting the flow angle coefficients versus the actual flow angle for at least 20 points over the range of angles of interest. A line is then fitted through the points in order to calculate the calibration curve slope. This process reduces the influence of scatter in the individual data points. Uncertainty in the angle coefficients as well as uncertainty in actual flow angles contributes to the overall uncertainty. Typically, the actual flow angle is measured using an inclinometer. The digital inclinometer that has been used by Aeroprobe for past calibrations has an uncertainty of 0.003°. Here, the angle uncertainty due to the inclinometer has been represented as $\Delta\alpha$ and $\Delta\beta$ for angles of attack and sideslip respectively.

The uncertainty in the slope of the calibration curve is conservatively estimated as the difference between the highest possible slope and the average slope. The highest slope is attained when the uncertainties in the curve's endpoints coalesce to form the steepest line. A typical value of K_α and K_β for conical probes is 0.060 deg^{-1}, and this value has been used for the following analysis.

Eqn (B-9) is used to calculate the slope of the line connecting the endpoints of the angle of attack calibration curve, $(\alpha_1, C_{\alpha,1})$ and $(\alpha_2, C_{\alpha,2})$.

$$K_\alpha = \frac{C_{\alpha,2} - C_{\alpha,1}}{(\alpha_2 - \alpha_1)} \tag{B-9}$$

The steepest possible slope is computed using Eqn (B-10).

$$K_{\alpha,max} = \frac{(C_{\alpha,2} + \Delta C_\alpha) - (C_{\alpha,1} - \Delta C_\alpha)}{(\alpha_2 - \Delta\alpha) - (\alpha_1 + \Delta\alpha)} = \frac{K_\alpha + \frac{2\Delta C_\alpha}{(\alpha_2 - \alpha_1)}}{1 - \frac{2\Delta C_\alpha}{(\alpha_2 - \alpha_1)}} \tag{B-10}$$

The uncertainty in the angle of attack calibration curve slope is then given by Eqn (B-11).

$$\Delta K_\alpha = K_{\alpha,\max} - K_\alpha \tag{B-11}$$

Angle of Sideslip Calibration Curve Slope

An analogous procedure is used to calculate the uncertainty in the angle of sideslip calibration curve slope. This process is done using Eqn (B-12) through Eqn (B-25).

$$K_\beta = \frac{C_{\beta,2} - C_{\beta,1}}{(\beta_2 - \beta_1)} \tag{B-12}$$

$$K_{\beta,max} = \frac{(C_{\beta,2} + \Delta C_\beta) - (C_{\beta,1} - \Delta C_\beta)}{(\beta_2 - \Delta\beta) - (\beta_1 + \Delta\beta)} = \frac{K_\beta + \frac{2\Delta C_\beta}{(\beta_2 - \beta_1)}}{1 - \frac{2\Delta C_\alpha}{(\beta_2 - \beta_1)}} \tag{B-13}$$

$$\Delta K_\beta = K_{\beta,\max} - K_\beta \tag{B-14}$$

Angle of Attack Zero-Offset Uncertainty

The calibration of the five-hole probe begins by aligning the probe with the freestream. This is accomplished by doing two sweeps in both the angle of attack and angle of sideslip. The first sweep in either direction is done with the probe in the upright position and then the probe is rotated 180° and the process is repeated for a second sweep. The angle coefficient versus angle plots of the upright and inverted curves intersect at the location of the zero-offset angles. The probe is the repositioned in order to eliminate this offset before the balance of the pitch and yaw calibrations are completed.

The subscripts *u* and *i* denote upright and inverted positions, respectively, in the following equations. The angle of attack coefficient of the misaligned probe is calculated using Eqn (B-15), which is applicable to both the upright and inverted configurations.

$$C_{\alpha,i} = C_{\alpha,0,i} + K_{\alpha,i}\alpha \tag{B-15}$$

The zero-offset angle of attack can then be computed using Equation (B-16).

$$\alpha_0 = \frac{C_{\alpha,0,u} - C_{\alpha,0,i}}{K_{\alpha,i} - K_{\alpha,u}} \tag{B-16}$$

The square of the zero-offset angle of attack uncertainty due to the probe can be written as shown in Eqn (B-17).

$$\Delta\alpha_{0,p}^2 = \left[\frac{\partial\alpha_0}{\partial C_{\alpha,0,u}}\right]^2 \left(\Delta C_{\alpha,0,u}\right)^2 + \left[\frac{\partial\alpha_0}{\partial C_{\alpha,0,i}}\right]^2 \left(\Delta C_{\alpha,0,i}\right)^2 + \left[\frac{\partial\alpha_0}{\partial K_{\alpha,i}}\right]^2 \left(\Delta K_{\alpha,i}\right)^2 \left[\frac{\partial\alpha_0}{\partial K_{\alpha,u}}\right]^2 \left(\Delta K_{\alpha,u}\right)^2 \tag{B-17}$$

The derivatives in the third and fourth terms of Equation (B-18) are of the form:

$$\frac{d\alpha_0}{dK_{\alpha,i}} = -\frac{\left(C_{\alpha,0,u} - C_{\alpha,0,i}\right)}{\left(K_{\alpha,i} - K_{\alpha,u}\right)^2} = -\frac{\alpha_0}{\left(K_{\alpha,i} - K_{\alpha,u}\right)} \tag{B-18}$$

Eqn (B-18) can be consolidated by recognizing that the zero-offset angle is small compared to the slopes of the upright and inverted curves.

$$\alpha_0 << \left(K_{\alpha,i} - K_{\alpha,u}\right) \tag{B-19}$$

This leads to the following simplifying assumption:

$$\frac{\partial\alpha_0}{\partial K_{\alpha,i}} = -\frac{\partial\alpha_0}{\partial K_{\alpha,u}} \approx 0 \tag{B-20}$$

Additionally, the uncertainty in the zero-offset angle of attack coefficient can be assumed to be equal to the uncertainty of the angle of attack coefficient.

$$\Delta C_{\alpha,0,u} = \Delta C_{\alpha,0,i} \approx \Delta C_{\alpha} \tag{B-21}$$

Also, the slopes of the upright and inverted curves can be assumed to be equal in magnitude and opposite in sign.

$$K_{\alpha} = K_{\alpha,u} = -K_{\alpha,i} \tag{B-22}$$

Applying these simplifying assumptions reduces Eqn (B-23) to the following:

$$\Delta\alpha_{0,p} = \sqrt{\left[\frac{1}{K_{\alpha,i} - K_{\alpha,u}}\right]^2 \left(\Delta C_{\alpha}\right)^2 + \left[\frac{-1}{K_{\alpha,i} - K_{\alpha,u}}\right]^2 \left(\Delta C_{\alpha}\right)^2} = \sqrt{2\left[\frac{1}{2K_{\alpha}}\right]^2 \left(\Delta C_{\alpha}\right)^2} \tag{B-23}$$

The overall error in zero-offset angle of attack is a combination of the uncertainty caused by the probe's pressure measurements and the uncertainty in the inclinometer's reference angle readings.

$$\Delta\alpha_0 = \sqrt{\left(\Delta\alpha_{0,p}\right)^2 + \left(\Delta\alpha\right)^2} \tag{B-24}$$

Angle of Sideslip Zero Offset Uncertainty

The uncertainty in the zero-offset angle of sideslip can be found in a manner analogous to the zero-offset angle of attack. This calculation is performed using Eqn (B-25) through Eqn (B-29).

$$K_{\beta} = \frac{C_{\beta,2} - C_{\beta,1}}{\left(\beta_2 - \beta_1\right)} \tag{B-25}$$

$$\beta_0 = \frac{C_{\beta,0,u} - C_{\beta,0,i}}{K_{\beta,i} - K_{\beta,u}} \tag{B-26}$$

$$\Delta\beta_{0,p}^2 = \left[\frac{\partial\beta_0}{\partial C_{\beta,0,u}}\right]^2 \left(\Delta C_{\beta,0,u}\right)^2 + \left[\frac{\partial\beta_0}{\partial C_{\beta,0,i}}\right]^2 \left(\Delta C_{\beta,0,i}\right)^2 + \left[\frac{\partial\beta_0}{\partial K_{\beta,i}}\right]^2 \left(\Delta K_{\beta,i}\right)^2 \left[\frac{\partial\beta_0}{\partial K_{\beta,u}}\right]^2 \left(\Delta K_{\beta,u}\right)^2 \tag{B-27}$$

$$\frac{\partial\beta_0}{\partial K_{\beta,i}} = \frac{-\left(C_{\beta,0,u} - C_{\beta,0,i}\right)}{\left(K_{\beta,i} - K_{\beta,u}\right)^2} = \frac{-\beta_0}{K_{\beta,i} - K_{\beta,u}} \tag{B-28}$$

$$\frac{\partial\beta_0}{\partial K_{\beta,u}} = \frac{\left(C_{\beta,0,u} - C_{\beta,0,i}\right)}{\left(K_{\beta,i} - K_{\beta,u}\right)^2} = \frac{\beta_0}{K_{\beta,i} - K_{\beta,u}} \tag{B-29}$$

The simplifying assumptions shown in Eqn (B-30) through Eqn (B-33) are made in the same fashion as those used for angle of attack.

$$\beta_0 << \left(K_{\beta,i} - K_{\beta,u}\right) \tag{B-30}$$

$$\frac{\partial \beta_0}{\partial K_{\beta,i}} = -\frac{\partial \beta_0}{\partial K_{\beta,u}} \approx 0 \tag{B-31}$$

$$\Delta C_{\beta,0,u} = \Delta C_{\beta,0,i} \approx \Delta C_\beta \tag{B-32}$$

$$K_\beta = K_{\beta,u} = -K_{\beta,i} \tag{B-33}$$

The sideslip angle's zero-offset uncertainty caused by probe's pressure measurements is given by Eqn (B-34).

$$\Delta\beta_{0,p} = \sqrt{\left[\frac{1}{K_{\beta,i} - K_{\beta,u}}\right]^2 \left(\Delta C_\beta\right)^2 + \left[\frac{-1}{K_{\beta,i} - K_{\beta,u}}\right]^2 \left(\Delta C_\beta\right)^2} = \sqrt{2\left[\frac{1}{2K_\beta}\right]^2 \left(\Delta C_\beta\right)^2} \tag{B-34}$$

The total zero-offset uncertainty in angle of sideslip is equal to the square root of the sum of the squares of the probe's uncertainty and the inclinometer's uncertainty, as in the case with angle of attack.

$$\Delta\beta_0 = \sqrt{\left(\Delta\beta_{0,p}\right)^2 + \left(\Delta\beta\right)^2} \tag{B-35}$$

It is important to note that uncertainties in the zero-offset angles of attack and sideslip due to the probe's mounting structure have been ignored. If the probe were to be used to measure absolute angles this uncertainty would need to be included. However, the probe on the SARGE project will act as a differential measurement tool. The SARGE probe's outputs will be calibrated with respect to a particular flight condition, thus systematic errors in the probe's measurement will be eliminated during this in-flight calibration process. The errors due to mounting misalignment are bias errors and will not affect the probe's accuracy with respect to differential measurements. However, it is important to include random errors in the zero-offset angles such as those due to pressure measurements or the inclinometer used during initial calibration.

Angle of Attack Uncertainty

The probe's angle of attack is given by Eqn (B-36). The total angle of attack uncertainty can then be calculated using Eqn (B-37).

$$\alpha = \alpha_0 + \frac{C_\alpha}{K_\alpha} \tag{B-36}$$

$$\Delta\alpha = \sqrt{\left(\Delta\alpha_0\right)^2 + \left[\frac{1}{K_\alpha}\right]^2 \left(\Delta C_\alpha\right)^2 + \left[\frac{-C_\alpha}{K_\alpha^2}\right]^2 \left(\Delta K_\alpha\right)^2} \tag{B-37}$$

Angle of Sideslip Uncertainty

The uncertainty in angle of sideslip can be computed similarly using Eqn (B-38) and Eqn (B-39).

$$\beta = \beta_0 + \frac{C_\beta}{K_\beta} \tag{B-38}$$

$$\Delta\beta = \sqrt{\left(\Delta\beta_0\right)^2 + \left[\frac{1}{K_\beta}\right]^2 \left(\Delta C_\beta\right)^2 + \left[\frac{-C_\beta}{K_\beta^2}\right]^2 \left(\Delta K_\beta\right)^2} \tag{B-39}$$

Total Pressure Uncertainty

The total pressure measured by the five-hole probe is computed by adding the differential pressure between port 1 and the static ring (port 6) to the static pressure measured at port 6 by the absolute pressure transducer. The uncertainty is estimated using Eqn (B-41).

$$P_T = P_6 + P_{1-6} \tag{B-40}$$

$$\Delta P_T = \sqrt{\Delta P_6^2 + \Delta P_{1-6}^2} \tag{B-41}$$

Static Pressure Uncertainty

The static pressure uncertainty is simply the uncertainty quoted for the absolute transducer used to measure the static ring's pressure.

$$\Delta P_S = \Delta P_6 \tag{B-42}$$

Mach Number Uncertainty

The local Mach number at the five-hole probe is calculated using the pressure difference between the center port and the static pressure ring. The isentropic flow equation for Mach number with respect to these pressures is shown in Eqn (B-43).

$$M = \sqrt{\frac{2}{\gamma - 1}\left[\left(\frac{P_T}{P_S}\right)^{\frac{\gamma-1}{\gamma}} - 1\right]} \tag{B-43}$$

The square of the uncertainty in Mach number is then calculated using Eqn (B-44).

$$\Delta M^2 = \left[\frac{dM}{dP_T}\right]^2 \left(\Delta P_T\right)^2 + \left[\frac{dM}{dP_S}\right]^2 \left(\Delta P_S\right)^2 \tag{B-44}$$

The derivatives in Eqn (B-44) are then computed as shown in Eqn (B-45) and Eqn (B-46).

$$\frac{dM}{dP_T} = \frac{1}{2}\left[\frac{2}{\gamma - 1}\left(\frac{P_T}{P_S}\right)^{\frac{\gamma-1}{\gamma}} - \frac{2}{\gamma - 1}\right]^{-\frac{1}{2}} \left(\frac{2}{\gamma}\right)\left(\frac{P_T}{P_S}\right)^{\left(\frac{\gamma-1}{\gamma}-1\right)} \left(\frac{1}{P_S}\right) \tag{B-45}$$

$$\frac{dM}{dP_S} = \frac{1}{2}\left[\frac{2}{\gamma - 1}\left(\frac{P_T}{P_S}\right)^{\frac{\gamma-1}{\gamma}} - \frac{2}{\gamma - 1}\right]^{-\frac{1}{2}} \left(\frac{2}{\gamma}\right)\left(\frac{P_T}{P_S}\right)^{\left(\frac{\gamma-1}{\gamma}-1\right)} \left(\frac{-P_T}{P_S^2}\right) \tag{B-46}$$

Eqn (B-44), Eqn (B-45), and Eqn (B-46) are then combined to calculate the Mach number uncertainty, as shown in Eqn (B-47).

$$\Delta M = \sqrt{\begin{array}{l}\left(\frac{1}{2}\left[\frac{2}{\gamma - 1}\left(\frac{P_T}{P_S}\right)^{\frac{\gamma-1}{\gamma}} - \frac{2}{\gamma - 1}\right]^{-\frac{1}{2}} \left(\frac{2}{\gamma}\right)\left(\frac{P_T}{P_S}\right)^{\left(\frac{\gamma-1}{\gamma}-1\right)} \left(\frac{1}{P_S}\right)\right)^2 (\Delta P_T)^2 + \\ \left(\frac{1}{2}\left[\frac{2}{\gamma - 1}\left(\frac{P_T}{P_S}\right)^{\frac{\gamma-1}{\gamma}} - \frac{2}{\gamma - 1}\right]^{-\frac{1}{2}} \left(\frac{2}{\gamma}\right)\left(\frac{P_T}{P_S}\right)^{\left(\frac{\gamma-1}{\gamma}-1\right)} \left(\frac{-P_T}{P_S^2}\right)\right)^2 (\Delta P_S)^2\end{array}} \tag{B-47}$$

Reynolds Number Uncertainty

Reynolds number is calculated using the static pressure and Mach number measured by the five-hole probe and the total temperature measured by the total temperature probe. Mach number is calculated using Eqn (B-48) as shown above. Static temperature is then calculated using the Mach number and the isentropic flow relationship for static and total temperature.

$$T_S = T_0 \left(1 + \frac{\gamma - 1}{2} M^2 \right)^{-1} \tag{B-48}$$

Density can then be calculated from static pressure and temperature using the ideal gas law.

$$\rho = \frac{P_S}{T_0 R} \left(1 + \frac{\gamma - 1}{2} M^2 \right) \tag{B-49}$$

Freestream velocity is computed using Mach number and stagnation temperature as shown in Eqn (B-50).

$$U_\infty = M \sqrt{\frac{\gamma R T_0}{\left(1 + \frac{\gamma - 1}{2} M^2 \right)}} \tag{B-50}$$

The freestream viscosity is calculated using the static temperature in conjunction with Sutherland's Law. This expression is shown in Eqn (B-51).

$$\mu = \mu_0 \frac{T_C + C}{T_S + C} \left(\frac{T_S}{T_C} \right)^{3/2} \tag{B-51}$$

Here, $\mu_0 = 17.16(10)^{-6}$ kg/m-s, $C = 110.56$ K, and $T_C = 273.11$ K. Eqn (B-48) can be substituted into Eqn (B-51) so as to make viscosity a function of stagnation temperature and Mach number as shown in Eqn (B-52).

$$\mu = \mu_0 \left(\frac{T_C + C}{T_0 \left(1 + \frac{\gamma - 1}{2} M^2 \right)^{-1} + C} \right) \left(\frac{T_0 \left(1 + \frac{\gamma - 1}{2} M^2 \right)^{-1}}{T_C} \right)^{3/2} \tag{B-52}$$

Reynolds number can then be written as a combination of Eqn (B-49), Eqn (B-50), and Eqn (B-52).

$$\mathrm{Re} = \frac{\frac{P_S}{T_0 R} M \sqrt{\gamma R T_0 \left(1 + \frac{\gamma - 1}{2} M^2\right)} L}{\mu_0 \left(\frac{273.11 + 110.56}{T_0 \left(1 + \frac{\gamma - 1}{2} M^2\right)^{-1} + 110.56} \right) \left(\frac{T_0 \left(1 + \frac{\gamma - 1}{2} M^2\right)^{-1}}{273.11} \right)^{3/2}} \tag{B-53}$$

Here, L is a reference length. In the case of the SARGE project, L would be the mid-span chord length of the wing glove. Eqn (B-53) shows that Reynolds number can be written as a function of Mach number, static pressure, stagnation temperature, and reference length as shown below.

$$\mathrm{Re} = f\left(P_S, M, T_0, L\right) \tag{B-54}$$

For the purposes of initial uncertainty analysis, the reference length, L, will be assumed to be a constant with zero uncertainty.

Unfortunately, taking derivatives of Eqn (B-53) for M and T_0 is difficult to do analytically. Fortunately, the numerical method of sequential perturbation can be used to approximate the propagation of uncertainty through Reynolds number without taking derivatives. The analysis begins by calculating a value of Reynolds number at some fixed operating condition. This value is termed Re_0. Next, each independent variable is individually increased by its uncertainty and a new value of Reynolds number is calculated.

$$Re_1^+ = f\left(P_S + u_{P_S}, M, T_0, L\right) \tag{B-55}$$

$$Re_2^+ = f(P_S, M + u_M, T_0, L) \tag{B-56}$$

$$Re_3^+ = f\left(P_S, M, T_0 + u_{T_0}, L\right) \tag{B-57}$$

In the same manner as in Eqn (B-55) through Eqn (B-57), the independent variables are then decreased by their uncertainties and a new Reynolds number is calculated.

$$Re_1^- = f\left(P_S - u_{P_S}, M, T_0, L\right) \tag{B-58}$$

$$Re_2^- = f(P_S, M - u_M, T_0, L) \tag{B-59}$$

$$Re_3^- = f\left(P_S, M, T_0 - u_{T_0}, L\right) \tag{B-60}$$

Next, the differences between the fixed condition Reynolds number and the perturbation Reynolds number are calculated. In the following equations i = 1, 2, 3.

$$\delta Re_i^+ = Re_i^+ - Re_0 \tag{B-61}$$

$$\delta Re_i^- = Re_i^- - Re_0 \tag{B-62}$$

The uncertainty contribution of each variable is then estimated using Eqn (B-63).

$$\delta \mathrm{Re}_i = \frac{\delta \mathrm{Re}_i^+ - \delta \mathrm{Re}_i^-}{2} \tag{B-63}$$

Finally, the total Reynolds number uncertainty is calculated using Eqn (B-64).

$$u_{\mathrm{Re}} = \pm \left[\sum_{i=1}^{3} \left(\delta \mathrm{Re}_i \right)^2 \right]^{1/2} (P\%) \tag{B-64}$$

This method yields nearly identical results to the analytical propagation of error equations presented previously (Figliola & Beasley 2006).

APPENDIX C

BOUNDARY LAYER SIMILARITY SOLUTIONS WITH HEAT TRANSFER

C-1: Stewartson's Transformation for X and U_e

The Matlab script contained within this appendix is used to transform the arc length along the airfoil's surface and the edge velocity along the wing using Stewartson's transformation. This transformation allows the compressible Falkner-Skan boundary layer to be solved in the same form as the incompressible problem. Inputs to this script include the static pressure, static temperature, and Mach number at the aircraft's flight condition; the chord length of the wing section under consideration; the thickness of the wing as function of chord length, and the pressure distribution along a line of constant chord. The script outputs the transformed edge velocity as a function of the transformed streamwise coordinate. A curve fit of the plot of transformed edge velocity versus the transformed streamwise coordinate can then be used to calculate the Hartree pressure gradient parameter in the region of interest.

```
clear all
clc

%% Flight Parameters

M = 0.75; % Mach number
gam = 1.4; % Ratio of specific heats
ts = 216.65; % static temperature, K
ps = 19746; % Pressure, Pa
chord = 4.41; % chord length, m
xc = 1; % x/c location of interest

pt = ps*(1+(gam-1)/2*M^2)^(gam/(gam-1)); % Stagnation pressure, Pa
tt = ts*(1+(gam-1)/2*M^2); % stagnation temperature, K

%% Load Cp Data

BL212 = load('CP-08R-212.dat');
BL264 = load('CP-08R-264.dat');

[r c] = find(BL264(:,2) == 0);

cp = [BL264(1:r,2) BL264(1:r,4) BL264(1:r,5)]; % pressure coefficent on suction
side [x/c y/c cp]
pdat = [cp(:,1) cp(:,2) ps.*(.5.*gam.*M^2.*cp(:,3)+1)];
[rp cp] = size(pdat);
pdat = flipud(pdat); % flip pdat so it starts at x = 0

%% Calcuate edge velocity quatities and Reshotko velocity
Me = zeros(rp,1);
for d = 1:rp
    Me(d) = sqrt(2/(gam-1)*((pt/pdat(d,3))^((gam-1)/gam)-1)); % edge Mach
number
end
```

```
te = tt.*(1+(gam-1)/2.*Me.^2).^(-1); % edge temperature, K
ue = Me.*sqrt(gam.*287.*te); % edge velocity, m/s
ae = sqrt(gam.*287.*te); % edge speed of sound, m/s
Ue = sqrt(gam*287*tt)./ae.*ue; % Adjusted velocity from Cohen & Reshotko, m/s

%% Arc Length Calculation
arc = zeros(rp,1);
arc(1,1) = chord*sqrt(pdat(1,1)^2+pdat(1,2)^2);
for kk = 2:rp
    arc(kk,1) = arc(kk-1,1)+chord*sqrt((pdat(kk,1)-pdat(kk-1,1))^2+(pdat(kk,2)-
pdat(kk-1,2))^2);
end

%% X integration
xloc = chord*xc; % x location of interest
[rn cn] = find(pdat(:,1)<xc); % find x/c locations equal or less than point of
interest
n = rn(length(rn))-1; % number of integration intervals

ds = zeros(rp,1); % initialize dx matrix (dx is arc lenght along curved
surface)
for nn = 1:rp-1
    ds(nn) = sqrt((chord*pdat(nn+1,1)-chord*pdat(nn,1))^2+(chord*pdat(nn+1,2)-
chord*pdat(nn,2))^2); % ds = sqrt(dx^2+dy^2)
end

X = zeros(n+1,1); % place holder for trapezoidal integration (distance along
curved surface until x/c = 0.3)
cs = 0; % arc distance confirmation variable

for jj = 1:n
    X(jj+1) = X(jj) +
(gam*pdat(jj,3)/pt*sqrt(te(jj)/tt)+0.95*pdat(jj+1,3)/pt*sqrt(te(jj+1)/tt))/2*ds
(jj); % X specified in Cohen & Reshotko
    cs = cs + ds(jj); % confirm arc distance
end

%% Record X and Ue in order to calculate Beta
bdat = zeros(n+1,2); %[X Ue]
bdat(:,1) = X;
bdat(:,2) = Ue(1:n+1);
save('beta_data.txt','bdat','-ascii','-tabs')

%% Plotting

figure(1)
plot(BL212(:,2),BL212(:,5),'linewidth',2);
set(gca,'YDir','reverse')
grid on
xlabel('x-location, x/c')
ylabel('C_p')

figure(2)
plot(BL264(:,2),BL264(:,5),'linewidth',2);
set(gca,'YDir','reverse')
grid on
xlabel('x-location, x/c')
ylabel('C_p')

figure(3)
```

```
a = plot(BL212(:,2),BL212(:,5),'b','linewidth',2);
hold on
b = plot(BL264(:,2),BL264(:,5),'r','linewidth',2);
set(gca,'YDir','reverse')
grid on
xlabel('x-location, x/c')
ylabel('C_p')
legend([a,b],'Inboard Pressure Ports','Outboard Pressure
Ports','location','SouthEast')

figure(4)
plot(bdat(:,1),bdat(:,2),'b','linewidth',2)
grid on
xlabel('X, m')
ylabel('U_e, m/s')
```

C-2: Solver for Falkner-Skan Boundary Layer with Heat Transfer

The similarity equations for the Falkner-Skan boundary layer with heat transfer were solved using a fourth order Runge-Kutta numerical integration technique. The system of equations was comprised of five simultaneous ordinary differential equations. The boundary conditions for the similarity shear stress second derivative and wall enthalpy derivative terms were not known at the wall. However, the similarity velocity and heat transfer equations were defined at the edge of the boundary layer. Thus, a successive approximation technique using the Newton-Raphson method was employed to converge on the boundary conditions at the wall by comparing final values of the similarity velocity and heat transfer at the boundary layer's edge.

A Matlab scrip was generated for performing these computations and is shown below. The Hartree pressure gradient parameter and maximum expected wall enthalpy function value are input into script, which then computes the Falkner-Skan similarity solutions and plots them as a function of wall enthalpy function. The script also outputs the file shear_data.txt that records the similarity shear stress and wall enthalpy derivate as functions of the wall enthalpy parameter for later use.

```
clear all
clc
format long

% Boundary Layer Parameters
beta = 0.3; % Hartree Parameter
s_max = 0.4; % maximum wall stagnation enthalpy ratio
s_int = 0.01; % interval for plotting f"

f_s = zeros(s_max/s_int+1,3); % initialize shear stress matrix [S S' f"]
count = 1; % initialize counting term

for s = 0:s_int:s_max

inter = 1000;     %number of points inside the BL
h=10/inter;    %h value used in Runge Kutta
eta = 0:h:10; % similarity variable eta

Y = zeros(inter+1,5); % initializes matrix for solutions with columns of (Y1,
Y2, Y3, Y4, Y5), [(f",f',f,S',S)]

A = [1.23 1.24]; % Initial guess at f''(0), [1.23 1.24] works for B=1 and below
G = zeros(100,1); % Initialize matrix to track value of velocity at BL edge
g = 1; % arbitrary initial condition greater than criteria

B = [-0.40 -0.41]; % Initial condition for stagnation enthalpy term
```

```
D = zeros(100,1); % Initialize matrix for recording stagnation enthalpy error
d = 1; % arbitrary initial condition greater than criteria

k = 1; % start BL iterations
m = 1; % start enthalpy iterations

while abs(d) > 0.00000001 % while loop for finding enthalpy derivative initial
conditions

    g=1; % reset velocity error initial value

    while abs(g) > 0.00000001 % while loop for finding velocity initial
conditions

        Y(1,1) = A(k); % initial shear stress, f"
        Y(1,2) = 0; % initial velocity, f'
        Y(1,3) = 0; % initial f
        Y(1,4) = B(m); % initial heat transfer, S' (FIND LATER WITH N-R)
        Y(1,5) = s; % initial stagnation enthalpy, S

        for n = 2:inter+1 % Runge-Kutta integration loop

            a1 = h*(-Y(n-1,1)*Y(n-1,3)+beta*(Y(n-1,2)^2-Y(n-1,5)-1));
            b1 = h*Y(n-1,1);
            c1 = h*Y(n-1,2);
            d1 = h*(-Y(n-1,3)*Y(n-1,4));
            g1 = h*Y(n-1,4);

            a2 = h*(-(Y(n-1,1)+a1/2)*(Y(n-1,3)+c1/2)+beta*((Y(n-1,2)+b1/2)^2-
(Y(n-1,5)+g1/2)-1));
            b2 = h*(Y(n-1,1)+a1/2);
            c2 = h*(Y(n-1,2)+b1/2);
            d2 = h*(-(Y(n-1,3)+c1/2)*(Y(n-1,4)+d1/2));
            g2 = h*(Y(n-1,4)+d1/2);

            a3 = h*(-(Y(n-1,1)+a2/2)*(Y(n-1,3)+c2/2)+beta*((Y(n-1,2)+b2/2)^2-
(Y(n-1,5)+g2/2)-1));
            b3 = h*(Y(n-1,1)+a2/2);
            c3 = h*(Y(n-1,2)+b2/2);
            d3 = h*(-(Y(n-1,3)+c2/2)*(Y(n-1,4)+d2/2));
            g3 = h*(Y(n-1,4)+d2/2);

            a4 = h*(-(Y(n-1,1)+a3)*(Y(n-1,3)+c3)+beta*((Y(n-1,2)+b3)^2-(Y(n-
1,5)+g3)-1));
            b4 = h*(Y(n-1,1)+a3);
            c4 = h*(Y(n-1,2)+b3);
            d4 = h*(-(Y(n-1,3)+c3)*(Y(n-1,4)+d3));
            g4 = h*(Y(n-1,4)+d3);

            Y(n,1) = Y(n-1,1)+(a1+2*a2+2*a3+a4)/6;
            Y(n,2) = Y(n-1,2)+(b1+2*b2+2*b3+b4)/6;
            Y(n,3) = Y(n-1,3)+(c1+2*c2+2*c3+c4)/6;
            Y(n,4) = Y(n-1,4)+(d1+2*d2+2*d3+d4)/6;
            Y(n,5) = Y(n-1,5)+(g1+2*g2+2*g3+g4)/6;

            if isnan(a1) == 1 % blow-up preventer

                if k == 1
                    Y(1,1) = Y(1,1)+0.01;
                    A(2) = Y(1,1)+0.01;
```

```
                else
                    G(k) = 10000;
                    A(k) = A(k-1) + 0.01;
                    A(k+1) = A(k)+0.01;
                end
                n = 2; % re-set n
            end

        end

        if k > 1
            G(k) = 1-Y(n,2);
            A(k+1) = A(k)-(G(k)*(A(k)-A(k-1)))/(G(k)-G(k-1));
        else
            G(k) = 1-Y(inter+1,2);
        end
        g = G(k); % record latest difference
        k = k+1;
    end

    if m > 1
        D(m) = Y(inter+1,5);
        B(m+1) = B(m)-(D(m)*(B(m)-B(m-1)))/(D(m)-D(m-1));
    else
        D(m) = Y(inter+1,5);
    end
    d = D(m); % record latest difference

    m = m+1;

end

sol = zeros(length(eta),4); % table of solution values
sol(:,1) = eta; % similarity variable
sol(:,2) = Y(:,3); % f
sol(:,3) = Y(:,2); % f'
sol(:,4) = Y(:,1); % f"

esol = zeros(length(eta),3); % table of solution values
esol(:,1) = eta; % similarity variable
esol(:,2) = Y(:,5); % S
esol(:,3) = Y(:,4); % S'

%% Plotting Module
% figure(count)
% plot(sol(:,3),sol(:,1))
% grid on
% xlabel('Non-dimensional Velocity')
% ylabel('Non-dimensional BL Height')

ng = find(G==0);
nd = find(D==0);
G(ng) = [];
D(nd) = [];

f_s(count,1) = s; % record wall stagnation enthalpy ratio, S
f_s(count,2) = Y(1,4); % record S'
f_s(count,3) = Y(1,1); % record shear stress, f"
count = count+1;
end
```

```
%% Shear plotting
figure(count)
plot(f_s(:,1),f_s(:,3),'b','linewidth',2)
grid on
xlabel('Wall Enthalpy Function, S')
ylabel('Shear Stress Parameter, f"')

save('shear_data.txt','f_s','-ascii','-tabs')
```

C-3: Falkner-Skan Skin Friction and Heat Transfer as a Function of Wall Temperature

The skin friction coefficient and heat transfer coefficient are both functions of wall temperature. The non-dimensional skin friction increases with increasing temperature while the dimensional convective heat transfer coefficient decreases. The Matlab script shown below is used to compute the skin friction coefficient and convection coefficient using the values of u_e, U_e, X, S, S', and f_η'' computed using the scripts detailed in the previous sections. The computations are done at a single chord location specified by the user.

```
clear all
clc

%% Flight Parameters (39,000 ft, M = 0.75)

M = 0.75; % Mach number
gam = 1.4; % Ratio of specific heats
ts = 216.65; % static temperature, K
ps = 19746; % Pressure, Pa
rs = 0.31752; % freestream static density, kg/m^3
chord = 4.41; % chord length, m
xc = 0.3; % x/c location of interest

pt = ps*(1+(gam-1)/2*M^2)^(gam/(gam-1)); % Stagnation pressure, Pa
tt = ts*(1+(gam-1)/2*M^2); % stagnation temperature, K
rt = rs*(1+(gam-1)/2*M^2)^(1/(gam-1)); % total density, kg/m^3
at = sqrt(gam*287*tt); % stagnation speed of sound, m/s

%% Load Cp Data

BL212 = load('CP-08R-212.dat'); % Load glove BL 212 Cp profile
BL264 = load('CP-08R-264.dat'); % Load glove BL 264 Cp profile

[r c] = find(BL264(:,2) == 0);

cp = [BL264(1:r,2) BL264(1:r,4) BL264(1:r,5)]; % pressure coefficient on
suction side [x/c y/c cp]
pdat = [cp(:,1) cp(:,2) ps.*(.5.*gam.*M^2.*cp(:,3)+1)];
[rp cp] = size(pdat);
pdat = flipud(pdat); % flip pdat so it starts at x = 0

%% Calculate edge velocity quantities and Reshotko velocity
Me = zeros(rp,1);
for d = 1:rp
    Me(d) = sqrt(2/(gam-1)*((pt/pdat(d,3))^((gam-1)/gam)-1)); % edge Mach
number
end

te = tt.*(1+(gam-1)/2.*Me.^2).^(-1); % edge temperature, K
ue = at.*Me./(1+(gam-1)/2.*Me.^2).^.5; % edge velocity, m/s
ae = sqrt(gam.*287.*te); % edge speed of sound, m/s
```

```
Ue = sqrt(gam*287*tt)./ae.*ue; % Adjusted velocity from Cohen & Reshotko, m/s

%% Arc Length Calculation
arc = zeros(rp,1);
arc(1,1) = chord*sqrt(pdat(1,1)^2+pdat(1,2)^2);
for kk = 2:rp
    arc(kk,1) = arc(kk-1,1)+chord*sqrt((pdat(kk,1)-pdat(kk-1,1))^2+(pdat(kk,2)-
pdat(kk-1,2))^2);
end

%% X integration
xloc = chord*xc; % x location of interest
[rn cn] = find(pdat(:,1)<xc); % find x/c locations equal or less than point of
interest
n = rn(length(rn))-1; % number of integration intervals

ds = zeros(rp,1); % initialize dx matrix (dx is arc lenght along curved
surface)
for nn = 1:rp-1
    ds(nn) = sqrt((chord*pdat(nn+1,1)-chord*pdat(nn,1))^2+(chord*pdat(nn+1,2)-
chord*pdat(nn,2))^2); % ds = sqrt(dx^2+dy^2)
end

X = zeros(n+1,1); % place holder for trapezoidal integration (distance along
curved surface until x/c = 0.3)
cs = 0; % arc distance confirmation variable

for jj = 1:n
    X(jj+1) = X(jj) +
(gam*pdat(jj,3)/pt*sqrt(te(jj)/tt)+gam*pdat(jj+1,3)/pt*sqrt(te(jj+1)/tt))/2*ds(
jj); % X specified in Cohen & Reshotko
    cs = cs + ds(jj); % confirm arc distance
end

%% Record X and Ue in order to calculate Cf, establish other relevant
parameters

Xf = X(n+1); % X for skin friction coefficient calculation
Uf = Ue(n+1); % Ue for skin friction coefficient calculation
uef = ue(n+1); % ue for skin friction coefficient calculation
ka = 0.0223; % thermal conductivity of air at 250K, W/m-K
ca = 1006; % specific heat of air, J/kg-K
% vwall = 0.00004; % kinematic viscosity m^2/s (vary with sutherland's law
later)

m = 0.174; % velocity power law exponent
sdat = load('shear_data.txt'); % load Sw, Sw' and f" data, [S S' f"]

mt = 17.16e-6*(273.11+110.56)/(110.56+tt)*(tt/273.11)^(3/2); % stagnation
viscosity from Sutherland's Law
vt = mt/rt; % stagnation kinematic viscosity

cfdat = zeros(length(sdat(:,1)),3); % initialize matrix for recording Cf as a
function of Sw, [Sw Cf h q"]
cfdat(:,1) = sdat(:,1); % fill in Sw into first column
twall = zeros(length(sdat(:,1)),1); % initialize twall matrix, K
tref = zeros(length(sdat(:,1)),2); % initialize tref matrix, K
tau = zeros(length(sdat(:,1)),1); % initialize shear stress matrix, N/m^2

for kk = 1:length(sdat(:,1))
```

```
    twall(kk) = tt*(sdat(kk,1)+1); % wall temperature, K
    rwall = pdat(n+1,3)/(287*twall(kk)); % density at wall, kg/m^3 rt*(1+(gam-
1)/2*Me(n+1)^2)^(-1/(gam-1));%
    mwall = 17.16e-
6*(273.11+110.56)/(110.56+twall(kk))*(twall(kk)/273.11)^(3/2); % wall viscosity
from Sutherland's Law
    vwall =  mwall/rwall; % wall kinematic viscosity vt%

    lam = (tt+111)/(twall(kk)+111)*sqrt(twall(kk)/tt); % lambda term

    cfdat(kk,2) = sdat(kk,3)*(2*lam*(1+cfdat(kk,1)))*sqrt((m+1)/2*vt/(Uf*Xf));
% skin friction coefficient
    cfdat(kk,3) = .5*(-
sdat(kk,2)/sdat(kk,1))*cfdat(kk,2)*uef*ka/(sdat(kk,3)*vwall); % heat transfer
coefficient, W/m^2-K

    tau(kk) = .5*rwall*uef^2*cfdat(kk,2);

    cfdat(kk,4) = cfdat(kk,3)*(tt-twall(kk)); % heat flux, W/m^2
end
hfit = [twall cfdat(:,3) cfdat(:,4)];

save('cf_ht_data.txt','cfdat','-ascii','-tabs')
save('h_curve_temp.txt','hfit','-ascii','-tabs')

figure(1)
plot(cfdat(:,1),cfdat(:,2),'b','linewidth',2)
xlabel('Wall Enthalpy Function, S')
ylabel('Skin Friction Coefficient, C_f')
grid on

figure(2)
plot(cfdat(:,1),cfdat(:,3),'b','linewidth',2)
xlabel('Wall Enthalpy Function, S')
ylabel('Convective Heat Transfer Coefficient, W/m^2-K')
grid on

figure(3)
plot(twall,cfdat(:,3),'b','linewidth',2)
xlabel('Wall Temperature, K')
ylabel('Convective Heat Transfer Coefficient, W/m^2-K')
grid on

figure(4)
plot(twall,-cfdat(:,4),'b','linewidth',2)
xlabel('Wall Temperature, K')
ylabel('Convective Heat Transfer out of Wall, W/m^2')
grid on
```

C-4: Surface Plot of Falkner-Skan Convection Coefficient vs. Wall Temperature

The Matlab script in the previous section was used to convert the non-dimensional similarity solutions of the Falkner-Skan boundary layer with heat transfer into convective heat transfer as a function of wall temperature. The convection coefficient also varies as a function of chord location on the glove's surface. Convective heat transfer within the laminar boundary layer decreases as chord location increases. As was done before, the convection coefficient is computed using the values of u_e, U_e, X, S, S', and f_η'' found by performing Stewartson's transformation and solving the boundary layer equations.

```
clear all
clc

%% Flight Parameters (39,000 ft, M = 0.75)

M = 0.75; % Mach number
gam = 1.4; % Ratio of specific heats
ts = 216.65; % static temperature, K
ps = 19746; % Pressure, Pa
rs = 0.31752; % freestream static density, kg/m^3
chord = 4.41; % chord length, m

dc = 0.01; % chord stepping interval
nc = 1;

%% Load Cp and Shear Data
BL212 = load('CP-08R-212.dat'); % Load glove BL 212 Cp profile
BL264 = load('CP-08R-264.dat'); % Load glove BL 264 Cp profile

sdat = load('shear_data.txt'); % load Sw, Sw' and f" data, [S S' f"]

hrec = zeros(length(sdat(:,1)),(0.55-0.15)/dc+1); % initialize matrix for
recording heat transfer coefficient
qrec = zeros(length(sdat(:,1)),(0.55-0.15)/dc+1); % initialize matrix for
recording heat flux
crec = zeros((0.55-0.15)/dc+1,1); % initialize matrix to record chord location

%% Loop to vary chord location
for xc = 0.15:dc:0.55; % x/c location of interest

    pt = ps*(1+(gam-1)/2*M^2)^(gam/(gam-1)); % Stagnation pressure, Pa
    tt = ts*(1+(gam-1)/2*M^2); % stagnation temperature, K
    rt = rs*(1+(gam-1)/2*M^2)^(1/(gam-1)); % total density, kg/m^3
    at = sqrt(gam*287*tt); % stagnation speed of sound, m/s

    [r c] = find(BL264(:,2) == 0);

    cp = [BL264(1:r,2) BL264(1:r,4) BL264(1:r,5)]; % pressure coefficent on
suction side [x/c y/c cp]
    pdat = [cp(:,1) cp(:,2) ps.*(.5.*gam.*M^2.*cp(:,3)+1)];
    [rp cp] = size(pdat);
```

```
    pdat = flipud(pdat); % flip pdat so it starts at x = 0

    %% Calcuate edge velocity quantities and Reshotko velocity
    Me = zeros(rp,1);
    for d = 1:rp
        Me(d) = sqrt(2/(gam-1)*((pt/pdat(d,3))^((gam-1)/gam)-1)); % edge Mach
number
    end

    te = tt.*(1+(gam-1)/2.*Me.^2).^(-1); % edge temperature, K
    ue = at.*Me./(1+(gam-1)/2.*Me.^2).^.5; % edge velocity, m/s
    ae = sqrt(gam.*287.*te); % edge speed of sound, m/s
    Ue = sqrt(gam*287*tt)./ae.*ue; % Adjusted velocity from Cohen & Reshotko,
m/s

    %% Arc Length Calculation
    arc = zeros(rp,1);
    arc(1,1) = chord*sqrt(pdat(1,1)^2+pdat(1,2)^2);
    for kk = 2:rp
        arc(kk,1) = arc(kk-1,1)+chord*sqrt((pdat(kk,1)-pdat(kk-
1,1))^2+(pdat(kk,2)-pdat(kk-1,2))^2);
    end

    %% X integration
    xloc = chord*xc; % x location of interest
    [rn cn] = find(pdat(:,1)<xc); % find x/c locations equal or less than point
of interest
    n = rn(length(rn))-1; % number of integration intervals

    ds = zeros(rp,1); % initialize dx matrix (dx is arc lenght along curved
surface)
    for nn = 1:rp-1
        ds(nn) = sqrt((chord*pdat(nn+1,1)-
chord*pdat(nn,1))^2+(chord*pdat(nn+1,2)-chord*pdat(nn,2))^2); % ds =
sqrt(dx^2+dy^2)
    end

    X = zeros(n+1,1); % place holder for trapezoidal integration (distance
along curved surface until x/c = 0.3)
    cs = 0; % arc distance confirmation variable

    for jj = 1:n
        X(jj+1) = X(jj) +
(gam*pdat(jj,3)/pt*sqrt(te(jj)/tt)+gam*pdat(jj+1,3)/pt*sqrt(te(jj+1)/tt))/2*ds(
jj); % X specified in Cohen & Reshotko
        cs = cs + ds(jj); % confirm arc distance
    end

    %% Record X and Ue in order to calculate Cf, establish other relevant
parameters

    Xf = X(n+1); % X for skin friction coefficient calculation
    Uf = Ue(n+1); % Ue for skin friction coefficient calculation
    uef = ue(n+1); % ue for skin friction coefficient calculation
    ka = 0.0223; % thermal conductivity of air at 250K, W/m-K
    ca = 1006; % specific heat of air, J/kg-K

    m = 0.174; % exponent in velocity power law
```

```
    mt = 17.16e-6*(273.11+110.56)/(110.56+tt)*(tt/273.11)^(3/2); % stagnation
viscosity from Sutherland's Law
    vt = mt/rt; % stagnation kinematic viscosity

    cfdat = zeros(length(sdat(:,1)),3); % initialize matrix for recording Cf as
a function of Sw, [Sw Cf h q"]
    cfdat(:,1) = sdat(:,1); % fill in Sw into first column
    twall = zeros(length(sdat(:,1)),1); % intialize twall matrix, K
    tref = zeros(length(sdat(:,1)),2); % intialize tref matrix, K

    for kk = 1:length(sdat(:,1))


        twall(kk) = tt*(sdat(kk,1)+1); % wall temperature, K
        rwall = pdat(n+1,3)/(287*twall(kk)); % density at wall, kg/m^3
rt*(1+(gam-1)/2*Me(n+1)^2)^(-1/(gam-1));%
        mwall = 17.16e-
6*(273.11+110.56)/(110.56+twall(kk))*(twall(kk)/273.11)^(3/2); % wall viscosity
from Sutherland's Law
        vwall =  mwall/rwall; % wall kinematic viscosity vt%
        lam = (tt+111)/(twall(kk)+111)*sqrt(twall(kk)/tt);
        cfdat(kk,2) =
sdat(kk,3)*(2*lam*(1+cfdat(kk,1)))*sqrt((m+1)/2*vt/(Uf*Xf)); % skin friction
coefficient
        cfdat(kk,3) = .5*(-
sdat(kk,2)/sdat(kk,1))*cfdat(kk,2)*uef*ka/(sdat(kk,3)*vwall); % heat transfer
coefficient, W/m^2-K

        cfdat(kk,4) = cfdat(kk,3)*(tt-twall(kk)); % heat flux, W/m^2
    end
    hrec(:,nc) = cfdat(:,3); % record convection coefficient as a function of
wall T and x/c
    qrec(:,nc) = -cfdat(:,4); % record convection heat transfer into the wall
as a function of wall T and x/c
    crec(nc,1) = xc; % record chord position



    nc = nc+1;
end
%% Original Plotting Module
figure(1)
plot(cfdat(:,1),cfdat(:,2),'b','linewidth',2)
xlabel('Wall Enthalpy Function, S')
ylabel('Skin Friction Coefficient, C_f')
grid on

figure(2)
plot(cfdat(:,1),cfdat(:,3),'b','linewidth',2)
xlabel('Wall Enthalpy Function, S')
ylabel('Convective Heat Transfer Coefficient, W/m^2-K')
grid on

figure(3)
plot(twall,cfdat(:,3),'b','linewidth',2)
xlabel('Wall Temperature, K')
ylabel('Convective Heat Transfer Coefficient, W/m^2-K')
grid on

figure(4)
```

```
plot(twall,-cfdat(:,4),'b','linewidth',2)
xlabel('Wall Temperature, K')
ylabel('Convective Heat Transfer into Wall, W/m^2')
grid on

%% Plot Heat Transfer Surface
figure(5)
[X Y] = meshgrid(crec,twall);
surf(X,Y,hrec)
xlabel('Chord Location, x/c')
ylabel('Wall Temperature, K')
zlabel('Heat Transfer Coefficient, W/m^2-K')

figure(6)
[XX YY] = meshgrid(crec,twall);
surf(XX,YY,qrec)
xlabel('Chord Location, x/c')
ylabel('Wall Temperature, K')
zlabel('Heat Transfer out of Wall, W/m^2-K')
```

C-5: Solver for Falkner-Skan-Cooke Boundary Layer with Heat Transfer

The similarity equations for the Falkner-Skan-Cooke boundary layer with heat transfer were solved using a fourth order Runge-Kutta numerical integration technique. The system of seven ordinary differential equations was reduced to five simultaneous equations because the crossflow and enthalpy functions are identical when the Prandtl number is one. The boundary conditions for the similarity shear stress second derivative and wall enthalpy derivative terms were not known at the wall. However, the similarity velocity and heat transfer equations were defined at the edge of the boundary layer. Thus, a successive approximation technique using the Newton-Raphson method was employed to converge on the boundary conditions at the wall by comparing final values of the similarity velocity and heat transfer at the boundary layer's edge.

A Matlab scrip was generated for performing these computations and is shown below. The Hartree pressure gradient parameter and maximum expected wall enthalpy function value are input into script, which then computes the Falkner-Skan-Cooke similarity solutions and plots them as a function of wall temperature ratio, which is the wall temperature divided by the stagnation temperature. The script also outputs the file fsc_shear_data.txt that records the similarity shear stress and wall enthalpy derivate as functions of the wall temperature ratio for later use.

```
clear all
clc
format long

% Boundary Layer Parameters
beta = 0.3; % Hartree Parameter


% Fligth conditions
lam = 35; % wing sweep angle, deg
gam = 1.4; % Ratio of Specific Heats
Ma = 0.75; % Mach number
Tinf = 216.5; % static temperature, K
T0 = Tinf*(1+(gam-1)/2*Ma^2); % total temperature, K
Ts = Tinf*(1+(gam-1)/2*Ma^2*cosd(lam)^2); % Stagnation line temperature, K
ws_fact = T0/Ts; % wing sweep paramter of Beckwith (1958)

inter = 1000;     %number of points inside the BL
h=10/inter;    %h value used in Runge Kutta
eta = 0:h:10; % similarity variable eta
```

```
tw_min = 1; % wall temperature ratio of Beckwith (1958)
tw_max = 1.4; % wall temperature ratio maximum
tw_int = 0.01; % temperature ratio step

f_s = zeros((tw_max-tw_min)/tw_int+1,3); % initialize shear stress matrix
[theta theta' f"]
count = 1;

for tw = tw_min:tw_int:tw_max

Twall = tw*T0; % wall temperature, K

Y = zeros(inter+1,5); % initializes matrix for solutions with columns of (Y1,
Y2, Y3, Y4, Y5), [(f",f',f,S',S)]

A = [1.23 1.24]; % Initial guess at f''(0), [1.23 1.24] works for B=1 and below
G = zeros(100,1); % Initialize matrix to track value of velocity at BL edge
g = 1; % arbitrary initial condition greater than criteria

B = [0.40 0.41]; % Initial condition for stagnation enthalpy term
D = zeros(100,1); % Initialize matrix for recording stagnation enthalpy error
d = 1; % arbitrary initial condition greater than criteria

k = 1; % start BL iterations
m = 1; % start enthalpy iterations

while abs(d) > 0.00000001 % while loop for finding enthalpy derivative initial
conditions

    g=1;

    while abs(g) > 0.00000001 % while loop for finding velocity initial
conditions

        % Set initial conditions, depends on number of iterations for finidng
        % proper intial conditions

        Y(1,1) = A(k); % initial shear stress, f"
        Y(1,2) = 0; % initial velocity, f'
        Y(1,3) = 0; % initial f
        Y(1,4) = B(m); % initial heat transfer, theta' (FIND LATER WITH N-R)
        Y(1,5) = 0; % initial stagnation enthalpy ratio, theta

        for n = 2:inter+1

            a1 = h*(-Y(n-1,1)*Y(n-1,3)+beta*(Y(n-1,2)^2-T0/Ts*((1-
Twall/T0)*Y(n-1,5)-(1-Ts/T0)*(Y(n-1,5))^2+Twall/T0)));
            b1 = h*Y(n-1,1);
            c1 = h*Y(n-1,2);
            d1 = h*(-Y(n-1,3)*Y(n-1,4));
            g1 = h*Y(n-1,4);
```

```
            a2 = h*(-(Y(n-1,1)+a1/2)*(Y(n-1,3)+c1/2)+beta*((Y(n-1,2)+b1/2)^2-
T0/Ts*((1-Twall/T0)*(Y(n-1,5)+g1/2)-(1-Ts/T0)*(Y(n-1,5)+g1/2)^2+Twall/T0)));
            b2 = h*(Y(n-1,1)+a1/2);
            c2 = h*(Y(n-1,2)+b1/2);
            d2 = h*(-(Y(n-1,3)+c1/2)*(Y(n-1,4)+d1/2));
            g2 = h*(Y(n-1,4)+d1/2);

            a3 = h*(-(Y(n-1,1)+a2/2)*(Y(n-1,3)+c2/2)+beta*((Y(n-1,2)+b2/2)^2-
T0/Ts*((1-Twall/T0)*(Y(n-1,5)+g2/2)-(1-Ts/T0)*(Y(n-1,5)+g2/2)^2+Twall/T0)));
            b3 = h*(Y(n-1,1)+a2/2);
            c3 = h*(Y(n-1,2)+b2/2);
            d3 = h*(-(Y(n-1,3)+c2/2)*(Y(n-1,4)+d2/2));
            g3 = h*(Y(n-1,4)+d2/2);

            a4 = h*(-(Y(n-1,1)+a3)*(Y(n-1,3)+c3)+beta*((Y(n-1,2)+b3)^2-
T0/Ts*((1-Twall/T0)*(Y(n-1,5)+g3)-(1-Ts/T0)*(Y(n-1,5)+g3)^2+Twall/T0)));
            b4 = h*(Y(n-1,1)+a3);
            c4 = h*(Y(n-1,2)+b3);
            d4 = h*(-(Y(n-1,3)+c3)*(Y(n-1,4)+d3));
            g4 = h*(Y(n-1,4)+d3);

            Y(n,1) = Y(n-1,1)+(a1+2*a2+2*a3+a4)/6;
            Y(n,2) = Y(n-1,2)+(b1+2*b2+2*b3+b4)/6;
            Y(n,3) = Y(n-1,3)+(c1+2*c2+2*c3+c4)/6;
            Y(n,4) = Y(n-1,4)+(d1+2*d2+2*d3+d4)/6;
            Y(n,5) = Y(n-1,5)+(g1+2*g2+2*g3+g4)/6;

            if isnan(a1) == 1 % blow-up preventer

                if k == 1
                    Y(1,1) = Y(1,1)+0.01;
                    A(2) = Y(1,1)+0.01;
                else
                    G(k) = 10000;
                    A(k) = A(k-1) + 0.01;
                    A(k+1) = A(k)+0.01;
                end
                n = 2; % re-set n
            end

        end

        if k > 1
            G(k) = 1-Y(n,2);
            A(k+1) = A(k)-(G(k)*(A(k)-A(k-1)))/(G(k)-G(k-1));
        else
            G(k) = 1-Y(inter+1,2);
        end
        g = G(k); % record latest difference
        k = k+1;
    end

    if m > 1
        D(m) = 1-Y(inter+1,5);
        B(m+1) = B(m)-(D(m)*(B(m)-B(m-1)))/(D(m)-D(m-1));
    else
        D(m) = 1-Y(inter+1,5);
```

```
    end
    d = D(m); % record latest difference

    m = m+1;

end

sol = zeros(length(eta),4); % table of solution values
sol(:,1) = eta; % similarity variable
sol(:,2) = Y(:,3); % f
sol(:,3) = Y(:,2); % f'
sol(:,4) = Y(:,1); % f"

esol = zeros(length(eta),3); % table of solution values
esol(:,1) = eta; % similarity variable
esol(:,2) = Y(:,5); % theta
esol(:,3) = Y(:,4); % theta'

% %% Plotting Module
% figure(1)
% plot(sol(:,3),sol(:,1))
% grid on
% xlabel('Non-dimensional Velocity')
% ylabel('Non-dimensional BL Height')

ng = find(G==0);
nd = find(D==0);
G(ng) = [];
D(nd) = [];



f_s(count,1) = tw; % record wall temperature
f_s(count,2) = Y(1,4); % record theta'
f_s(count,3) = Y(1,1); % record shear stress, f"
count = count+1;

end

%% Shear plotting
figure(1)
plot(f_s(:,1),f_s(:,3),'b','linewidth',2)
grid on
xlabel('Wall Temperature, K')
ylabel('Shear Stress Parameter, f"')

save('fsc_shear_data.txt','f_s','-ascii','-tabs') %[tw, g', f"]
```

C-6: Falkner-Skan-Cooke Skin Friction and Heat Transfer as a Function of Wall Temperature

The skin friction coefficient and heat transfer coefficient are both functions of wall temperature. The non-dimensional skin friction increases with increasing temperature while the dimensional convective heat transfer coefficient decreases. The Matlab script shown below is used to compute the skin friction coefficient and convection coefficient using the values of, u_e, U_e, X, $\frac{T_w}{T_0}$, θ'_{HT}, and f''_η computed using the scripts detailed in the previous sections. The computations are done at a single chord location specified by the user. The flight conditions and wing sweep angle are also set by the user.

```
clear all
clc

%% Flight Parameters (39,000 ft, M = 0.75)

sweep = 35; % Wing sweep, deg
M = 0.75; % Mach number
gam = 1.4; % Ratio of specific heats
ts = 216.65; % static temperature, K
ps = 19746; % Pressure, Pa
rs = 0.31752; % freestream static density, kg/m^3
chord = 4.41; % chord length, m
xc = 0.3; % x/c location of interest

pt = ps*(1+(gam-1)/2*M^2)^(gam/(gam-1)); % Stagnation pressure, Pa
tt = ts*(1+(gam-1)/2*M^2); % stagnation temperature, K
rt = rs*(1+(gam-1)/2*M^2)^(1/(gam-1)); % total density, kg/m^3
at = sqrt(gam*287*tt); % stagnation speed of sound, m/s

%% Load Cp Data

BL212 = load('CP-08R-212.dat'); % Load glove BL 212 Cp profile
BL264 = load('CP-08R-264.dat'); % Load glove BL 264 Cp profile

[r c] = find(BL264(:,2) == 0);

cp = [BL264(1:r,2) BL264(1:r,4) BL264(1:r,5)]; % pressure coefficent on suction
side [x/c y/c cp]
pdat = [cp(:,1) cp(:,2) ps.*(.5.*gam.*M^2.*cp(:,3)+1)];
[rp cp] = size(pdat);
pdat = flipud(pdat); % flip pdat so it starts at x = 0

%% Calcuate edge velocity quatities and Reshotko velocity
Me = zeros(rp,1);
for d = 1:rp
    Me(d) = sqrt(2/(gam-1)*((pt/pdat(d,3))^((gam-1)/gam)-1)); % edge Mach
number
end
```

```
te = tt.*(1+(gam-1)/2.*Me.^2).^(-1); % edge temperature, K
ue = at.*Me./(1+(gam-1)/2.*Me.^2).^.5; % edge velocity, m/s
ae = sqrt(gam.*287.*te); % edge speed of sound, m/s
Ue = sqrt(gam*287*tt)./ae.*ue; % Adjusted velocity from Cohen & Reshotko, m/s

%% Arc Length Calculation
arc = zeros(rp,1);
arc(1,1) = chord*sqrt(pdat(1,1)^2+pdat(1,2)^2);
for kk = 2:rp
    arc(kk,1) = arc(kk-1,1)+chord*sqrt((pdat(kk,1)-pdat(kk-1,1))^2+(pdat(kk,2)-
pdat(kk-1,2))^2);
end

%% X integration
xloc = chord*xc; % x location of interest
[rn cn] = find(pdat(:,1)<xc); % find x/c locations equal or less than point of
interest
n = rn(length(rn))-1; % number of integration intervals

ds = zeros(rp,1); % initialize dx matrix (dx is arc lenght along curved
surface)
for nn = 1:rp-1
    ds(nn) = sqrt((chord*pdat(nn+1,1)-chord*pdat(nn,1))^2+(chord*pdat(nn+1,2)-
chord*pdat(nn,2))^2); % ds = sqrt(dx^2+dy^2)
end

X = zeros(n+1,1); % place holder for trapezoidal integration (distance along
curved surface until x/c = 0.3)
cs = 0; % arc distance confirmation variable

for jj = 1:n
    X(jj+1) = X(jj) +
(gam*pdat(jj,3)/pt*sqrt(te(jj)/tt)+gam*pdat(jj+1,3)/pt*sqrt(te(jj+1)/tt))/2*ds(
jj); % X specified in Cohen & Reshotko
    cs = cs + ds(jj); % confirm arc distance
end

%% Record X and Ue in order to calculate Cf, establish other relevant
parameters

Xf = X(n+1); % X for skin friction coefficient calculation
Uf = Ue(n+1); % Ue for skin friction coefficient calculation
uef = ue(n+1); % ue for skin friction coefficient calculation
ka = 0.0223; % thermal conductivity of air at 250K, W/m-K
ca = 1006; % specific heat of air, J/kg-K
% vwall = 0.00004; % kinematic viscosity m^2/s (vary with sutherland's law
later)

m = 0.174; % velocity power law exponent
sdat = load('fsc_shear_data.txt'); % load tw, gw' and f" data, [tw g' f"]

mt = 17.16e-6*(273.11+110.56)/(110.56+tt)*(tt/273.11)^(3/2); % stagnation
viscosity from Sutherland's Law
vt = mt/rt; % stagnation kinematic viscosity
```

```
cfdat = zeros(length(sdat(:,1)),3); % initialize matrix for recording Cf as a
function of tw, [tw Cf h q"]
cfdat(:,1) = sdat(:,1); % fill in tw into first column
twall = zeros(length(sdat(:,1)),1); % intialize twall matrix, K
tref = zeros(length(sdat(:,1)),2); % intialize tref matrix, K
tau = zeros(length(sdat(:,1)),1); % initialize shear stress matrix, N/m^2

for kk = 1:length(sdat(:,1))

    twall(kk) = tt*(sdat(kk,1)); % wall temperature, K
    rwall = pdat(n+1,3)/(287*twall(kk)); % density at wall, kg/m^3 rt*(1+(gam-
1)/2*Me(n+1)^2)^(-1/(gam-1));%
    mwall = 17.16e-
6*(273.11+110.56)/(110.56+twall(kk))*(twall(kk)/273.11)^(3/2); % wall viscosity
from Sutherland's Law
    vwall =  mwall/rwall; % wall kinematic viscosity vt%
    lam = (tt+111)/(twall(kk)+111)*sqrt(twall(kk)/tt); % lambda term
    cfdat(kk,2) =
(sdat(kk,3)*cosd(sweep)+sdat(kk,2)*sind(sweep))*(2*lam*(cfdat(kk,1)))*sqrt((m+1
)/2*vt/(Uf*Xf)); % skin friction coefficient
    cfdat(kk,3) =
.5*(sdat(kk,2))*cfdat(kk,2)*uef*ka/((sdat(kk,3)*cosd(sweep)+sdat(kk,2)*sind(swe
ep))*vwall); % heat transfer coefficient, W/m^2-K

    tau(kk) = .5*rwall*uef^2*cfdat(kk,2);

    cfdat(kk,4) = cfdat(kk,3)*(tt-twall(kk)); % heat flux, W/m^2
end
hfit = [twall cfdat(:,3) cfdat(:,4)];

save('cf_ht_data.txt','cfdat','-ascii','-tabs')
save('h_curve_temp.txt','hfit','-ascii','-tabs')

figure(1)
plot(cfdat(:,1),cfdat(:,2),'b','linewidth',2)
xlabel('Wall Enthalpy Function, S')
ylabel('Skin Friction Coefficient, C_f')
grid on

figure(2)
plot(cfdat(:,1),cfdat(:,3),'b','linewidth',2)
xlabel('Wall Enthalpy Function, S')
ylabel('Convective Heat Transfer Coefficient, W/m^2-K')
grid on

figure(3)
plot(twall,cfdat(:,3),'b','linewidth',2)
xlabel('Wall Temperature, K')
ylabel('Convective Heat Transfer Coefficient, W/m^2-K')
grid on

figure(4)
plot(twall,-cfdat(:,4),'b','linewidth',2)
xlabel('Wall Temperature, K')
ylabel('Convective Heat Transfer out of Wall, W/m^2')
grid on
```

C-7: Surface Plot of Falkner-Skan-Cooke Convection Coefficient vs. Wall Temperature

The Matlab script in the previous section was used to convert the non-dimensional similarity solutions of the Falkner-Skan-Cooke boundary layer with heat transfer into convective heat transfer as a function of wall temperature. The convection coefficient also varies as a function of chord location on the glove's surface. Convective heat transfer within the laminar boundary layer decreases as chord location increases. As was done before, the convection coefficient is computed using the values of u_e, U_e, X, $\frac{T_w}{T_0}$, θ'_{HT}, and f''_η found by performing Stewartson's transformation and solving the boundary layer equations.

```
clear all
clc

%% Flight Parameters (39,000 ft, M = 0.75)

sweep = 35; % Wing sweep, deg
M = 0.75; % Mach number
gam = 1.4; % Ratio of specific heats
ts = 216.65; % static temperature, K
ps = 19746; % Pressure, Pa
rs = 0.31752; % freestream static density, kg/m^3
chord = 4.41; % chord length, m

dc = 0.01; % chord stepping interval
nc = 1;

%% Load Cp and Shear Data
BL212 = load('CP-08R-212.dat'); % Load glove BL 212 Cp profile
BL264 = load('CP-08R-264.dat'); % Load glove BL 264 Cp profile

sdat = load('shear_data.txt'); % load Sw, Sw' and f" data, [S S' f"]

hrec = zeros(length(sdat(:,1)),(0.55-0.15)/dc+1); % initialize matrix for
recording heat transfer coefficient
qrec = zeros(length(sdat(:,1)),(0.55-0.15)/dc+1); % initialize matrix for
recording heat flux
crec = zeros((0.55-0.15)/dc+1,1); % initialize matrix to record chord location

%% Loop to vary chord location
for xc = 0.15:dc:0.55; % x/c location of interest

    pt = ps*(1+(gam-1)/2*M^2)^(gam/(gam-1)); % Stagnation pressure, Pa
    tt = ts*(1+(gam-1)/2*M^2); % stagnation temperature, K
    rt = rs*(1+(gam-1)/2*M^2)^(1/(gam-1)); % total density, kg/m^3
    at = sqrt(gam*287*tt); % stagnation speed of sound, m/s

    [r c] = find(BL264(:,2) == 0);
```

```
    cp = [BL264(1:r,2) BL264(1:r,4) BL264(1:r,5)]; % pressure coefficent on
suction side [x/c y/c cp]
    pdat = [cp(:,1) cp(:,2) ps.*(.5.*gam.*M^2.*cp(:,3)+1)];
    [rp cp] = size(pdat);
    pdat = flipud(pdat); % flip pdat so it starts at x = 0

    %% Calcuate edge velocity quatities and Reshotko velocity
    Me = zeros(rp,1);
    for d = 1:rp
        Me(d) = sqrt(2/(gam-1)*((pt/pdat(d,3))^((gam-1)/gam)-1)); % edge Mach
number
    end

    te = tt.*(1+(gam-1)/2.*Me.^2).^(-1); % edge temperature, K
    ue = at.*Me./(1+(gam-1)/2.*Me.^2).^.5; % edge velocity, m/s
    ae = sqrt(gam.*287.*te); % edge speed of sound, m/s
    Ue = sqrt(gam*287*tt)./ae.*ue; % Adjusted velocity from Cohen & Reshotko,
m/s

    %% Arc Length Calculation
    arc = zeros(rp,1);
    arc(1,1) = chord*sqrt(pdat(1,1)^2+pdat(1,2)^2);
    for kk = 2:rp
        arc(kk,1) = arc(kk-1,1)+chord*sqrt((pdat(kk,1)-pdat(kk-
1,1))^2+(pdat(kk,2)-pdat(kk-1,2))^2);
    end

    %% X integration
    xloc = chord*xc; % x location of interest
    [rn cn] = find(pdat(:,1)<xc); % find x/c locations equal or less than point
of interest
    n = rn(length(rn))-1; % number of integration intervals

    ds = zeros(rp,1); % initialize dx matrix (dx is arc lenght along curved
surface)
    for nn = 1:rp-1
        ds(nn) = sqrt((chord*pdat(nn+1,1)-
chord*pdat(nn,1))^2+(chord*pdat(nn+1,2)-chord*pdat(nn,2))^2); % ds =
sqrt(dx^2+dy^2)
    end

    X = zeros(n+1,1); % place holder for trapezoidal integration (distance
along curved surface until x/c = 0.3)
    cs = 0; % arc distance confirmation variable

    for jj = 1:n
        X(jj+1) = X(jj) +
(gam*pdat(jj,3)/pt*sqrt(te(jj)/tt)+gam*pdat(jj+1,3)/pt*sqrt(te(jj+1)/tt))/2*ds(
jj); % X specified in Cohen & Reshotko
        cs = cs + ds(jj); % confirm arc distance
    end

    %% Record X and Ue in order to calculate Cf, establish other relevant
parameters

    Xf = X(n+1); % X for skin friction coefficient calculation
    Uf = Ue(n+1); % Ue for skin friction coefficient calculation
```

```
    uef = ue(n+1); % ue for skin friction coefficient calculation
    ka = 0.0223; % thermal conductivity of air at 250K, W/m-K
    ca = 1006; % specific heat of air, J/kg-K
    % vwall = 0.00004; % kinematic viscosity m^2/s (vary with sutherland's law
later)

    m = 0.174; % velocity power law exponent
    sdat = load('fsc_shear_data.txt'); % load tw, gw' and f" data, [tw g' f"]

    mt = 17.16e-6*(273.11+110.56)/(110.56+tt)*(tt/273.11)^(3/2); % stagnation
viscosity from Sutherland's Law
    vt = mt/rt; % stagnation kinematic viscosity

    cfdat = zeros(length(sdat(:,1)),3); % initialize matrix for recording Cf as
a function of tw, [tw Cf h q"]
    cfdat(:,1) = sdat(:,1); % fill in tw into first column
    twall = zeros(length(sdat(:,1)),1); % intialize twall matrix, K
    tref = zeros(length(sdat(:,1)),2); % intialize tref matrix, K
    tau = zeros(length(sdat(:,1)),1); % initialize shear stress matrix, N/m^2

    for kk = 1:length(sdat(:,1))

        twall(kk) = tt*(sdat(kk,1)); % wall temperature, K
        rwall = pdat(n+1,3)/(287*twall(kk)); % density at wall, kg/m^3
rt*(1+(gam-1)/2*Me(n+1)^2)^(-1/(gam-1));%
        mwall = 17.16e-
6*(273.11+110.56)/(110.56+twall(kk))*(twall(kk)/273.11)^(3/2); % wall viscosity
from Sutherland's Law
        vwall =  mwall/rwall; % wall kinematic viscosity vt%

        lam = (tt+111)/(twall(kk)+111)*sqrt(twall(kk)/tt); % lambda term

        cfdat(kk,2) =
(sdat(kk,3)*cosd(sweep)+sdat(kk,2)*sind(sweep))*(2*lam*(cfdat(kk,1)))*sqrt((m+1
)/2*vt/(Uf*Xf)); % skin friction coefficient
        cfdat(kk,3) =
.5*(sdat(kk,2))*cfdat(kk,2)*uef*ka/((sdat(kk,3)*cosd(sweep)+sdat(kk,2)*sind(swe
ep))*vwall); % heat transfer coefficient, W/m^2-K

        tau(kk) = .5*rwall*uef^2*cfdat(kk,2);

        cfdat(kk,4) = cfdat(kk,3)*(tt-twall(kk)); % heat flux, W/m^2
    end
    hrec(:,nc) = cfdat(:,3); % record convection coefficient as a function of
wall T and x/c
    qrec(:,nc) = -cfdat(:,4); % record convection heat transfer into the wall
as a function of wall T and x/c
    crec(nc,1) = xc; % record chord position



    nc = nc+1;
end
%% Original Plotting Module
figure(1)
plot(cfdat(:,1),cfdat(:,2),'b','linewidth',2)
```

```
xlabel('Wall Enthalpy Function, S')
ylabel('Skin Friction Coefficient, C_f')
grid on

figure(2)
plot(cfdat(:,1),cfdat(:,3),'b','linewidth',2)
xlabel('Wall Enthalpy Function, S')
ylabel('Convective Heat Transfer Coefficient, W/m^2-K')
grid on

figure(3)
plot(twall,cfdat(:,3),'b','linewidth',2)
xlabel('Wall Temperature, K')
ylabel('Convective Heat Transfer Coefficient, W/m^2-K')
grid on

figure(4)
plot(twall,-cfdat(:,4),'b','linewidth',2)
xlabel('Wall Temperature, K')
ylabel('Convective Heat Transfer into Wall, W/m^2')
grid on

%% Plot Heat Transfer Surface
figure(5)
[X Y] = meshgrid(crec,twall);
surf(X,Y,hrec)
xlabel('Chord Location, x/c')
ylabel('Wall Temperature, K')
zlabel('Heat Transfer Coefficient, W/m^2-K')

figure(6)
[XX YY] = meshgrid(crec,twall);
surf(XX,YY,qrec)
xlabel('Chord Location, x/c')
ylabel('Wall Temperature, K')
zlabel('Heat Transfer out of Wall, W/m^2-K')
```

APPENDIX D

ONE-DIMENSIONAL HEAT TRANSFER MODEL

D-1: Standard Atmosphere Equations

One of the goals of the one-dimensional model was to evaluate the behavior of the glove's surface temperature during the aircraft's climb phase. Finding static temperature, pressure, and viscosity as functions of altitude is critical for analyzing heat transfer on an aircraft. The Gulfstream G-III aircraft typically climbs through the troposphere and cruises in the tropopause. The troposphere extends from the surface of the Earth to approximately 11 km and is characterized by a linear decrease in temperature as a function of altitude. Ambient pressure also decreases non-linearly. The tropopause is characterized by constant temperature but still decreasing ambient pressure.

At altitudes less than 11 km the temperature in Kelvin and the pressure in Pascal are determined by Eqn (D-1) and Eqn (D-2), respectively. Here *H* represents altitude above mean sea level in meters.

$$T_\infty = 288.19 - 0.00649H \tag{D-1}$$

$$P_\infty = 101325\left(\frac{T_\infty}{288.08}\right)^{5.256} \tag{D-2}$$

For altitudes between 11 km and 25 km the ambient air temperature is a constant value of 216.65 K. The ambient pressure in this altitude band is described by Eqn (D-3).

$$P_\infty = 22650e^{(1.73-0.000157H)} \tag{D-3}$$

Most aircraft flight manuals give performance numbers in terms of indicated airspeed or Mach number. Therefore, it is important to understand how these parameters are related to freestream values and each other. The following equations were used to convert airspeed values to infinite freestream velocity and Mach number and vice versa.

Indicated airspeed is defined as the square root of twice the difference between total and freestream pressure divided by standard sea level density. This relationship is shown in Eqn (D-4).

$$V_{IAS} = \sqrt{\frac{2(P_0 - P_\infty)}{\rho_{SSL}}} \tag{D-4}$$

Indicated airspeed and Mach number are related by inserting the isentropic expression for stagnation pressure into Eqn (D-5).

$$V_{IAS} = \sqrt{\frac{2P_\infty\left(\left(1+\frac{\gamma-1}{2}M_\infty^2\right)^{\frac{\gamma}{\gamma-1}}-1\right)}{\rho_{SSL}}} \tag{D-5}$$

Eqn (D-6) can be solved for Mach number to yield the opposite relationship.

$$M_\infty = \sqrt{\frac{2}{\gamma-1}\left(\left(\frac{\rho_{SSL}V_{IAS}^2}{2P_\infty}+1\right)^{\frac{\gamma-1}{\gamma}}-1\right)} \tag{D-6}$$

The velocity of the infinite freestream can then be found from Eqn (D-7).

$$V_\infty = M_\infty\sqrt{\gamma R T_\infty} \tag{D-7}$$

D-2: Matlab Script for Computing Standard Atmosphere Conditions

The equations for the pressure and temperature as functions of altitude and airspeed were compiled into a Matlab script for computing the properties of air during the G-III's climb and cruise phases. The user is able to specify the aircraft's initial and cruise altitudes, airspeed or Mach number during the climb, climb rate, and time step between each calculated point. This script is printed below.

```
clear all
clc

%% Setup Parameters

dt = 0.001; % time step, s
cr = 2000; % climb rate, FPM
ta = 39000; % target altitude, ft
tpm = .75; % test point Mach number
rho_s = 1.225; % see level density, kg/m^3
vy = 180*.514444; % best climb speed, m/s
my = 0.7; % best climb Mach number
gam = 1.4; % ratio of specific heats
f_elev = 39000; % field elevation, ft
t_hold = 0.001; % time waiting on ground, s
t_cruise = 1800; % time cruising on condition, s
x_re = 4.41; % x location of interest for Re calcs, m

%% Ground Holding Module

nh = t_hold/dt; % number of iterations required for ground holding
h = f_elev*.3048; %altitude of airport, m

hdat = zeros(nh,8); % initialize data matrix for holding data [h,T,P,rho,mu]

for n = 1:nh
    hdat(n,1) = h; % record altitude, m
    hdat(n,2) = 15.04+273.15-0.00649*hdat(n,1); % temperature, K
    hdat(n,3) = 101325*(hdat(n,2)/288.08)^5.256; % pressure, Pa
    hdat(n,4) = hdat(n,3)/(287*hdat(n,2));   %density, kg/m^3
    hdat(n,5) = 17.16e-
6*((273.11+110.56)/(hdat(n,2)+110.56))*(hdat(n,2)/273.11)^1.5; % viscosity,
kg/m-s
    hdat(n,6) = 0; % KIAS
    hdat(n,7) = 0; % Mach
    hdat(n,8) = 0; % Vinf, m/s
end

%% Climb Module

t_climb  = (ta-h/.3048)/cr*60; % time to climb, s
nc = floor(t_climb/dt)+1; % number of iterations required for climb
cdat = zeros(nc,8); % initialize data matrix for holding data [h,T,P,rho,mu]
cdat(1,:) = hdat(nh,:); %import last values of ground matrix as starting point
cdat(1,6) = 180; % KIAS
```

```
cdat(1,7) = sqrt(2/(gam-
1)*((rho_s*(cdat(1,6)*.514444)^2/(2*cdat(1,3))+1)^((gam-1)/gam)-1)); % Mach
number
cdat(1,8) = cdat(1,7)*sqrt(gam*287*cdat(1,2)); % V_inf, m/s

for n = 2:nc
    cdat(n,1) = cdat(n-1,1)+dt*cr*.3048/60; % altitude, m

    if cdat(n,1)<11000 % loop to determine temperature in tropopause
        cdat(n,2) = 15.04+273.15-0.00649*cdat(n,1); % temperature, K
    else
        cdat(n,2) = 216.65;
    end

    if cdat(n,1) < 11000 % loop to determine pressure in tropopause
        cdat(n,3) = 101325*(cdat(n,2)/288.08)^5.256; % pressure, Pa
    else
        cdat(n,3) = 22650*exp(1.73-0.000157*cdat(n,1));
    end

    cdat(n,4) = cdat(n,3)/(287*cdat(n,2));   %density, kg/m^3
    cdat(n,5) = 17.16e-
6*((273.11+110.56)/(cdat(n,2)+110.56))*(cdat(n,2)/273.11)^1.5; % viscosity,
kg/m-s
    cdat(n,6) = 180; % KIAS
    cdat(n,7) = sqrt(2/(gam-
1)*((rho_s*(cdat(n,6)*.514444)^2/(2*cdat(n,3))+1)^((gam-1)/gam)-1)); % Mach
number
    if cdat(n,7) > my % Loop to correct speeds when climb Mach number is
exceeded
        cdat(n,7) = my;
        cdat(n,6) = sqrt((2*crudat(n,3)*((1+(gam-1)/2*crudat(n,7)^2)^(gam/(gam-
1))-1))/rho_s)/.51444444; %KIAS
    end
    cdat(n,8) = cdat(n,7)*sqrt(gam*287*cdat(n,2)); % V_inf, m/s
end

%% Cruise Module

ncru = t_cruise/dt; % number of points at cruise condition
crudat = zeros(ncru,8); % initialize data matrix for holding data
[h,T,P,rho,mu]

for n = 1:ncru
    crudat(n,1) = ta*.3048; % altitude, m

    if crudat(n,1)<11000 % loop to determine temperature after tropopause
        crudat(n,2) = 15.04+273.15-0.00649*crudat(n,1); % temperature, K
    else
        crudat(n,2) = 216.65;
    end

    if crudat(n,1) < 11000 % loop to determine pressure above tropopause
        crudat(n,3) = 101325*(crudat(n,2)/288.08)^5.256; % pressure, Pa
    else
        crudat(n,3) = 22650*exp(1.73-0.000157*crudat(n,1));
    end

    crudat(n,4) = crudat(n,3)/(287*crudat(n,2));   %density, kg/m^3
```

```
    crudat(n,5) = 17.16e-
6*((273.11+110.56)/(crudat(n,2)+110.56))*(crudat(n,2)/273.11)^1.5; % viscosity,
kg/m-s
    crudat(n,7) = tpm; % test point Mach number

    crudat(n,6) = sqrt((2*crudat(n,3)*((1+(gam-1)/2*crudat(n,7)^2)^(gam/(gam-
1))-1))/rho_s)/.51444444; %KIAS

    crudat(n,8) = crudat(n,7)*sqrt(gam*287*crudat(n,2)); % V_inf, m/s
end

%% Combine Data

data = zeros(nh+nc+ncru,10); % pre-allocate data matrix

data(1,1) = 0; % initial time
for n = 2:nc+nh+ncru
    data(n,1) = data(n-1,1)+dt; % time, s (fill in elapsed time in matrix)
end

data(1:nh,2:9) = hdat;
data(nh+1:nh+nc,2:9) = cdat;
data(nh+nc+1:nh+nc+ncru,2:9) = crudat;
data(:,10) = data(:,5).*data(:,9).*x_re./data(:,6); % Reynolds number

save('ht_atm_data2.txt','data','-ascii','-tabs')

%% Plotting

% figure(1)
% plot(data(:,2)/.3048,data(:,3))
% xlabel('Altitude, ft')
% ylabel('Temperature, K')
% title('Temperature vs. Altitude')
% grid on
%
% figure(2)
% plot(data(:,2)/.3048,data(:,4)/1000)
% xlabel('Altitude, ft')
% ylabel('Pressure, kPa')
% title('Pressure vs. Altitude')
% grid on
%
% figure(3)
% plot(data(:,2)/.3048,data(:,5))
% xlabel('Altitude, ft')
% ylabel('Density, kg/m^3')
% title('Density vs. Altitude')
% grid on
%
% figure(4)
% plot(data(:,2)/.3048,data(:,6))
% xlabel('Altitude, ft')
% ylabel('Viscosity, kg/m-s')
% title('Viscosity vs. Altitude')
% grid on
%
% figure(5)
% plot(data(:,2)/.3048,data(:,9)/.51444444,'b')
% hold on
```

```
% plot(data(:,2)/.3048,data(:,7),'r')
% xlabel('Altitude, ft')
% ylabel('Airspeed, Knots')
% title('Airspeed vs. Altitude')
% grid on
% legend('KTAS','KIAS')
%
% figure(6)
% plot(data(:,2)/.3048,data(:,8))
% xlabel('Altitude, ft')
% ylabel('Mach Number')
% title('Mach Number vs. Altitude')
% grid on
%
% figure(7)
% plot(data(:,2)/.3048,data(:,10))
% xlabel('Altitude, ft')
% ylabel('x-Reynolds Number')
% title('Reynolds Number vs. Altitude')
% grid on
```

D-3: Matlab Script for Computing Solar Radiation

The ASHRAE tables for solar radiation as a function of time of the year and position on the surface of the Earth were used to estimate the solar radiation incident on the glove's surface. A Matlab script was written to calculate solar radiation as a function of month of the year for a location at 35º N latitude.

```
clear all
clc

ash = [1202 0.141 0.103
    1187 0.142 0.104
    1164 0.149 0.109
    1130 0.164 0.12
    1106 0.177 0.13
    1092 0.185 0.137
    1093 0.186 0.138
    1107 0.182 0.134
    1136 0.165 0.121
    1166 0.152 0.111
    1190 0.142 0.106
    1204 0.141 0.103]; % ASHRAE Radiation Table

n = 1:12;
beta = 90-35+23.5*cos((n-6)/6*pi); % maximum daily sun elevation angle, deg
% beta = beta./2; % morning sun

cn = 1.1; % clearness factor

srad = zeros(12,4); % initialize solar radiation matrix [month, max normal
radiation, diffuse radiation, beta]

for n = 1:12
    srad(n,1) = n; % input month number
    srad(n,2) = ash(n,1)/exp(ash(n,2)/sind(beta(n)))*cn; % normal direct
radiation
    srad(n,3) = srad(n,2)*ash(n,3); % diffuse radiation
    srad(n,4) = beta(n); % maximum sun elevation angle
end

save('solar_rad.txt','srad','-ascii','-tabs')
```

D-4: One Dimensional Heat Transfer Equations

This appendix describes the equations used to calculate one-dimensional heat transfer through the wing glove. Heat transfer is assumed to only exist normal to the glove's surface in this model. The thicknesses of each layer of the model are assumed to be as follows: L_{CF} = 0.125 in, L_F = 1 in, L_{AU} = 0.125 in, L_{FU} = 6 in, and L_{AL} = 0.125 in. In the following equations k represents thermal conductivity, c represents specific heat at constant pressure, and ρ stands for density of the material. The subscripts CF, F, AU, FU, and AL stand for carbon fiber, foam, upper aluminum skin, fuel, and lower aluminum skin, respectively. The letter n with a material subscript represents the total number of nodes in that particular layer. The node temperatures at a particular time step are defined by the variable T_m^p.

The interval between nodes in the CFRP layer is calculated using the formula

$$\Delta y_{CF} = \frac{L_{CF}}{n_{CF} - 1} \tag{D-8}$$

When the aircraft is hot soaking on the ground in quiescent air the natural convection coefficient can be computed using Eqn (D-9).

$$h_{xu} = \frac{k_{AIR}}{x}\left(0.332\right)\mathrm{Re}_x^{1/2}\,\mathrm{Pr}^{1/3} \tag{D-9}$$

When the air on the surface of the wing is assumed to be turbulent the convection coefficient is estimated using the equation for the turbulent flat plate boundary layer:

$$h_{xu} = \frac{k_{AIR}}{x}\left(0.0296\right)\mathrm{Re}_x^{4/5}\,\mathrm{Pr}^{1/3} \tag{D-10}$$

Laminar convection coefficients are computed based on curve fits of convection coefficient versus wall temperature calculated with the method of Cohen & Reshotko (1956). During the climb condition with a turbulent boundary layer the convective heat transfer is assumed to be calculated based on the adiabatic recovery temperature of the wall. The turbulent recovery temperature is calculated using Eqn (D-11).

$$T_{RU} = T_\infty\left(1 + Pr^{1/3}\frac{\gamma - 1}{2}M_\infty^2\right) \tag{D-11}$$

The explicit formula for the temperature at node 1 on the surface of the model can then be written as:

$$T_1^{p+1} = \frac{2\Delta t}{\rho_{CF} c_{CF} \Delta y_{CF}} \left(h_{xu} \left(T_{RU} - T_1^p \right) + \frac{k_{CF}}{\Delta y_{CF}} \left(T_2^p - T_1^p \right) + \alpha_{CF-S} G_{SUN} - \varepsilon_{CF} \sigma \left(T_1^{p4} - T_{SKY}^4 \right) + \frac{\rho_{CF} c_{CF} \Delta y_{CF}}{2\Delta t} T_1^p \right) \quad \text{(D-12)}$$

Here the superscript p indicates a value at the current time step.

The equations for the interior nodes of CFRP are more simplistic as these points only interact with the nodes immediately above and below themselves. The explicit formula for these nodes is shown in Eqn (D-13).

$$T_m^{p+1} = \frac{k_{CF} \Delta t}{\rho_{CF} c_{CF} \Delta y_{CF}^2} \left(T_{m+1}^p + T_{m-1}^p \right) + \left(1 - \frac{2k_{CF} \Delta t}{\rho_{CF} c_{CF} \Delta y_{CF}^2} \right) T_m^p \quad \text{(D-13)}$$

The nodes that lie on the interface between the foam and CFRP draw on the properties of both materials, as shown in Eqn (D-14). The term q_B'' represents the heat flux generated by a heating blanket placed between the CFRP and foam.

$$T_m^{p+1} = \frac{2k_F \Delta t \left(T_{m+1}^p - T_m^p \right)}{\Delta y_F \left(\Delta y_{CF} \rho_{CF} c_{CF} + \Delta y_F \rho_F c_F \right)} + \frac{2k_{CF} \Delta t \left(T_{m-1}^p - T_m^p \right)}{\Delta y_{CF} \left(\Delta y_{CF} \rho_{CF} c_{CF} + \Delta y_F \rho_F c_F \right)} + \frac{2q_B'' \Delta t}{\left(\Delta y_{CF} \rho_{CF} c_{CF} + \Delta y_F \rho_F c_F \right)} + T_m^p \quad \text{(D-14)}$$

Here the distance between the foam nodes is defined by the equation:

$$\Delta y_F = \frac{L_F}{n_F - 1} \quad \text{(D-15)}$$

The foam's interior node temperatures are governed by Eqn (D-22).

$$T_m^{p+1} = \frac{k_F \Delta t}{\rho_F c_F \Delta y_F^2} \left(T_{m+1}^p + T_{m-1}^p \right) + \left(1 - \frac{2k_F \Delta t}{\rho_F c_F \Delta y_F^2} \right) T_m^p \quad \text{(D-16)}$$

The node temperatures at the interface between the foam and the upper surface of the wing are computed with the formula:

$$T_m^{p+1} = \frac{2k_F \Delta t \left(T_{m-1}^p - T_m^p \right)}{\Delta y_F \left(\Delta y_F \rho_F c_F + \Delta y_{AU} \rho_{AU} c_{AU} \right)} + \frac{2k_{AU} \Delta t \left(T_{m+1}^p - T_m^p \right)}{\Delta y_{AU} \left(\Delta y_F \rho_F c_F + \Delta y_{AU} \rho_{AU} c_{AU} \right)} + T_m^p \quad \text{(D-17)}$$

Here the distance between the nodes in the aluminum wing skin is defined as:

$$\Delta y_{AU} = \frac{L_{AU}}{n_{AU} - 1} \tag{D-18}$$

The temperatures of the inner aluminum nodes are computed using Eqn (D-19).

$$T_m^{p+1} = \frac{k_{AU}\Delta t}{\rho_{AU} c_{AU} \Delta y_{AU}^2}\left(T_{m+1}^p + T_{m-1}^p\right) + \left(1 - \frac{2k_{AU}\Delta t}{\rho_{AU} c_{AU} \Delta y_{AU}^2}\right) T_m^p \tag{D-19}$$

The temperature at the interface between the fuel and the wing skin is defined by Eqn (D-20).

$$T_m^{p+1} = \frac{2k_{AU}\Delta t\left(T_{m-1}^p - T_m^p\right)}{\Delta y_{AU}\left(\Delta y_{AU}\rho_{AU}c_{AU} + \Delta y_{FU}\rho_{FU}c_{FU}\right)} + \frac{2k_{FU}\Delta t\left(T_{m+1}^p - T_m^p\right)}{\Delta y_{FU}\left(\Delta y_{AU}\rho_{AU}c_{AU} + \Delta y_{FU}\rho_{FU}c_{FU}\right)} + T_m^p \tag{D-20}$$

Here the distance between the nodes in the fuel is determined by:

$$\Delta y_{FU} = \frac{L_{FU}}{n_{FU} - 1} \tag{D-21}$$

The temperatures of the inner nodes of the fuel layer are computed using Eqn (D-22). The physical situation in the fuel is drastically simplified because the effects of temperature strata within the fluid are ignored. If the fuel were cooled from above the fluid would tend to want to sink and mix with the warmer layer below.

$$T_m^{p+1} = \frac{k_{FU}\Delta t}{\rho_{FU} c_{FU} \Delta y_{FU}^2}\left(T_{m+1}^p + T_{m-1}^p\right) + \left(1 - \frac{2k_{FU}\Delta t}{\rho_{FU} c_{FU} \Delta y_{FU}^2}\right) T_m^p \tag{D-22}$$

The interface between the fuel and the lower aluminum skin is defined by the formula:

$$T_m^{p+1} = \frac{2k_{FU}\Delta t\left(T_{m-1}^p - T_m^p\right)}{\Delta y_{FU}\left(\Delta y_{AL}\rho_{AL}c_{AL} + \Delta y_{FU}\rho_{FU}c_{FU}\right)} + \frac{2k_{AL}\Delta t\left(T_{m+1}^p - T_m^p\right)}{\Delta y_{AL}\left(\Delta y_{AL}\rho_{AL}c_{AL} + \Delta y_{FU}\rho_{FU}c_{FU}\right)} + T_m^p \tag{D-23}$$

Here the distance between the nodes in the lower aluminum skin is defined as:

$$\Delta y_{AL} = \frac{L_{AL}}{n_{AL} - 1} \tag{D-24}$$

The equations for the interior node temperatures within the lower wing skin have the same form as the upper aluminum skin. The lower skin's temperature is calculated using Eqn (D-25).

$$T_m^{p+1} = \frac{k_{AL}\Delta t}{\rho_{AL} c_{AL} \Delta y_{AL}^2}\left(T_{m+1}^p + T_{m-1}^p\right) + \left(1 - \frac{2k_{AL}\Delta t}{\rho_{AL} c_{AU} \Delta y_{AL}^2}\right) T_m^p \tag{D-25}$$

The underside of the wing skin is exposed to the flow around the wing, which is assumed to always be turbulent during flight. The turbulent convection coefficient is approximated using the incompressible flat plate equation:

$$h_{xl} = \frac{k_{AIR}}{x}(0.0296) Re_x^{4/5} Pr^{1/3} \tag{D-26}$$

In the case that the aircraft is hot-soaked on the ground in quiescent air, the natural convection coefficient on the lower surface of the wing is approximated using Eqn (D-27).

$$h_{xl} = \frac{k_{AIR}}{x}(0.27)\left(\frac{\rho_{AIR}^2 c_{AIR} g (T_S - T_\infty) L^3}{\mu_{AIR} k_{AIR} T_\infty}\right) \tag{D-27}$$

The convective heat transfer on the lower surface of the wing is based on the difference with the adiabatic recovery temperature on the lower surface of the wing. This temperature is calculated using Eqn (D-28).

$$T_{RL} = T_\infty\left(1 + \mathrm{Pr}^{1/3}\frac{\gamma - 1}{2} M^2\right) \tag{D-28}$$

The temperature of the node on the lower surface of the wing can then be computed with Eqn (D-29).

$$T_m^{p+1} = T_m^p + \frac{2h_{xl}\Delta t}{\rho_{AL} c_{AL} \Delta y_{AL}}\left(T_{RL} - T_m^p\right) + \frac{2k_{AL}\Delta t}{\rho_{AL} c_{AL} \Delta y_{AL}^2}\left(T_{m-1}^p - T_m^p\right) - \frac{2\varepsilon_{AL}\sigma\Delta t}{\rho_{AL} c_{AL} \Delta y_{AL}}\left(T_m^{p4} - T_G^4\right) \tag{D-29}$$

The explicit finite difference equations shown above are subject to a numerical instability. If the time step is too large the equations may diverge towards an infinite value for node temperatures or violate the second law of thermodynamics. A stability criterion has been developed in order to avoid this phenomenon. The maximum allowable time step for the equations shown above is equal to the smallest value of Δt calculated using Eqn (D-30) through Eqn (D-40).

$$\Delta t \le \frac{\left(\Delta y_{CF} \rho_{CF} c_{CF}\right)}{2\left(h_{xu} + \frac{k_{CF}}{\Delta y_{CF}}\right)} \tag{D-30}$$

$$\Delta t \le \frac{\Delta y_{CF}^2 \rho_{CF} c_{CF}}{2k_{CF}} \tag{D-31}$$

$$\Delta t \le \frac{\left(\Delta y_{CF} \rho_{CF} c_{CF} + \Delta y_F \rho_F c_F\right)}{2\left(\frac{k_{CF}}{\Delta y_{CF}} + \frac{k_F}{\Delta y_F}\right)} \tag{D-32}$$

$$\Delta t \le \frac{\Delta y_F^2 \rho_F c_F}{2k_F} \tag{D-33}$$

$$\Delta t \le \frac{\left(\Delta y_{AU} \rho_{AU} c_{AU} + \Delta y_F \rho_F c_F\right)}{2\left(\frac{k_{AU}}{\Delta y_{AU}} + \frac{k_F}{\Delta y_F}\right)} \tag{D-34}$$

$$\Delta t \le \frac{\Delta y_{AU}^2 \rho_{AU} c_{AU}}{2k_{AU}} \tag{D-35}$$

$$\Delta t \le \frac{\left(\Delta y_{AU} \rho_{AU} c_{AU} + \Delta y_{FU} \rho_{FU} c_{FU}\right)}{2\left(\frac{k_{AU}}{\Delta y_{AU}} + \frac{k_{FU}}{\Delta y_{FU}}\right)} \tag{D-36}$$

$$\Delta t \le \frac{\Delta y_{FU}^2 \rho_{FU} c_{FU}}{2k_{FU}} \tag{D-37}$$

$$\Delta t \le \frac{\left(\Delta y_{AL} \rho_{AL} c_{AL} + \Delta y_{FU} \rho_{FU} c_{FU}\right)}{2\left(\frac{k_{AL}}{\Delta y_{AL}} + \frac{k_{FU}}{\Delta y_{FU}}\right)} \tag{D-38}$$

$$\Delta t \le \frac{\Delta y_{AL}^2 \rho_{AL} c_{AL}}{2k_{AL}} \tag{D-39}$$

$$\Delta t \le \frac{\left(\Delta y_{AL} \rho_{AL} c_{AL}\right)}{2\left(h_{xl} + \frac{k_{AL}}{\Delta y_{AL}}\right)} \tag{D-40}$$

D-5: One-Dimensional Heat Transfer Matlab Script

A Matlab script was generated in order to execute the one-dimensional finite element computations detailed previously. The contents of this script are shown below.

```
clear all
clc
tic
%% Data Archiving Names
%Used
fdat_file = 'ht_atm_data2.txt'; % name of flight data file to be loaded
icond = 'init74.txt'; % Initial conditions input into code

%Produced
case_name = 'case75.txt'; % Name of final case file
init_name = 'init76.txt'; % Name of initial condition file produced

%% Physical Properties of Materials
bc = 5.67e-8; % Stefan-Boltzmann Constant, W/m^2-K^4
gam = 1.4; % ratio of specific heats (air)
qgen = 300; % rate of heat generated by heating blanket, W/m^2
Tstart = load(icond); % initial temperature of all nodes, K

% Dimensions of Layers
Lcf = 0.125*0.0254; % thickness of carbon fiber, m
Lf = 1*0.0254; % thickness of construction foam, m
Lau = 0.125*0.0254; % thickness of upper aluminum skin, m
Lfu = 6*0.0254; % depth of fuel tank, m
Lal = 0.125*0.0254; % thickness of lower aluminum skin, m

% Glove Dimensions
chord = 4.41; % chord lenght of mid-glove, m
xc = 0.3; % x/c location of interest
xeval = 4.41*xc; % x-location evaluated, m

% Thermal Properties
% AIR
ka = 0.0223; % thermal conductivity of air at 250K, W/m-K
ca = 1006; % specific heat of air, J/kg-K
pr = 0.72; % Prandtl number
% SUN
month = 12; % number of month used
srad = load('solar_rad_am.txt'); % load ASHRAE solar irradiation data
za = 90-srad(month,4); % zenith angle, deg
Gsun = srad(month,2)*cosd(za)+srad(month,3); % total solar irradiation, W/m^2
% SKY
Tsky = 215; % Sky temperature, K
% GROUND
Tg = 288; % Ground temperature, K
% CFRP
rcf = 1400; % density of carbon fiber, kg/m^3
kcf = 0.78; % thermal conductivity of CFRP perpendicular to fibers, W/m-K
ccf = 790; % specific heat of CFRP, J/kg-K
ecf = 0.9; % emissivity of glove surface (0.9 W, 0.98 B)
acfs = 0.2; % absorbtivity of glove surface in solar wave band (0.2 W, 0.98 B)
% FOAM
```

```
rf = 110; % density of construction foam, kg/m^3
kf = 0.038; % thermal conductivity of construction foam, W/m-K
cf = 1000; % specific heat of construction foam, J/kg-K
% UPPER SURFACE ALUMINUM
rau = 2700; % density of upper aluminum, kg/m^3
kau = 167; % thermal conductivity of upper aluminum, W/m-K
cau = 896; % specific heat of upper aluminum, J/kg-K
% FUEL
rfu = 800; % density of fuel, kg/m^3
kfu = 0.115; % thermal conductivity of fuel, W/m-K
cfu = 1800; % specific heat of fuel, J/kg-K
% LOWER SURFACE ALUMINUM
ral = 2700; % density of lower aluminum, kg/m^3
kal = 167; % thermal conductivity of lower aluminum, W/m-K
cal = 896; % specific heat of lower aluminum, J/kg-K
eal = 0.9; % emissivity of white paint

% Number of Nodes Used (nodes at material interfaces are counted as part of
% both materials' totals).
ncf = 21; % of nodes in carbon fiber layer
nf = 21; % of nodes in foam layer
nau = 6; % of nodes in upper aluminum layer
nfu = 21; % of nodes in fuel layer
nal = 6;  % of nodes in lower aluminum layer

ntot = ncf+nf-1+nau-1+nfu-1+nal-1;

% Spacial Increment Calculator
dycf = Lcf/(ncf-1);
dyf = Lf/(nf-1);
dyau = Lau/(nau-1);
dyfu = Lfu/(nfu-1);
dyal = Lal/(nal-1);

%% Calculate Numerical Stability Restrictions

% Maximum convection coefficients
hxu_max = ka/(chord*.3)*.332*(10e6)^.5*pr^(1/3);
hxl_max = ka/(chord*.3)*.0296*(10e6)^(4/5)*pr^(1/3);
% Maximum time steps for numerical stability
dtlim = zeros(11,1); % initialize vector
dtlim(1) = dycf*rcf*ccf/(2*(hxu_max+kcf/dycf));
dtlim(2) = dycf^2*rcf*ccf/(2*kcf);
dtlim(3) = (dycf*rcf*ccf+dyf*rf*cf)/(2*(kcf/dycf+kf/dyf));
dtlim(4) = dyf^2*rf*cf/(2*kf);
dtlim(5) = (dyau*rau*cau+dyf*rf*cf)/(2*(kau/dyau+kf/dyf));
dtlim(6) = dyau^2*rau*cau/(2*kau);
dtlim(7) = (dyau*rau*cau+dyfu*rfu*cfu)/(2*(kau/dyau+kfu/dyfu));
dtlim(8) = dyfu^2*rfu*cfu/(2*kfu);
dtlim(9) = (dyal*ral*cal+dyfu*rfu*cfu)/(2*(kal/dyal+kfu/dyfu));
dtlim(10) = dyal^2*ral*cal/(2*kal);
dtlim(11) = dyal*ral*cal/(2*(hxl_max+kal/dyal));

dtmax = min(dtlim);

%% Load Flight Profile and Convection Data

fdat = load(fdat_file); % glove flight data: [t alt T P rho mu KIAS M Vinf Rec]
dt = fdat(2,1)-fdat(1,1); % time step from flight data
[rfdat cfdat] = size(fdat);
```

```
%% Spacial Location of Nodes

ypos = zeros(ntot,2); % initialize position matrix for nodes
ypos(1,1) = 1; % node number
ypos(1,2) = 0; % location of point on top surface
%CFRP Layer
for n = 2:ncf
    ypos(n,1) = ypos(n-1,1)+1; % number of next node
    ypos(n,2) = ypos(n-1,2)+dycf; % position of next node
end

%Foam Layer
for n = ncf+1:ncf+nf-1
    ypos(n,1) = ypos(n-1,1)+1; % number of next node
    ypos(n,2) = ypos(n-1,2)+dyf; % position of next node
end

%Upper Aluminum Layer
for n = ncf+nf:ncf+nf+nau-2
    ypos(n,1) = ypos(n-1,1)+1; % number of next node
    ypos(n,2) = ypos(n-1,2)+dyau; % position of next node
end

%Fuel Layer
for n = ncf+nf+nau-1:ncf+nf+nau+nfu-3
    ypos(n,1) = ypos(n-1,1)+1; % number of next node
    ypos(n,2) = ypos(n-1,2)+dyfu; % position of next node
end

%Lower Aluminum Layer
for n = ncf+nf+nau+nfu-2:ncf+nf+nau+nfu+nal-4
    ypos(n,1) = ypos(n-1,1)+1; % number of next node
    ypos(n,2) = ypos(n-1,2)+dyal; % position of next node
end

%% Temporal Heat Transfer Calculations

htdat = zeros(rfdat,ntot+1); % initialize heat transfer data storage matrix
htdat(1,:) = Tstart; % Set all nodes to initial temperature

for m = 2:rfdat % cycle through all flight conditon points
    % Convective HT Paramters
    tru = fdat(m,3)*(1+pr^(1/2)*(gam-1)/2*fdat(m,8)^2); % wall recovery
temperature on suction side, K
    trl = fdat(m,3)*(1+pr^(1/3)*(gam-1)/2*fdat(m,8)^2); % wall recovery
temperature on pressure side, K
    ttot = fdat(m,3)*(1+(gam-1)/2*fdat(m,8)^2); % freestream total temperature,
K

    if fdat(m,9)== 0 % use natural convection if velocity = 0
        if htdat(m-1,2)-fdat(1,3) > 0
            hxu = 0.15*(fdat(1,5)^2*ca*9.81*abs(htdat(m-1,2)-
fdat(1,3))*chord^3/(fdat(1,6)*ka*fdat(1,3)))^(1/3)*ka/chord;
        else
            hxu = 0.27*(fdat(1,5)^2*ca*9.81*abs(htdat(m-1,2)-
fdat(1,3))*chord^3/(fdat(1,6)*ka*fdat(1,3)))^(1/4)*ka/chord;
        end
        if htdat(m-1,ntot+1)-fdat(1,3) > 0
            hxl = 0.27*(fdat(1,5)^2*ca*9.81*abs(htdat(m-1,ntot+1)-
fdat(1,3))*chord^3/(fdat(1,6)*ka*fdat(1,3)))^(1/4)*ka/chord;
```

```
        else
            hxl = 0.15*(fdat(1,5)^2*ca*9.81*abs(htdat(m-1,ntot+1)-
fdat(1,3))*chord^3/(fdat(1,6)*ka*fdat(1,3)))^(1/3)*ka/chord;
        end
    else
%         hxu = ka/xeval*0.332*(fdat(m,10)*0.3)^(1/2)*pr^(1/3); % suction side
convective HT coefficient (laminar flat plate)
        hxu = 0.0003*htdat(m-1,2)^2-0.224*htdat(m-1,2)+52.795; % suction side
convective HT coefficient (laminar F-S curve fit)
        hxl = ka/xeval*0.0296*(fdat(m,10)*xc)^(4/5)*pr^(1/3); % pressure side
convective HT coefficient (turbulent)
    end

    % CFRP HT Equations
    htdat(m,2) =2*dt/(rcf*ccf*dycf)*(hxu*(ttot-htdat(m-1,2))+kcf/dycf*(htdat(m-
1,3)-htdat(m-1,2))+acfs*Gsun-ecf*bc*(htdat(m-1,2)^4-
Tsky^4)+rcf*ccf*dycf/(2*dt)*htdat(m-1,2)); %Glove surface temperature node
(laminar BL)
%     htdat(m,2) = 2*dt/(rcf*ccf*dycf)*(hxl*(trl-htdat(m-
1,2))+kcf/dycf*(htdat(m-1,3)-htdat(m-1,2))+acfs*Gsun-ecf*bc*(htdat(m-1,2)^4-
Tsky^4)+rcf*ccf*dycf/(2*dt)*htdat(m-1,2)); % Glove surface temperature node
(turbulent BL)
    for n = 2:ncf-1 % fill in CFRP interior nodes
        htdat(m,n+1) = kcf*dt/(rcf*ccf*dycf^2)*(htdat(m-1,n+2)+htdat(m-
1,n))+(1-2*kcf*dt/(rcf*ccf*dycf^2))*htdat(m-1,n+1); % CFRP interior node
temperature
    end
    htdat(m,ncf+1) = 2*kf*dt*(htdat(m-1,ncf+2)-htdat(m-
1,ncf+1))/(dyf*(dycf*rcf*ccf+dyf*rf*cf))+2*kcf*dt*(htdat(m-1,ncf)-htdat(m-
1,ncf+1))/(dycf*(dycf*rcf*ccf+dyf*rf*cf))+2*qgen*dt/(dycf*rcf*ccf+dyf*rf*cf)+ht
dat(m-1,ncf+1); % CFRP/foam boundary node

    % Foam HT Eqautions
    for n = ncf+1:ncf+nf-2
        htdat(m,n+1) = kf*dt/(rf*cf*dyf^2)*(htdat(m-1,n+2)+htdat(m-1,n))+(1-
2*kf*dt/(rf*cf*dyf^2))*htdat(m-1,n+1); % CFRP interior node temperature
    end
    htdat(m,ncf+nf) = 2*kf*dt*(htdat(m-1,ncf+nf-1)-htdat(m-
1,ncf+nf))/(dyf*(dyau*rau*cau+dyf*rf*cf))+2*kau*dt*(htdat(m-1,ncf+nf+1)-
htdat(m-1,ncf+nf))/(dyau*(dyau*rau*cau+dyf*rf*cf))+htdat(m-1,ncf+nf); %
Foam/upper aluminum boundary node

    % Upper Aluminum HT Equations
    for n = ncf+nf:ncf+nf+nau-3
        htdat(m,n+1) = trl; % set aluminum temp equal to turbulent recovery
temp
%         htdat(m,n+1) = kau*dt/(rau*cau*dyau^2)*(htdat(m-1,n+2)+htdat(m-
1,n))+(1-2*kau*dt/(rau*cau*dyau^2))*htdat(m-1,n+1); % Upper aluminum interior
node temperature
    end
    htdat(m,ncf+nf+nau-1) = 2*kau*dt*(htdat(m-1,ncf+nf+nau-2)-htdat(m-
1,ncf+nf+nau-1))/(dyau*(dyau*rau*cau+dyfu*rfu*cfu))+2*kfu*dt*(htdat(m-
1,ncf+nf+nau)-htdat(m-1,ncf+nf+nau-
1))/(dyfu*(dyau*rau*cau+dyfu*rfu*cfu))+htdat(m-1,ncf+nf+nau-1); % Fuel/upper
aluminum boundary node

    % Fuel HT Equations
    for n = ncf+nf+nau-1:ncf+nf+nau+nfu-4
```

```
        htdat(m,n+1) = kfu*dt/(rfu*cfu*dyfu^2)*(htdat(m-1,n+2)+htdat(m-
1,n))+(1-2*kfu*dt/(rfu*cfu*dyfu^2))*htdat(m-1,n+1); % Fuel interior node
temperature
    end
    htdat(m,ncf+nf+nau+nfu-2) = 2*kfu*dt*(htdat(m-1,ncf+nf+nau+nfu-3)-htdat(m-
1,ncf+nf+nau+nfu-2))/(dyfu*(dyal*ral*cal+dyfu*rfu*cfu))+2*kal*dt*(htdat(m-
1,ncf+nf+nau+nfu-1)-htdat(m-1,ncf+nf+nau+nfu-
2))/(dyal*(dyal*ral*cal+dyfu*rfu*cfu))+htdat(m-1,ncf+nf+nau+nfu-2); %
Fuel/lower aluminum boundary node

    % Lower Aluminum HT Equations
    for n = ncf+nf+nau+nfu-2:ncf+nf+nau+nfu+nal-5
        htdat(m,n+1) = kal*dt/(ral*cal*dyal^2)*(htdat(m-1,n+2)+htdat(m-
1,n))+(1-2*kal*dt/(ral*cal*dyal^2))*htdat(m-1,n+1); % Lower aluminum interior
node temperature
    end
    htdat(m,ncf+nf+nau+nfu+nal-3) = 2*hxl*dt/(ral*cal*dyal)*(trl-htdat(m-
1,ncf+nf+nau+nfu+nal-3))+2*kal*dt/(ral*cal*dyal^2)*(htdat(m-
1,ncf+nf+nau+nfu+nal-4)-htdat(m-1,ncf+nf+nau+nfu+nal-3))-
2*eal*bc*dt/(ral*cal*dyal)*(htdat(m-1,ncf+nf+nau+nfu+nal-3)^4-Tg^4)+htdat(m-
1,ncf+nf+nau+nfu+nal-3); % Lower aluminum/air boundary

    htdat(m,1) = htdat(m-1)+dt; % set time
end

%% HT Archiving and Sparsing
[rht cht] = size(htdat);

dtsto = 10; % time step of archived node temperatures
drow = dtsto/dt; % row increment needed to acheive desired storage time step

nsparse = floor((rht-1)/drow+1); % number of rows in sparsed data matrix
hts = zeros(nsparse,cht); % initialize sparsed matrix
nhts = 1; % initialize counter
for n = 1:drow:rht
    hts(nhts,:) = htdat(n,:); %input data from dense matrix
    nhts = nhts+1; % increment counter
end

save(case_name,'hts','-ascii','-tabs')

[rfin cfin] = size(htdat);
initcond = htdat(rfin,:);
save(init_name,'initcond','-ascii','-tabs')

%% HT Plotting Module

figure(1) % spacial temperature distribution of final state
plot(ypos(:,2),hts(nsparse,2:cht))
hold on
plot(ypos(:,2),hts(1,2:cht),'r')

% %% Multiple Plotting Module
% figure(2)
% for n = 1:nsparse
%     plot(ypos(:,2)/.0254,hts(n,2:cht))
%     axis([0 8 220 300])
%     xlabel('Depth from Surface, in')
%     ylabel('Temperature, K')
%     title('Temperature as a Function of Location')
```

```
%     M(n) = getframe;
% end
%
% movie(M,1,12)
%
% toc

Tsurf = initcond(1,2)

toc
```

APPENDIX E

TWO-DIMENSIONAL HEAT TRANSFER MODEL

E-1: Two-Dimensional Heat Transfer Equations

Computations of the heat transfer within a two-dimensional cross section of the wing glove were made using an explicit finite difference method. Here only the 1/8 in thick CFRP glove skin and a 1 in Rohacell 110 WF construction foam substrate layer were analyzed. A computational grid was superimposed on a cross section at a location of constant span such that there were 21 nodes in the surface-normal direction in each layer and 41 nodes along the line of constant span. The nodes along the interface between the CFRP and foam were counted once towards each material's node count. A total of 1681 nodes were analyzed. The area of interest on the glove stretched from 15% to 55% chord, meaning that chordwise spacing between the nodes was in intervals of 1% chord. The total chord length assumed for the gloved section of the wing was 4.41 meters.

The edges of the computational domain at 15% and 55% chord were assumed to be adiabatic. This assumption is a reasonable starting place because these locations are likely to have low temperature gradients in the chordwise direction. The equations for the nodes at the corners of the CFRP layer at 15% and 55% chord that interface with the freestream are shown in Eqn (E-1) and Eqn (E-2). In each of the following equations the *x* is the chordwise direction and *y* is the wall normal direction. The subscripts *m* and *n* correspond to the *x* and *y* directions, respectively. The variable x_c stands for x-location normalized by total chord length. In the equations below *k* represents thermal conductivity, *c* represents specific heat at constant pressure, and ρ stands for density of the material. The subscripts CF, and F stand for carbon fiber and foam, respectively. The letter *n* with a material subscript represents the total number of nodes in that particular layer. The node temperatures at a particular time step are defined by the variable $T_{m,n}^{p}$. Assuming that the datum of the *x* direction is placed at 15% chord, the corner node at 15% is governed by the equation:

$$T_{m.n}^{P+1} = T_{m,n}^{P} + \frac{2\Delta t}{\rho_{CF} C_{CF}} \left(\frac{h}{\Delta y_{CF}} \left(T_0 - T_{m,n}^{P} \right) + \frac{k_{CFX}}{\Delta x^2} \left(T_{m+1,n}^{P} - T_{m,n}^{P} \right) + \frac{k_{CFY}}{\Delta y_{CF}^2} \left(T_{m,n+1}^{P} - T_{m,n}^{P} \right) + \frac{1}{\Delta y_{CF}} \left(\alpha_{SUN} G_{SUN} - \varepsilon\sigma \left({T_{m,n}^{P}}^4 - T_{SKY}^4 \right) \right) \right) \tag{E-1}$$

The temperature of the CFRP corner node at 55% is then

$$T_{m.n}^{P+1} = T_{m,n}^{P} + \frac{2\Delta t}{\rho_{CF} C_{CF}} \left(\frac{h}{\Delta y_{CF}} \left(T_0 - T_{m,n}^{P} \right) + \frac{k_{CFX}}{\Delta x^2} \left(T_{m-1,n}^{P} - T_{m,n}^{P} \right) \right.$$
$$\left. + \frac{k_{CFY}}{\Delta y_{CF}^2} \left(T_{m,n+1}^{P} - T_{m,n}^{P} \right) + \frac{1}{\Delta y_{CF}} \left(\alpha_{SUN} G_{SUN} - \varepsilon\sigma \left({T_{m,n}^{P}}^4 - T_{SKY}^4 \right) \right) \right) \quad \text{(E-2)}$$

Here the convection coefficient along the CFRP surface is computed using a surface fit of the results of Beckwith (1958) for the Falkner-Skan boundary layer. The variable It should be noted that this equation is only valid for the 0.75 Mach, 39,000 ft test point.

$$h = 83.89 - 168x_c - 0.3479T_{m,n}^{P} + 214x_c^2 + 0.3365x_c T_{m,n}^{P} + 0.0006778\left(T_{m,n}^{P}\right)^2$$
$$- 112.9x_c^3 - 0.1668x_c^2 T_{m,n}^{P} - 0.0002551x_c\left(T_{m,n}^{P}\right)^2 \quad \text{(E-3)}$$
$$- 0.0000005104\left(T_{m,n}^{P}\right)^3$$

The surface fit for the Falkner-Skan boundary layer is also shown in Eqn (E-4).

$$h = 63.82 - 130.6x_c - 0.2544T_{m,n}^{P} + 169.5x_c^2 + 0.2487x_c T_{m,n}^{P}$$
$$+ 0.0004903\left(T_{m,n}^{P}\right)^2 - 90.84x_c^3 - 0.1244x_c^2 T_{m,n}^{P} \quad \text{(E-4)}$$
$$- 0.0001855x_c\left(T_{m,n}^{P}\right)^2 - 0.0000003667\left(T_{m,n}^{P}\right)^3$$

The temperature of the surface nodes between 15% and 55% chord are calculated using Eqn (E-5).

$$T_{m.n}^{P+1} = T_{m,n}^{P} + \frac{\Delta t}{\rho_{CF} C_{CF}} \left(\frac{2h}{\Delta y} \left(T_0 - T_{m,n}^{P} \right) + \frac{k_{CFX}}{\Delta x^2} \left(T_{m+1,n}^{P} + T_{m-1,n}^{P} - 2T_{m,n}^{P} \right) \right.$$
$$\left. + \frac{2k_{CFY}}{\Delta y^2} \left(T_{m,n+1}^{P} - T_{m,n}^{P} \right) + \frac{2}{\Delta y} \left(\alpha_{SUN} G_{SUN} - \varepsilon\sigma \left({T_{m,n}^{P}}^4 - T_{SKY}^4 \right) \right) \right) \quad \text{(E-5)}$$

The temperatures of the side walls of the CFRP at 15% and 55% chord between the surface and foam layer interfaces are given by Eqn (E-6) and Eqn (E-7), respectively.

$$T_{m.n}^{P+1} = T_{m,n}^{P} + \frac{\Delta t}{\rho_{CF} C_{CF}} \left(\frac{k_{CFY}}{\Delta y^2} \left(T_{m,n+1}^{P} + T_{m,n-1}^{P} - 2T_{m,n}^{P} \right) + \frac{2k_{CFX}}{\Delta x^2} \left(T_{m+1,n}^{P} - T_{m,n}^{P} \right) \right) \quad \text{(E-6)}$$

$$T_{m.n}^{P+1} = T_{m,n}^{P} + \frac{\Delta t}{\rho_{CF} C_{CF}} \left(\frac{k_{CFY}}{\Delta y^2} \left(T_{m,n+1}^{P} + T_{m,n-1}^{P} - 2T_{m,n}^{P} \right) + \frac{2k_{CFX}}{\Delta x^2} \left(T_{m-1,n}^{P} - T_{m,n}^{P} \right) \right) \quad \text{(E-7)}$$

The interior node temperatures of the CFRP are computed using Eqn (E-8).

$$T_{m.n}^{P+1} = T_{m,n}^{P} + \frac{\Delta t}{\rho_{CF} C_{CF}} \left(\frac{k_{CFY}}{\Delta y^2} \left(T_{m,n+1}^{P} + T_{m,n-1}^{P} - 2T_{m,n}^{P} \right) + \frac{k_{CFX}}{\Delta x^2} \left(T_{m+1,n}^{P} + T_{m-1,n}^{P} - 2T_{m,n}^{P} \right) \right) \tag{E-8}$$

The nodes at the interface between the CFRP and foam layers were assumed to be influenced by the properties of both materials. The temperatures at of the nodes at this interface at 15% and 55% chord were determined using Eqn (E-9) and Eqn (E-10), respectively. Here the term q_B'' is the heat flux generated by an internal heating blanket between the CFRP and foam.

$$T_{m.n}^{P+1} = T_{m,n}^{P} + \frac{2\Delta t}{\Delta x(\rho_{CF} C_{CF} \Delta y_{CF} + \rho_F C_F \Delta y_F)} \left(\frac{k_{CFY} \Delta x}{\Delta y_{CF}} \left(T_{m,n-1}^{P} - T_{m,n}^{P} \right) + \frac{k_F \Delta x}{\Delta y_F} \left(T_{m,n+1}^{P} - T_{m,n}^{P} \right) + \left(\frac{k_{CFX} \Delta y_{CF}}{\Delta x} + \frac{k_F \Delta y_F}{\Delta x} \right) \left(T_{m+1,n}^{P} - T_{m,n}^{P} \right) + q_B'' \Delta x \right) \tag{E-9}$$

$$T_{m.n}^{P+1} = T_{m,n}^{P} + \frac{2\Delta t}{\Delta x(\rho_{CF} C_{CF} \Delta y_{CF} + \rho_F C_F \Delta y_F)} \left(\frac{k_{CFY} \Delta x}{\Delta y_{CF}} \left(T_{m,n-1}^{P} - T_{m,n}^{P} \right) + \frac{k_F \Delta x}{\Delta y_F} \left(T_{m,n+1}^{P} - T_{m,n}^{P} \right) + \left(\frac{k_{CFX} \Delta y_{CF}}{\Delta x} + \frac{k_F \Delta y_F}{\Delta x} \right) \left(T_{m-1,n}^{P} - T_{m,n}^{P} \right) + q_B'' \Delta x \right) \tag{E-10}$$

The node temperatures along the CFRP interface between the 15% and 55% chord were computed with Eqn (E-11).

$$T_{m.n}^{P+1} = T_{m,n}^{P} + \frac{2\Delta t}{\Delta x(\rho_{CF} C_{CF} \Delta y_{CF} + \rho_F C_F \Delta y_F)} \left(\frac{k_{CFY} \Delta x}{\Delta y_{CF}} \left(T_{m,n-1}^{P} - T_{m,n}^{P} \right) + \frac{k_F \Delta x}{\Delta y_F} \left(T_{m,n+1}^{P} - T_{m,n}^{P} \right) + \left(\frac{k_{CFX} \Delta y_{CF}}{2\Delta x} + \frac{k_F \Delta y_F}{2\Delta x} \right) \left(T_{m+1,n}^{P} + T_{m-1,n}^{P} - 2T_{m,n}^{P} \right) + q_B'' \Delta x \right) \tag{E-11}$$

The nodes along the foam's sidewalls at 15% and 55% chord are governed by Eqn (E-12) and Eqn (E-13), respectively.

$$T_{m.n}^{P+1} = T_{m,n}^{P} + \frac{\Delta t k_F}{\rho_F C_F}\left(\frac{1}{\Delta y^2}\left(T_{m,n+1}^{P} + T_{m,n-1}^{P} - 2T_{m,n}^{P}\right) + \frac{2}{\Delta x^2}\left(T_{m+1,n}^{P} - T_{m,n}^{P}\right)\right) \tag{E-12}$$

$$T_{m.n}^{P+1} = T_{m,n}^{P} + \frac{\Delta t k_F}{\rho_F C_F}\left(\frac{1}{\Delta y^2}\left(T_{m,n+1}^{P} + T_{m,n-1}^{P} - 2T_{m,n}^{P}\right) + \frac{2}{\Delta x^2}\left(T_{m-1,n}^{P} - T_{m,n}^{P}\right)\right) \tag{E-13}$$

The temperatures of the interior nodes of the foam layer were determined using Eqn (E-14).

$$T_{m.n}^{P+1} = T_{m,n}^{P} + \frac{\Delta t k_F}{\rho_F C_F}\left(\frac{1}{\Delta y^2}\left(T_{m,n+1}^{P} + T_{m,n-1}^{P} - 2T_{m,n}^{P}\right) + \frac{1}{\Delta x^2}\left(T_{m+1,n}^{P} + T_{m-1,n}^{P} - 2T_{m,n}^{P}\right)\right) \tag{E-14}$$

The nodes at the bottom of the foam layer along the wing were set to equal the stagnation temperature of the freestream. This approximated a cold aluminum wing surface beneath the glove structure.

Like the one-dimensional explicit model, the two-dimensional explicit model was also subject to a numerical instability that could result due to too large a time step being used. The stability criteria for the system of equations listed previously are shown in Eqn (E-15) through Eqn (E-19). The smallest of these time steps should be considered the maximum allowable for the model in order for numerical stability to be maintained.

$$\Delta t \leq \frac{\rho_{CF} C_{CF}}{2}\left(\frac{h}{\Delta y_{CF}} + \frac{k_{CFX}}{\Delta x^2} + \frac{k_{CFY}}{\Delta y_{CF}^2}\right)^{-1} \tag{E-15}$$

$$\Delta t \leq \rho_{CF} C_{CF}\left(\frac{2h}{\Delta y_{CF}} + \frac{2k_{CFX}}{\Delta x^2} + \frac{2k_{CFY}}{\Delta y_{CF}^2}\right)^{-1} \tag{E-16}$$

$$\Delta t \leq \rho_{CF} C_{CF}\left(\frac{2k_{CFX}}{\Delta x^2} + \frac{2k_{CFY}}{\Delta y_{CF}^2}\right)^{-1} \tag{E-17}$$

$$\Delta t \leq \frac{\Delta x(\rho_{CF} C_{CF} \Delta y_{CF} + \rho_F C_F \Delta y_F)}{2}\left(\frac{k_{CFY}\Delta x}{\Delta y_{CF}} + \frac{k_F \Delta x}{\Delta y_F} + \frac{k_{CFX}\Delta y_{CF}}{\Delta x} + \frac{k_F \Delta y_F}{\Delta x}\right)^{-1} \tag{E-18}$$

$$\Delta t \leq \frac{\rho_F C_F}{k_F}\left(\frac{2}{\Delta x^2} + \frac{2}{\Delta y_F^2}\right)^{-1} \tag{E-19}$$

E-2: Two-Dimensional Heat Transfer Matlab Script

A Matlab script was developed in order to compute the heat transfer through a cross section of the wing glove using the two-dimensional heat transfer equations. The current script contains the atmospheric properties specific to the 0.75 Mach, 39,000 ft test point. The contests of this script are displayed below.

```
clear all
clc
tic
%% Data Archiving Names
%Used
% fdat_file = 'ht_atm_data2.txt'; % name of flight data file to be loaded

t_eval = 120; % Time over which surface temperature is evaluated,s

%Produced
case_name = '2D_case30_nodes.txt'; % Name of nodes case file
surf_name = '2D_case30_sfc.txt'; % Name of surface temperature case file

%% Physical Properties of Materials
bc = 5.67e-8; % Stefan-Boltzmann Constant, W/m^2-K^4
gam = 1.4; % ratio of specific heats (air)
qgen = 300; % rate of heat generated by heating blanket, W/m^2

% Dimensions of Layers
Lcf = 0.125*0.0254; % thickness of carbon fiber, m
Lf = 1*0.0254; % thickness of construction foam, m

% Glove Dimensions
chord = 4.41; % chord lenght of mid-glove, m
xc_min = 0.15; % Forward most x/c location of interest
xc_max = 0.55; % Aft most x/c location of interest
xc_tr = 0.40; % x/c location of BL transition
xeval = 4.41*xc_min; % x-location evaluated, m

% Thermal Properties
% AIR
ka = 0.0223; % thermal conductivity of air at 250K, W/m-K
ca = 1006; % specific heat of air, J/kg-K
pr = 0.72; % Prandtl number
% SUN
month = 12; % number of month used
srad = load('solar_rad_am.txt'); % load ASHRAE solar irradiation data
za = 90-srad(month,4); % zenith angle, deg
Gsun = srad(month,2)*cosd(za)+srad(month,3); % total solar irradiation, W/m^2
% SKY
Tsky = 215; % Sky temperature, K
% GROUND
Tg = 288; % Ground temperature, K
% CFRP
rcf = 1400; % density of carbon fiber, kg/m^3
kcfy = 0.78; % thermal conductivity of CFRP perpendicular to fibers, W/m-K
```

```
kcfx = 9.9; % thermal conductivity of CFRP parallel to fibers, W/m-K
ccf = 790; % specific heat of CFRP, J/kg-K
ecf = 0.9; % emissivity of glove surface (0.9 W, 0.98 B)
acfs = 0.2; % absorbtivity of glove surface in solar wave band (0.2 W, 0.98 B)
% FOAM
rf = 110; % density of construction foam, kg/m^3
kf = 0.038; % thermal conductivity of construction foam, W/m-K
cf = 1000; % specific heat of construction foam, J/kg-K

% Number of Nodes Used (nodes at material interfaces are counted as part of
% both materials' totals).
ncf = 21; % of nodes in carbon fiber layer
nf = 21; % of nodes in foam layer

ntot = ncf+nf-1;
nx = 41; % number of x direction nodes

% Spacial Increment Calculator
dycf = Lcf/(ncf-1);
dyf = Lf/(nf-1);
dx = (xc_max-xc_min)*chord/(nx-1); % chord-wise distance between nodes
dxc = (xc_max-xc_min)/(nx-1); % normalized chord-wise distance between nodes

% Initialize spacial node matrix for inputing temperature data
node = zeros(ntot,nx); % [increasing depth, increasing chord]
node2 = zeros(ntot,nx); % initialize matrix for recording next time step
information

%% Calculate Numerical Stability Restrictions

% Maximum convection coefficients
hmax = 150; % Maximum expected convection coefficient, W/m^2-K
% Maximum time steps for numerical stability
dtlim = zeros(5,1); % initialize vector
dtlim(1) = 0.5*rcf*ccf/(hmax/dycf+kcfx/dx^2+kcfy/dycf^2);
dtlim(2) = rcf*ccf/(2*hmax/dycf+2*kcfx/dx^2+2*kcfy/dycf^2);
dtlim(3) = rcf*ccf/(2*kcfy/dycf^2+2*kcfx/dx^2);
dtlim(4) =
0.5*dx*(rcf*ccf*dycf+rf*cf*dyf)/(kcfy*dx/dycf+kf*dx/dyf+kcfx*dycf/dx+kf*dyf/dx)
;
dtlim(5) = rf*cf/kf/(2/dx^2+2/dyf^2);

dtmax = min(dtlim);
dt = 10^floor(log10(dtmax))/2;

%% Load Flight Profile and Convection Data

% fdat = load(fdat_file); % glove flight data: [t alt T P rho mu KIAS M Vinf
Rec]
% dt = fdat(2,1)-fdat(1,1); % time step from flight data
% [rfdat cfdat] = size(fdat); % (time vector from 1:rdat)

% dt = 0.001;
t = 0:dt:t_eval; % time step, s
M = 0.75; % Mach number
Ts = 216.5; % static temperature, K
```

```
 %% Spacial Location of Nodes

ypos = zeros(ntot,2); % initialize position matrix for nodes
ypos(1,1) = 1; % node number
ypos(1,2) = 0; % location of point measured from top surface
%CFRP Layer
for n = 2:ncf
    ypos(n,1) = ypos(n-1,1)+1; % number of next node
    ypos(n,2) = ypos(n-1,2)+dycf; % position of next node
end

%Foam Layer
for n = ncf+1:ntot
    ypos(n,1) = ypos(n-1,1)+1; % number of next node
    ypos(n,2) = ypos(n-1,2)+dyf; % position of next node
end

% x position
xpos = xc_min*chord:dx:xc_max*chord; % spacial position vector
xcpos = xc_min:dxc:xc_max; % normalized spacial position vector

%% Initial Conditions Matrix
i_ttot = Ts*(1+(gam-1)/2*M^2); % freestream total temperature, K
node(:,:) = i_ttot; % set initial temperature equal to total temperature, K

%% Temporal Heat Transfer Calculations

k = 1; % time step (loop this later)
tsurf = zeros(10,1+nx);

for k = 1:length(t) % current h equations are only valid for M=0.75 at 39,000
ft

    ttot =  Ts*(1+(gam-1)/2*M^2); % freestream total temperature, K

    node2(ntot,:) = ttot; % set bottom of foam to total temperature
(approximate wing surface temp)

    % top CFRP corners
    h1 = 66.54-136.5*(xc_min)-
0.2657*node(1,1)+177.5*(xc_min)^2+.2596*(xc_min)*node(1,1)+0.0005136*node(1,1)^
2-95.29*(xc_min)^3-0.1299*(xc_min)^2*node(1,1)-0.0001943*(xc_min)*node(1,1)^2-
0.0000003857*node(1,1)^3;
%     h1 = h1*2;
    node2(1,1) = node(1,1)+dt/(rcf*ccf)*(2*h1/dycf*(ttot-
node(1,1))+2*kcfx/dx^2*(node(1,2)-node(1,1))+2*kcfy/dycf^2*(node(2,1)-
node(1,1))+2/dycf*(acfs*Gsun-ecf*bc*(node(1,1)^4-Tsky^4)));

    hnx = 66.54-136.5*(xc_max)-
0.2657*node(1,nx)+177.5*(xc_max)^2+.2596*(xc_max)*node(1,nx)+0.0005136*node(1,n
x)^2-95.29*(xc_max)^3-0.1299*(xc_max)^2*node(1,nx)-
0.0001943*(xc_max)*node(1,nx)^2-0.0000003857*node(1,nx)^3;
    if xcpos(nx)>= xc_tr
        hnx = hnx*10; % order of magnitude increase for turbulence
    end
%     hnx = hnx*2;
```

```
    node2(1,nx) = node(1,nx)+dt/(rcf*ccf)*(2*hnx/dycf*(ttot-
node(1,nx))+2*kcfx/dx^2*(node(1,nx-1)-node(1,nx))+2*kcfy/dycf^2*(node(2,nx)-
node(1,nx))+2/dycf*(acfs*Gsun-ecf*bc*(node(1,nx)^4-Tsky^4)));

    % top CFRP surface
    for m = 2:nx-1
        hm = 66.54-136.5*(xcpos(m))-
0.2657*node(1,nx)+177.5*(xcpos(m))^2+.2596*(xcpos(m))*node(1,nx)+0.0005136*node
(1,nx)^2-95.29*(xcpos(m))^3-0.1299*(xcpos(m))^2*node(1,nx)-
0.0001943*(xcpos(m))*node(1,nx)^2-0.0000003857*node(1,nx)^3;

        %BL Transition checker
        if xcpos(m) >= xc_tr
            hm = hm*10; % order of magnitude increase in convection due to
turbulence
        end
%         hm = hm*2;
        node2(1,m) = node(1,m)+dt/(rcf*ccf)*(2*hm/dycf*(ttot-
node(1,m))+kcfx/dx^2*(node(1,m-1)+node(1,m+1)-
2*node(1,m))+2*kcfy/dycf^2*(node(2,m)-node(1,m))+2/dycf*(acfs*Gsun-
ecf*bc*(node(1,m)^4-Tsky^4)));
    end

    % CFRP Side wall
    for n = 2:ncf-1
        % FWD side wall
        node2(n,1) = node(n,1)+dt/(rcf*ccf)*(kcfy/dycf^2*(node(n-
1,1)+node(n+1,1)-2*node(n,1))+2*kcfx/dx^2*(node(n,2)-node(n,1)));
        % AFT side wall
        node2(n,nx) = node(n,nx)+dt/(rcf*ccf)*(kcfy/dycf^2*(node(n-
1,nx)+node(n+1,nx)-2*node(n,nx))+2*kcfx/dx^2*(node(n,nx-1)-node(n,nx)));
    end

    %CFRP inner nodes
    for n = 2:ncf-1
        for m = 2:nx-1
            node2(n,m) = node(n,m)+dt/(rcf*ccf)*(kcfy/dycf^2*(node(n-
1,m)+node(n+1,m)-2*node(n,m))+kcfx/dx^2*(node(n,m-1)+node(n,m+1)-2*node(n,m)));
        end
    end

    % CFRP/Foam sidewall
    node2(ncf,1) =
node(ncf,1)+2*dt/(dx*(rcf*ccf*dycf+rf*cf*dyf))*(kcfy*dx/dycf*(node(ncf-1,1)-
node(ncf,1))+kf*dx/dyf*(node(ncf+1,1)-
node(ncf,1))+(kcfx*dycf/dx+kf*dyf/dx)*(node(ncf,2)-node(ncf,1))+qgen*dx);
    node2(ncf,nx) =
node(ncf,nx)+2*dt/(dx*(rcf*ccf*dycf+rf*cf*dyf))*(kcfy*dx/dycf*(node(ncf-1,nx)-
node(ncf,nx))+kf*dx/dyf*(node(ncf+1,nx)-
node(ncf,nx))+(kcfx*dycf/dx+kf*dyf/dx)*(node(ncf,nx-1)-node(ncf,nx))+qgen*dx);

    % CFRP/Foam boundary
    for m = 2:nx-1 % combine into previous for-loop of same interval
        node2(ncf,m) =
node(ncf,m)+2*dt/(dx*(rcf*ccf*dycf+rf*cf*dyf))*(kcfy*dx/dycf*(node(ncf-1,m)-
node(ncf,m))+kf*dx/dyf*(node(ncf+1,m)-
node(ncf,m))+(kcfx*dycf/(2*dx)+kf*dyf/(2*dx))*(node(ncf,m+1)+node(ncf,m-1)-
2*node(ncf,m))+qgen*dx);
```

```
    end

    % Foam Sidewall
    for n = ncf+1:ntot-1
        node2(n,1) = node(n,1)+dt*kf/(rf*cf)*(1/dyf^2*(node(n-1,1)+node(n+1,1)-
2*node(n,1))+2/dx^2*(node(n,2)-node(n,1)));
        node2(n,nx) = node(n,nx)+dt*kf/(rf*cf)*(1/dyf^2*(node(n-
1,nx)+node(n+1,nx)-2*node(n,nx))+2/dx^2*(node(n,nx-1)-node(n,nx)));
    end

    % Foam interior
    for n = ncf+1:ntot-1
        for m =2:nx-1
            node2(n,m) = node(n,m)+dt*kf/(rf*cf)*(1/dyf^2*(node(n+1,m)+node(n-
1,m)-2*node(n,m))+1/dx^2*(node(n,m+1)+node(n,m-1)-2*node(n,m)));
        end
    end

    node(:,:) = node2(:,:); % set next iteration's initial temperature values
to current values

    tsurf(k,1) = t(k); % insert current time elapsed
    tsurf(k,2:nx+1) = node(1,:); % record current surface temperatures
end

%% Sparsing and Data plotting

dts = 5; % delta t for plotted surface temp profiles
dns = floor(dts/dt);
nsp = 1:dns:length(t);
figure(1)
tsur_comp = zeros(length(nsp),nx+1); % initialize compressed surface
temperature matrix
for jj = 1:length(nsp)
    hold on
    plot(xcpos,tsurf(nsp(jj),2:nx+1))
    tsur_comp(jj,:) = tsurf(nsp(jj),:); % record compressed surface temp matrix
values
end
grid on
xlabel('Chord Location, x/c')
ylabel('Surface Temperature, K')
xlim([0.15 0.55])

%% HT Archiving

save(case_name,'node','-ascii','-tabs')
save(surf_name,'tsur_comp','-ascii','-tabs')

%% HT Plotting Module

figure(2)
pcolor(xcpos,-ypos(:,2)*.3048,node);
caxis([floor(min(min(node))) ceil(max(max(node)))]);
xlabel('x/c location')
ylabel('Position Below Upper Surface, m')
```

```
shading faceted
colorbar

toc

min(tsur_comp(length(nsp),2:nx+1))
max(tsur_comp(length(nsp),2:nx+1))
```

APPENDIX F

HOTFILM SIGNAL PROCESSING

F-1: Matlab Script for Extracting Data from Binary Files

The data reduction process for the hotfilm experiment on the FRL's O-2 begins by extracting the hotfilm voltage data from the binary files produced by the data acquisition software, LabView. A Matlab script for performing this extraction is shown below.

```
clear all
clc

file2 = fopen('HF2.bin','r','ieee-be');
Data(:,1) = fread(file2,inf,'double', 'ieee-be');
file3 = fopen('HF3.bin','r','ieee-be');
Data(:,2) = fread(file3,inf,'double', 'ieee-be');
file6 = fopen('HF6.bin','r','ieee-be');
Data(:,3) = fread(file6,inf,'double', 'ieee-be');
file7 = fopen('HF7.bin','r','ieee-be');
Data(:,4) = fread(file7,inf,'double', 'ieee-be');
file8 = fopen('HF8.bin','r','ieee-be');
Data(:,5) = fread(file8,inf,'double', 'ieee-be');
file9 = fopen('HF9.bin','r','ieee-be');
Data(:,6) = fread(file9,inf,'double', 'ieee-be');
file10 = fopen('HF10.bin','r','ieee-be');
Data(:,7) = fread(file10,inf,'double', 'ieee-be');

fclose('all');


%size(Data2)

Data1 = Data(6001:35624,:);
Data2 = Data(120001:149624,:);

fs=3000;                            %FrEqn of data acq.

%% Archiving
save('hf_data.txt','Data','-ascii','-tabs')

%% Plotting Module

t = linspace(0,(length(Data(:,1))-1)/fs,length(Data(:,1))); % generate time
plot(t,Data(:,1),'b')
hold on
plot(t,Data(:,2),'r')
```

F-2: Matlab Script for Performing Spectral Correlation

Once the hotfilm voltage data has been converted into a file format usable by Matlab using the script published in the previous section, a spectral analysis may be performed. The Fourier transforms of a datum sensor and comparison sensor are computed and then used for spectral correlations. A Matlab script has been written for this purpose and is shown below. The user inputs the voltage signals from the datum and comparison sensors as well as the sampling frequency. The code then outputs the signal Fourier transforms, spectral correlation function, and phase shift between the datum and comparison sensors.

```
clear all
clc

%% Inputs

Dataf = load('hf_data.txt'); % load flight data
fs = 3000; % Hz, Sample rate given by data acquisition parameters
nd = 10; % number of windows to be used for spectral correlation
nop = 10; % number of overlapping points

%% Data processing

[rd cd] = size(Dataf);
Dataf(1:(rd-10000),:) = []; % trim data into smaller windows that are several
times the dominant period
Data = Dataf;

nyquist = fs/2;
t = linspace(0,(length(Data(:,1))-1)/fs,length(Data(:,1))); % generate time
(not neccessary if time is given in data output)

%% Time series division

[ri ci] = size(Data); % size of trimmed matrix

int = floor((ri-nop+nop*nd)/nd); %size of window interval
no = int-nop; % number of non-overlapping points

%% Modulate window size to be power of 2 and adjust number of windows
accordingly

% int = 2^(nextpow2(int)); % make int a power of 2
% nd = floor((ri-nop)/(int-nop)); % adjust number of windows so that windows do
not exceed data

%% Loop to Generate Multiple Windows

Mavamp = zeros(int/2,ci); % initialize matrix to store average values of
amplitude for all windows
```

```
Mgam = zeros(int,ci-1); % initialize cross correlation of data and comparison
sensors
Mphase = zeros(int,ci-1); % initialize phase angle matrix

for jj = 2:ci
    %Initialize matrices for recording FFT data and frequencies
    Y = zeros(int,nd); % matrix for holding signal fft for each window
    Y2 = zeros(int,nd);
    amp = zeros(int/2,nd);
    amp2 = zeros(int/2,nd);
    freq = (1:int/2)/(int/2)*nyquist; % set up frequencies for plotting FFT

    count = 0; % initialize interval counter
    for k = 1:nd

        count = count+1; % interval counter
        Data_trim = Data((k-1)*no+1:(k-1)*no+int,:); % Data within window of
interest

        %% Windowing Function

        wind = zeros(int,1); % initialize window function matrix

%         wind(:,1)=hamming(int); % Hamming Window
        wind(:,1) = hann(int); % Hann Window

        for nn = 1:ci
            Data_trim(:,nn) = Data_trim(:,nn).*wind(:,1); % Apply window to
data
        end

        %% First FFT Module

        Y(:,count) = fft(Data_trim(:,1));
        amp(:,count) = 2*abs(Y(1:floor(int/2),count))/int; % Amplitude of
signal (Correct to single sided spectrum by multiplying by two, normalize Y
magnitude by signal length)

        %% Second FFT Module (can collapse into a loop with the other sensor
later)

        Y2(:,count) = fft(Data_trim(:,jj));
        amp2(:,count) = 2*abs(Y2(1:floor(int/2),count))/int;

    end

    avamp = 0; % average of amplitudes across windows
    avamp2 = 0;

    for nn = 1:nd
        avamp = avamp + amp(:,nn);
        avamp2 = avamp2 + amp2(:,nn);
    end
    Mavamp(:,1) = avamp./nd; % make into average value and record in average
amplitude value matrix (columns correspond to comparing signal 1 to signal n of
column n-1)
    Mavamp(:,jj) = avamp2./nd;

    %% Spectral Correlation
```

```
    Ga = 0;
    Gb = 0;
    Gab = 0;

    for nn = 1:nd
        Ga = Ga + abs(Y(:,nn)).^2;
        Gb = Gb + abs(Y2(:,nn)).^2;
        Gab = Gab + conj(Y(:,nn)).*Y2(:,nn); % Spectral correlation
    end

    gam = abs(Gab).^2./(Ga.*Gb); % Spectral correlation coefficient
    Mgam(:,jj-1) = gam;

    %% Phase Calculator
    phase = zeros(length(Gab),1); % initialize row vector for phase angles

    for n = 1:length(Gab)
        phase(n,1) = 180/pi*atan2(imag(Gab(n)),real(Gab(n)));
    end

    Mphase(:,jj-1) = phase(:,1); % enter phase into matrix (columns correspond
to comparing signal 1 to signal n of column n-1)

end

%% Plots (loop in order to generate subplots for each sensor)

for jj = 2:ci

    figure(jj-1)
    subplot(2,2,1)
    plot(t,Data(:,1),'b')
    hold on
    plot(t,Data(:,jj),'r')
    grid on
    xlabel('Time, s')
    ylabel('Amplitude, V')
    title('Hotfilm Signal vs. Time')

    subplot(2,2,2)
    loglog(freq,Mavamp(:,1),'b')
    hold on
    loglog(freq,Mavamp(:,jj),'r')
    grid on
    xlabel('Frequency, Hz')
    ylabel('Signal Amplitude, V')
    title('Signal Discrete Fourier Transform')

    sc = Mgam(1:floor(length(Gab)/2),jj-1);

    subplot(2,2,3)
    semilogx(freq,sc)
    grid on
    ylim([0 1])
    xlabel('Frequency, Hz')
    ylabel('Correlation Coefficient')
    title('Spectral Correlation')

    subplot(2,2,4)
    phi = Mphase(1:floor(length(Gab)/2),jj-1);
```

```
    semilogx(freq,phi)
    ylim([-180 180])
    set(gca,'YTick',[-180 -150 -120 -90 -60 -30 0 30 60 90 120 150 180])
    grid on
    xlabel('Frequency, Hz')
    ylabel('Phase Angle, deg')
    title('Phase Angle Between Signals')

end

%% Welch's Method PSD

wdat = zeros(floor(int/2)+1,cd); % initialize matrix for storing pwelch data

for n = 1:cd
    [Pxx,f_welch] = pwelch(Data(:,n),int,nop,int,fs,'onesided'); % [Pxx,w] =
pwelch(x,window,noverlap,nfft,fs,'onesided')
    wdat(:,n) = Pxx; %Pwelch power data

    %% Plotter
    figure(jj)
    loglog(f_welch,Pxx)
    grid on
    xlabel('Frequency, Hz')
    ylabel('Power Density, dB/Hz')
    aa = double('Hotfilm ');
    aa(length(aa)+1) = num2str(n);
    title(char(aa));

    jj = jj+1;
end
```

F-3: Wave Vector Uncertainty Analysis Equations

Understanding the uncertainties in the magnitude and direction of the wave vector predicted by hotfilms designed to detect traveling disturbances is important for establishing the quality of the experimental hotfilm data. The primary source of uncertainty is erroneous assumptions of where the wave must be located on an individual element in order for it to register the wave's presence. It is not known if the wave is detected on the edges or in the middle of the wire. To this end equations were developed to account for errors in the assumed detection location on each sensing element.

Uncertainty analysis begins by defining the maximum position errors on each sensor, δx_n and δy_n, anticipated due to the geometry of the sensing elements. The wave vector velocity magnitude, V, and wave vector angle, θ, for the wave under analysis are also specified. The angle that the wave front makes with the *x* axis is computed using Eqn (F-1).

$$\theta_w = \theta - \frac{\pi}{2} \tag{F-1}$$

The geometry of the hotfilm elements with respect to the datum sensor is also an input for the computations. The datum sensor is indicated by the subscript 1.

$$\Delta x_n = x_n - x_1 \tag{F-2}$$

$$\Delta y_n = y_n - y_1 \tag{F-3}$$

The Cartesian distance between sensor *n* and the datum and the angle the vector pointing from the datum to sensor *n* makes with respect to the *x* axis are given by Eqn (F-4) and Eqn (F-5).

$$d_n = \sqrt{\Delta x_n^2 + \Delta y_n^2} \tag{F-4}$$

$$\phi_n = \tan^{-1}\left(\frac{\Delta y_n}{\Delta x_n}\right) \tag{F-5}$$

The geometric parameters calculated with Eqn (F-4) and Eqn (F-5) represent the configuration that the experimental calculations assume to be correct. The uncertainty values δx and δy are the differences between the assumed locations used for calculation and the actual locations at which the wave is detected. The geometric positions of the actual wave detection locations with respect to the datum position are described by Eqn (F-6) through Eqn (F-10).

$$x_{n\delta} = x_n + \delta x_n \tag{F-6}$$

$$y_{n\delta} = y_n + \delta y_n \tag{F-7}$$

$$\Delta x_{n\delta} = x_{n\delta} - x_{1\delta} \tag{F-8}$$

$$\Delta y_{n\delta} = y_{n\delta} - y_{1\delta} \tag{F-9}$$

$$d_{n\delta} = \sqrt{\Delta x_{n\delta}^2 + \Delta y_{n\delta}^2} \tag{F-10}$$

The next step in the uncertainty analysis is to simulate the desired wave front and determine the times at which it will impact the sensors whose actual detection locations were calculated previously. The times of impact are referenced to the time at which the wave impacts the datum sensor, which is taken to be $t_{w1} = 0$ for the current analysis. The distance that the two-dimensional wave front must travel between impacting sensor *n* and the datum sensor is given by Eqn (F-11). The time required for the wave to travel between signal *n* and the datum is computed using Eqn (F-12).

$$d_{wn} = (\Delta y_{n\delta} - \Delta x_{n\delta} \tan(\theta_w)) \cos(\theta_w) \tag{F-11}$$

$$t_{wn} = \frac{d_{wn}}{V} \tag{F-12}$$

The polar plot of vectors described in Section 4 derives its magnitude from the group velocity computed using spectral techniques and its direction from the geometry of the hotfilm sensors. The spectral techniques used to determine group velocity are also subject to errors due to slight differences in the predicted and actual sensing locations. The magnitude of the velocity vector between the datum sensor and sensor *n* in the direction ϕ_n is given by Eqn (F-13).

$$V_n = \frac{d_n}{t_{wn}} \tag{F-13}$$

A first order curve fit of the form $z = z_0 + z_1 x$ can then be used to fit a line through the tips of the V_n vectors. The y-intercept and slope and of the line can then be used to determine the angle that the wave's normal vector makes with the *x* axis. The four possible combinations of the signs of y_0 and y_1 are listed in Table F-1.

Table F-1 Effect of y-intercept and slope combinations on θ_e

Combination 1:	$z_0 > 0$	$z_1 > 0$	$\theta_e = \tan^{-1}(z_1) + \frac{\pi}{2}$
Combination 2:	$z_0 < 0$	$z_1 > 0$	$\theta_e = \tan^{-1}(z_1) + \frac{3\pi}{2}$
Combination 3:	$z_0 > 0$	$z_1 < 0$	$\theta_e = \tan^{-1}(z_1) + \frac{\pi}{2}$
Combination 4:	$z_0 < 0$	$z_1 < 0$	$\theta_e = \tan^{-1}(z_1) + \frac{3\pi}{2}$

The magnitude of the wave front's velocity vector can then be computed from Eqn (F-14). It should be noted that there are *n*-1 possible resultants for this vector, so the results can be averaged or some other statistical method can be used to determine the most likely magnitude of the vector.

$$w_n = \frac{\left(\Delta y_n - \Delta x_n \tan\left(\theta_e - \frac{\pi}{2}\right)\right)\cos\left(\theta_e - \frac{\pi}{2}\right)}{t_{wn}} \tag{F-14}$$

F-4: Matlab Script for Computing Maximum Uncertainty for a Specified Configuration

The uncertainty equations for the hotfilm sensors mentioned previously were consolidated into a Matlab script for the purpose of computing the maximum uncertainty in wave vector magnitude and direction for a particular sensor configuration. The user inputs the physical dimensions of the sensor as well as the phase speed and direction of the wave under analysis. The expected uncertainty in detection location along the individual sensors can also be controlled to study the impact of using elements of different lengths.

```
clear all
clc

dx = 0.005; % uncertainty in x
dy = 0.005; % uncertainty in y
sim = 10000; %number of simulations to run

%WAVE PARAMETERS [WILL BE UNKNOWN IN ACTUAL CASE]
theta = 280; %deg, angle of wave vector wrt sensor cs
V = 1575; %in/s, wave velocity (SWIFT TAS = 304 ft/s)
thetaw = theta-90; %deg, angle of wave front wrt sensor cs

%PHYSICAL PARAMETERS OF SENSOR [FOUND FROM MEASUREMENTS ON ACTUAL SENSOR]

lam = 30; %deg, wing leading edge sweep (for aligning wave vector with AC CS)

%Origin is set to (0,0) at center of sensor 1 (x1=y1=0)
%The actual sensor 1 is arbitrary and fluctuates with whichever sensor is
%the current datum.  Other sensor numbers can be rearranged accordingly

XY = [0 0
    1.24/25.4 2.45/25.4
    2.24/25.4 0
    3.48/25.4 2.45/25.4
    4.51/25.4 0
    5.75/25.4 2.45/25.4
    6.77/25.4 0
    7.97/25.4 2.45/25.4
    8.99/25.4 0
    10.21/25.4 2.45/25.4
    11.23/25.4 0
    12.43/25.4 2.45/25.4
    13.48/25.4 0]; % x,y coordinates of sensor 1-13, inches

[rw cl] = size(XY);

DP = zeros(rw,2); %Initialize resultant distance and angle phi
for n = 1:rw
    DP(n,1) = sqrt(XY(n,1)^2+XY(n,2)^2);
    DP(n,2) = atan2(XY(n,2),XY(n,1))*180/pi;
end
```

```
t1 = 0; %[THIS WILL BE REPLACED WITH AN ACTUAL TIME FOR READ DATA

res = zeros(sim,2); %initialize angle, V storage matrix

for nm = 1:sim


    XYn = XY; % reset XP new matrix to original values before applying each
uncertainty

    for jj = 1:rw % construct new XY matrix
        if mod(jj,2)==0 %check to is see if j is even
            XYn(jj,1) = XY(jj,1)-dx+(2*dx).*rand(1,1); %add x uncertainty to
horizontal sensors
        else
            XYn(jj,2) = XY(jj,2)-dy+(2*dy).*rand(1,1); %add y uncertainty to
vertical sensors
        end
    end


    DPn = zeros(rw,2); %Initialize new resultant distance and angle phi
    for n = 1:rw
        DPn(n,1) = sqrt((XYn(n,1)-XYn(1,1))^2+(XYn(n,2)-XYn(1,2))^2); %
reference point is point 1
        DPn(n,2) = atan2((XYn(n,2)-XYn(1,2)),(XYn(n,1)-XYn(1,1)))*180/pi;
    end

    %CALCULATED PARAMETERS FOR TEST RUN [USE ACTUAL SENSOR LOCATION]

    wdn = zeros(rw-1,1); %in, distance from wave front to actual sensor
measuring point along direction of propagation
    for n = 2:rw
        wdn(n-1,1) = ((XYn(n,2)-XYn(1,2))-(XYn(n,1)-
XYn(1,1))*tand(thetaw))*cosd(thetaw);
    end

    tn = zeros(rw-1,1); %time for wave to impact sensor n
    for n = 2:rw
        tn(n-1,1) = wdn(n-1,1)/V;
    end

    %WAVE ANGLE CALCULATOR [THIS MODULE WILL BE USED FOR ACTUAL FLIGHT DATA]

    %Vector lengths using assumed sensor x and y positions with actual time
    vect = zeros(rw-1,2); %vector containing x and y coordinates to be curve
fitted
    for n = 1:rw-1
        vect(n,1) = DP(n+1,1)/(tn(n,1)-t1)*cosd(DP(n+1,2));
        vect(n,2) = DP(n+1,1)/(tn(n,1)-t1)*sind(DP(n+1,2));
    end

%     %Plot individual sensor vectors
%     figure(1)
%     [row col] = size(vect);
%     quiv = zeros(row,4);
%     quiv(:,3:4) = vect;
%     quiver(quiv(:,1),quiv(:,2),quiv(:,3),quiv(:,4),'b')

    %Curve fit to vector endpoints
```

```
    coeff = curvefit(vect,1);

    %Vector angle calculator based on slope and y-intercept of fit line
    if coeff(1)>0 && coeff(2)>0
        theta_exp = atand(coeff(2))+90; % angle of inclination of curve fit
line
    elseif coeff(1)<0 && coeff(2)>0
        theta_exp = atand(coeff(2))+270; %
    elseif coeff(1)>0 && coeff(2)<0
        theta_exp = atand(coeff(2))+90;
    else coeff(1)<0 && coeff(2)<0;
        theta_exp = atand(coeff(2))+270;
    end

    res(nm,1) = theta_exp; %Experimentally determined vector angle, deg
    %     theta_exp_ac = theta_exp-lam %deg, wave vector in AC CS

    vtot = zeros(rw-1,1);
    for n = 2:rw
        vtot(n-1,1) = (XY(n,2)-XY(n,1)*tand(theta_exp-90))*cosd(theta_exp-
90)/(tn(n-1,1)-t1);
    end

    res(nm,2) = mean(vtot); % magnitude of phase speed vector

end

resr = zeros(sim,2);
resr(:,1) = res(:,1).*pi./180; % convert angle to radians
resr(:,2) = res(:,2);

%% Plotting Module
% hold on
figure(2)
polar(resr(:,1),resr(:,2),'b.')
% polar(theta*180/pi,V,'r.')

data = [max(res(:,1)) (max(res(:,2))-mean(res(:,2)))/mean(res(:,2))*100 %column
1: theta, column 2: velocity
    mean(res(:,1)) (mean(res(:,2))-mean(res(:,2)))/mean(res(:,2))*100
    min(res(:,1)) (min(res(:,2))-mean(res(:,2)))/mean(res(:,2))*100]

title('Polar Plot of Possible Instrument Readings');
```

F-5: Matlab Script for Studying Uncertainty as a Function of Sensor Position

Dimensioning the hotfilm sensor array is a challenging multi-variable problem. To aide in this task a script was desired that would vary the dimensions of a sensor array in order to study the different configurations' effects on the wave vector uncertainty. The script shown below is capable of varying the position of a sensor in order to create a surface plot of the uncertainty in phase speed and direction as a function of the sensor's location.

```
clear all
% clc

dx = 0.005; % uncertainty in x
dy = 0.005; % uncertainty in y
sim = 1000; %number of simulations to run

%WAVE PARAMETERS [WILL BE UNKNOWN IN ACTUAL CASE]
theta = 280; %deg, angle of wave vector wrt sensor cs
V = 146; %in/s, wave velocity (SWIFT TAS = 304 ft/s)
thetaw = theta-90; %deg, angle of wave front wrt sensor cs

%PHYSICAL PARAMETERS OF SENSOR [FOUND FROM MEASUREMENTS ON ACTUAL SENSOR]

lam = 30; %deg, wing leading edge sweep (for aligning wave vector with AC CS)

%Origin is set to (0,0) at center of sensor 1 (x1=y1=0)
%The actual sensor 1 is arbitrary and fluctuates with whichever sensor is
%the current datum.  Other sensor numbers can be rearranged accordingly

%LOOPING PARAMETERS
itx = 9; % number of x points to evaluate minus 1
ity = 10; % number of y points to evaluate

deltx = 0.089/itx;
delty = 0.1/ity;

x = -deltx; %placeholders for actual x and y values of sensor element
num = 1; % row number placeholder for results matrix
data = zeros((itx+1)*ity,3); %ititialize final results matrix

for nx = 1:itx+1 %use +1 in order to start x location of middle sensor at 0
    x = x+deltx; %create new x location for sensor
    y = 0; % reset y to zero before beginning new x location sequence
    for ny = 1:ity
        y = y+delty; % create new y location for sensor

        XY = [0 0
            x y
            0.089 0];
        %     0.0376+2.25/25.4 0.051
        %     0.089+2.25/25.4 0
        %     0.0376+2*2.25/25.4 0.051
        %     0.089+2*2.25/25.4 0
```

```
%     0.0376+3*2.25/25.4 0.051
%     0.089+3*2.25/25.4 0
%     0.0376+4*2.25/25.4 0.051
%     0.089+4*2.25/25.4 0
%     0.0376+5*2.25/25.4 0.051
%     0.089+5*2.25/25.4 0]; % x,y coordinates of sensor 1-13

[rw cl] = size(XY);

DP = zeros(rw,2); %Initialize resultant distance and angle phi
for n = 1:rw
    DP(n,1) = sqrt(XY(n,1)^2+XY(n,2)^2);
    DP(n,2) = atan2(XY(n,2),XY(n,1))*180/pi;
end

t1 = 0; %[THIS WILL BE REPLACED WITH AN ACTUAL TIME FOR READ DATA

res = zeros(sim,2); %initialize angle, V storage matrix

for nm = 1:sim


    XYn = XY; % reset XP new matrix to original values before applying
each uncertainty

    for jj = 1:rw % construct new XY matrix
        if mod(jj,2)==0 %check to is see if j is even
            XYn(jj,1) = XY(jj,1)-dx+(2*dx).*rand(1,1); %add x
uncertainty to horizontal sensors
        else
            XYn(jj,2) = XY(jj,2)-dy+(2*dy).*rand(1,1); %add y
uncertainty to vertical sensors
        end
    end


    DPn = zeros(rw,2); %Initialize new resultant distance and angle phi
    for n = 1:rw
        DPn(n,1) = sqrt((XYn(n,1)-XYn(1,1))^2+(XYn(n,2)-XYn(1,2))^2); %
reference point is point 1
        DPn(n,2) = atan2((XYn(n,2)-XYn(1,2)),(XYn(n,1)-
XYn(1,1)))*180/pi;
    end

    %CALCULATED PARAMETERS FOR TEST RUN [USE ACTUAL SENSOR LOCATION]

    wdn = zeros(rw-1,1); %in, distance from wave front to actual sensor
measuring point along direction of propagation
    for n = 2:rw
        wdn(n-1,1) = ((XYn(n,2)-XYn(1,2))-(XYn(n,1)-
XYn(1,1))*tand(thetaw))*cosd(thetaw);
    end

    tn = zeros(rw-1,1); %time for wave to impact sensor n
    for n = 2:rw
        tn(n-1,1) = wdn(n-1,1)/V;
    end

    %WAVE ANGLE CALCULATOR [THIS MODULE WILL BE USED FOR ACTUAL FLIGHT
DATA]
```

```
            %Vector lengths using assumed sensor x and y positions with actual
time
            vect = zeros(rw-1,2); %vector containing x and y coordinates to be
curve fitted
            for n = 1:rw-1
                vect(n,1) = DP(n+1,1)/(tn(n,1)-t1)*cosd(DP(n+1,2)); % x
velocity component
                vect(n,2) = DP(n+1,1)/(tn(n,1)-t1)*sind(DP(n+1,2)); % y
velcoity component
            end

            % %Plot individual sensor vectors
            % [row col] = size(vect);
            % quiv = zeros(row,4);
            % quiv(:,3:4) = vect;
            % quiver(quiv(:,1),quiv(:,2),quiv(:,3),quiv(:,4),'b')

            %Curve fit to vector endpoints
            coeff = curvefit(vect,1);

            %Vector angle calculator based on slope and y-intercept of fit line
            if coeff(1)>0 && coeff(2)>0
                theta_exp = atand(coeff(2))+90; % angle of inclination of curve
fit line
            elseif coeff(1)<0 && coeff(2)>0
                theta_exp = atand(coeff(2))+270; %
            elseif coeff(1)>0 && coeff(2)<0
                theta_exp = atand(coeff(2))+90;
            else coeff(1)<0 && coeff(2)<0;
                theta_exp = atand(coeff(2))+270;
            end

            res(nm,1) = theta_exp; %Experimentally determined vector angle, deg
            %     theta_exp_ac = theta_exp-lam %deg, wave vector in AC CS

            vtot = zeros(rw-1,1);
            for n = 2:rw
                vtot(n-1,1) = (XY(n,2)-XY(n,1)*tand(theta_exp-
90))*cosd(theta_exp-90)/(tn(n-1,1)-t1); % total velocity equation using assumed
positions with real time
            end

            res(nm,2) = mean(vtot); % magnitude of phase speed vector

        end

        data(num,1) = x;
        data(num,2) = y;
        data(num,3) = abs(max(res(:,1))-min(res(:,1)))/2; %average of angle
error
        data(num,4) = abs(max(res(:,2))-min(res(:,2)))/2; %average of velocity
error

        num = num+1; % set to value for next iteration
    end
end

%finding mimimums
[rt,ct]=find(data(:,3)==min(data(:,3)));
data(rt,:) % prints minimum angle error row
```

```
[rv,cv]=find(data(:,4)==min(data(:,4)));
data(rv,:)%prints minimum velocity error row

%% Plotting Module
%making surface plots
xlin = linspace(0,1,100); %make arbitrary mesh to fit to data points later
ylin = linspace(delty,0.1,100);
[X Y] = meshgrid(xlin,ylin);
Zt = griddata(data(:,1),data(:,2),data(:,3),X,Y,'cubic');
figure(1)
mesh(X,Y,Zt)
% axis tight;
hold on
plot3(data(:,1),data(:,2),data(:,3),'r.')
hold off
xlim([0 0.1])
ylim([0 0.1])
xlabel('x-Position, in')
ylabel('y-Position, in')
zlabel('Angle Uncertainty, deg')
title('Angle Uncertainty Surface Plot')

figure(2)
Zv = griddata(data(:,1),data(:,2),data(:,4),X,Y,'cubic');
mesh(X,Y,Zv)
% axis tight;
hold on
plot3(data(:,1),data(:,2),data(:,4),'r.')
hold off
xlim([0 0.1])
ylim([0 0.1])
xlabel('x-Position, in')
ylabel('y-Position, in')
zlabel('Velocity Uncertainty, in/s')
title('Velocity Uncertainty Surface Plot')

%% Saving Module
save 'SWIFT_TS_data.txt' data -ASCII -double -tabs % saves into 16 digit ascII
.txt file
```

F-6: Equations for Converting Spectral Correlation Data into a Wave Vector

The required parameters for computing the wave vector of a traveling disturbance using a hotfilm sensor are the physical locations of each sensor, the frequency of the disturbance being analyzed, and the phase shift at each sensor referenced to a datum sensor. The locations of each sensing element are described below in a Cartesian coordinate system by the position vectors x_n and y_n. The subscript 1 is used to denote the coordinates of the datum sensor. The difference in location for each sensor relative to the datum sensor is described by Eqn (F-15) and Eqn (F-16).

$$\Delta x_n = x_n - x_1 \tag{F-15}$$

$$\Delta y_n = y_n - y_1 \tag{F-16}$$

The magnitude of the distance between the datum sensor and the *n*th sensor can then by computed with Eqn (F-17). Likewise the angle formed between the *x* axis and the position vector pointing to the *n*th sensor is calculated using Eqn (F-18).

$$d_n = \sqrt{\Delta x_n^2 + \Delta y_n^2} \tag{F-17}$$

$$\phi_n = \tan^{-1}\left(\frac{\Delta y_n}{\Delta x_n}\right) \tag{F-18}$$

The frequency of the traveling disturbance under analysis, f, is determined through careful examination of the spectra of the hotfilms and the correlation functions. The frequencies with the highest correlation coefficient in the band of interest should be chosen for analysis. The magnitudes of the group and phase velocities of the wave are determined using Eqn (F-19) and Eqn (F-20), respectively.

$$c_{ph,n}(f) = 2\pi d_n \frac{f}{\Delta\theta(f)} \tag{F-19}$$

$$c_{gr,n}(f) = 2\pi d_n \frac{df}{d(\Delta\theta)} \tag{F-20}$$

The magnitude of the phase velocity is given by Eqn (F-19) and the direction is determined by Eqn (F-18). An example of the results of these calculations is shown in Figure F-1 for an arbitrary case.

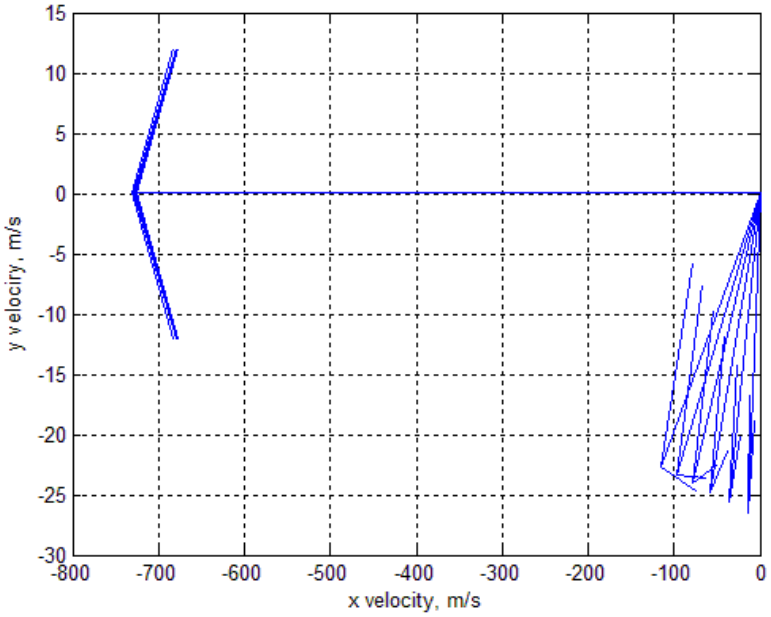

Figure F-1 Quiver Plot of Phase Velocity Vectors

The vectors are then plotted in a Cartesian system and a line is fit using the tips of the vectors originating at the datum sensor. The line is of the form$z = z_0 + z_1 x$ and the slope and y-intercept can be used to determine the direction of the wave vector. There are four possible combinations of the sign of the y-intercept and slope that effect the way the wave vector angle, θ_e, is calculated. These combinations and the resulting angle formulas are listed in Table F-2.

Table F-2 Effect of y-Intercept and Slope Combinations on θ_e

Combination 1:	$z_0 > 0$	$z_1 > 0$	$\theta_e = \tan^{-1}(z_1) + \frac{\pi}{2}$
Combination 2:	$z_0 < 0$	$z_1 > 0$	$\theta_e = \tan^{-1}(z_1) + \frac{3\pi}{2}$
Combination 3:	$z_0 > 0$	$z_1 < 0$	$\theta_e = \tan^{-1}(z_1) + \frac{\pi}{2}$
Combination 4:	$z_0 < 0$	$z_1 < 0$	$\theta_e = \tan^{-1}(z_1) + \frac{3\pi}{2}$

The information found in the previous equations can then be combined to solve for the magnitude of the wave front's velocity, as shown in Eqn (F-21).

$$w_n = \left(c_{ph}\sin(\phi_n) - c_{ph}\cos(\phi_n)\tan\left(\theta_e - \frac{\pi}{2}\right)\right)\cos\left(\theta_e - \frac{\pi}{2}\right) \tag{F-21}$$

A sample output of the wave vector angle and magnitude for the arbitrary case presented previously in Figure F-1 is shown in Fig F-2.

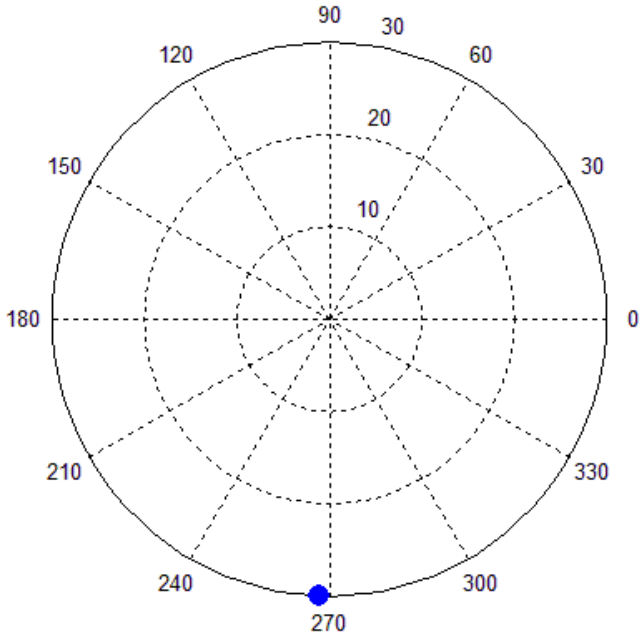

Figure F-2 Polar Plot of Wave Velocity Magnitude and Direction

F-7: Matlab Script to Convert Correlation Data into a Wave Vector

A Matlab script has been written for converting the phase shifts between sensors and their relative positions into a wave vector. The user inputs the frequency of the disturbance being used for measurements and the phase angles between the datum and comparison sensor elements as well as the geometry of the sensors. The code then outputs the wave velocity vector's magnitude and direction.

```
clear all
% clc

%% PHYSICAL PARAMETERS OF SENSOR [FOUND FROM MEASUREMENTS ON ACTUAL SENSOR]

lam = 30; %deg, wing leading edge sweep (for aligning wave vector with AC CS)
%Origin is set to (0,0) at center of sensor 1 (x1=y1=0)
%The actual sensor 1 is arbitrary and fluctuates with whichever sensor is
%the current datum.  Other sensor numbers can be rearranged accordingly

f = 1000; % frequency of the disturbance being analzyed
% Input phases for each sensor referenced to datum
phase = [-30
    -1
    -31
    -2
    -32
    -3
    -33
    -4
    -34
    -5
    -35
    -6]; % Phase angle for sensors 2 to n with respect to sensor 1, deg

XY = [0 0
    1.24 2.45
    2.24 0
    3.48 2.45
    4.51 0
    5.75 2.45
    6.77 0
    7.97 2.45
    8.99 0
    10.21 2.45
    11.23 0
    12.43 2.45
    13.48 0]; % x,y coordinates of sensor 1-13, mm

[rw cl] = size(XY);

DP = zeros(rw,2); %Initialize resultant distance and angle phi [dist (in), phi
(deg)]
for n = 1:rw
    DP(n,1) = sqrt(XY(n,1)^2+XY(n,2)^2);
    DP(n,2) = atan2(XY(n,2),XY(n,1))*180/pi;
```

```
end

res = zeros(1,2); %initialize angle, V storage matrix

%% WAVE ANGLE CALCULATOR [THIS MODULE WILL BE USED FOR ACTUAL FLIGHT DATA]

%Vector lengths using assumed sensor x and y positions with actual time
vect = zeros(rw-1,2); %vector containing x and y coordinates to be curve fitted
for n = 1:rw-1
    vect(n,1) = 2*pi*DP(n+1,1)*f/(phase(n)*pi/180)*cosd(DP(n+1,2)); % x-
component of phase speed, mm/s
    vect(n,2) = 2*pi*DP(n+1,1)*f/(phase(n)*pi/180)*sind(DP(n+1,2)); % y-
component of phase speed, mm/s
end

%Plot individual sensor vectors
figure(1)
[row col] = size(vect);
quiv = zeros(row,4);
quiv(:,3:4) = vect/1000; % convert velocity to m/s
quiver(quiv(:,1),quiv(:,2),quiv(:,3),quiv(:,4),'b')
grid on
xlabel('x velocity, m/s')
ylabel('y velociry, m/s')

%Curve fit to vector endpoints
coeff = curvefit(vect,1);

%Vector angle calculator based on slope and y-intercept of fit line
if coeff(1)>0 && coeff(2)>0
    theta_exp = atand(coeff(2))+90; % angle of inclination of curve fit line
elseif coeff(1)<0 && coeff(2)>0
    theta_exp = atand(coeff(2))+270; %
elseif coeff(1)>0 && coeff(2)<0
    theta_exp = atand(coeff(2))+90;
else coeff(1)<0 && coeff(2)<0;
    theta_exp = atand(coeff(2))+270;
end

res(1,1) = theta_exp; %Experimentally determined vector angle, deg
%     theta_exp_ac = theta_exp-lam %deg, wave vector in AC CS

vtot = zeros(rw-1,1);
for n = 2:rw
    vtot(n-1,1) = (vect(n-1,2)-vect(n-1,1)*tand(res(1,1)-90))*cosd(res(1,1)-
90);
end

res(1,2) = mean(vtot)/1000; % average magnitude of phase speed vector, m/s

resr = zeros(1,2);
resr(:,1) = res(:,1).*pi./180; % convert angle to radians
resr(:,2) = res(:,2);

%% Plotting Module
% hold on
figure(2)
polar(resr(:,1),resr(:,2),'b.')
% polar(theta*180/pi,V,'r.')
title('Polar Plot of Possible Instrument Readings');
```